

A Thesis Submitted for the Degree of PhD at the University of Warwick

Permanent WRAP URL:

<http://wrap.warwick.ac.uk/176302>

Copyright and reuse:

This thesis is made available online and is protected by original copyright.

Please scroll down to view the document itself.

Please refer to the repository record for this item for information to help you to cite it.

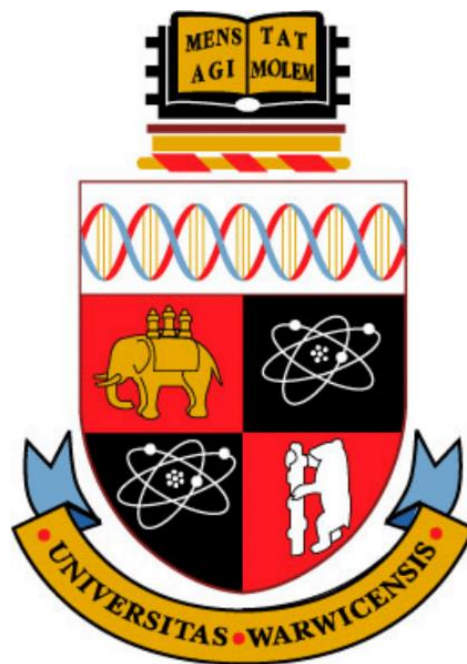
Our policy information is available from the repository home page.

For more information, please contact the WRAP Team at: wrap@warwick.ac.uk

Synthesis, Characterisation and Analysis of Metal-organic Frameworks for Sustainable Catalysis Applications

by

Katie Jayne Everden



A thesis submitted in partial fulfilment of the requirements for the degree of

Doctor of Philosophy in Engineering

Supervised by Dr Volkan Degirmenci and Professor Richard Walton

School of Engineering and Department of Chemistry

University of Warwick

September 2022

Table of Contents

| | |
|---|----|
| Chapter 1: Introduction | 1 |
| 1.1 - Background..... | 1 |
| 1.2 - Carbon Dioxide and The Greenhouse Effect..... | 2 |
| 1.3 - MOFs | 4 |
| 1.3.1 - History..... | 4 |
| 1.3.2 - Structure | 4 |
| 1.3.3 - Nomenclature | 9 |
| 1.3.4 - Applications | 9 |
| 1.3.5 – Mixed-metal MOFs and mixed-linker MOFs..... | 9 |
| 1.3.6 – Ti-based MOFs | 12 |
| 1.3.7 – Sn-based coordination polymers and MOFs..... | 16 |
| 1.4 – Synthesis of MOFs | 19 |
| 1.4.1 – Hydrothermal and solvothermal synthesis..... | 19 |
| 1.4.2 – Electrochemical synthesis..... | 21 |
| 1.4.3 – Microwave-assisted synthesis..... | 21 |
| 1.4.4 – Mechanochemical synthesis | 22 |
| 1.4.5 – Sonochemical synthesis | 22 |
| 1.5 – Photocatalysis | 23 |
| 1.5.1 – Traditional inorganic semiconductors | 24 |
| 1.5.2 – MOFs for photocatalysis | 25 |
| 1.5.3 – MOFs for the photocatalytic reduction of CO ₂ | 26 |
| 1.6 – MOFs for CO ₂ Conversion to Cyclic Carbonates using Epoxides | 27 |
| 1.7 – MOFs for Glucose Conversion to 5-HMF Epoxides | 31 |
| 1.8 – Project Aims..... | 33 |
| 1.9 – References | 34 |
| | |
| Chapter 2: Experimental Techniques and MOF Syntheses..... | 44 |
| 2.1 – Chapter Summary..... | 44 |
| 2.2 – Characterisation Methods | 44 |
| 2.2.1 – Powder X-ray Diffraction (PXRD)..... | 44 |
| 2.2.1.1 - Background | 44 |
| 2.2.1.2 – Experimental Details | 47 |
| 2.2.2 – Single Crystal X-ray Diffraction..... | 48 |

| | |
|--|----|
| 2.2.2.1 – Background | 48 |
| 2.2.2.2 – Experimental Details | 48 |
| 2.2.3 – Thermogravimetric analysis (TGA) | 48 |
| 2.2.3.1 – Background | 48 |
| 2.2.3.2 – Experimental Details | 49 |
| 2.2.4 – Scanning Electron Microscopy (SEM) and Energy Dispersive X-ray Analysis (EDXA) | 49 |
| 2.2.4.1 – Background | 49 |
| 2.2.4.2 – Experimental Details | 49 |
| 2.2.5 – ¹ H Nuclear Magnetic Resonance (NMR) Spectroscopy | 49 |
| 2.2.5.1 – Background | 49 |
| 2.2.5.2 – Experimental Details | 51 |
| 2.2.6 – X-ray Photoelectron Spectroscopy (XPS) | 51 |
| 2.2.6.1 – Background | 51 |
| 2.2.6.2 – Experimental Details | 52 |
| 2.2.7 – Extended X-ray Absorption Fine Structure (EXAFS) and X-ray Absorption Near Edge Spectroscopy (XANES) | 53 |
| 2.2.7.1 – Background | 53 |
| 2.2.7.2 – Experimental Details | 53 |
| 2.2.8 – Ultraviolet-Visible (UV-Vis) Spectroscopy | 54 |
| 2.2.8.1 – Background | 54 |
| 2.2.8.2 – Experimental Details | 55 |
| 2.2.9 – Brunauer-Emmett-Teller (BET) Surface Area Analysis | 55 |
| 2.2.9.1 – Background | 55 |
| 2.2.9.2 – Experimental Details | 58 |
| 2.2.10 – High Performance Liquid Chromatography (HPLC) | 59 |
| 2.2.10.1 – Background | 59 |
| 2.2.10.2 – Experimental Details | 59 |
| 2.2.11 – CHN Analysis | 60 |
| 2.2.11.1 – Background | 60 |
| 2.2.11.2 – Experimental Details | 60 |
| 2.2.12 – Inductively Coupled Plasma-Optical Emission Spectroscopy (ICP-OES) | 60 |
| 2.2.12.1 – Background | 60 |
| 2.2.12.2 – Experimental Details | 61 |
| 2.2.13 – Infrared (IR) Spectroscopy | 61 |
| 2.2.13.1 – Background | 61 |

| | |
|---|-----------|
| 2.2.13.2 – Experimental Details | 62 |
| 2.3 – Software | 62 |
| 2.3.1 – ChemDraw..... | 62 |
| 2.3.2 – Mercury..... | 62 |
| 2.3.3 – Diamond..... | 62 |
| 2.3.4 – Topspin..... | 62 |
| 2.3.5 – CasaXPS | 63 |
| 2.3.6 – GSAS-II..... | 63 |
| 2.3.7 – OriginPro | 63 |
| 2.4 – Synthetic Methods..... | 63 |
| 2.4.1 – Solvothermal Synthesis | 63 |
| 2.4.2 – Reflux | 65 |
| 2.4.3 – Microwave | 65 |
| 2.4.4 – Reactor-Ready™ | 66 |
| 2.5 – Catalysis Set-Ups..... | 67 |
| 2.5.1 – Photocatalytic reduction of CO ₂ using a Solar Simulator | 67 |
| 2.5.2 – Conversion of Epoxides to Cyclic Carbonates using CO ₂ | 68 |
| 2.5.3 – Conversion of Glucose to 5-HMF | 69 |
| 2.6 – Specific Syntheses..... | 70 |
| 2.6.1 – Synthesis of MUV-10..... | 70 |
| 2.6.2 – Synthesis of UiO-66..... | 71 |
| 2.6.3 – Synthesis of Ce-BDC-NH ₂ | 71 |
| 2.6.4 – Other MOF syntheses..... | 72 |
| 2.7 - References | 72 |
| | |
| Chapter 3: Modifications to MUV-10, a Ti(IV)-based MOF | 75 |
| 3.1 – Chapter Summary | 75 |
| 3.2 – Introduction..... | 75 |
| 3.3 – Initial Synthesis and Characterisation of MUV-10 | 78 |
| 3.4 – Synthesis and Scalability of MUV-10..... | 83 |
| 3.5 – Attempted Metal(II) Substitution in MUV-10..... | 92 |
| 3.6 – Substitution of Titanium(IV) in MUV-10..... | 93 |
| 3.7 – Exchanging the Organic Linker in MUV-10..... | 112 |
| 3.8 – Conclusions..... | 123 |
| 3.9 – References | 124 |

| | |
|--|------------|
| Chapter 4: An Investigation into Syntheses of Novel Ti(IV) and Sn(IV) MOFs | 126 |
| 4.1 – Introduction..... | 126 |
| 4.2 – Attempted Synthesis of Novel Ti(IV) MOFs..... | 127 |
| 4.3 – Attempted Synthesis of Mixed-Metal Ti MOFs | 150 |
| 4.4 – Attempted Synthesis of Sn(IV) MOFs..... | 155 |
| 4.5 – Conclusions | 183 |
| 4.6 – References | 184 |
| | |
| Chapter 5: Sustainable Catalysis using MOFs | 186 |
| 5.1 – Introduction..... | 186 |
| 5.2 - MOFs for the Photocatalytic Reduction of CO ₂ | 186 |
| 5.3 – MOFs for the Conversion of Glucose to 5-HMF | 199 |
| 5.4 – MOFs for the Conversion of CO ₂ to Cyclic Carbonates using Epoxides | 209 |
| 5.5 – Conclusions | 222 |
| 5.6 – References | 224 |
| | |
| Chapter 6: Conclusions and Future Work | 225 |
| 6.1 – Introduction..... | 225 |
| 6.2 - Modifications to MUV-10: Conclusions and Future Possibilities | 225 |
| 6.3 - Attempted Syntheses of Novel Ti(IV) and Sn(IV) MOFs: Conclusions and Future Possibilities | 226 |
| 6.4 - Sustainable Catalysis Applications: Conclusions and Future Possibilities ... | 228 |

Acknowledgements

Firstly, I would like to thank my supervisors, Professor Richard Walton and Dr Volkan Degirmenci for their support and guidance throughout my research. I have learned a lot during these 4 years and will miss the MOF meetings. I would also like to thank Dr Michael Katz and his research group from Memorial University, Newfoundland, where I had an incredible three months living in Canada, looking at gas adsorptions and amorphous MOF materials.

I would also like to thank many others from Warwick, including Dr Marc Walker for XPS data, Professor Ross Hatton for help with Tauc plot analysis and Dr Guy Clarkson for single crystal XRD. I would also like to thank Dr James Crosland for HPLC for glucose conversion experiments and thank Dr Thomas Chamberlain for sharing his knowledge on using MOFs for catalysis.

I would like to thank the rest of the Walton Group for being a pleasure to work alongside for the duration of my studies and am grateful for the friendships that I have formed within the group. I would also like to thank Jasmine Clayton and Katie Pickering for helping to run some XRD and TGA samples when there was restricted lab access during lockdown.

Finally, I'd like to thank my family and friends, who have supported and encouraged me throughout my studies.

Abstract

A range of metal-organic frameworks (MOFs) have been synthesised and characterised by a variety of techniques, primarily including powder X-ray diffraction (PXRD), thermogravimetric analysis (TGA), UV-Vis and Scanning Electron Microscopy (SEM). Some of these MOFs have been investigated for applications related to CO₂ capture and catalysis.

A mixed-metal MOF, MUV-10, comprised of titanium in combination with Ca or Mn, is thoroughly investigated with the aim of making modifications, including the substitution of some Ti for Sn. Synchrotron X-ray absorption spectroscopy confirmed the successful incorporation of Sn(IV) into the mixed-metal MOFs. Gas adsorption studies were also completed and a brief investigation into the modification of the organic linker used in the material, with effects on the band gap of the material discussed. The modified MUV-10 MOFs have been extensively analysed and their activity tested in the photoreduction of carbon dioxide, the reduction of carbon dioxide to cyclic carbonates using epoxides and in the conversion of glucose to 5-hydroxymethylfurfural (5-HMF). For the formation of cyclic carbonates using epoxides and carbon dioxide, MUV-10 offered excellent conversion, recyclability, and stability. For the conversion of glucose, when small quantities of HCl were used, MUV-10 demonstrated a greater production of 5-HMF compared to the UiO-66 reference material, with enhanced performance for MUV-10 substituted with Sn.

The synthesis of novel Ti MOFs has been attempted, and although none were produced in a form for structure solution, some promising materials were identified for future study. Similar studies on the synthesis of Sn(IV) MOFs, not yet known in the literature, also proved not to form large enough crystals for structure solution, although a new anionic Sn(II) coordination polymer based on the chelidamate ligand was crystallised.

Declaration

This thesis is submitted to the University of Warwick in support of my application for the degree of Doctor of Philosophy. The work presented in this thesis has been completed at the University of Warwick. This thesis has not been submitted to any other academic institution or as part of any other higher degree.

The work presented in this thesis was carried by myself, with the following exceptions: XPS was carried out by Dr Marc Walker, Single crystal XRD was carried out by Dr Guy Clarkson, Mott Schottky was carried out by Irina Rodríguez Terrero, HPLC was carried out by Dr James Crosland, XRD analysis was carried out by either Dr David Walker, Dr Thomas Chamberlain or Jasmine Clayton during the pandemic and some TGA was carried out by either Jasmine Clayton or Katie Pickering during the pandemic. EXAFS and XANES were carried out at Diamond Light Source, and some samples for ICP and CHN analysis were either sent to Medac Ltd or Exeter Analytical.

It is expected that some work from this thesis will be published in due course.

Abbreviations

- 5-HMF** 5-hydroxymethylfurfural
- aMOF** Amorphous metal-organic framework
- BET** Brunauer-Emmett-Teller
- BPDA** 4,4'-Biphenyldicarboxaldehyde
- CALF** Calgary framework
- CAT** Catecholate
- CIFs** Crystallographic information files
- DEET** *N,N*-Diethyl-3-methylbenzamide
- DEF** *N,N*-Diethylformamide
- DMA** Dimethylacetamide
- DMF** *N,N*-Dimethylformamide
- DMSO** Dimethyl sulfoxide
- EDXA** Energy dispersive X-ray analysis
- ELSD** Evaporative Light Scattering Detector
- EXAFS** Extended X-ray absorption fine structure
- FTIR** Fourier-Transform Infrared
- GC** Glassy carbon
- H₂AIP** 5-aminoisophthalic acid
- H₂ATP** 2-aminoterephthalic acid
- H₂BDC** Terephthalic acid
- H₂BPDC** Biphenyl-4,4'-dicarboxylic acid
- H₂CDC** Trans-1,4-cyclohexanedicarboxylic acid

H₂NBDC 2-nitro-benzene-1,4-dicarboxylic acid

H₂NDC 1,4-naphthalenedicarboxylic acid

H₃BTB 1,3,5-tri(4-carboxyphenyl) benzene

H₃BTC Benzene-1,3,5-tricarboxylic acid/trimesic acid

H₃BTCA 4',4''',4''''-nitriлотris([1,1'-biphenyl]-4-carboxylic acid))

H₃TCA/4,4,4-NTB 4,4',4''-nitriлотribenzoic acid

H₃TTC Trithiocyanuric acid

H₄BTEC 1,2,4,5-benzenetetracarboxylic acid

H₄DOBDC 2,5-dihydroxyterephthalic acid

H₄TBApy 4,4',4'',4'''-(pyrene-1,3,6,8-tetrayl)tetrabenzoic acid

H₄TBP 5,10,15,20-tetra(p-benzoato)porphyrin

HOMO Highest occupied molecular orbital

HT High temperature

ICP Inductively coupled plasma

IUPAC International Union of Pure and Applied Chemistry

LCCT Ligand to cluster charge transfer

LT Low temperature

LUMO Lowest unoccupied molecular orbital

MDIP 3,3',5,5'-tetracarboxydiphenylmethane

MIBK Methyl isobutyl ketone

MIL Materials Institute Lavoisier

MIP Molecularly imprinted polymer

MOF Metal-organic framework

MUV Materials of Universidad de Valencia

NMR Nuclear magnetic resonance

NTU Nanyang Technological University

PCN Porous coordination network

PDA Photo-diode array

PDF Pair distribution function

PXRD Powder X-ray diffraction

SBU Secondary building unit

SEM Scanning electron microscopy

TBAB Tetrabutylammonium bromide

TCPP Tetra-kis(4-carboxyphenyl)porphyrin

TEA Triethylamine

TEM Transmission Electron Microscopy

TEOA Triethanolamine

TGA Thermogravimetric analysis

THF Tetrahydrofuran

THO Triphenylene-2,3,6,7,10,11-hexakis(olate)

UiO University of Oslo

UPS Ultraviolet photoelectron spectroscopy

XANES X-ray absorption near edge structure

XPS X-ray photoemission spectroscopy

XRD X-ray diffraction

ZSTU Zhejiang Sci-Tech University

Chapter One

Introduction

1.1 Background

Due to rising atmospheric carbon dioxide (CO₂) levels, which will have detrimental effects on the planet if not urgently addressed, efforts to reduce CO₂ emissions, and the subsequent environmental impacts, have become imperative. Rising CO₂ levels are increasing the frequency of extreme weather events, causing rising sea levels, destroying habitats, and reducing biodiversity. The rise in CO₂ is affecting availability of food sources and is compromising life until it is addressed.¹

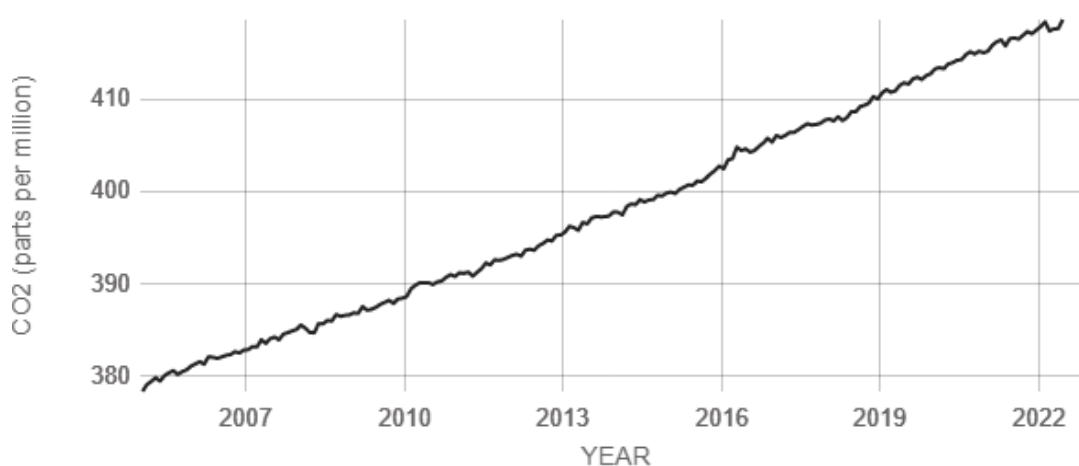
Metal-organic frameworks (MOFs) are a class of porous materials, where the structure is comprised of metallic clusters with bridging organic linkers and the pores range from micro- to mesopores.² MOFs can offer high surface areas, high stabilities, and high porosities, making them attractive for a range of applications, including CO₂ capture and conversion.

One application that MOFs are being increasingly investigated in, is the photocatalytic reduction of CO₂.³ This application is a potential remedy to the current rising atmospheric CO₂ levels. Alongside photocatalytic reduction, other applications to assist with combating rising CO₂ levels include converting CO₂ into cyclic carbonates using epoxides. Both conversion applications are arguably better than some current methods used to reduce atmospheric CO₂ levels, as some existing methods, such as CO₂ capture, can cause CO₂ leakage that can then cause problems such as the acidification of natural water resources.⁴ By converting CO₂, as opposed to a method such as storing it, these potential drawbacks to the environment are avoided, and it is an added benefit if conversion products can be of economic advantage.

Another relevant application of MOFs is the conversion of glucose to 5-hydroxymethylfurfural (5-HMF), a valuable platform chemical. This conversion is beneficial since it uses biomass instead of fossil fuels, which is readily available and sustainable, provided that waste is used, and that the biomass is not valuable food. Many widely reported methods for this conversion have previously used toxic reagents and long synthesis times, and so using alternative MOFs in greener conditions is also of environmental advantage and is being explored in greater depth.⁵

1.2 Carbon Dioxide and The Greenhouse Effect

CO₂ is a greenhouse gas and contributes to the warming of the Earth. The greenhouse effect is a natural process, allowing human life to exist on Earth in the first place. However, over the last century, human activities, such as the burning of fossil fuels and deforestation, have contributed to increased carbon dioxide levels in the atmosphere, in turn enhancing the greenhouse effect, harming wildlife, food sources, and ultimately life on Earth. The latest reported measurement from July 2022 of carbon dioxide in the atmosphere is 419 ppm, where rapid growth from 2005 to the present year is shown below in Figure 1.1.⁶



Source: climate.nasa.gov

Figure 1.1: A graph to show the amount of CO₂ (parts per million) with the corresponding year.⁶

The greenhouse effect describes the way in which heat is trapped close to the surface of the Earth by greenhouse gases, such as carbon dioxide, methane and nitrous oxides.⁷ The surface of the Earth is initially warmed by the sun, where heat is then radiated back into the atmosphere. Greenhouse gas molecules, such as CO₂, can absorb some of this heat and radiate it back to space (shown by pathway A in Figure 1.2).⁸ Another possibility is that heat does not interact with greenhouse gases and goes directly back to space (shown by pathway B in Figure 1.2). A third option is that greenhouse gas molecules absorb some of the heat and radiate it back towards the surface of the Earth (shown by pathway C in Figure 1.2). However, with the increased prevalence of greenhouse gas molecules such as CO₂, more heat is being absorbed by greenhouse gases and radiated back to the surface of the Earth rather than traveling directly back to space (see right-hand side of Figure 1.2). Consequently, the increased temperature of the surface of the Earth is having devastating effects on life on Earth and needs rapid intervention and a move towards the reduction in production of greenhouse gases.

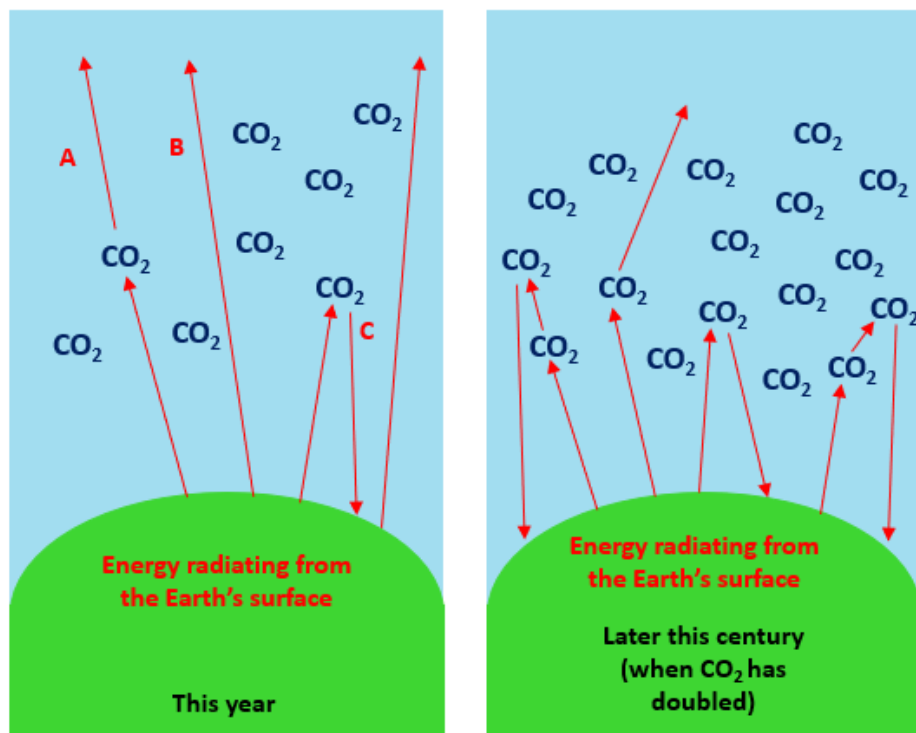


Figure 1.2: A diagram showing the three different pathways of heat being radiated from the surface of the Earth (left-hand side) and how this is affected later this century when it is predicted that CO₂ has doubled (right-hand side). Pathway A shows CO₂ absorbing some heat and radiating it back to space. Pathway B shows no interaction between heat and CO₂, where the heat travels directly back to space. Pathway C shows CO₂ absorbing some heat and radiating it back towards the surface of the Earth.⁸

One key aim of this project has been to use MOFs as catalysts to convert CO₂ to less harmful products such as methanol and formic acid via photocatalysis. These products can then be used in a variety of other chemical reactions, for example formic acid in esterifications.⁹ CO₂ conversion to cyclic carbonates via epoxides was also explored as a way of reducing CO₂ levels and gaining valuable products. MOFs were also examined in applications such as glucose conversion to valuable platform chemicals such as 5-HMF, in a greener process to those previously used.

1.3 MOFs

1.3.1 History

The field of metal-organic frameworks (MOFs) has received great attention and has grown significantly since their initial systematic synthesis and naming by Li and Yaghi in 1995.^{10,11} Since then, over 20,000 different MOF structures have been reported, with a great variety of different metals and organic linkers being exploited for different properties and applications.¹²

1.3.2 Structure

MOFs are highly crystalline, porous structures with large surface areas and low densities.¹³ The International Union of Pure and Applied Chemistry (IUPAC) recommended definition of a MOF is “a coordination network with organic ligands containing potential voids.”¹⁴ MOFs consist of metal oxide clusters, commonly known as Secondary Building Units (SBUs) or nodes, and are connected by organic linkers (see Figure 1.3) in an infinite two- or three- dimensional structure.¹⁵ The length and functionality of the organic linker affect the chemical nature and pore volume in MOFs.¹⁶

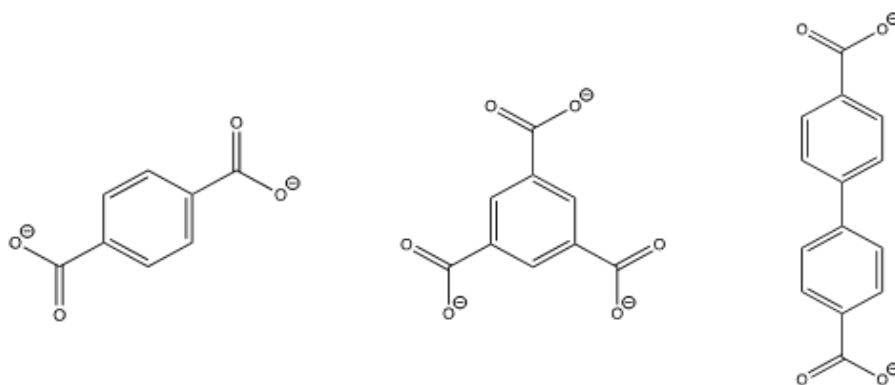


Figure 1.3: Commonly used organic linkers. From left to right: benzene-1,4-dicarboxylate (BDC), benzene-1,3,5-tricarboxylate (BTC) and biphenyl-4,4'-dicarboxylate (BPDC).

A major benefit of MOFs is their versatility. Metals and linkers can be tuned to alter a variety of properties of MOFs. For example, mixed-metal MOFs can be synthesised, creating highly stable materials with unique properties.

A range of different linkers can be used in MOF synthesis, containing a range of different atoms. Most reported MOFs contain linkers with an aromatic ring for structural rigidity, and often contain carboxylate groups for the coordination to the metal ions/metal-oxo clusters (as shown previously in Figure 1.3). However, some MOFs also contain other elements, such as nitrogen, that can bind to the metals via a lone pair of electrons, or elements such as sulfur (shown in Figure 1.4).

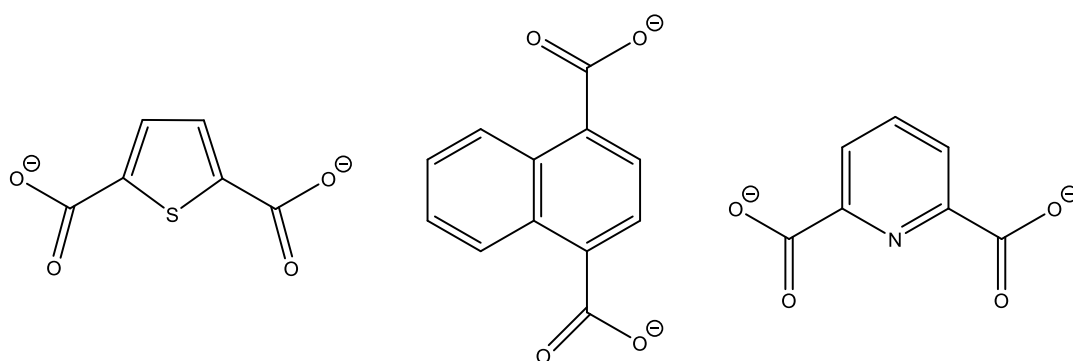


Figure 1.4: Further examples of organic linkers used in MOF synthesis. 2,5-thiophenedicarboxylic acid (left-hand side) is an example of a linker containing a 5-membered ring and a S atom, 1,4-naphthalenedicarboxylic acid (middle) is an example of a linker containing two aromatic rings and 2,6-pyridinedicarboxylic acid (right-hand side) is an example of an organic linker containing a 6-membered ring with a N atom. All linkers are shown here in their protonated form.

Functional groups can be added to the aromatic rings of linkers, to enhance certain properties, an example being the addition of an amine group (-NH₂) to enhance visible light adsorption in photocatalytic MOFs. This enhanced photocatalytic effect has been seen with NH₂-UiO-66(Zr), NH₂-MIL-125(Ti) and NH₂-MIL-101(Fe).³ Examples of linkers containing an -NH₂ functional group are 2-aminoterephthalic acid and 5-aminoisophthalic acid (Figure 1.5).

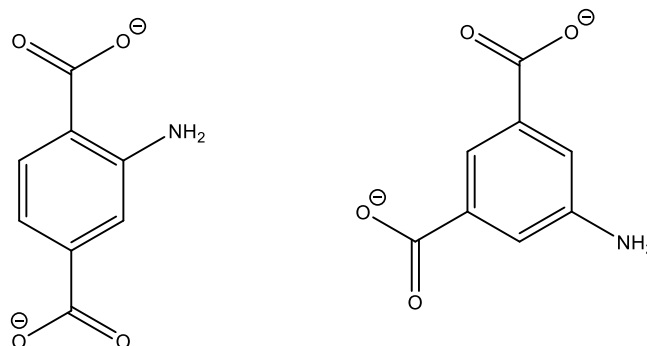


Figure 1.5: Examples of organic linkers containing an -NH₂ functional group. 2-aminoterephthalate (left-hand side) and 5-aminoisophthalate (right-hand side).

An example of a highly stable MOF is UiO-66, which consists of a cubic framework comprised of strong bonds between Zr(IV) ions and terephthalic acid (H₂BDC) linkers. UiO-66 is utilised for a variety of applications due to its excellent thermal, aqueous and acidic stability.¹⁷ The structure is shown in Figure 1.6 below where hexameric Zr clusters are shown in purple, O atoms are shown in red, C atoms are shown in black and H atoms are shown in grey.

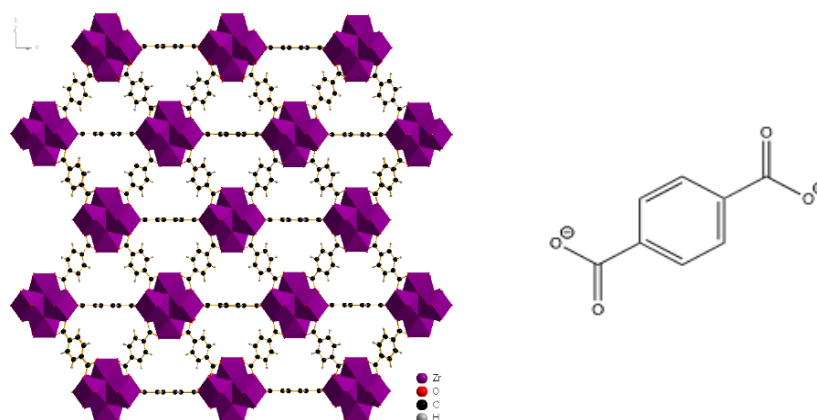


Figure 1.6: The structure of UiO-66 (left-hand side) containing Zr(IV) clusters and BDC linker (right-hand side). Zr clusters are shown in purple, O atoms are in red, C atoms are in black and H atoms are shown in grey.

Many research efforts have also involved looking into defect engineering into MOFs for enhanced effects in applications. Defects naturally occur in MOF synthesis, where unsaturated metal sites can enhance catalysis for many applications, however efforts are now turning to deliberately introducing more defective sites. Examples of defect engineering in MOFs include the introduction of missing linker and cluster defects. This can be by de novo synthesis or post-synthetic treatment. The introduction of defects can create additional active sites, can optimise acidity/basicity, can improve conductivity, can tailor mechanical responses, and can create greater pore sizes for enhanced diffusion and mass transfer.¹⁸ Whilst the introduction of defects can enhance properties, such as adsorption capacities and band structures, occasionally it has negative effects on properties, such as for gas adsorption and diffusion. An example of a defective MOF is defect-engineered UiO-66 modulated with trifluoroacetic acid, which has been used for conversion of cyclohexanone to cyclohexanol.¹⁹

In MOF synthesis, larger organic linkers tend to give larger pores and internal surface areas, however, this causes reduced mechanical stability of the MOF with respect to collapse. UiO-66, UiO-67 and UiO-68 are isoreticular, meaning they have the same topology, but differ in linker length (Figure 1.7) causing differences in porosity of the material formed (Figure 1.8).

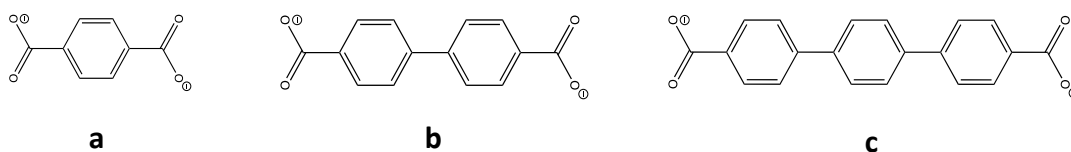


Figure 1.7: Linkers used in UiO-66 (labelled a), UiO-67 (labelled b) and UiO-68 (labelled c), respectively.

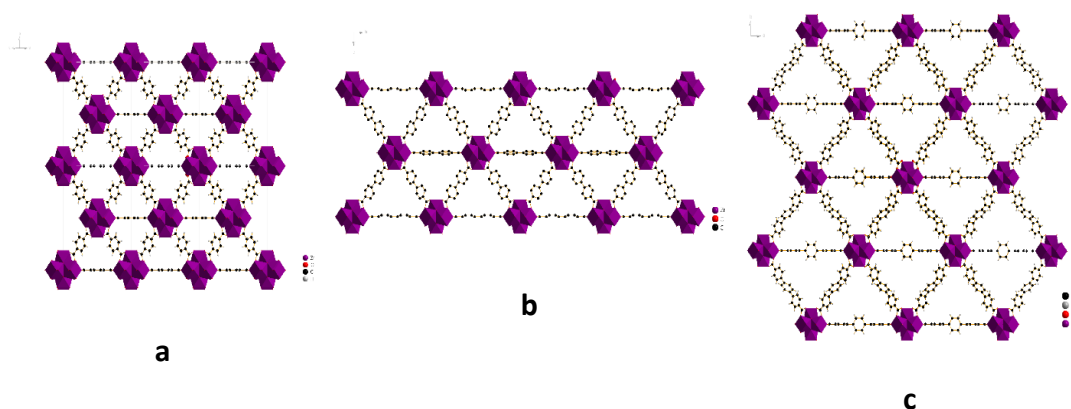


Figure 1.8: The structure of UiO-66 (labelled a), UiO-67 (labelled b) and UiO-68 (labelled c), respectively.

Whilst some MOFs, such as UiO-66, are known to have an incredibly rigid structure, others are known to be flexible through a “breathing effect.”² When an external stimulus is applied, such as temperature, pressure or chemical inclusion, some MOFs can be seen to expand.²⁰ An example of this effect is observed in MIL-53(Fe), where hydration and dehydration or solvent exchange causes the structure to alternate between a closed phase and an open phase, as shown in Figure 1.9.²¹

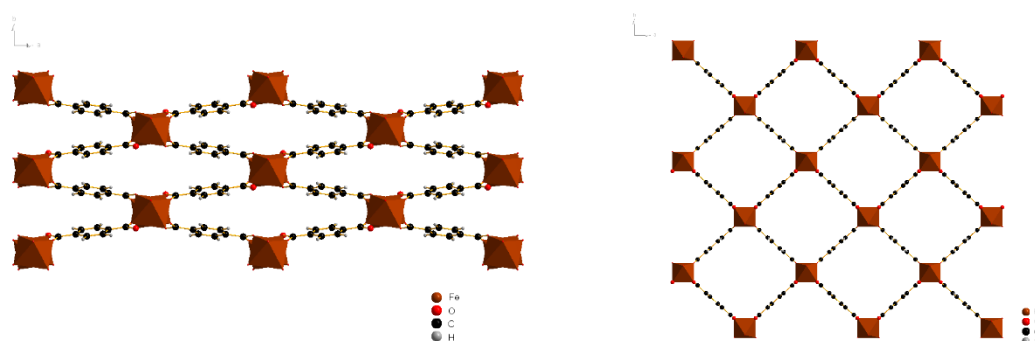


Figure 1.9: MIL-53(Fe) in the closed phase (left-hand side) and the open phase (right-hand side).

1.3.3 Nomenclature

The International Union of Pure and Applied Chemistry (IUPAC) recommended definition of a MOF is “a coordination network with organic ligands containing potential voids.”¹⁴ MOFs are a subclass of several more general terms, including ‘coordination polymer’, ‘coordination framework’, ‘metallo-supramolecular network’ and ‘hybrid material’, which all refer to a diverse range of materials where atoms are linked by molecular or ionic ligands.²²

1.3.4 Applications

Owing to the many different combinations of metals and linkers possible, with varying chemical properties and functionalities, MOFs are incredibly versatile materials with a wide range of applications. MOFs have found applications in drug delivery,^{23,24} such as in ibuprofen and procainamide release, and in gas storage applications,^{25,26} such as MOF-5 and MOF-177 being used for CO₂ storage. Other applications of MOFs include gas separation^{27,28} and catalysis.^{29,30}

1.3.5 Mixed-metal MOFs and mixed-linker MOFs

Many MOF structures exist with just one metallic element present and one type of organic linker bridging. However, multivariate MOFs have also emerged.

Mixed-metal MOFs contain at least two different metal ions or nodes as part of their framework, and are typically prepared by a one-pot synthesis or by post-synthetic ion exchange (Figure 1.10).³¹ Mixed-metal MOFs can be synthesised in a one-pot synthesis using mixtures of different metals, or by using metalloligands, however post-synthetic methods are often preferentially employed. In a post-synthetic ion-exchange (transmetalation), a monometallic MOF is soaked in a concentrated solution of another metal ion that is compatible with the framework. In general, the metal ions should have the same Coulombic charge, ionic radius and similar chemical behaviour.³²

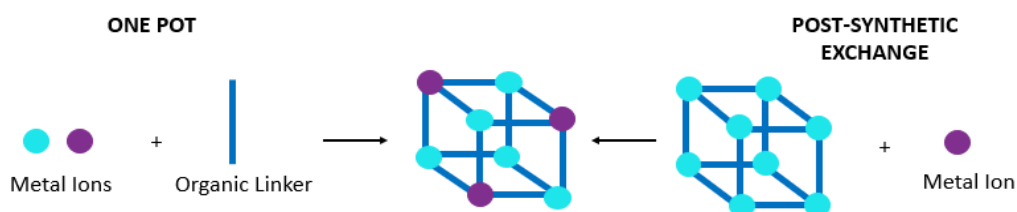


Figure 1.10: The formation of MOFs by either a one-pot synthesis or by post-synthetic exchange, reproduced from the literature.³⁰

The synthesis of mixed-metal MOFs has expanded the number of applications of some materials due to the synergistic effects created as a result of combining the properties of two or more different metals. Also, exchanging specific amounts of one metal for another can mean that properties of materials are precisely tuned for specific applications. An example of this is shown by a series of isostructural mixed-metal MOFs that were synthesised for use with hydrogen technology. A series of M-Cu-BTC MOFs were produced, where M is Zn^{2+} , Ni^{2+} , Co^{2+} or Fe^{2+} . These MOFs were produced by a post-synthetic exchange method. Upon partial exchange of some Cu^{2+} for the various other +2 metal ions, the gravimetric hydrogen uptake was shown to increase, which was attributed to increased binding enthalpy of H_2 with the unsaturated metal sites.³³

When synthesising mixed-metal MOFs, it is important to confirm whether the MOF formed contains both metals in the same structure as opposed to having formed a mixture of monometallic MOFs. It should also be confirmed as to how the metals are distributed within the structure, which can be done by methods such as transmission electron microscopy (TEM) and fourier-transform infrared (FTIR) spectroscopy. Compared to monometallic MOFs, mixed-metal MOFs can display enhanced effects, for example greater affinity towards target gases in gas sorption and storage applications. It is also possible to form MOFs containing the same metal ion but in two different oxidation states, where an example is a MOF utilising Mn(III) and Mn(II)

in $[\text{Mn}^{\text{III}}_2\text{Mn}^{\text{II}}_4\text{O}_2(\text{PYZ})_2(\text{C}_6\text{H}_5\text{CH}_2\text{COO})_{10}]$, which is used as a catalyst for a catecholase oxidation reaction.³⁴

It is also possible to form isostructural lattices by replacing one linker with another linker, containing additional substituents. This causes a decrease in pore volume and size but can provide other enhanced effects. For example, it has been found that exchanging all terephthalic acid for 2-aminoterephthalic acid can form exactly the same MOF structure, however due to the presence of the amino group, shows reduced pore volume, mild basicity and a yellow colour caused by an additional absorption band in optical spectroscopy.³⁴

It has also been found that MOFs can be prepared with more than one linker in the same structure (Figure 1.11).³⁴ Mixed-linker MOFs can be formed using linkers that do not vary much in terms of relative size and coordination mode, but also have been formed using linkers that contrast significantly. By forming MOFs with mixed linkers, the use of different functional groups can modify the pore environments and can create a synergy of complementary or contradictory properties.³⁵



Figure 1.11: A schematic showing the formation of a mixed-linker MOF, reproduced from the literature.³³

As well as one-pot syntheses, post-synthetic modifications can also be carried out with the organic linker. Solvent-assisted ligand exchange has been shown to produce MOFs with a range of structures, with the thermodynamic driving force being the formation of more stable coordination bonds upon exchange.³⁶

1.3.6 Ti-based MOFs

Titanium MOFs started to emerge in 2006 with the discovery of MIL-91, which was the first Ti diphosphonate material with porosity (See Figure 1.12).³⁷ This was followed by a dicarboxylate-based MOF, MIL-125, in 2009.³⁸ MIL-125 was found to adsorb alcohols inside the framework and displayed photochromic effects upon UV-visible irradiation, which were attributed to electron transfer between Ti(III) and Ti(IV) centers. Subsequent work included the synthesis of the amine functionalised version of MIL-125, NH₂-MIL-125, which has shown greater photocatalytic activity in the photoreduction of CO₂ than the unfunctionalised version due to a reduction in band gap creating a better alignment with the bands of CO₂.³⁹ NH₂-MIL-125 has been used in the photocatalytic hydrogen production reaction⁴⁰ and for concurrent photocatalytic hydrogen generation and dye degradation under visible light irradiation.⁴¹

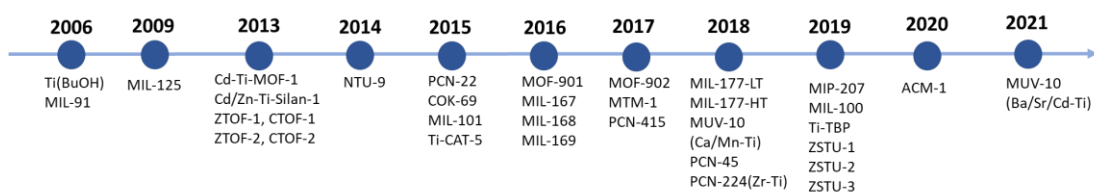


Figure 1.12: A timeline of titanium MOFs reported in the literature to date.

Following the synthesis of MIL-125, some mixed-metal materials were synthesised in 2013, including Cd-Ti-MOF-1, Cd/Zn-Ti-Silan-1, ZTOF-1/CTOF-1 and ZTOF-2/CTOF-2. In 2014, NTU-9 was synthesised which, at present, exhibits the smallest experimentally determined band gap in Ti MOFs.⁴²

In 2018 a mixed-metal Ti MOF coined MUV-10 was reported, which additionally contained Ca/Mn in the structure.⁴³ The MUV-10 materials proved to be extremely chemically robust under acidic and basic conditions. The band gap of the Ca version was 3.1 eV, whilst the Mn version had a value of 2.6 eV and displayed greater stability

in acidic and basic conditions compared to the Ca version. The MUV-10 band gaps are smaller than that of TiO₂ but were hoped to be reduced further, particularly in the case of MUV-10(Ca), and could be investigated in photocatalytic applications. In the literature, experiments were previously completed on photocatalytic H₂ production using gas chromatography (GC). MUV-10 was then further modified in 2021 and was shown to be able to incorporate other metallic elements (Cd²⁺, Sr²⁺ and Ba²⁺) as well as introducing other ions (H⁺, Li⁺, Na⁺, K⁺) into the pores to alter the electronic properties of the catalyst.⁴⁴ In 2022, it was reported that up to five functionalised modulators were able to be introduced into the MUV-10 structure, which increased the porosity compared to the original material.⁴⁵ The functionalised modulators contained NO₂, F, ^tBu, OH and NH₂ units.

MIL-177(LT) and MIL-177(HT) (where LT = low temperature and HT = high temperature, referring to their synthetic procedure) were also synthesised in 2018, using titanium isopropoxide and the 3,3',5,5'-tetracarboxydiphenylmethane (MDIP) linker.⁴⁶ The HT version is a thermally induced phase transformation of MIL-177(LT). It was found that the introduction of a conductive polymer into the pores of these MOFs led to an increase in charge separation lifetime under irradiation. The MOFs were also found to withstand extremely acidic environments.

Table 1.1 shows a summary of metal sources and linker precursors used in solely Ti MOFs (single metal). Over time, various methods have been developed to synthesise the same MOF, including reduction in synthesis time and changing the solvent(s) employed, and therefore in Table 1.1 only one example is included per entry. Many titanium MOFs that currently exist use titanium isopropoxide (Ti(ⁱOPr)₄) as the metal source in the synthesis. Other sources of Ti have been used, such as titanium chloride (TiCl₃), however this undergoes vigorous hydrolysis and releases hydrochloric acid vapour under ambient conditions. TiCl₃ has, however, still been used in some direct syntheses and post-synthetic metal exchanges.⁴⁷ Hydrous titanium dioxide (TiO₂) has

also been used, however, requires high reaction temperatures, long synthesis times and toxic media such as hydrofluoric acid (HF), which is an acute poison.⁴⁸

A key disadvantage of using Ti in MOF synthesis is that the reactive Ti precursors are prone to hydrolysis under the solvothermal conditions that MOF synthesis often utilises. This produces TiO₂, which is unreactive, and therefore great care needs to be taken to avoid the presence of water and to prevent hydrolysis during MOF synthesis.

Table 1.1: A summary of Ti MOFs including their metal source, linker precursor and synthesis conditions.

| MOF | Metal Source | Linker precursor | Synthesis conditions |
|--|---|--|---|
| MIL-91 ⁴⁹ | Titanium oxyacetylacetonate | <i>N,N'</i> -piperazinebis(methylene phosphonic acid) | Reflux synthesis: 68 hours |
| MIL-125 ³⁸ | Ti(O ⁱ Pr) ₄ (O ⁱ Pr) ₄ = tetraisopropoxide | Benzene-1,4-dicarboxylic acid (H ₂ BDC) | Solvothermal synthesis: 150°C 15 hours DMF (dimethylformamide) Methanol |
| NH ₂ -MIL-125 ⁴¹ | Ti(O ⁱ Pr) ₄ | 2-aminoterephthalic acid (H ₂ ATP) | Solvothermal synthesis: 120°C 72 hours DMF Methanol |
| NTU-9 ⁴² | Ti(O ⁱ Pr) ₄ | 2,5-dihydroxyterephthalic acid (H ₄ DOBDC) | Solvothermal synthesis: 120°C 5 days Acetic acid |
| PCN-22 ⁵⁰ | Ti ₆ O ₆ (O ⁱ Pr) ₆ (abz) ₆ Abz = 4-aminobenzoate | Tetra-kis(4-carboxyphenyl)porphyrin (TCPP) | Solvothermal synthesis: 150°C 48 hours Benzoic acid Diethylformamide (DEF) |
| COK-69 ⁵¹ | Titanocene dichloride (Cp ₂ TiCl ₂) | trans-1,4-cyclohexanedicarboxylic acid (H ₂ CDC) | Solvothermal synthesis: 110°C 48 hours DMF & Acetic acid |
| MIL-101 ⁴⁷ | TiCl ₃ | H ₂ BDC | Solvothermal synthesis: 120°C 18 hours Anhydrous DMF/Ethanol |
| Ti-CAT-5 ⁵² | Ti(O ⁱ Pr) ₄ | H ₆ THO (THO = triphenylene-2,3,6,7,10,11-hexakis(olate)) | Solvothermal synthesis: 180°C 48 hours TBAB (tetrabutylammonium bromide) DMF Amylamine |
| MOF-901 ⁵³ | Ti(O ⁱ Pr) ₄ | Benzene-1,4-dialdehyde | Solvothermal synthesis: 125°C 72 hours Methanol 4-aminobenzoic acid |

| | | | |
|---|--|--|---|
| MIL-167 ⁵⁴ | Ti(O ⁱ Pr) ₄ | H ₄ DOBDC | Solvothermal synthesis: 180°C 24 hours DEF Methanol |
| MIL-168 ⁵⁴ | Ti(O ⁱ Pr) ₄ | H ₄ DOBDC | Solvothermal synthesis: 180°C 48 hours DEF Catechol |
| MIL-169 ⁵⁴ | Ti ₄ O ₄ (ox) ₇ ·(pipH ₂) ₃ ·2H ₂ O pipH ₂ = piperazinium | H ₄ DOBDC | Solvothermal synthesis: 150°C 72 hours Distilled water Catechol |
| MOF-902 ⁵⁵ | Ti(O ⁱ Pr) ₄ | 4,4'-Biphenyldicarboxaldehyde (BPDA) | Solvothermal synthesis: 140°C 72 hours Methanol 4-aminobenzoic acid |
| MIL-177-LT ⁴⁶ (Also known as MIP-177) | Ti(O ⁱ Pr) ₄ | H ₄ mdip (mdip = 3,3',5,5'-tetracarboxydiphenylmethane) | Reflux synthesis: Formic acid 24 hours |
| MIL-177-HT ⁴⁶ | - | - | MIL-177-LT (as made above) 280°C 12 hours |
| MIP-207 ⁵⁶ | Ti(O ⁱ Pr) ₄ | BTC | Solvothermal synthesis: Acetic Acid Acetic Anhydride 120°C 48 hours (Also possible by reflux at 120°C for 12 hours). |
| MIL-100 ⁵⁷ | Ti ₆ | BTC | Solvothermal synthesis: Acetonitrile Tetrahydrofuran Acetic acid 160°C 48 hours |
| Ti-TBP ⁵⁸ | TiCl ₄ ·2THF THF = Tetrahydrofuran | 5,10,15,20-tetra(<i>p</i> -benzoato)porphyrin (H ₄ TBP) | Solvothermal synthesis: Acetic acid DMF 120°C 168 hours |
| ZSTU-1 ⁵⁹ | Ti(O ⁱ Pr) ₄ | 4,4',4''-nitrilotribenzoic acid (H ₃ TCA) | Solvothermal synthesis: 5 mL extra dry DMF 180°C 24 hours |
| ZSTU-2 ⁵⁹ | Ti(O ⁱ Pr) ₄ | 1,3,5-Tri (4-carboxyphenyl) benzene (H ₃ BTB) | Solvothermal synthesis: 5 mL extra dry DMF 180°C 30 hours |
| ZSTU-3 ⁵⁹ | Ti(O ⁱ Pr) ₄ | 4',4''',4''''-nitrilotris(((1,1'-biphenyl]-4-carboxylic acid)) (H ₃ BTCA) | Solvothermal synthesis: 5 mL extra dry DMF 180°C 30 hours |
| ACM-1 ⁶⁰ | Ti(O ⁱ Pr) ₄ | 4,4',4'',4'''-(pyrene-1,3,6,8-tetrayl)tetrabenzoic acid (H ₄ TBApy) | Solvothermal synthesis: Propionic acid DEF Chlorobenzene 150°C 24 hours |

1.3.7 Sn-based coordination polymers and MOFs

Currently various Sn(II) structures and MOFs exist, however Sn(IV) MOFs have not been reported in the literature, where it is unknown as to why they cannot easily form.

Several water-stable Sn(II) coordination polymers have been reported in the literature which have included the use of linkers such as 1,2,4,5-benzenetetracarboxylic acid, 1,3,5-benzenetricarboxylic acid, 4-hydroxypyridine-2,6-dicarboxylic acid and 1,3,5-cyclohexanetricarboxylic acid.⁶¹ Their structures were proved by single crystal X-ray diffraction, whilst ¹¹⁹Sn Mössbauer spectroscopy confirmed the number of different tin centres and their oxidation states. Other Sn(II) coordination polymers have been synthesised using pyridine-2,5-dicarboxylic acid and naphthalene-2,6-dicarboxylic acid.⁶²

Very few Sn(IV) coordination polymers exist, and those that do are formed by Sn(IV)-porphyrin building blocks, exhibiting photocatalytic properties. One Sn(IV)-porphyrin-based MOF was reported where the MOF consisted of Sn(IV) porphyrin struts which linked Zn atoms.⁶³ The Sn(IV) in this material is not integral to the framework structure and is only bound to the porphyrin. Another Sn(IV) material reported has been an Sn(IV) triphosphonate framework named CALF-28, which was proved to be robust, porous and water stable, however, cannot be classed as a MOF due to poor crystallinity seen in XRD data.⁶⁴

A Sn(II) MOF was reported, named KGF-10, which utilises trithiocyanuric acid (H₃TTC) as the organic linker.⁶⁵ Also reported was KGF-4, however this was termed a coordination polymer due to its lack of porosity, and therefore the key focus became working on the porous KGF-10 MOF. This material was synthesised based on some previous work, where a MOF comprised of Pb and H₃TTC was synthesised. Due to its toxicity, the Pb was then exchanged for Sn, which is less toxic. Strategies had

previously been developed in other fields to effectively replace Pb for Sn, and so similar strategies were then applied in the case of synthesising KGF-10. After the successful synthesis, KGF-10 was found to have a semiconducting band structure and redox properties, where Sn(II) was oxidised to Sn(IV), and it was also possible to migrate carriers upon photoexcitation.

Another Sn(II) MOF was formed with H₂BDC as the organic linker, and was able to be synthesised via a green method. The MOF proved efficient for dye removal and exhibited high aqueous and thermal stability.⁶⁶ Few MOFs are stable in aqueous environments, however the stability of this Sn(II) MOF can be accounted for by Sn(II) being a hard Lewis acid and being able to form strong coordination bonds with hard Lewis bases, such as carboxylate linkers.

It is unusual that Sn(IV) MOFs have not been reported since Sn(II) readily oxidises to Sn(IV) since it is more stable in the +4 oxidation state. It would be expected that the high charge of the metal cation in a +4 oxidation state would be able to form strong electrostatic interactions with organic linkers, forming robust and stable structures. Many other MOFs based on metal(IV) ions are among the most stable reported to date, including UiO-66, which is comprised of Zr(IV). Since Ti(IV) MOFs have been reported, and Sn(IV) is similar in size to Ti(IV), it could be expected that similar structures could form.

A previous investigation attempting the synthesis of novel Sn(II) and Sn(IV) MOFs using a range of different approaches proved highly challenging, and only yielded a Sn(II) coordination polymer.⁶⁷ The attempts involved investigating the effects of longer synthesis times, altering concentrations of base used to deprotonate organic linkers and using a molten ligand approach. The Sn(II) coordination polymer that was formed was comprised of the 4,4',4''-nitriлотribenzoic acid (4,4,4-NTB) linker (Figure 1.13), where it was initially hoped that a Sn(IV) MOF would form due to the presence

of three carboxylate sites and lone pair on the nitrogen atom in the linker. This possibility to bind via several sites was hoped to increase the stability of a MOF and was hoped to promote its formation. Instead, the 4,4,4-NTB ligands, and some hydroxide ions present from the synthesis, linked the metals to give a three-dimensional coordination polymer. Due to the structure being dense with no evidence for potential porosity, it could not be termed a MOF. The structure was found to be monoclinic with chemical formula: $\text{Sn}_4\text{K}(4,4,4\text{-NTB})_{2.5}(\text{OH})_{1.5}(\text{H}_2\text{O})$, where the unit cell contained tin in four different environments. This is an example demonstrating the difficult nature of forming a MOF with Sn in the +4 oxidation state, where efforts are still ongoing today.

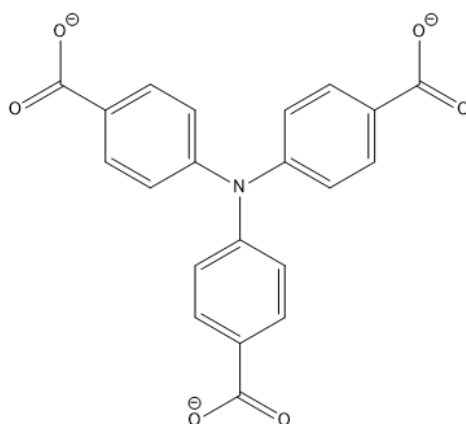


Figure 1.13: The structure of 4,4,4-NTB, containing three carboxylate groups and a central N atom, shown in deprotonated form.

Sn(IV) MOFs could be useful for a variety of reasons, but one key use could be to exploit the Lewis acidity of the Sn(IV), providing applications in heterogeneous catalysis. Also, by incorporating Sn(IV) into mixed-metal MOFs or alongside functionalised linkers, Sn(IV) MOFs could be formed that are tuned to specific applications, such as the photocatalytic reduction of CO_2 .

Another useful application of Sn(IV) MOFs could be in the conversion of glucose to 5-hydroxymethylfurfural (5-HMF). It has been shown in zeolite-beta, that substituting

a small percentage of either Al(III) or Si(IV) for Sn(IV), increases the activity and selectivity of the catalyst for the isomerisation of glucose to fructose in water, and is the current benchmark for a heterogeneous catalyst for this reaction.⁶⁸ The high activity and selectivity makes it a viable route in converting glucose from biomass into chemicals. Comparatively, MOFs have greater surface areas and greater structural diversity through the wide range of organic linkers that can be used, which can also control pore size and shape with the additional benefit of chemical functionalities being able to be added. One key potential drawback is the fact that MOFs are thermally and chemically less stable than zeolites due to the organic component.¹³ Overall, there has been a lot of potential for Sn(IV) MOFs if a synthetically viable route could be developed.

1.4 Synthesis of MOFs

Various methods have been used for the synthesis of MOFs over the years. In addition to conventional heating, other methods have included using: electrochemistry, microwave-assisted heating, mechanochemistry and sonochemistry.⁶⁹

The use of conventional heating methods to produce MOFs typically take days to weeks, and subsequently consumes large amounts of energy. Therefore, alternatives using reduced synthesis time have been greatly explored.

1.4.1 Hydrothermal and solvothermal synthesis

Hydrothermal synthesis involves the combination of metal salt, organic linker and aqueous solution being heated to above the boiling point of water, usually in a sealed TeflonTM-lined autoclave. This method is advantageous compared to solvothermal synthesis since it reduces the use of environmentally unfriendly organic solvents.⁷⁰

However, traditional MOF synthesis usually utilises solvothermal synthesis, which involves taking a metal salt, organic linker and solvent, usually in a sealed TeflonTM-lined autoclave, and heating above the boiling point of a solvent, under autogenous pressure.

N,N-Dimethylformamide (DMF) has often been used as a solvent in MOF synthesis since it easily solubilises both organic and inorganic substances. However, there have been some safety concerns surrounding the use of DMF, meaning searches into alternative solvents have been completed.⁷¹ In addition, DMF can decompose during synthesis or with time, leading to unexpected frameworks.⁷² *N,N*-Diethylformamide (DEF) has also similarly been widely used instead of DMF.

One solvent that emerged as an alternative to DMF and DEF is the commonly used ingredient in insect repellent, *N,N*-Diethyl-3-methylbenzamide (DEET), where a selection of prototypical MOFs were found to form in this solvent, despite it being known that slight alterations to the solvent employed during synthesis can cause drastic effects on structure and properties of MOFs.⁷³

Many other solvents have been utilised in MOF synthesis, including methanol, acetic acid and isopropanol. Additions of varying amounts of deprotonating agents and modulators, such as triethylamine (TEA), have been shown to affect crystal growth and size.⁷⁴ Occasionally hydrofluoric acid (HF) or hydrochloric acid (HCl) have been used to aid MOF synthesis. Hydrochloric acid has been used to improve the solubility of starting materials, which can cause products to be obtained faster. For example, in UiO-66, the addition of hydrochloric acid improves the solubility of the zirconium chloride (ZrCl₄) starting material in the DMF solvent, meaning a crystalline material is obtained more quickly.⁷⁵ The use of HF has also been reported to control the nucleation and crystal growth in UiO-66.⁷⁶

In contrast to solvothermal synthesis, some MOFs can be formed at ambient pressure at room temperature or at the boiling point of the solvent, without needing to exceed it. The reagents are still added to a sealed TeflonTM-lined autoclave or alternative reaction vessel in the same way, just heated at the same or lower temperature than the solvent boiling point. These methods are explored below.

1.4.2 Electrochemical synthesis

The synthesis of MOFs using electrochemistry was first reported in 2005 by researchers at BASF who successfully developed procedures for some Cu- and Zn-based MOFs.⁷⁷ Using electrochemistry for MOF synthesis offers several advantages, including: the option to run a continuous process, the possibility to obtain higher solids content compared to normal batch reactions, and the possibility to exclude anions (such as nitrate or perchlorate) during synthesis, which are a concern in large scale-production.⁶⁹ Metal ions are continuously introduced through anodic dissolution. The organic linker is dissolved in the reaction medium, where the metal ions then combine. Metal deposition at the cathode is prevented by using protic solvents.

1.4.3 Microwave-assisted heating

The use of microwave heating has been long established in organic chemistry, and only later became used in MOFs.⁷⁸ Microwave heating is advantageous compared to more traditional MOF synthesis methods, due to the reduction in reaction times, fast kinetics of crystal nucleation and growth, and high yields of desired products. The key drawbacks are safety concerns and reproducibility.

Studies have been previously completed on MOF-5, where the effects of microwave power level, irradiation time, temperature, solvent concentration, and substrate composition on product crystallinity and morphology were studied.⁷⁹ It was found that under optimum conditions, MOF-5 could be synthesised with uniform, cubic

crystals within 30 minutes, whereas under normal convection heating this took 24 hours. Microwave synthesis produced smaller crystals than the conventional method (the average size being 20-25 μm , compared to an average of 400-500 μm), but did not differ much in CO_2 adsorption capacity (812 mg/g compared to 823 mg/g at 298 K/40 bar).

1.4.4 Mechanochemical synthesis

Mechanochemical synthesis of MOFs was first reported in 2006.⁸⁰ Mechanochemistry can be viewed as a simplistic method, since it involves grinding reactants together with a pestle and mortar or ball milling.⁸¹

Mechanochemical synthesis involves the mechanical breaking of intramolecular bonds and subsequent chemical transformation.⁶⁹ This type of MOF synthesis offers several advantages, mostly environmental, since reactions can be carried out at room temperature, without the use of solvents, and generally require shorter reaction times compared to conventional synthesis.

1.4.5 Sonochemical synthesis

Sonochemical synthesis involves high-energy ultrasound radiation, with frequency between 20 kHz and 10 MHz, being applied to a reaction mixture.⁶⁹ The application of the high-energy ultrasound does not directly interact with reactant molecules, but instead causes cyclic alternating areas of high pressure and low pressure in liquids. The low-pressure region causes small bubbles/cavities to form, which then grow under the alternating pressure. After bubbles reach their maximum size, they eventually become unstable and collapse. This process is known as cavitation, and causes rapid release of energy, making sonochemical synthesis a viable method of MOF synthesis. The advantages of sonochemical synthesis compared to conventional methods include fast synthesis times and room temperature synthesis, making it more environmentally friendly. An example of a MOF synthesised under

sonochemical conditions is MOF-5, where the synthesis time was able to be reduced from 24 hours using a conventional method, to 30 minutes using a sonicator.⁸²

1.5 Photocatalysis

Catalysis is widely known as a process by which a catalyst is able to speed up a chemical reaction without being used up or modified.⁸³ The catalyst works by lowering the activation energy without affecting the position of equilibrium.

Today, the accepted definition of photocatalysis is the “change in the rate of a chemical reaction or its initiation under the action of ultraviolet, visible, or infrared radiation in the presence of a substance, the photocatalyst, that absorbs light and is involved in the chemical transformation of the reaction partners.”⁸⁴ The accepted definition of a photocatalyst is a “substance able to produce, by absorption of ultraviolet, visible, or infrared radiation, chemical transformations of the reaction partners, repeatedly coming with them into intermediate chemical interactions and regenerating its chemical composition after each cycle of such interactions.” Examples of applications of photocatalysis include the photocatalytic splitting of water, photodegradation of organic molecules and photoreduction of CO₂.

Some of the focus of the work in this thesis is on the photoreduction of CO₂, where the photochemical transformation of CO₂ has been observed by plants via photosynthesis for millions of years, and is now being mimicked in the laboratory.⁸⁵ Due to an increase in the concentration of atmospheric carbon dioxide and increasing environmental concerns, work has been conducted with the aim of reducing CO₂ levels via conversion to other useful products. One possible conversion is into formic acid, which is a useful product for a range of other syntheses, such as esterifications and amidations.⁸⁶ It can also be used in biomass preservation, textiles, feed additives, pharmaceuticals and more.

1.5.1 Traditional inorganic semiconductors

When atoms form solids, their combined electron energy states result in many close energy levels that form allowed energy bands. Energy bands are separated by forbidden energy gaps, where electrons cannot exist.⁸⁷ The position and size of allowed and forbidden energy gaps determine the property of the solid. In semiconductors, almost all the states in the lowest energy band (valence band) are filled by electrons, whereas the highest energy band (conduction band) is empty at absolute zero. The difference between the valence band (VB) and conduction band (CB) is called the energy band gap, defined by E_g . The band gap is an appropriate size such that thermal population of the conduction band is possible.

Traditional inorganic semiconductors include gallium arsenide and titanium dioxide.⁸⁸ If a photon of light has greater energy than the band gap of the material, then an electron has enough energy to move from the valence band to the conduction band, therefore making applications possible in areas such as solar cells. Once the electron is promoted from the valence band to the conduction band, a positive “hole” is left in the valence band, with a negative charge in the conduction band. These charges then need to flow somewhere for the energy to be utilised, otherwise electron-hole recombination occurs. A diagram showing this is seen in Figure 1.14. Semiconductors can be doped to provide specific characteristics and are often doped so that they have an excess of electrons (n-type semiconductors) or a deficiency of electrons (p-type semiconductors). Common issues associated with the use of inorganic semiconductors include limitations in materials choice and methods of fabrication.⁸⁹

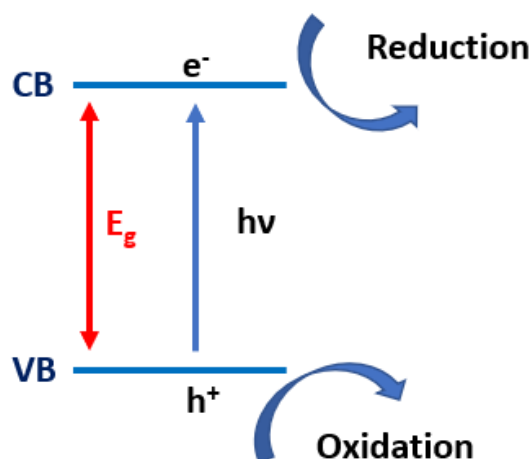


Figure 1.14: A diagram showing the process of electron promotion for an inorganic semiconductor. VB = valence band, CB = conduction band, $h\nu$ = a photon of energy, E_g = band gap of the material, e^- = electron and h^+ = hole.

The first photocatalytic transformation was a UV light driven water splitting using TiO_2 by Fujishima and Honda in 1972.⁹⁰ For many years TiO_2 has also been used as an inorganic semiconductor for photocatalytic applications such as air and water purification, water splitting and energy conversion.⁹¹ TiO_2 exhibits good photostability, is low in cost, has high efficiency, is available in a large abundance and has low toxicity. However, TiO_2 has a large band gap of 3.2 eV which limits its applications to the UV region, which comprises only 5% of the solar spectrum.^{39,43,42} The fast electron-hole recombination in TiO_2 also makes it inefficient. Therefore, research is continuing to take place investigating MOFs as an alternative to TiO_2 .

1.5.2 MOFs for photocatalysis

Since the initial discovery of photocatalytic transformations using traditional inorganic semiconductors, MOFs have also been found to have applications in photocatalysis. A variety of metals have been used in these MOFs such as Fe in MIL-101(Fe) and MIL-88B(Fe) and Zr in UiO-66, alongside its $-\text{NH}_2$ functionalised version.⁹² Other MOFs that have already been reported for applications in photocatalysis include MOF-5 and MIL-125(Ti).⁹³ In addition, $\text{NH}_2\text{-MIL-125(Ti)}$, has proven effective for use in hydrogen production.⁴⁰

MOFs have been explored for photocatalytic applications as they offer a variety of advantages in comparison to conventional inorganic semiconductors such as TiO₂.⁹⁴ The high porosity of MOFs means that active catalytic sites are easily accessible and the transport of substrates and products is facilitated. The tunability of MOFs, for example by functionalising the organic linker, also means a wide light absorbance range is possible, including in the visible region, which is not possible with TiO₂. MOFs also experience less electron-hole recombination due to their crystallinity, and have improved electron-hole separation due to the porosity creating short migration paths for charge carriers. Photosensitisers and cocatalysts can also easily be added on the framework or in the pores.

Ti MOFs are a useful focus for photocatalysis since Ti exhibits redox activity, has photochemical properties and has the ability to form strong bonds with the oxygen atoms of organic linkers in MOFs.⁴⁸ Ti MOFs could also have enhanced properties, such as shape selectivity or dual activity, as a result from the possibility to add additional functional groups.

1.5.3 MOFs for the photocatalytic reduction of CO₂

Based on the current concerns surrounding atmospheric carbon dioxide levels, it is important to investigate the possible synthesis of some novel MOFs, as well as exploring those already established, for the photoreduction of CO₂ to other useful chemicals, such as formic acid and methanol. Challenges that need to be considered are the high stability of CO₂ and to develop a photocatalyst that is not limited to the UV region.

Photocatalytic CO₂ reduction has been investigated previously with materials such as TiO₂, BiVO₄, BiWO₆ and Zn₂GeO₄.⁹⁵ Some Ti MOFs have already been shown to reduce CO₂ to formic acid, where examples include NH₂-MIL-125 using visible light irradiation in the presence of triethanolamine (TEOA) as a sacrificial agent.⁹⁶ Electron donors can also include water, methanol, or triethylamine (TEA).⁹⁷ The reaction scheme for this is shown in Figure 1.15.

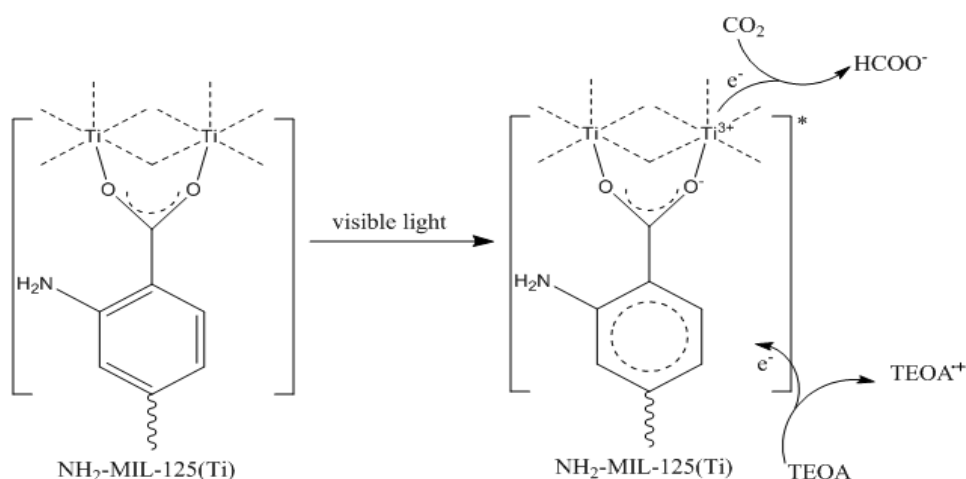


Figure 1.15: A schematic showing the reduction of CO₂ using NH₂-MIL-125(Ti) with TEOA as a sacrificial electron donor, based on the scheme found in reference 93.

Other MOFs that have been previously reported for the photoreduction of CO₂ include NH₂-UiO-66, which produced 13.2 μmol of formate in 10 hours.⁹⁸ This was shown to be superior to NH₂-MIL-125 under similar conditions, which yielded 8.14 μmol of formate. Both experiments used 50 mg photocatalyst, acetonitrile/TEOA (5:1) and a solution volume of 60 mL. These materials have therefore been considered as reference materials in this thesis.

1.6 MOFs for CO₂ Conversion to Cyclic Carbonates using Epoxides

Another possible aid to the rising levels of atmospheric CO₂ is to utilise MOF catalysts with CO₂ and epoxides for cycloaddition reactions, to produce value-added cyclic carbonates (Figure 1.16).⁹⁹ The reaction between CO₂ and epoxides is highly atom-

economical and produces minimal by-products.¹⁰⁰ The cyclic carbonate products can be used in a range of applications, including polar aprotic solvents, electrolytes for lithium-ion batteries, and valuable intermediates for the synthesis of polycarbonate and polyurethane. Cyclic carbonates have also been widely applied as intermediates to produce engineering plastics, degreasers, and fuel additives.¹⁰¹ However, due to the chemical and thermodynamic stability of CO₂, suitable materials for this conversion require an optimum amount of surface porosity, as well as Lewis acidity and basicity.

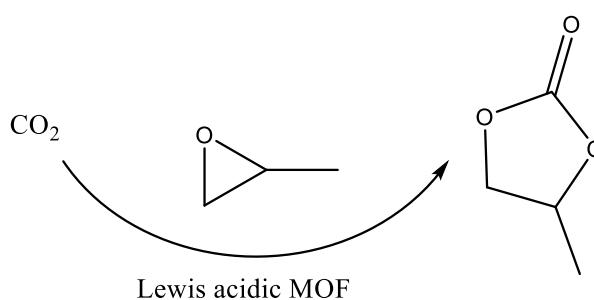


Figure 1.16: A schematic showing a cycloaddition reaction using CO₂, a Lewis acidic MOF and an epoxide (specifically styrene oxide here) to produce a value-added cyclic carbonate (propylene carbonate shown here).

MOFs, including Ce-BDC-NH₂, have exhibited efficient CO₂ fixation to produce cyclic carbonates at room temperature and pressure, as well as also being successful in the photoreduction of CO₂ (mentioned previously).⁹⁹ Ce-BDC-NH₂ has been used as a reference material in this thesis, due to the simple balloon set-up being replicated in this project. Ce-BDC-NH₂ was used to convert propylene oxide, where the initial rate was found to be $6.11 \times 10^{-3} \text{ mmol h}^{-1}$, which was three times greater than when Ce-BDC without the -NH₂ functionality was tested. Ce-BDC-NH₂ was also used as a reference since it was reported to have good recyclability, high conversion, and was already superior to many other benchmark materials.

Other MOFs, including hafnium-based MOFs, have been reported, denoted Hf-VPI-100 (Cu) and Hf-VPI-100 (Ni).¹⁰⁰ These MOFs are isostructural and demonstrated high catalytic efficiency for the cycloaddition of CO₂ to epoxides under ambient pressure. It was determined that the open metal centres in the structure act as the primary

Lewis acid sites required to facilitate the conversion of CO₂. These MOFs and some other references for the conversion of epichlorohydrin are listed below in Table 1.2. As can be seen from the data, several MOFs offer the advantage that they can achieve good conversion, selectivity and yields without the use of a co-catalyst, however, require elevated CO₂ pressures. Likewise, some experiments completed at atmospheric pressure require long reaction time with low conversion achieved. Therefore, finding a superior material that is improved in all of these areas is of interest.

Table 1.2: A table comparing different MOF catalysts for the conversion of epichlorohydrin, with details on the reported co-catalyst, CO₂ pressure, reaction temperature (°C), reaction time (hours), conversion (%), yield (%) and selectivity (%).

| MOF | Co-catalyst | CO ₂ pressure | Reaction temperature (°C) | Reaction time (hours) | Conversion (%) | Yield (%) | Selectivity (%) |
|--|-------------|--------------------------|---------------------------|-----------------------|----------------------|----------------------|----------------------|
| USTC-253-TFA ¹⁰² | TBAB | 1 bar | 25 | 72 | 38.2 | / | / |
| TMOF-1 ¹⁰³ | TBAB | 1 atm | RT | 48 | / | 92 | / |
| ZIF-8 ¹⁰⁴ | TBAB | 7 bar | 70 80 100 | 4 4 4 | 65.5 84.1 98.2 | 63.4 52.0 33.4 | 41.5 43.7 32.8 |
| Amine function alised ZIF-8 ¹⁰⁴ | / | 7 bar | 70 80 100 | 4 4 4 | 74.6 100 100 | 71.8 73.1 49.1 | 53.6 73.1 49.1 |
| BIT-103 ¹⁰⁵ | / | 3 MPa, | 160 | 8 | 100 | / | 90.8 |
| ZIF-67 ¹⁰⁶ | / | 7 bar | 120 | 6 | 97 | / | 98 |
| II-ZIF-90 ¹⁰⁷ | / | 1 MPa | 120 | 3 | 94 | / | 88 |
| (I-)Meim-Uio-66 ¹⁰⁸ 0.052m mol | / | 0.1 MPa | 119.85 | 24 | 100 | 93 | / |
| [Zn ₄ O(PDBDC) _{1.5}] ·1.5DMF·2H ₂ O ¹⁰⁹ | TBAB | 1 bar | 60 | 12 | / | 99 | >99 |
| Hf-VPI-100 (Cu), Hf-VPI-100 (Ni) ¹⁰⁰ | TBAB | 1.5 bar | 90 | 6 | / | 97.2 89.5 | / |

A mechanism for the cycloaddition of CO_2 to epoxides has been proposed (Figure 1.17).⁹⁷ This involves taking an acid catalyst, usually a metal ion or a proton, that activates the epoxide for subsequent nucleophilic attack by the co-catalyst, which is usually a tetraalkylammonium halide, which then forms a halo-alkoxide. This halo-alkoxide intermediate then reacts with CO_2 through cycloaddition, releasing a cyclic carbonate product and regenerating the tetraalkylammonium halide co-catalyst. To provide Lewis acid sites, MOFs for this process usually contain structural defects, -OH hydrogen-bond donors, open metal sites from metal nodes, and/or linkers. The exact location of the catalysis inside the framework is hard to precisely define, particularly since multiple Lewis acid sites are possible within the same MOF structure and the catalysis may take place on the surface of the MOF crystals, especially if bulky substrate molecules are used.

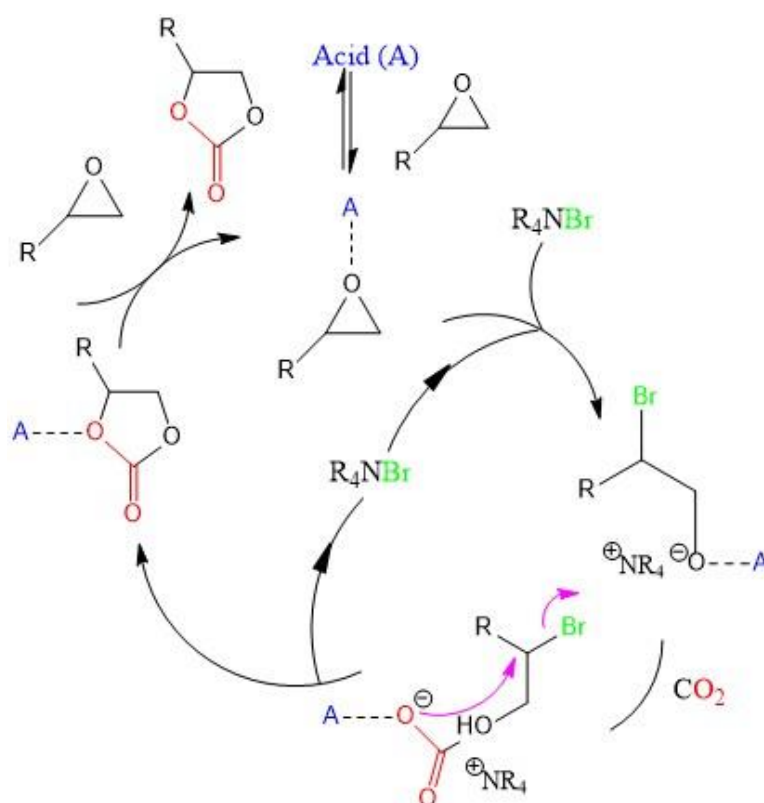


Figure 1.17: A schematic showing the proposed mechanism for addition of CO_2 to epoxides using an acid catalyst and co-catalyst to produce a cyclic carbonate, based on the scheme in reference 97.

Various other MOFs have been shown for the conversion of CO₂ using epoxides, including a Cu(II)-based MOF named FJI-H14.¹¹⁰ This MOF contains a high density of active sites, excellent stability in acidic and basic conditions, and a high volumetric uptake of CO₂ under ambient conditions (171 cm³ cm⁻³ at 298 K and 1 atm). The adsorption capacity combined with the catalytic activity of the MOF means that the material could be used as a potential adsorbing agent for post-combustion CO₂. This MOF was shown to have a high catalytic activity for the cycloaddition of styrene oxide with simulated flue gas (0.15 atm CO₂, 0.85 atm N₂) to replicate the emissions from power plants. Since the MOF proved effective for the conversion of CO₂ with styrene oxide, it would be applicable to use directly from power plants, capturing and transforming CO₂ to useful, less harmful products.

1.7 MOFs for Glucose Conversion to 5-HMF

Due to increasing atmospheric levels of CO₂ from the combustion of fossil fuels, the move towards biomass as a renewable resource is becoming significantly more important.¹¹¹ The conversion of glucose to valuable platform chemicals, such as 5-hydroxymethylfurfural (5-HMF), has been thoroughly investigated over recent years. The conversion of glucose to 5-HMF via fructose is shown below in Figure 1.18. The first step is the isomerisation of glucose to fructose and the second step is the dehydration of fructose to 5-HMF.

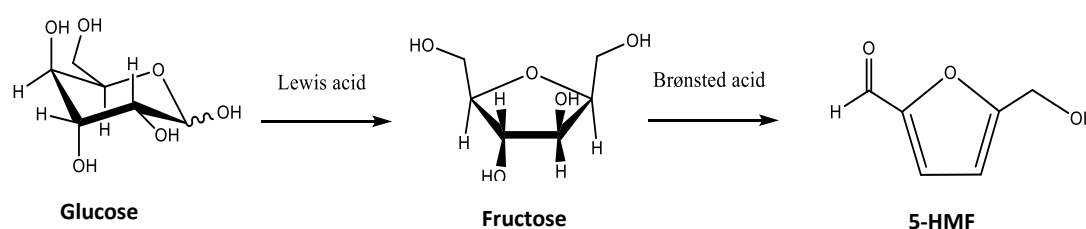


Figure 1.18: A schematic showing the isomerisation of glucose to fructose and the subsequent conversion to 5-HMF.

MOFs have started to emerge as a promising alternative to materials such as Sn-beta zeolite, which is a benchmark material for this process. Sn-beta is formed from exchanging some Si(IV) for Sn(IV), which alters the electronic properties and reduced the band gap of the material.^{68,112} Sn-beta is hydrothermally stable at low pH and the catalyst can be recycled, however MOFs have become preferential to Sn-beta as they avoid the long hydrothermal synthesis time (40 days), requirement of seed crystals and the use of highly toxic hydrofluoric acid.⁵ Some MOFs have already been reported for the conversion of glucose, and include MIL-101, UiO-66, ZIF-8, MIL-100, MIL-53 and MIL-88B.¹¹³ Sn MOFs could be particularly interesting for this process since it is Sn that provides the active sites in Sn-beta, and so having a structure formed entirely of Sn(IV) could drastically improve the activity for the conversion. UiO-66 has been used as a reference MOF in this thesis, due to it being a highly stable MOF that has previously been used as a reference for glucose conversion, where it exhibited 16% conversion and 10% product yielded 140°C in 3 hours.¹¹⁴ A summary of some other existing MOFs used for the conversion of glucose to 5-HMF, the conditions used and the yields of 5-HMF are shown in Table 1.3.¹¹⁵

Table 1.3: MOFs used for the conversion of glucose to 5-HMF with solvents and reaction temperatures used, alongside reported yields of 5-HMF.

| MOF | Solvent | Reaction temperature (°C) | Yield of 5-HMF (%) |
|-------------------------------|------------|---------------------------|--------------------|
| MIL-88B(Sc) | DMSO | 150 | 3.2 |
| MIL-88B(Fe) | DMSO | 150 | 3.8 |
| UiO-66(Zr) | DMSO | 150 | 9.0 |
| MIL-101(Cr)-SO ₃ H | DMSO | 150 | 22.2 |
| MIL-101(Cr)-SO ₃ H | DMSO | 120 | 7.0 |
| UiO-66(Zr)-SO ₃ H | DMSO | 120 | 14.1 |
| MIL-101(Cr) | DMSO/water | 150 | 11.1 |
| Fe/MIL-101(Cr) | DMSO/water | 150 | 48.7 |
| MIL-101(Cr,Fe) | DMSO/water | 150 | 21.2 |

5-HMF can be further converted to other compounds, as shown in Figure 1.19.¹¹¹ Adipic acid is the precursor of nylon, and 2,5-furandicarboxylic acid and *p*-xylene can be further converted to a range of valuable products including fuel additives.

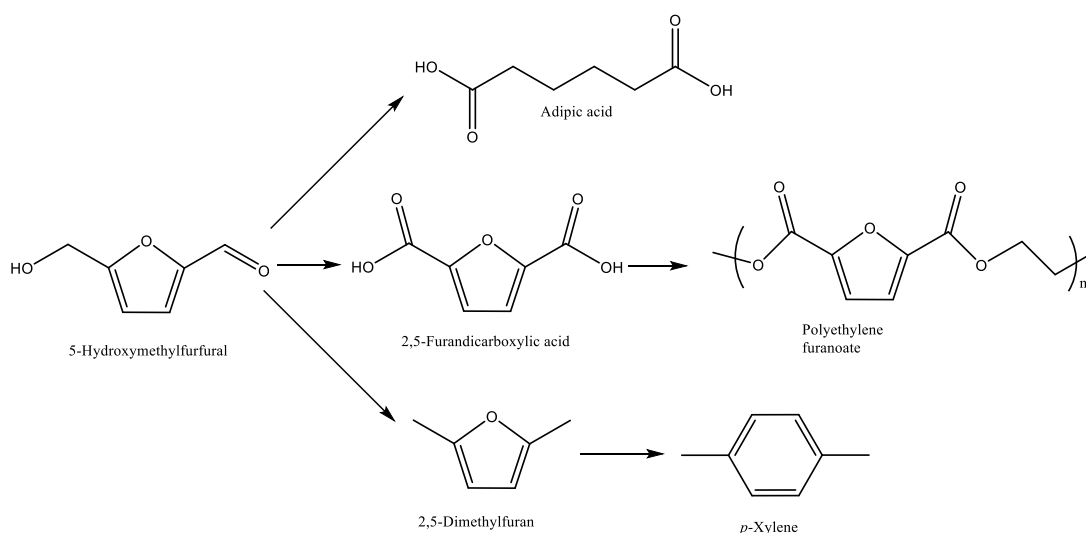


Figure 1.19: A scheme showing the possible further transformations of 5-HMF into valuable products, based on the scheme in reference 100.

1.8 Project Aims

One key aim of this project was to investigate modifications to the MOF, MUV-10. Investigations into the substitution of trimesic acid were made, as well as the substitution of Ti(IV) for Sn(IV). If partial substitution of Ti(IV) for Sn(IV) were possible, it would be highly interesting to see if any synergistic effects were observed as a result of having two slightly different +4 metal cations in the structure. Additionally, there would be the presence of a +2 metal cation, as the original MUV-10 structure also contains Ca(II) or Mn(II). Changes in properties of these substituted versions, such as electronic, could be observed, and a superior material could be formed compared to a monometallic or bimetallic MOF. Ti(IV) and Sn(IV) both exhibit Lewis acidity and both cations can accept a pair of electrons, enabling applications in heterogeneous catalysis, using a range of different reactants. Sn(IV) has a slightly larger ionic radius (0.83 Å) compared to Ti(IV) (0.605 Å), meaning there could be a slight difference in porosities of the structures formed, but the exchange could still be possible.¹¹⁶ If partially substituted materials were able to be formed, they could be tested for applications such as the photocatalytic reduction of CO₂, since the presence of Sn(IV), even in small amounts, would likely affect the electronic properties of the material and could potentially better align with the energy levels of

CO₂ for the reduction to take place more efficiently. Substituted materials could be additionally tested in the conversion of epoxides to cyclic carbonates, also utilising CO₂. Finally, the materials could be tested in glucose conversion. It has been reported previously that Sn doped into Zeolite Beta, in replacement of some Si atoms, improved the activity and selectivity of the catalyst.¹¹⁷ Exchange of Si for Sn in Zeolite Beta reduced the band gap of the material, and so applying this same principle to MOFs could create the same outcome, potentially meaning more efficient photocatalysis.¹¹² The Sn(IV) ions are the active sites in the conversion, and so incorporating them into a MOF could have advantages compared to the zeolite reference, such as increased accessibility to the active sites due to increased surface area and porosity. If 100% exchange of Ti(IV) for Sn(IV) were possible, activity and selectivity would be expected to be even greater since even more active sites would be present.

It was also of interest to try to synthesise novel Ti(IV) MOFs for sustainable catalysis applications, as well as to research further into possible methods to synthesise Sn(IV) MOFs, since none have currently been reported. If successful, it would be extremely interesting to screen materials for a range of uses, and also to have formed a potential method of forming other Sn(IV) MOFs in the future.

1.9 References

- 1 The Effects of Climate Change, <https://climate.nasa.gov/effects/>, (accessed August 2022).
- 2 D. Farrusseng, *Metal-Organic Frameworks: Applications from Catalysis to Gas Storage*, Wiley-VCH, Weinheim, 2011.
- 3 R. Li, W. Zhang and K. Zhou, *Adv. Mater.*, 2018, **30**, 1-31.
- 4 E. Akimana, J. Wang, N. V. Likhanova, S. Chaemchuen and F. Verpoort, *Catalysts.*, 2020, **10**, 1-12.

- 5 D. L. Burnett, R. Oozeerally, R. Pertiwi, T. W. Chamberlain, N. Cherkasov, G. J. Clarkson, Y. K. Krisnandi, V. Degirmenci and R. I. Walton, *Chem. Commun.*, 2019, **55**, 11446-11449.
- 6 Vital Signs, <https://climate.nasa.gov/vital-signs/carbon-dioxide/>, (accessed August 2022).
- 7 What is the greenhouse effect?, <https://climate.nasa.gov/faq/19/what-is-the-greenhouse-effect/>, (accessed May 2021).
- 8 The Greenhouse Effect, <https://scied.ucar.edu/learning-zone/how-climate-works/greenhouse-effect>, (accessed May 2021).
- 9 B. Saha and M. M. Sharma, *React. Funct. Polym.*, 1996, **28**, 263-278.
- 10 H. C. Zhou, J. R. Long and O. M. Yaghi, *Chem. Rev.*, 2012, **112**, 673–674.
- 11 O. Yaghi and H. Li, *J. Am. Chem. Soc.*, 1995, **117**, 10401-10402.
- 12 L. Jiao, J. Y. R. Seow, W. S. Skinner, Z. U. Wang and H. L. Jiang, *Mater. Today*, 2019, **27**, 43–68.
- 13 M. Weller, T. Overton, J. Rourke and F. Armstrong, in *Inorganic Chemistry*, Oxford University Press, Oxford, 2014.
- 14 S. R. Batten, N. R. Champness, X.-M. Chen, J. Garcia-Martinez, S. Kitagawa, L. Öhrström, M. O’Keeffe, M. Paik Suh and J. Reedijk, *Pure Appl. Chem.*, 2013, **85**, 1715-1724.
- 15 V. V Butova, M. A. Soldatov, A. A. Guda, K. A. Lomachenko and C. Lamberti, *Russ. Chem. Rev.*, 2016, **85**, 280–307.
- 16 J. L. C. Rowsell and O. M. Yaghi, *Microporous Mesoporous Mater.*, 2004, **73**, 3–14.
- 17 M. J. Katz, Z. J. Brown, Y. J. Colón, P. W. Siu, K. A. Scheidt, R. Q. Snurr, J. T. Hupp and O. K. Farha, *Chem. Commun.*, 2013, **49**, 9449-9451.
- 18 J. Wang, L. Liu, C. Chen, X. Dong, Q. Wang, L. Alfilfil, M. R. Alalouni, K. Yao, J. Huang, D. Zhang and Y. Han, *J. Mater. Chem. A*, 2020, **8**, 4464-4472.

- 19 J. Wang, L. Liu, C. Chen, X. Dong, Q. Wang, L. Alfilfil, M. R. Alalouni, K. Yao, J. Huang, D. Zhang and Y. Han, *J. Mater. Chem. A*, DOI:10.1039/c9ta12230c.
- 20 G. Férey and C. Serre, *Chem. Soc. Rev.*, 2009, **38**, 1380-1399.
- 21 A. S. Munn, A. J. Ramirez-Cuesta, F. Millange and R. I. Walton, *Chem. Phys.*, 2013, **427**, 30-37.
- 22 D. W. Bruce, D. O'Hare and R. I. Walton, *Porous Materials*, Wiley, Chichester, 2010.
- 23 R. C. Huxford, J. Della Rocca and W. Lin, *Curr. Opin. Chem. Biol.*, 2010, **14**, 262–268.
- 24 M. X. Wu and Y. W. Yang, *Adv. Mater.*, 2017, **29**, 1-20.
- 25 N. A. A. Qasem, R. Ben-Mansour and M. A. Habib, *Appl. Energy*, 2018, **210**, 317–326.
- 26 N. M. Musyoka, J. Ren, H. W. Langmi, B. C. North, M. Mathe and D. Bessarabov, *J. Alloys Compd.*, 2017, **724**, 450–455.
- 27 E. Adatoz, A. K. Avci and S. Keskin, *Sep. Purif. Technol.*, 2015, **152**, 207–237.
- 28 O. Kadioglu and S. Keskin, *Sep. Purif. Technol.*, 2018, **191**, 192–199.
- 29 M. H. Yap, K. L. Fow and G. Z. Chen, *Green Energy Environ.*, 2017, **2**, 218-245.
- 30 I. Luz, F. X. Llabrés I Xamena and A. Corma, *J. Catal.*, 2010, **276**, 134–140.
- 31 S. Abednatanzi, P. Gohari Derakhshandeh, H. Depauw, F. X. Coudert, H. Vrielinck, P. Van Der Voort and K. Leus, *Chem. Soc. Rev.*, 2019, **48**, 2497-2658.
- 32 M. Y. Masoomi, A. Morsali, A. Dhakshinamoorthy and H. Garcia, *Angew. Chemie - Int. Ed.*, 2019, **58**, 15188-15205.
- 33 A. M. P. Peedikakkal and I. H. Aljundi, *ACS Omega.*, 2020, **5**, 28493-28499.
- 34 A. Dhakshinamoorthy, A. M. Asiri and H. Garcia, *Catal. Sci. Technol.*, 2016, **6**, 5238-5261.

- 35 J. S. Qin, S. Yuan, Q. Wang, A. Alsalme and H. C. Zhou, *J. Mater. Chem. A*, 2017, **5**, 4280-4291.
- 36 D. Yu, Q. Shao, Q. Song, J. Cui, Y. Zhang, B. Wu, L. Ge, Y. Wang, Y. Zhang, Y. Qin, R. Vajtai, P. M. Ajayan, H. Wang, T. Xu and Y. Wu, *Nat. Commun.*, 2020, **11**, 1-10.
- 37 C. Serre, J. A. Groves, P. Lightfoot, A. M. Z. Slawin, P. A. Wright, N. Stock, T. Bein, M. Haouas, F. Taulelle and G. Férey, *Chem. Mater.*, 2006, **18**, 1451-1457.
- 38 M. Dan-Hardi, C. Serre, T. Frot, L. Rozes, G. Maurin, C. Sanchez and G. Férey, *J. Am. Chem. Soc.*, 2009, **131**, 10857–10859.
- 39 H. L. Nguyen, *New J. Chem.*, 2017, **41**, 14030–14043.
- 40 Y. Horiuchi, T. Toyao, M. Saito, K. Mochizuki, M. Iwata, H. Higashimura, M. Anpo and M. Matsuoka, *J. Phys. Chem. C*, 2012, **116**, 20848-20853.
- 41 T. N. Nguyen, S. Kampouri, B. Valizadeh, W. Luo, D. Ongari, O. M. Planes, A. Züttel, B. Smit and K. C. Stylianou, *ACS Appl. Mater. Interfaces.*, 2018, **10**, 30035-30039.
- 42 J. Gao, J. Miao, P. Z. Li, W. Y. Teng, L. Yang, Y. Zhao, B. Liu and Q. Zhang, *Chem. Commun.*, 2014, **50**, 3786-3788.
- 43 J. Castells-Gil, N. M. Padial, N. Almora-Barrios, J. Albero, A. R. Ruiz-Salvador, J. González-Platas, H. García and C. Martí-Gastaldo, *Angew. Chemie - Int. Ed.*, 2018, **57**, 8453-8457.
- 44 K. Fabrizio, K. A. Lazarou, L. I. Payne, L. P. Twight, S. Golledge, C. H. Hendon and C. K. Brozek, *J. Am. Chem. Soc.*, 2021, **143**, 12609–12621.
- 45 Isabel Abánades Lázaro, *J. Mater. Chem. A*, 2022, **10**, 10466–10473.
- 46 S. Wang, T. Kitao, N. Guillou, M. Wahiduzzaman, C. Martineau-Corcós, F. Nouar, A. Tissot, L. Binet, N. Ramsahye, S. Devautour-Vinot, S. Kitagawa, S. Seki, Y. Tsutsui, V. Briois, N. Steunou, G. Maurin, T. Uemura and C. Serre, *Nat. Commun.*, 2018, **9**, 1-9.

- 47 J. A. Mason, L. E. Darago, W. W. Lukens and J. R. Long, *Inorg. Chem.*, 2015, **54**, 10096-10104.
- 48 J. Zhu, P. Z. Li, W. Guo, Y. Zhao and R. Zou, *Coord. Chem. Rev.*, 2018, **359**, 80-101.
- 49 V. Benoit, R. S. Pillai, A. Orsi, P. Normand, H. Jobic, F. Nouar, P. Billemont, E. Bloch, S. Bourrelly, T. Devic, P. A. Wright, G. De Weireld, C. Serre, G. Maurin and P. L. Llewellyn, *J. Mater. Chem. A*, 2016, **4**, 1383-1389.
- 50 S. Yuan, T. F. Liu, D. Feng, J. Tian, K. Wang, J. Qin, Q. Zhang, Y. P. Chen, M. Bosch, L. Zou, S. J. Teat, S. J. Dalgarno and H. C. Zhou, *Chem. Sci.*, 2015, **6**, 3926-3930.
- 51 B. Bueken, F. Vermoortele, D. E. P. Vanpoucke, H. Reinsch, C. C. Tsou, P. Valvekens, T. De Baerdemaeker, R. Ameloot, C. E. A. Kirschhock, V. Van Speybroeck, J. M. Mayer and D. De Vos, *Angew. Chemie - Int. Ed.*, 2015, **54**, 13912-13917.
- 52 N. T. T. Nguyen, H. Furukawa, F. Gándara, C. A. Trickett, H. M. Jeong, K. E. Cordova and O. M. Yaghi, *J. Am. Chem. Soc.*, 2015, **137**, 15394-15397.
- 53 H. L. Nguyen, F. Gándara, H. Furukawa, T. L. H. Doan, K. E. Cordova and O. M. Yaghi, *J. Am. Chem. Soc.*, 2016, **138**, 4330-4333.
- 54 H. Assi, L. C. Pardo Pérez, G. Mouchaham, F. Ragon, M. Nasalevich, N. Guillou, C. Martineau, H. Chevreau, F. Kapteijn, J. Gascon, P. Fertey, E. Elkaim, C. Serre and T. Devic, *Inorg. Chem.*, 2016, **55**, 7192-7199.
- 55 H. L. Nguyen, T. T. Vu, D. Le, T. L. H. Doan, V. Q. Nguyen and N. T. S. Phan, *ACS Catal.*, 2017, **7**, 338-342.
- 56 S. Wang, H. Reinsch, N. Heymans, M. Wahiduzzaman, C. Martineau-Corcos, G. De Weireld, G. Maurin and C. Serre, *Matter.*, 2020, **2**, 440-450.
- 57 J. Castells-Gil, N. M. Padial, N. Almora-Barrios, I. Da Silva, D. Mateo, J. Albero, H. García and C. Martí-Gastaldo, *Chem. Sci.*, 2019, **10**, 4313-4321.
- 58 G. Lan, K. Ni, S. S. Veroneau, X. Feng, G. T. Nash, T. Luo, Z. Xu and W. Lin, *J.*

- Am. Chem. Soc.*, 2019, **141**, 4204-4208.
- 59 C. Li, H. Xu, J. Gao, W. Du, L. Shangguan, X. Zhang, R. B. Lin, H. Wu, W. Zhou, X. Liu, J. Yao and B. Chen, *J. Mater. Chem. A*, , DOI:10.1039/c9ta01942a.
- 60 A. Cadiau, N. Kolobov, S. Srinivasan, M. G. Goesten, H. Haspel, A. V. Bavykina, M. R. Tchalala, P. Maity, A. Goryachev, A. S. Poryvaev, M. Eddaoudi, M. V. Fedin, O. F. Mohammed and J. Gascon, *Angew. Chemie - Int. Ed.*, 2020, **59**, 13468-13472.
- 61 G. M. De Lima, R. I. Walton, G. J. Clarkson, R. S. Bitzer and J. D. Ardisson, *Dalt. Trans.*, 2018, **47**, 8013-8022.
- 62 A. C. Wibowo, M. D. Smith and H. C. Zur Loye, *Solid State Sci.*, 2011, **13**, 607–615.
- 63 M. H. Xie, X. L. Yang, C. Zou and C. De Wu, *Inorg. Chem.*, 2011, **50**, 5318–5320.
- 64 R. K. Mah, M. W. Lui and G. K. H. Shimizu, *Inorg. Chem.*, 2013, **52**, 7311–7313.
- 65 Y. Kamakura, S. Fujisawa, K. Takahashi, H. Toshima, Y. Nakatani, H. Yoshikawa, A. Saeki, K. Ogasawara and D. Tanaka, *Inorg. Chem.*, 2021, **60**, 12691-12695.
- 66 A. Ghosh and G. Das, *Microporous Mesoporous Mater.*, 2020, **297**, 1-10.
- 67 K. J. Everden, MChem thesis, University of Warwick, 2018.
- 68 M. Moliner, Y. Román-Leshkov and M. E. Davis, *Proc. Natl. Acad. Sci. U. S. A.*, 2010, **107**, 6164-6168.
- 69 N. Stock and S. Biswas, *Chem. Rev.*, 2012, **112**, 933-969.
- 70 C. W. Huang, V. H. Nguyen, S. R. Zhou, S. Y. Hsu, J. X. Tan and K. C. W. Wu, *Sustain. Energy Fuels*, 2020, **4**, 504-521.
- 71 Q. Yang, M. Sheng and Y. Huang, *Org. Process Res. Dev.*, 2020, **24**, 1586-1601.

- 72 A. D. Burrows, K. Cassar, R. M. W. Friend, M. F. Mahon, S. P. Rigby and J. E. Warren, *CrystEngComm*, 2005, **7**, 548.
- 73 R. A. Dodson, A. P. Kalenak, D. R. Du Bois, S. L. Gill-Ljunghammer and A. J. Matzger, *Chem. Commun.*, 2020, **56**, 9966-9969.
- 74 E. Burgaz, A. Erciyas, M. Andac and O. Andac, *Inorganica Chim. Acta*, 2019, **485**, 118-124.
- 75 M. J. Katz, Z. J. Brown, Y. J. Colón, P. W. Siu, K. A. Scheidt, R. Q. Snurr, J. T. Hupp and O. K. Farha, *Chem. Commun.*, 2013, **49**, 9449.
- 76 Y. Han, M. Liu, K. Li, Y. Zuo, Y. Wei, S. Xu, G. Zhang, C. Song, Z. Zhang and X. Guo, *CrystEngComm*, 2015, **17**, 6434–6440.
- 77 U. Mueller, M. Schubert, F. Teich, H. Puetter, K. Schierle-Arndt and J. Pastré, in *Journal of Materials Chemistry*, 2005, **16**, 626-636.
- 78 J. Klinowski, F. A. Almeida Paz, P. Silva and J. Rocha, *Dalt. Trans.*, 2011, **40**, 321-330.
- 79 J. S. Choi, W. J. Son, J. Kim and W. S. Ahn, *Microporous Mesoporous Mater.*, 2008, **116**, 727-731.
- 80 A. Pichon, A. Lazuen-Garay and S. L. James, *CrystEngComm*, 2006, **8**, 211-214.
- 81 A. L. Garay, A. Pichon and S. L. James, *Chem. Soc. Rev.*, 2007, **36**, 846-855.
- 82 W. J. Son, J. Kim, J. Kim and W. S. Ahn, *Chem. Commun.*, 2008, 6336-6338.
- 83 V. Augugliaro, G. Palmisano, L. Palmisano and J. Soria, in *Heterogeneous Photocatalysis: Relationships with Heterogeneous Catalysis and Perspectives*, 2019.
- 84 S. E. Braslavsky, A. M. Braun, A. E. Cassano, A. V. Emeline, M. I. Litter, L. Palmisano, V. N. Parmon and N. Serpone, *Pure Appl. Chem.*, 2011, **83**, 931-1014.
- 85 J. L. Wang, C. Wang and W. Lin, *ACS Catal.*, 2012, **2**, 2630-2640.

- 86 J. Hietala, A. Vuori, P. Johnsson, I. Pollari, W. Reutemann and H. Kieczka, in *Ullmann's Encyclopedia of Industrial Chemistry*, Wiley-VCH, Berlin, 2016.
- 87 M. Shur, *The Electrical Engineering Handbook*, Elsevier Academic Press, Amsterdam, 2005.
- 88 IUPAC Semiconductors,
<https://iupac.org/materialschemistryedu/computing/semiconductors/>,
(accessed May 2022).
- 89 K. J. Yu, Z. Yan, M. Han and J. A. Rogers, *npj Flex. Electron.*, 2017, **1**, 1-14.
- 90 A. Fujishima and K. Honda, *Nature.*, 1972, **238**, 37-38.
- 91 K. Nakata and A. Fujishima, *J. Photochem. Photobiol. C Photochem. Rev.*, 2012, **13**, 169-189.
- 92 Y. Li, H. Xu, S. Ouyang and J. Ye, *Phys. Chem. Chem. Phys.*, 2016, **18**, 7563-7572.
- 93 Q. Wang, Q. Gao, A. M. Al-Enizi, A. Nafady and S. Ma, *Inorg. Chem. Front.*, 2020, **7**, 300-339.
- 94 J. D. Xiao and H. L. Jiang, *Acc. Chem. Res.*, 2019, **52**, 356-366.
- 95 C. C. Wang, Y. Q. Zhang, J. Li and P. Wang, *J. Mol. Struct.*, 2015, **1083**, 127-136.
- 96 Y. Fu, D. Sun, Y. Chen, R. Huang, Z. Ding, X. Fu and Z. Li, *Angew. Chemie - Int. Ed.*, 2012, **51**, 3364-3367.
- 97 W. Zhan, H. Gao, Y. Yang, X. Li and Q. Zhu, *Adv. Energy Sustain. Res.*, 2022, **3**, 1-30.
- 98 D. Sun, Y. Fu, W. Liu, L. Ye, D. Wang, L. Yang, X. Fu and Z. Li, *Chem. - A Eur. J.*, 2013, **19**, 14279-14285.
- 99 S. Payra and S. Roy, *Chem. C.*, 2021, **125**, 8497-8507.
- 100 J. Zhu, J. Liu, Y. Machain, B. Bonnett, S. Lin, M. Cai, M. C. Kessinger, P. M.

- Usov, W. Xu, S. D. Senanayake, D. Troya, A. R. Esker and A. J. Morris, *J. Mater. Chem. A*, 2018, **6**, 22195-22203.
- 101 M. Ding, R. W. Flaig, H. L. Jiang and O. M. Yaghi, *Chem. Soc. Rev.*, 2019, **48**, 2783-2828.
- 102 Z. R. Jiang, H. Wang, Y. Hu, J. Lu and H. L. Jiang, *ChemSusChem*, 2015, **8**, 878-885.
- 103 G. Zhang, G. Wei, Z. Liu, S. R. J. Oliver and H. Fei, *Chem. Mater.*, 2016, **28**, 6276-6281.
- 104 C. M. Miralda, E. E. Maclas, M. Zhu, P. Ratnasamy and M. A. Carreon, *ACS Catal.*, 2012, **2**, 180-183.
- 105 X. Huang, Y. Chen, Z. Lin, X. Ren, Y. Song, Z. Xu, X. Dong, X. Li, C. Hu and B. Wang, *Chem. Commun.*, 2014, **50**, 2624-2627.
- 106 R. R. Kuruppathparambil, T. Jose, R. Babu, G. Y. Hwang, A. C. Kathalikkattil, D. W. Kim and D. W. Park, *Appl. Catal. B Environ.*, 2016, **182**, 562-569.
- 107 J. Tharun, K. M. Bhin, R. Roshan, D. W. Kim, A. C. Kathalikkattil, R. Babu, H. Y. Ahn, Y. S. Won and D. W. Park, *Green Chem.*, 2016, **18**, 2479-2487.
- 108 J. Liang, R. P. Chen, X. Y. Wang, T. T. Liu, X. S. Wang, Y. B. Huang and R. Cao, *Chem. Sci.*, 2017, **8**, 1570-1575.
- 109 H. F. Zhou, B. Liu, L. Hou, W. Y. Zhang and Y. Y. Wang, *Chem. Commun.*, 2018, **54**, 456-459.
- 110 L. Liang, C. Liu, F. Jiang, Q. Chen, L. Zhang, H. Xue, H. L. Jiang, J. Qian, D. Yuan and M. Hong, *Nat. Commun.*, 2017, **8**, 1-10.
- 111 J. Gong, M. J. Katz and F. M. Kerton, *RSC Adv.*, 2018, 21618-31627.
- 112 R. Bermejo-Deval, R. Gounder and M. E. Davis, *ACS Catal.*, 2012, **2**, 2705-2713.
- 113 R. Oozeerally, D. L. Burnett, T. W. Chamberlain, R. J. Kashtiban, S. Huband, R. I. Walton and V. Degirmenci, *ChemCatChem*, 2021, **13**, 2517-2529.

- 114 R. Oozeerally, D. L. Burnett, T. W. Chamberlain, R. I. Walton and V. Degirmenci, *ChemCatChem.*, 2017, **10**, 706-709.
- 115 C. Lu, Y. Zhou, L. Li, H. Chen and L. Yan, *Fuel*, 2023, **333**, 126415.
- 116 R. D. Shannon, *Acta Crystallogr. Sect. A*, 1976, **32**, 751-767.
- 117 M. Moliner, Y. Roman-Leshkov and M. E. Davis, *Proc. Natl. Acad. Sci.*, 2010, **107**, 6164–6168.

Chapter Two

Experimental Techniques and MOF Syntheses

2.1 Chapter Summary

This chapter details the background and theory for each analytical technique used in this project. It also describes the specific experimental details and conditions for the work completed in this thesis. Software used throughout this project is also included and discussed.

2.2 Characterisation Methods

2.2.1 Powder X-ray Diffraction (PXRD)

2.2.1.1 Background

The initial discovery of X-ray diffraction was by Max von Laue and colleagues, who identified X-rays as waves. William Henry Bragg and William Lawrence Bragg then solved the first crystal structure and determined the rule governing diffraction patterns, now known as Bragg's Law, which is given by Equation 2.1:

$$n \lambda = 2 d \sin \theta$$

where n = a positive integer, λ = wavelength, d = path difference and θ = angle of incidence. This is derived by using Pythagoras' theorem, from the diagram shown in Figure 2.1.

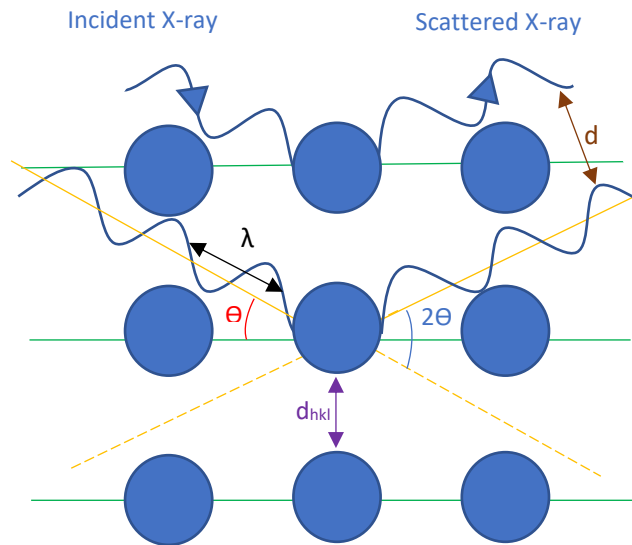


Figure 2.1: A diagram showing the different components involved in the formation of the Bragg equation by Pythagoras' theorem, where λ = wavelength, d = path difference and θ = angle of incidence.

Bragg showed that diffraction was caused by repeating planes of atoms and that it occurs when the spacing between the planes is comparable to the wavelength of the X-ray. Since crystals are comprised of a regular, repeating array of atoms and the wavelength of the X-ray is similar to the distance between the atoms in the crystal, diffraction can be used to measure the distance between the atoms in structures.

Samples are placed inside a diffractometer, and an X-ray tube and detector move in a synchronised motion, whilst a beam of X-rays are aimed at the sample. Constructive interference occurs when the waves are in phase, causing amplification of the wave (Figure 2.2). For constructive interference to occur, waves must satisfy Bragg's law (equation discussed above), where the second wave must travel an integer value of wavelengths to the first wave. This interference provides peaks on a XRD pattern for a material, with sharp peaks present for a crystalline material.

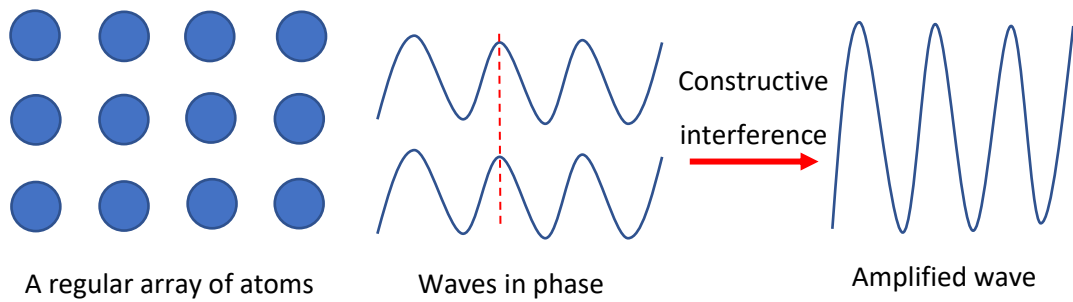


Figure 2.2: A diagram showing how waves interfere constructively for a regular array of atoms to produce an amplified wave.

If waves are not in phase, destructive interference occurs where the waves cancel, causing amorphous XRD patterns (Figure 2.3).

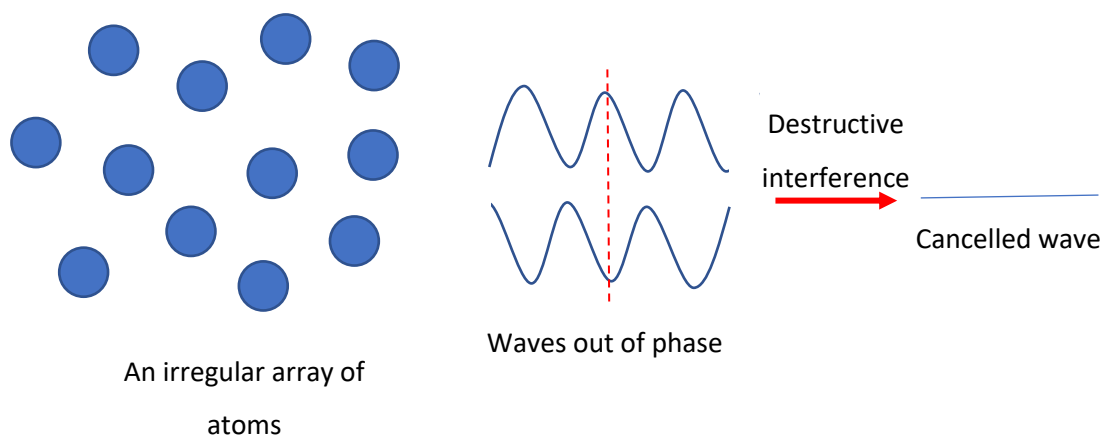


Figure 2.3: A diagram showing how waves interfere destructively for an irregular array of atoms to produce a cancelled wave.

X-rays are scattered elastically (with no change in energy) by electrons in atoms, where an atom or ion scatters X-rays in proportion to the number of electrons it contains, and the subsequent intensities of peaks on a diffraction pattern are proportional to the square of the number of electrons present.¹ Therefore, XRD can provide information on types of atoms and their positions in a structure.

With powder X-ray diffraction (PXRD), the powdered sample contains many very small crystallites ranging in dimension and orientated at random.¹ When an X-ray beam strikes the polycrystalline sample, it is scattered in all directions, some at which constructive interference occurs. Each set of planes of atoms with lattice spacing d then gives rise to a cone of diffraction intensity. Each cone consists of a set of closely spaced diffraction rays, each one representing diffraction from individual crystallites within the powdered sample. When there are many of these crystallites, the rays merge together to form a diffraction cone, where a powder diffractometer can then measure the angles of the diffracted beams. Cell parameters, crystal system, lattice type, and wavelength of the diffractometer all contribute to the number and positions of reflections. Peak intensities depend on atom type and position.

2.2.1.2 Experimental Details

After synthesis (see later chapters) MOF samples were removed from a drying oven set to around 70°C and were crushed into a fine powder using a pestle and mortar. A small amount was then added to a silicon sample holder and pressed flat with a glass slide. The sample holder was then mounted into a Bruker D5000 X-ray diffractometer, with a Cu source producing X-rays with an average wavelength of 1.5418 Å. Data were generally obtained from diffraction angles 5 to 50° with step size 0.02°.

Occasionally, a Malvern Panalytical Empyrean diffractometer was used, again generally with diffraction angles 5 to 50° with step size 0.02° used. A Cu source was used giving Cu K α 1/2 radiation, with an average wavelength of 1.5418 Å.

Data were obtained at angles as low as 3° for certain samples, when it was observed that the usual minimum angle of 5° appeared to be cutting off lower angle peaks. Additionally, data were plotted with the highest angle being lower than 50° for samples that did not show features at higher angles, allowing lower angle peaks and interesting features to be presented more clearly in this work.

2.2.2 Single Crystal X-ray Diffraction

2.2.2.1 Background

Single crystal X-ray diffraction works on a similar principal to that detailed above. Crystals must be of a sufficient size and quality for single crystal XRD to be completed, and if this criteria is met, single crystal XRD can provide definitive information about structures.² In single crystal XRD, the crystal is rotated around three orthogonal directions in an X-ray beam.

2.2.2.2 Experimental Details

A single crystal was selected from a sample and was mounted on a glass fibre with Fomblin oil. This was then placed on a Rigaku Oxford Diffraction SuperNova diffractometer with a dual source (Cu at zero) equipped with an AtlasS2 CCD area detector. The crystal was kept at 150(2) K during data collection. Using Olex2³, the structure was solved with the ShelXT⁴ structure solution program using Intrinsic Phasing and refined with the ShelXL⁵ refinement using least squares minimisation. These experiments were completed and structures solved by Guy Clarkson (Warwick).

2.2.3 Thermogravimetric analysis (TGA)

2.2.3.1 Background

Thermogravimetric analysis (TGA) works by heating samples over a specified temperature range at a specified rate and recording the mass continuously. The environment is also controlled and is usually N₂ or air. Organic components combust at a certain temperature and any residual mass in the sample is attributed to the formation of metal oxides if metals are present in the sample. With MOFs, the conventional order of steps going from lower temperature to higher temperature include loss of solvent molecules from the pores, followed by combustion of the organic linker, leaving residual metal oxides as the remaining mass.

2.2.3.2 Experimental Details

A Mettler Toledo TGA instrument was used, where approximately 5-10 mg of sample was placed into a 40 μ l alumina crucible. All samples were heated in air with a flow rate of 50 mL/minute, and data was obtained between 25-1000 °C at a rate of 10 °C per minute. Sample mass measurements were continuously obtained, and a blank curve was subtracted from each measurement.

2.2.4 Scanning Electron Microscopy (SEM) and Energy Dispersive X-ray Analysis (EDXA)

2.2.4.1 Background

SEM is a technique whereby high-resolution images of materials can be obtained using focused beams of electrons. In SEM, the beam is scanned over the object, and the reflected (scattered) beam is then imaged by a detector.⁶ This enables the shapes of particles to be observed, and approximate size distributions to be obtained. EDXA can provide approximate percentages of selected elements in the sample by measurement of fluorescent X-rays produced.

2.2.4.2 Experimental Details

SEM was carried out using a Zeiss Supra 55-VP FEGSEM. Firstly, 2 mL of isopropyl alcohol (IPA) were added to 1-5 mg of sample and then sonicated for a few minutes. Two drops of the resulting suspension were then added to a silicon wafer. The IPA was then evaporated by using compressed air, leaving the remaining sample on the silicon wafer. The SEM images were then obtained.

2.2.5 ¹H Nuclear Magnetic Resonance (NMR) Spectroscopy

2.2.5.1 Background

NMR spectroscopy involves samples absorbing electromagnetic radiation in the radio-frequency region while a magnetic field is applied, where nuclear magnetic resonances depend on the magnetic property of the atomic nuclei in the sample. The

classical model of NMR works on the basis that atoms behave as though the positively charged nucleus spins on an axis, which creates a small magnetic field.⁷ When placed in a strong magnetic field, the magnetic nucleus tries to align with the field. The nucleus is spinning and has angular momentum, therefore meaning the torque exerted by the external field results in a circular motion called precession. The rate of precession is proportional to the external magnetic field strength and to the strength of the nuclear magnet, where the relationship is shown by Equation 2.2:

$$\nu_o = \gamma B_o / 2\pi$$

where ν_o is the precession rate (Larmor frequency) (Hz), γ is the strength of the nuclear magnet (magnetogyric ratio) and B_o is the strength of the external magnetic field. The resonant frequency is in the radio frequency range for strong magnetic fields.

A diagram showing the precession of a hydrogen nucleus when a magnetic field is applied is shown below in Figure 2.4.

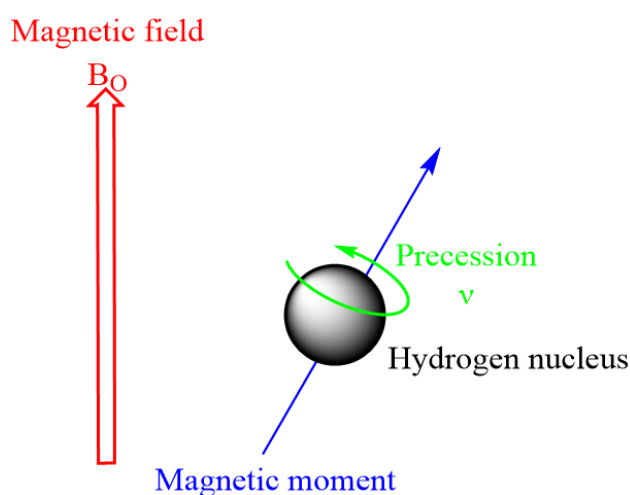


Figure 2.4: A diagram depicting the precession of a hydrogen nucleus when a magnetic field (B_o) is applied.

The key components of an NMR spectrum are the chemical shift and the intensity of the peaks obtained. Resonance frequency is usually quoted as the difference, in parts per million (ppm), from a reference arbitrarily set to 0 ppm.⁸ Each end of an NMR

spectrum are defined as either high field (or high frequency) and low field (or low frequency). Individual ^1H nuclei resonate at different frequencies since they are shielded from the applied magnetic field by the electrons around them. Therefore, protons that are at lower field have additional de-shielding of the nucleus, whilst protons that are at higher field have shielding. For example, aromatic systems containing a cyclic π -electron system generate their own magnetic field when they are placed in an external field, affecting the chemical shift of nearby nuclei, moving them to lower field. The intensity (or integral) of a resonance is proportional to the number of nuclei contributing to it. Therefore, integration of peaks in an NMR spectrum can be used to show the number of each type of nucleus present in a complex molecule.

2.2.5.2 Experimental Details

All ^1H NMR spectra were obtained using a Bruker A VIII HD-300 MHz spectrometer. Samples were filtered and placed in NMR tubes, generally using 1,4-dioxane (for experiments involving the photocatalytic reduction of CO_2) or 2,5-dimethylfuran (for experiments converting epoxides to cyclic carbonates) as internal standards. NMR tubes were then made up to the required concentration using $\text{d-H}_2\text{O}$ (for photocatalytic reduction experiments) or d-chloroform (for epoxide conversion experiments), where “d” stands for deuterated.

2.2.6 X-ray Photoelectron Spectroscopy (XPS)

2.2.6.1 Background

XPS is a surface analysis tool where elemental composition, oxidation states and the surface chemistry of materials can be probed.⁹ XPS works by using the photoelectric effect; the atoms in the material absorb a photon of light, the core electrons are then photoexcited and are ejected from the parent atom.¹⁰ In an XPS spectrum, ejected electrons are detected over a range of kinetic energies, where peaks are due to specific atoms emitting electrons of an energy unique to them. The kinetic energy (E_k) of this ejected electron depends both on the binding energy (E_B) of the electron,

which is specific to each element, and the photon energy ($h\nu$). This then enables information about the surface of a material to be deduced, including the identity of the element, chemical environment, oxidation state and the orbital from which the electron was ejected. Electrons from deeper within the sample are also detected, but they lose some energy upon ejection, and so end up contributing to the background. A basic XPS experiment will typically use a monochromated Al $K\alpha$ source ($h\nu = 1486.7$ eV). The kinetic energy of the ejected electron is determined as shown in Equation 2.3:

$$E_K = h\nu - E_B + \phi$$

where E_K = kinetic energy (J), h = Planck's constant (6.626×10^{-34} J s), ν = frequency (s^{-1}), E_B = binding energy (J) and ϕ = combined work function of the sample and electron analyser.

2.2.6.2 Experimental Details

Samples were attached to electrically conductive carbon tape, mounted onto a sample bar, and loaded into a Kratos Axis Ultra DLD spectrometer. Samples were illuminated using a monochromated Al $K\alpha$ X-ray source. Measurements were conducted at room temperature. The core level spectra were recorded using a pass energy of 20 eV (resolution approximately 0.4 eV), from an analysis area of 300 microns x 700 microns. The spectrometer work function and binding energy scale of the spectrometer were calibrated using the Fermi edge and 3d_{5/2} peak recorded from a polycrystalline Ag sample prior to the experiments taking place. Data were analysed using CasaXPS, using Shirley backgrounds and mixed Gaussian-Lorentzian line shapes. XPS throughout this project was completed by Marc Walker (University of Warwick).

2.2.7 Extended X-ray Absorption Fine Structure (EXAFS) and X-ray Absorption Near Edge Spectroscopy (XANES)

2.2.7.1 Background

EXAFS is an elemental specific technique and is used to determine the local environment of the absorbing atom.¹¹ EXAFS can provide information on the coordination number, distances and neighbours of absorbing atoms. Like EXAFS, XANES is another type of X-ray absorption spectroscopy, which refers to the absorption fine structure close to an absorption edge, about 10 eV below the edge and 20 eV above the edge, and gives information about oxidation state as well as coordination environment.¹² The data processing for EXAFS involves normalization, alignment and data merge. Next is the fitting with the software.¹³ The energy to excite core electrons into unoccupied energy levels above the Fermi energy is at least several tens of electron volts (eV) and can be as high as 10^5 eV. Therefore, photon energy required for electron excitation is in the vacuum ultraviolet (VUV) or X-ray range.¹⁴

2.2.7.2 Experimental Details

Sn K-edge EXAFS and XANES data were recorded on B18 at Diamond Light Source. The beamline receives X-rays over the energy range 2.05-35 keV and beam size at the sample of 200 (H) x 250 (V) μm . Incident energies were selected using a water-cooled, fixed-exit, double-crystal monochromator with Si(311) crystals. The spectra were recorded in QEXAFS mode. The beam was focussed horizontally and vertically using a double toroidal mirror, coated with Cr, 25 m from the source, while a pair of smaller plane mirrors were used for harmonic rejection. XANES spectra were recorded from samples pressed into pellets in fluorescence mode using a 36-element germanium detector. The raw data were normalised using the software ATHENA⁵ to produce XANES spectra and EXAFS spectra for modelling using the software ARTEMIS,¹⁵ which uses the FEFF code for the calculation of phase shifts and effective scattering amplitudes, with starting structural models produced from published crystal structures to refine interatomic distances and thermal parameters.

The fitted parameters in EXAFS include N , which is the number of neighbouring atoms, R (Å), which is the fitted distance, R_{cryst} (Å), which is the expected distance, σ^2 (Å²), which is the Debye-Waller factor, S_0^2 , which is an amplitude reduction factor (which should be approximately 1), E_0 (eV), which is the refined threshold energy and the R-factor, which shows the extent to which the experimental data and model are in agreement.

2.2.8 Ultraviolet-Visible (UV-Vis) Spectroscopy

2.2.8.1 Background

UV-Vis spectroscopy is a technique to determine the absorbances of solutions or solids. Using the Beer-Lambert law, concentrations of samples can be determined from the absorption spectrum obtained. From UV-Vis spectra, other information can also be extrapolated, such as to do with the bonding within a material, or the band gap of a material.

The Beer-Lambert law is shown most commonly in the form shown in Equation 2.4:

$$A = \epsilon c l$$

where A is the absorbance, ϵ is the molar absorption coefficient, c is the molar concentration and l is the optical path length.

The ultraviolet region ranges from 10-400 nm and the visible region ranges from 400-800 nm.¹⁶ The absorption of radiation from these regions can cause excitation of electrons from lower to higher energy molecular orbitals. If the sample receives light with an energy matching that required for a transition from a highest occupied molecular orbital (HOMO) to a lowest occupied molecular orbital (LUMO), then an electron gets promoted to the higher level, and the spectrometer records the wavelength that the absorption occurred at, as well as how much absorption occurred.

Tauc plot analysis can be completed, where an optical band gap can be estimated by taking the linear region of a spectrum and extrapolating.¹⁷ The interception on the x-axis provides the band gap in eV. Owing to slight subjection in where the x-axis is read, extrapolating the band gap by this method holds some inaccuracy.

2.2.8.2 Experimental Details

For solid state UV-Vis measurements, a small amount of sample was loaded between quartz slides. UV-Vis diffuse reflectance spectra (DRS) were recorded on a Shimadzu UV-2401 PC spectrometer in diffuse reflectance mode with a 60 mm integrating sphere. BaSO₄ was used as the reference. Data were obtained between 200-900 nm.

2.2.9 Brunauer-Emmett-Teller (BET) Surface Area Analysis

2.2.9.1 Background

BET theory allows the specific surface area of materials to be determined at an atomic level by the adsorption of unreactive gas, which is typically nitrogen.

Adsorption can be categorised as either chemisorption (irreversible adsorption) or physisorption (reversible adsorption), where physisorption is most suitable for surface area analysis measurements.¹⁸ This is because physical adsorption is accompanied by low heats of adsorption, with no disruptive structural changes occurring to the surface during an adsorption measurement. Physisorption also may lead to surface coverage by more than one layer of adsorbate (whereas chemisorption does not). Physisorption also enables pores to be completely filled by the adsorptive for pore volume measurements to also be possible. Pore sizes and distribution are also possible. Equilibrium in physisorption is also achieved rapidly since no activation energy is required (whereas generally this is needed in chemisorption). The exception to this is in adsorption in small pores, where diffusion can limit the rate of adsorption. Finally, physisorption is required since the fully reversible nature allows both adsorption and desorption in materials to be studied. Physisorbed molecules are also not restricted to specific sites and are able to cover

the entire surface of a material, meaning surface area calculations, rather than active sites, are possible to be calculated. Prior to surface area analysis, samples must be degassed to remove physically bonded impurities from the surface, such as solvent molecules that may be present from the MOF washing process.

In 1985, IUPAC published a classification of six sorption isotherms after an extensive literature survey by Brunauer, Demming, Demming and Teller (BDDT).¹⁹ The shape of the sorption isotherm obtained of a pure fluid on planar surfaces and porous materials depends on the strength of fluid-wall and fluid-fluid interactions as well as effects of confined pore space on the state and thermodynamic stability of fluids confined to narrow pores. IUPAC proposed to classify pores by their internal pore width, where a micropore was defined as a pore of internal width less than 2 nm, a mesopore was defined as a pore of internal width between 2 and 50 nm, and a macropore was defined as a pore of internal width greater than 50 nm.

The six sorption isotherms are shown in Figure 2.5.¹⁹ Reversible type I isotherms are formed when microporous solids have relatively small external surfaces, for example, activated carbons, molecular sieve zeolites and certain porous oxides, where the limiting uptake is caused by the accessible micropore volume as opposed to the internal surface area. This is sometimes referred to as a Langmuir isotherm.²⁰

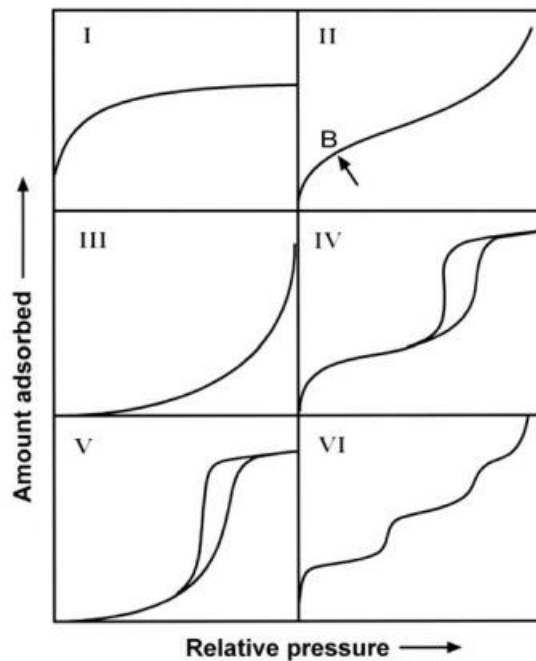


Figure 2.5: A diagram showing the six different isotherms that can be obtained during gas adsorption studies.¹⁸

Reversible type II isotherms are usually formed with a non-porous or macroporous adsorbent. Unrestricted monolayer-multilayer adsorption is possible here. The point where the “B” is shown on Figure 2.5 (often referred to as the inflexion point/knee of the isotherm) is where the monolayer coverage is complete and multilayer adsorption starts.

Reversible type III isotherms are not common. They are distinct from type II in that they do not have the visible point where the monolayer coverage is complete and the multilayer adsorption begins.

Type IV isotherms display a hysteresis loop, which is indicative that capillary condensation is taking place in mesopores, which limits gas uptake at high relative pressures. The initial part of the isotherm is due to monolayer-multilayer adsorption, as is observed in a type II isotherm. Type IV isotherms are often observed with mesoporous adsorbents.

Type V isotherms are uncommon and are similar to type III isotherms in that adsorbent-adsorbate interactions are weak but are possible with some porous

adsorbents. Type VI isotherms represent stepwise multilayer adsorption on a uniform non-porous surface. The step-height represents the monolayer capacity for each adsorbed layer.

2.2.9.2 Experimental Details

Samples were first degassed on a Micromeritics SmartVac. Samples were typically degassed at 150 °C under vacuum, unless otherwise stated. Occasionally higher activation temperatures were used (400 °C) to remove bound water molecules in the MUV-10 structure, after it had been confirmed that TGA suggested the materials were thermally stable enough to withhold those conditions.

Firstly, the empty glassware was weighed. This consisted of a glass sample holder, glass rod used for space filling, and a cap. Then the glassware with the sample was weighed, where roughly 60 mg of sample were added each time. The samples were then loaded to the SmartVac and degassed at their required temperature. The sample was then weighed again after it had been activated. Degassed samples were then loaded to a Micromeritics TriStar II Surface Area and Porosity instrument, where N₂ isotherms were obtained at 77 K, providing surface areas of materials.

CO₂ adsorption and desorption isotherms were then obtained on either the same Micromeritics TriStar II instrument or, more often, on a Micromeritics 3Flex instrument. Three temperatures were selected, 288.15 K (15 °C), 283.15 K (10 °C) and 278.15 K (5 °C), to observe the differences in CO₂ adsorption and desorption with temperature, and to subsequently calculate the heats of adsorptions. Data was fitted using OriginPro graph fitting software, where the Langmuir equation was used when working with Type I isotherms. Graph fitting enabled K values to be determined to subsequently calculate values such as enthalpy of adsorptions, ΔH , and entropy, ΔS .

2.2.10 High Performance Liquid Chromatography (HPLC)

2.2.10.1 Background

HPLC is a separation technique where a column is used alongside a pump delivering solvent at a stable flow rate.²¹ HPLC separates compounds dissolved in a liquid sample and enables qualitative and quantitative analysis of the components of the sample. The solvent used to separate the components of the liquid sample is called the mobile phase, whilst the column where the separation takes place is called the stationary phase. Different components of a mixture will interact differently with the stationary and mobile phases, causing differences in elution times. A known amount of sample is injected into the column, and the separated compounds are then identified and quantified by a detector at the end of the column.

2.2.10.2 Experimental Details

A Shimadzu Prominence was used for HPLC for experiments involving glucose conversion. The mobile phase of HPLC 'gradient grade' water was pumped through the instrument at a flow rate of 0.400 mL/min. Samples were injected via an autosampler. An Aminex HPX-87P carbohydrate analysis column maintained at a temperature of 50 °C was used for solution component separation. This column did not allow for the identification of acidic reaction side-products but facilitated a much better separation of fructose and mannose than the alternative HPX-87H column.

Solution components were detected and quantified using an Evaporative Light Scattering Detector (ELSD) at a sample temperature of 65 °C with ~3.3 bar compressed air (for glucose, fructose & mannose) and UV-Vis with photo-diode array (PDA) detector (for 5-HMF).

Calibration of the instrument was via producing a calibration curve relating ELSD and UV-Vis peak areas to concentration following measurement of solutions of glucose, fructose, mannose and HMF of various known concentrations. Dilution was required for HMF as otherwise the concentrations in the reaction samples were too great for the PDA detector. Performance/results were sufficient that separate or additional

calibration for non-acidic/acidic/methyl isobutyl ketone (MIBK) conditions was not necessary. Instrument performance was checked with each batch of samples via measurement of calibration solutions of known concentration. The original glucose stock solution used for each batch of reactions was also analysed each time.

2.2.11 CHN Analysis

2.2.11.1 Background

CHN analysis is an analytical method enabling the amounts of carbon, hydrogen and nitrogen to be determined in a sample via sample combustion. This therefore can enable the identification of components of a product. The method involves the complete combustion of a sample, converting organic and inorganic components into combustion products. The resulting combustion products then pass through a reduction furnace and enter a chromatographic column by He carrier gas. At the column, the products are separated and eluted as nitrogen, carbon dioxide, water and sulphur dioxide. A thermal conductivity detector (TCD) is used to detect the products, where the output signal is proportional to the individual components in the sample.²²

2.2.11.2 Experimental Details

CHN analysis was completed at either Exeter Analytical or MEDAC Ltd. The minimum sample required for analysis is from 2 mg, and MEDAC Ltd state their accuracy of CHN analysis is $\pm 0.30\%$ absolute.²² Exeter Analytical use a CE440 Elemental Analyser.²³

2.2.12 Inductively Coupled Plasma-Optical Emission Spectroscopy (ICP-OES)

2.2.12.1 Background

ICP-OES is a technique used to identify the atomic composition of a sample, where the type and relative amount of each element in a sample can be determined.²⁴ ICP-OES involves atoms and ions absorbing energy, causing electron promotion from the

ground state to an excited state. The excited atoms then release light at a wavelength specific to that atom when the electron then returns to a lower energy level.

Once ICP-OES data is obtained, the intensity of light emitted at certain wavelengths can be compared to calibration data. This then allows the concentration of atoms emitted at a particular wavelength to be determined.

2.2.12.2 Experimental Details

ICP analysis was completed by MEDAC LTD.²⁵ Analysis uses a Varian Vista MPX ICP-OES system, where the instrument has high precision and sensitivity. The minimum sample size required is from 5 mg, with larger quantities being required for trace analysis. The samples were digested with sulphuric acid and perchloric acid.

2.2.13 Infrared (IR) Spectroscopy

2.2.13.1 Background

IR spectroscopy enables information on the types of bonds in molecules to be deduced.²⁶ Absorption occurs in the infrared region of the electromagnetic spectrum, causing different bonds in molecules to vibrate at different wavenumbers. IR spectra arise from transitions in vibrational and rotational energy levels within a molecule. The position of absorptions are often expressed in terms of wavenumber (cm^{-1}) since it is directly proportional to energy.

The wavenumber where peaks appear on an IR spectrum can be compared to data tables, where different functional groups, for example alkanes, alkenes, halogens, alcohols and more, have regions where they absorb infrared radiation where it is associated to a certain type of vibration, for example symmetrical stretching vs. asymmetrical stretching. Other types of vibrations include bending vibrations, where scissoring, rocking, wagging, and twisting are all possible.

2.2.13.2 Experimental Details

IR measurements were taken using a Bruker ALPHA FTIR ATR spectrometer in transmission mode. A background scan was obtained, and then a small amount of sample was loaded onto a diamond ATR crystal. Data were generally obtained for wavenumbers 4000-400 cm^{-1} .

2.3 Software

2.3.1 ChemDraw

ChemDraw 20.1.1 (PerkinElmer) was used to draw all organic linkers and reaction schemes in this project.

2.3.2 Mercury

Mercury (The Cambridge Crystallographic Data Centre) was used for simulating powder patterns of MOFs in the literature from Crystallographic Information Files (CIFs). It was also used for examining crystal structures and being able to look at features such as atom arrangements and connectivity.

2.3.3 Diamond

Diamond 3.2 (Crystal Impact) was used to generate structure crystal images in order to be able to examine and discuss the arrangement of atoms and linkers in the MOFs detailed in this project.

2.3.4 Topspin

Topspin 4.0.9 was used to generate and analyse all ^1H NMR spectra in this project.

2.3.5 CasaXPS

CasaXPS was used to fit XPS data in this project.

2.3.6 GSAS-II

GSAS-II was used to fit XRD data using the Pawley method to determine unit cell parameters and crystal systems for this project.²⁷

2.3.7 OriginPro

OriginPro 2019 was used to plot all XRD, UV-Vis, TGA, IR and BET data. The software was also used for fittings of isotherms, enabling extractions of K values for subsequent calculation of enthalpies and entropies associated with CO₂ adsorption to be possible.

2.4 Synthetic Methods

2.4.1 Solvothermal Synthesis

Solvothermal synthesis was completed in Teflon™-lined stainless steel autoclaves of varying size. MOFs were typically synthesised under solvothermal conditions using a 23 mL Teflon™-lined autoclave. Larger autoclaves were used in the investigations of scaling up reactions. These included the use of 45 mL and 200 mL autoclaves. Figure 2.6 shows the three different sizes of autoclaves used in solvothermal MOF synthesis.



Figure 2.6: An image showing the three different sizes of autoclaves used in this thesis (left-right: 200 mL, 45 mL and 23 mL).

The components of autoclaves are depicted below in Figure 2.7. Each stainless-steel autoclave contains a Teflon™-liner with lid which contains the relevant solvent(s) and reagents. Within the autoclave there are also bursting and corrosion discs, pressure plates and a spring. Once assembled, the autoclave is manually tightened before placing into an oven.

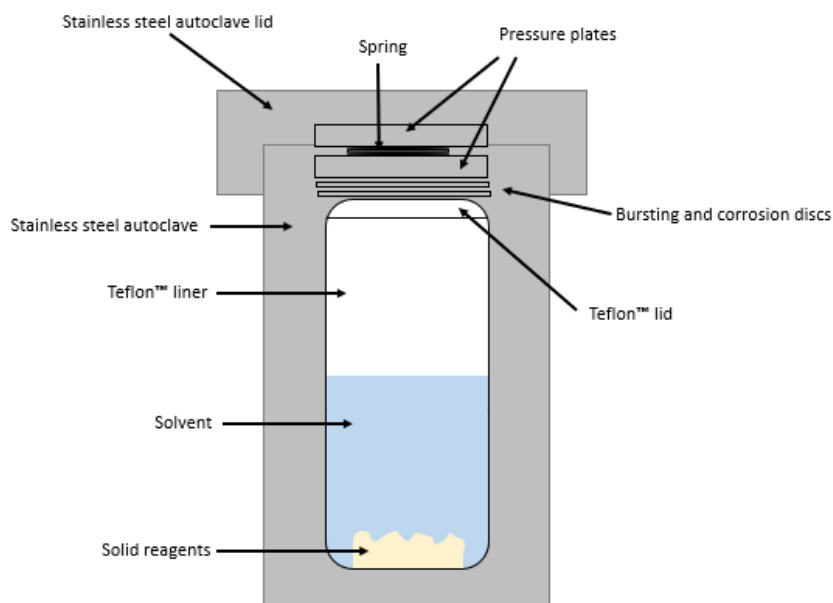


Figure 2.7: A diagram showing the components of an autoclave.

Despite different sized reaction vessels being used, the same basic method for MOF synthesis was adopted. Powdered linkers were added to the vessel alongside any powdered metals, followed by the solvent(s). Any metals to be added that were liquid, or that were in solution, were then injected after the solvent was added, and the vessels immediately sealed and heated to the correct temperature for the correct duration, under autogenous pressure. After the reaction was complete, the reaction vessel was removed from the heat source. Once cooled, reactions were centrifuged and subsequently washed with DMF and then with MeOH, before being added to a drying oven set to 70 °C before any sample analysis could take place.

2.4.2 Reflux

When MOF synthesis was scaled up further than using the solvothermal synthesis methods previously mentioned, reflux conditions were adopted that utilised a 500 mL round-bottomed flask. A similar method to the solvothermal method (described above) was adopted. The solid reagents and solvent were added to the round-bottomed flask containing a stirrer bar. Any metals to be added that were liquid, or that were in solution, were able to be injected before the condenser was added. The flask was then connected to a reflux condenser, which contained an inlet for the water supply and an outlet for the water to be removed from. The round-bottomed flask was then placed in an oil bath set to the desired synthesis temperature, with the stirring set. The set-up is shown below in Figure 2.8.



Figure 2.8: An image showing the synthesis of MOFs using reflux conditions.

2.4.3 Microwave

An Anton Paar Monowave 200 microwave (Figure 2.9) was used for certain MOF syntheses to synthesise materials in reduced time, and to see if this affected the yield and crystal structure. Reagents were added in the same order as with the autoclave and reflux experiments, but instead were added to a 30 mL glass vial, that was inserted into the microwave. A method was then created for the experiment, where the correct temperature, stirrer speed, hold time and cooling time were selected. Once complete, the vial was removed, and sample was washed and dried in the same way as mentioned previously for autoclave and reflux experiments.



Figure 2.9: An image of the microwave reactor used for synthesis of MOFs.

2.4.4 Reactor-Ready™

A Radleys Reactor-Ready™ was also used to scale MOF synthesis since it has a capacity of 250 mL, which is significantly larger than the autoclaves previously used. This equipment was used in order to make large batches of MOFs, whilst ensuring there was no compromise to the crystalline structure and yield of the product. Similarly to the procedures mentioned before, the solid reagents and solvent(s) were added through an arm of the reactor and finally any metals in solution were injected through the side arm, before the reactor was sealed. The reactor was programmed to heat to the desired temperature for a set duration, whilst being continuously stirred. Images of the Reactor-Ready™ can be seen below in Figure 2.10.



Figure 2.10: An image showing MOF synthesis using a Reactor-Ready™.

2.5 Catalysis Set-Ups

The three applications for the MOFs synthesised in this project consisted of the photocatalytic reduction of CO₂ using a solar simulator, the conversion of epoxides to cyclic carbonates using CO₂ and the conversion of glucose to 5-HMF. More detail and images of the respective experimental set-ups are shown below.

2.5.1 Photocatalytic reduction of CO₂ using a Solar Simulator

The first application that was investigated using MUV-10 and its modified versions was the photocatalytic reduction of CO₂ using a solar simulator that was designed and assembled at the University of Warwick (Figure 2.11). The set up was such that an Xe lamp was used, where the intensity of light irradiated upon the sample was set to 1 sun using a reference cell, where 1 sun is a common reference point in the literature. A shield was placed around the sample, with the inside painted black. This was both to prevent the entry of any light from inside the lab, meaning only the light from the lamp was entering the sample, and also to avoid eye damage. A stirrer plate was placed underneath where the sample would sit. A Quartz round-bottomed flask was used to contain the MOF sample and relevant solvent(s), with a bung attached containing two needles: one as a gas inlet, and one as a gas outlet. The Quartz flask was required to enable the light to pass through and to avoid absorptions that would otherwise happen if glass was used. The flow of CO₂ was controlled using a mass flow meter, which was connected to a computer.

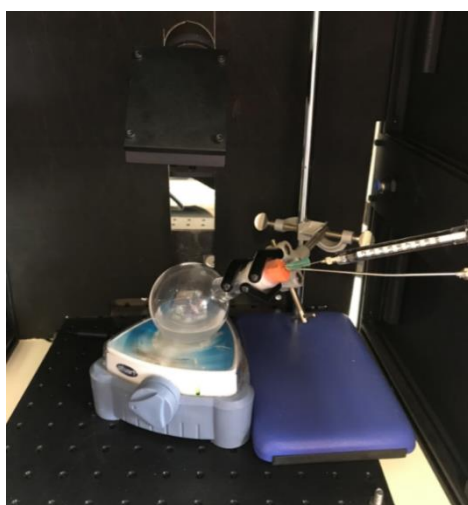


Figure 2.11: An image showing the set-up of experiments for the photocatalytic reduction of CO₂.

For most experiments, 50 mg or 100 mg of MOF were used (unless otherwise stated in the discussion present in Chapter 5) with CO₂ flowing at a rate of 5 mL/min. Initial experiments used 25 mL of H₂O with 5 mL of TEOA as the solvent and sacrificial electron donor system. Later experiments used 50 mL of H₂O with 1 mL of TEOA. Each specific example is discussed in Chapter 5, with the relevant conditions and quantities reported.

2.5.2. Conversion of Epoxides to Cyclic Carbonates using CO₂

For the experiments converting epoxides to cyclic carbonates using CO₂, a round-bottomed flask with a side arm was used, where the main inlet had a balloon attached and was held tightly in place with parafilm. The side arm had a Suba-Seal™ attached, which was then also covered with an extra layer of parafilm to prevent the escape of CO₂ once all the reagents had been added. Generally, 50 mg of MOF catalyst were added to the flask along with a stirrer bar and a few pellets of dry ice to generate CO₂. On other occasions, 10 mg and 30 mg of catalyst were used to see the effects on product yield from using a reduced amount of catalyst. 30 mg of tetrabutylammonium bromide (TBAB) co-catalyst were also generally used, where specific quantities are further discussed in Chapter 5. The epoxide precursor was then injected into the side arm, and then a Suba-Seal™ was placed in the inlet and was covered with parafilm. Periodically, the flask had more dry ice pellets added through this side arm when it appeared that the amount of CO₂ had reduced. Therefore, the system was continuously saturated with CO₂. NMR was the analytical technique used for product analysis, where 2,5-dimethylfuran was used as the internal standard. D-chloroform was then added to the NMR tube to make up the required quantity of solution to be analysed.

For experiments conducted at room temperature, these were completed with a relatively simple set up as shown below in Figure 2.12, where the stirrer plate is seen below the reaction flask. For experiments completed at 40 °C, 50 °C, 60 °C and 80 °C,

an oil bath with magnetic stirrer were used, with the rest of the procedure kept the same as detailed above.



Figure 2.12: An image showing the experimental set-up for the conversions of epoxides to cyclic carbonates using CO₂. This particular set up is shown at room temperature. Experiments at elevated temperatures were completed in oil baths containing a magnetic stirrer and temperature probe.

2.5.3 Conversion of Glucose to 5-HMF

Glucose conversion reactions to produce HMF were carried out using different MOFs, where they were stirred and heated in aqueous glucose solution. In most cases, 10 mg of catalyst was added to 3 mL glucose solution of a concentration 100 mg/mL. For reactions requiring addition of H⁺ as a catalyst, glucose solutions were prepared via dissolution of glucose in HCl stock solutions of the desired concentration/pH. All aqueous solutions were prepared using HPLC 'gradient grade' water. Reaction mixtures were contained in 4 mL glass vials sealed with Teflon and silicone seals by aluminium crimped caps. 6 mm magnetic stirrer bars were used for agitation. Vials were heated in a paraffin oil bath at 140 °C for 24 hours using a stirrer-hotplate. Control reactions for comparison were prepared as above but with the MOF catalyst and/or HCl omitted.

'Bi-phasic' reactions employing methyl isobutyl ketone (MIBK) as the organic HMF extraction layer were prepared similarly, however the 3 mL aqueous glucose solution was replaced by 1.5 mL aqueous glucose solution and 1.5 mL MIBK.

Post-heating, the vials were immediately quenched in ice-cold water to cease further reaction. The liquid reaction mixture in the vials were extracted via needle and syringe and passed through 0.4 μm nylon filters to remove all solids prior to HPLC analysis. For determination of glucose, fructose and mannose content, samples were analysed 'as-is' with HPLC equipment. For determination of HMF content, samples were first diluted x25 and then analysed. For bi-phasic reactions, the glucose, fructose, mannose and HMF content of both the aqueous and organic layers were determined separately. Dilutions were carried out with both HPLC grade water and MIBK where appropriate.

2.6 Specific Syntheses

Many MOF syntheses from this thesis are included in the relevant results chapters. For those that form the foundation of this work, their method is listed below.

2.6.1 Synthesis of MUV-10

MUV-10 was synthesised by adapting the original method reported in the literature.²⁸ The usual method in this thesis involved using a 23 mL autoclave. 12 mL DMF and 3.5 mL AcOH were added to 120 μmol CaCl_2 or $\text{MnCl}_2 \cdot 4\text{H}_2\text{O}$ and 595 μmol H_3BTC . 120 μmol $\text{Ti}(\text{O}^i\text{Pr})_4$ were injected into the solution, and the autoclave was sealed and placed in an oven set to 120 $^\circ\text{C}$ for 48 hours. This synthesis time was then able to be reduced to 24 hours. The product was then washed once with DMF and once with methanol.

Where scaled up reactions of MUV-10 took place in larger autoclaves, under reflux or using the Reactor-Ready™, the same ratios of metals and organic linker were used, along with the same reaction temperature and time. Each experiment was simply scaled from the original synthesis, as has been reported in greater detail in Chapter 3.

Sn-substituted MUV-10 materials were synthesised by following the above procedure for MUV-10 but with the relevant percentage of Ti changed exchanged for Sn. The reagents were all added as before, but with the Sn(OⁱPr)₄ reagent being injected simultaneously with the solvents being added. Likewise, ATP/AIP substituted samples had the relevant % of BTC substituted for ATP/AIP, as detailed in Chapter 3.

2.6.2 Synthesis of UiO-66

UiO-66 was synthesised by a method developed previously at the University of Warwick. 232 mg ZrCl₄ were added to 330 mg H₂BDC with 5 mL DMF and 1 mL HCl in a 23 mL autoclave. The autoclave was then heated in an oven set to 120 °C for 24 hours. After 24 hours, the autoclave was removed, allowed to cool, and the product washed with DMF and methanol.

2.6.3 Synthesis of Ce-BDC-NH₂

The synthesis of Ce-BDC-NH₂ to act as a reference material for the epoxide conversion experiments was completed as was reported in the literature previously.²⁹ 822.34 mg (1.5 mmol) of ceric ammonium nitrate and 1.086 g (6 mmol) BDC-NH₂ were dissolved in a mixed solvent of 18 mL DMF and 2 mL methanol under magnetic stirring for 30 minutes. The solution was then heated in an autoclave at 150 °C for 72 hours. After 72 hours, the autoclave was removed, allowed to cool and then washed with DMF and methanol and dried in an 80 °C oven.

2.6.4 Other MOF syntheses

Attempted syntheses of novel Ti(IV) and Sn(IV) MOFs from Chapter 4 were synthesised in the molar ratios reported in the tables within the chapter, along with the relevant solvents, synthesis temperature and synthesis duration also reported. As discussed previously in this section, solid reagents were added to the bottom of autoclaves followed by the addition of the solvents, and finally the injection of any metals in liquid or solution form. The autoclaves were then immediately placed in pre-programmed ovens for a set duration and then the product was washed with DMF and methanol after the autoclave had cooled.

2.7 References

- 1 M. Weller, T. Overton, J. Rourke and F. Armstrong, in *Inorganic Chemistry*, Oxford University Press, Oxford, 6th edn., 2014, ch. 8, pp. 234–236.
- 2 M. Weller, T. Overton, J. Rourke and F. Armstrong, in *Inorganic Chemistry*, Oxford University Press, Oxford, 6th edn., 2014, ch. 8, pp. 237–238.
- 3 O. V. Dolomanov, L. J. Bourhis, R. J. Gildea, J. A. K. Howard and H. J. Puschmann, *J. Appl. Crystallogr.*, 2009, **42**, 339–341.
- 4 G. M. Sheldrick, *Cryst. Struct. Refinement A Crystallogr. Guid. to SHELXL*, 2015, **71**, 3–8.
- 5 G. M. Sheldrick, *Acta Crystallogr. Sect. C Struct. Chem.*, 2015, **71**, 3–8.
- 6 M. Weller, T. Overton, J. Rourke and F. Armstrong, in *Inorganic Chemistry*, Oxford University Press, Oxford, 6th edn., 2014, ch.8, pp. 267–268.
- 7 N. E. Jacobsen, *NMR Spectroscopy Explained: Simplified Theory, Applications and Examples for Organic Chemistry and Structural Biology*, John Wiley & Sons Inc, New Jersey, 1st edn, 2007, ch. 1 , pp1-2.
- 8 C. Jones, B. Mulloy and A. H. Thomas, in *Methods in Molecular Biology*, Humana Press Inc., New Jersey, 1st edn, 1993, ch. 1, pp. 2–5.
- 9 D. W. Bruce, D. O’Hare and R. I. Walton, in *Local Structural Characterisation*,

- ed., John Wiley & Sons Ltd, Chichester, 1st edn, 2014, ch. 1, pp. 11-13.
- 10 D. W. Bruce, D. O'Hare and R. I. Walton, in *Local Structural Characterisation*, ed., John Wiley & Sons Ltd, Chichester, 1st edn, 2014, ch. 1, pp. 301–303.
- 11 Diamond Light Source, EXAFS: Extended X-ray Absorption Fine Structure, <https://www.diamond.ac.uk/Instruments/Techniques/Spectroscopy/EXAFS.html>, (accessed April 2022).
- 12 Diamond Light Source, XANES: X-ray Absorption Near Edge Structure, <https://www.diamond.ac.uk/Instruments/Techniques/Spectroscopy/XANES.html>, (accessed April 2022).
- 13 H. Husain, M. Sulthonul, B. Hariyanto, C. Cholsuk and S. Pratapa, in *Materials Today: Proceedings*, 2020, **44**, 3296-3300.
- 14 D. W. Bruce, D. O'Hare and R. I. Walton, in *Local Structural Characterisation*, ed., John Wiley & Sons Ltd, Chichester, 1st edn, 2014, ch. 1, pp. 89–93.
- 15 B. R. and M. Newville, *J. Synchrotron Radiat.*, 2005, **12**, 537–541.
- 16 L. D. Yadav, in *Organic Spectroscopy*, Kluwer Academic Publishers, Dordrecht, 1st edn, 2005, ch. 2, pp. 7.
- 17 P. Makuła, M. Pacia and W. Macyk, *J. Phys. Chem. Lett.*, 2018, **9**, 6814-6817.
- 18 S. Lowell, J. E. Shields, M. A. Thomas and M. Thommes, in *Characterization of Porous Solids and Powders: Surface Area, Pore Size and Density*, Kluwer Academic Publishers, Dordrecht, 1st edn, 2004, ch. 2, pp. 6–7.
- 19 K. S. W. Sing, *Pure Appl. Chem.*, 1982, **54**, 2201-2218.
- 20 S. Lowell, J. E. Shields, M. A. Thomas and M. Thommes, in *Characterization of Porous Solids and Powders: Surface Area, Pore Size and Density*, Kluwer Academic Publishers, Dordrecht, 1st edn, 2004, ch. 2, pp. 12–13.
- 21 Shimadzu, What is HPLC (High Performance Liquid Chromatography)?, https://www.shimadzu.com/an/service-support/technical-support/analysis-basics/basic/what_is_hplc.html#1, (accessed April 2022).

- 22 MEDAC LTD, CH&N Analysis, <http://medacltd.com/services-view/chn-analysis/>, (accessed April 2022).
- 23 Exeter Analytical, CHN Analysis, <https://www.exeteranalytical.co.uk/chn-analysis/>, (accessed April 2022).
- 24 ICP-OES – ICP Chemistry, ICP-OES Analysis, Strengths and Limitations, <https://www.technologynetworks.com/analysis/articles/icp-oes-icp-chemistry-icp-oes-analysis-strengths-and-limitations-342265>, (accessed April 2022).
- 25 MEDAC LTD, Metals (ICP), <http://medacltd.com/services-view/metals-icp/>, (accessed April 2022).
- 26 L. D. Yadav, in *Organic Spectroscopy*, Kluwer Academic Publishers, Dordrecht, 1st edn, 2005, ch. 3, pp. 52–56.27 B. H. Toby and R. B. Von Dreele, *J. Appl. Crystallogr.*, 2013, **46**, 544-549.
- 28 J. Castells-Gil, N. M. Padial, N. Almora-Barrios, J. Albero, A. R. Ruiz-Salvador, J. González-Platas, H. García and C. Martí-Gastaldo, *Angew. Chemie - Int. Ed.*, 2018, **57**, 8453-8457.
- 29 S. Payra and S. Roy, *J. Phys. Chem. C.*, 2021, **125**, 8497-8507.

Chapter Three

Modifications to MUV-10, a Ti(IV)-based MOF

3.1 Chapter Summary

In this chapter, a previously published MOF, MUV-10, is examined, with modifications made to the metal composition and organic linkers.¹ The effects of modification were characterised by X-ray diffraction, thermogravimetric analysis, UV-Vis, X-ray photoemission spectroscopy and other methods are explored. Scale up of the original reported synthesis is explored, and various synthetic methods including reflux and microwave synthesis are also investigated.

3.2 Introduction

MUV-10 is reported as a highly stable and chemically robust mixed-metal MOF with benzene-1,3,5-tricarboxylate (BTC) as the organic linker, with repeat unit, $[\text{Ti}^{\text{IV}}_3\text{M}^{\text{II}}_3(\mu_3\text{-O})_2(\text{BTC})_4(\text{H}_2\text{O})_6]$, where M is either Ca or Mn.¹ The MUV-10(Ca) structure is built from the interlinking of fully deprotonated trimesate anions and tetranuclear $\text{Ti}^{\text{IV}}_2\text{Ca}^{\text{II}}_2(\mu_3\text{-O})_2(\text{CO}_2)_8(\text{H}_2\text{O})_4$ clusters (Figure 3.1).

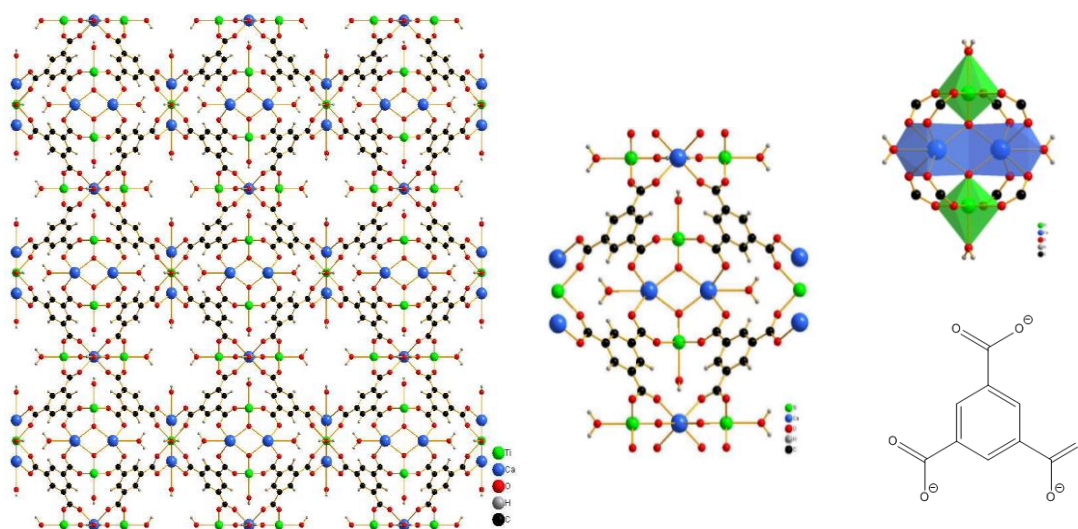


Figure 3.1: The MUV-10(Ca) structure where Ti is shown in green, Ca in blue, O in red, H in grey and C in black, with BTC linker shown in the bottom right. A $\text{Ti}^{\text{IV}}_2\text{Ca}^{\text{II}}_2(\mu_3\text{-O})_2(\text{H}_2\text{O})_4(\text{CO}_2)_8$ tetramer, acting as an SBU, is shown in the top right.

Replacement of Ca with Mn in the structure was reported after calculations suggested that Mn would be a thermodynamically favourable replacement. Theoretical studies had suggested that high-spin d^5 configurations, such as with Mn^{II} , prefer a trigonal prismatic coordination, such as that which exists in the MUV-10 structure. Therefore, under solvothermal synthesis conditions, MUV-10(Mn) was able to be directly synthesised, and proved isostructural to the calcium analogue, which was confirmed by Le Bail refinement against the PXRD patterns obtained.

Despite a slight contraction in unit cell due to the smaller ionic radius of Mn (0.83 Å) compared with Ca (1.06 Å), MUV-10(Mn) has equivalent CO_2 sorption capabilities. MUV-10(Mn) was found to be stable for a wider pH range compared to MUV-10(Ca), where structural integrity remains between pH 1-12, compared to pH 2-12 for the Ca equivalent, possibly due to stronger Mn-O bonds. MUV-10(Mn) also exhibits a smaller band gap in comparison to the calcium analogue, due to the incorporation of d electrons. Photoactivity of the MUV-10 material is therefore controlled by metal doping as opposed to linker functionalisation.

MUV-10(Mn) also has double the activity of MUV-10(Ca) as a photocatalyst for H_2 production. One key difference, however, is in paramagnetic properties. Mn exhibits paramagnetism that Ca does not, meaning some analytical techniques are limited or have additional difficulties. An example of this is in techniques such as solid-state NMR. A comparison of some of the properties of MUV-10(Ca) and MUV-10(Mn) can be seen in Table 3.1 below.

Table 3.1: A comparison of some of the properties of MUV-10(Ca) and MUV-10(Mn) reported in the literature.¹

| Property | MUV-10(Ca) | MUV-10(Mn) |
|----------|--|--|
| Formula | $[Ti^{IV}_3Ca^{II}_3(\mu_3-O)_2(BTC)_4(H_2O)_6]$ | $[Ti^{IV}_3Mn^{II}_3(\mu_3-O)_2(BTC)_4(H_2O)_6]$ |

| | | |
|---|--|---|
| BET surface area (obtained at 77 K) | 1041 m ² g ⁻¹ | 970 m ² g ⁻¹ |
| CO₂ adsorption | 4.56 mmol g ⁻¹ (at 293 K and 1 bar) | ≈4.56 mmol g ⁻¹ (at 293 K and 1 bar) |
| Maintenance of structural integrity | pH 2-12 | pH 1-12 |
| Band gap calculated by DFT calculations | 3.1 eV | 2.6 eV |
| Photocatalytic activity for H₂ generation (25 mg of catalyst in 25 mL H₂O:CH₃OH (4:1, v:v) with 300 W Xe lamp, 24 hours of irradiation) | ≈3250 μmol g ⁻¹ | 6500 μmol g ⁻¹ |

MUV-10 has therefore been of great interest to study further, particularly due to its excellent reported stabilities. In this thesis, it was decided that this material could be investigated and modified further, focussing on substituting the metal(II) ion, substituting or fully exchanging the metal(IV) ion and substituting or fully exchanging the organic linker used. Since the original MUV-10 paper was published in 2018, some follow-up work has been published throughout the duration of this project. In 2020, it was reported that transmetallation of MUV-10(Ca) was possible such that the Ca²⁺ could be exchanged for Fe²⁺, Co²⁺, Ni²⁺ or Zn²⁺ to yield MUV-101, and could be swapped with Cu²⁺ to yield MUV-102.² In 2021, it was reported that MUV-10 could be synthetically modified such that Lewis acid cations were installed in the MOF cluster (Cd²⁺, Sr²⁺ and Ba²⁺) or were introduced in the pores (H⁺, Li⁺, Na⁺ and K⁺) to tune the electronic structure and band gaps.³ In 2022, it was reported that up to five functionalised modulators possessing NO₂, F, *t*Bu, OH and NH₂ units could be added into MUV-10, which in turn increased the porosity of the material.⁴

3.3 Initial Synthesis and Characterisation of MUV-10

The PXRD patterns of as-synthesised MUV-10(Ca) and MUV-10(Mn) match that of the simulated pattern from the original paper (Figure 3.2), with differences in peak intensities being attributed to preferred orientation of the powder. MUV-10 belongs to the cubic crystal system and belongs to the space group $Pm\bar{3}$ (space group number 200).

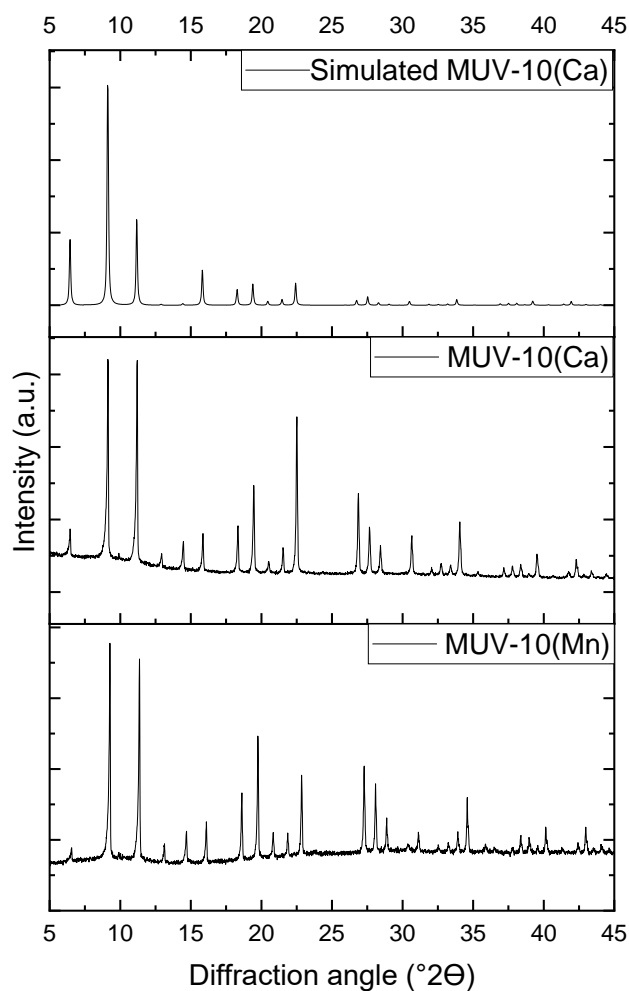


Figure 3.2: Powder XRD patterns for as-synthesised MUV-10(Mn), MUV-10(Ca) and the simulated pattern for MUV-10(Ca).

TGA and BET surface area measurements were compared with those reported in the literature before further experiments were completed using the MUV-10 materials. TGA data are in similar agreement with that reported in the literature (Figure 3.3).

The first loss (between 25 and 150°C) is attributed to loss of solvent molecules (MeOH) from the pores, and the second loss (between 300 and 400°C) is attributed to the loss of water molecules that are coordinated to the metal ions. The decomposition of the MOF then takes place at around 450°C, where the organic linker combusts, leaving residual metal oxides. These final residual masses are similar to those expected from the repeat unit reported in the literature, $[\text{Ti}^{\text{IV}}_3\text{M}^{\text{II}}_3(\mu_3\text{-O})_2(\text{BTC})_4(\text{H}_2\text{O})_6]$, where small differences can be accounted for by error on the instrument. The residual mass for MUV-10(Ca) was calculated to be 23.9% and was found experimentally to be 22.73%. The residual mass for MUV-10(Mn) was calculated to be 27.8% and was found experimentally to be 20.89%.

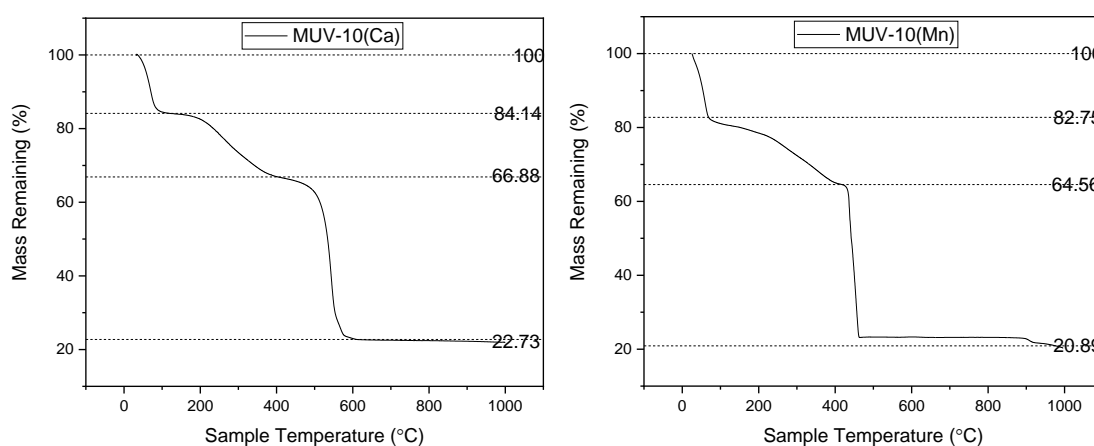


Figure 3.3: TGA plots for MUV-10(Ca) (left-hand side) and MUV-10(Mn) (right-hand side).

Nitrogen adsorption experiments were then completed. Interestingly, following the activation temperature of 150 °C that was reported in the literature previously, MUV-10(Ca) and MUV-10(Mn) yielded BET surface areas of 405 m²g⁻¹ and 183 m²g⁻¹, respectively, whereas the literature reported a BET surface area of 1041 m²g⁻¹ for MUV-10(Ca) and 970 m²g⁻¹ for MUV-10(Mn). The data obtained in this experiment are concordant with the data reported in the literature in that the surface area was found to be greater for MUV-10(Ca) compared to MUV-10(Mn), however, the isotherms for these samples showed that the adsorptions and desorptions did not match and the surface areas were much lower than expected.

It was then decided to activate the samples at a higher temperature, of 400 °C, since TGA showed that this was before the decomposition temperature of MUV-10, but after the temperature required to remove the solvent and bound water in the structure. After an activation temperature of 400 °C, the BET measurements were closer to those initially reported in the literature. MUV-10(Ca) gave a BET surface area of 1114 m²g⁻¹, which is slightly larger than that initially reported. MUV-10(Mn) gave a BET surface area of 455 m²g⁻¹, which is still greater than the surface area obtained at an activation temperature of 150 °C but is still significantly lower than the 970 m²g⁻¹ that was initially reported.

This higher activation temperature of 400 °C improved the isotherms since the bound water in the MUV-10 structure was removed. The adsorptions and desorptions matched better, with some hysteresis seen, which is indicative of micropores being present. There is a greater amount of hysteresis observed for MUV-10(Mn) compared to MUV-10(Ca). Figure 3.4 shows the isotherms for MUV-10(Ca) and MUV-10(Mn) after activation at 400 °C.

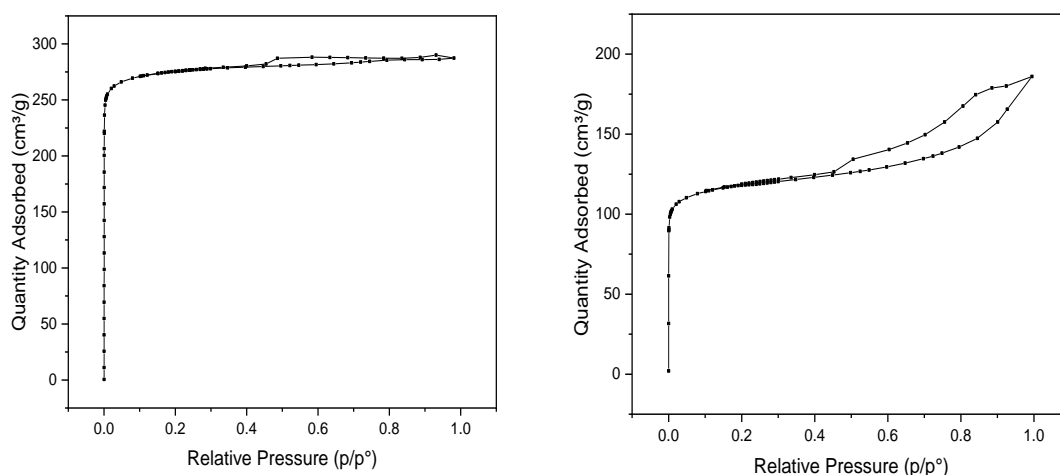


Figure 3.4: Nitrogen isotherms for MUV-10. The left-hand side is MUV-10(Ca) after activation at 400 °C, the right-hand side is MUV-10(Mn) after 400 °C activation.

XRD was completed after the adsorption experiments and showed that the MUV-10 structure was maintained at both 150°C and 400°C (Figure 3.5). The decrease in

intensity for the lowest angle peak for two of the samples is attributed to the pores being blocked when the XRD pattern was obtained.

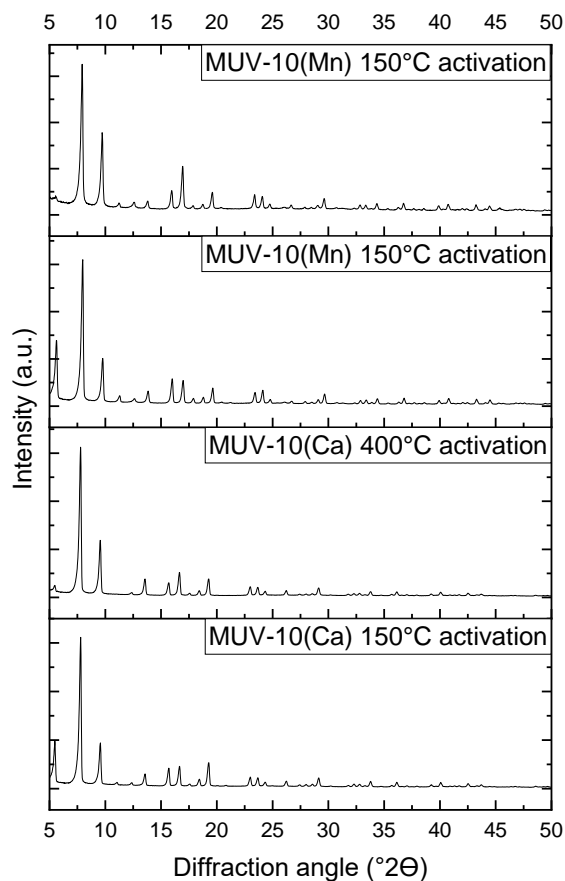


Figure 3.5: Powder XRD patterns for MUV-10 materials after activation at different temperatures and isotherm measurements.

SEM images of both MUV-10(Mn) and MUV-10(Ca) were obtained and show the size and morphology of the MUV-10 samples, as shown in Figure 3.6 and Figure 3.7. The crystals observed match the octahedral geometry observed in the literature.¹

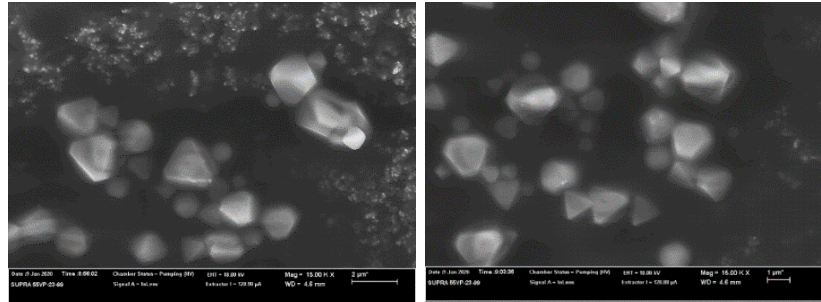


Figure 3.6: SEM images of MUV-10(Mn)

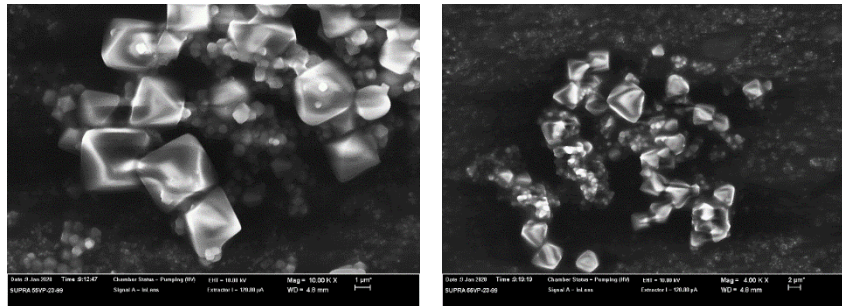


Figure 3.7: SEM images of MUV-10(Ca).

EDXA data were also obtained to show the approximate amounts of each element present, and for both MUV-10(Mn) and MUV-10(Ca) the elements were roughly present in the expected amounts. It was expected that the Ti and Mn/Ca atomic % should have been equal, which given the slight inaccuracy that EDXA holds, proved correct. The EDX spectra and corresponding data for MUV-10(Mn) are shown below in Figure 3.8 and Table 3.2.

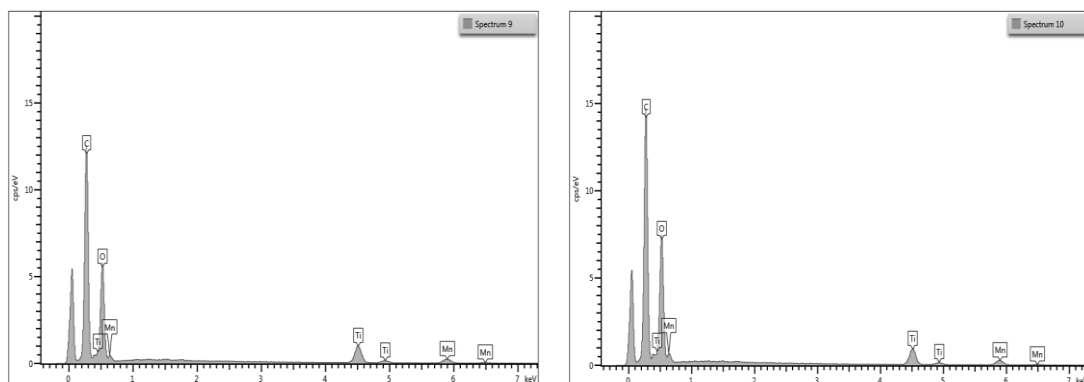


Figure 3.8: EDXA spectra for two sites of the MUV-10(Mn) sample.

Table 3.2: EDXA data for two sites of the MUV-10(Mn) sample.

| Spectrum 9: Elements | Atomic % | Spectrum 10: Elements | Atomic % |
|-------------------------|----------|--------------------------|----------|
| Ti | 5.8 | Ti | 4.7 |
| Mn | 3.4 | Mn | 3.3 |

The spectra and corresponding table for MUV-10(Ca) is shown below in Figure 3.9 and Table 3.3.

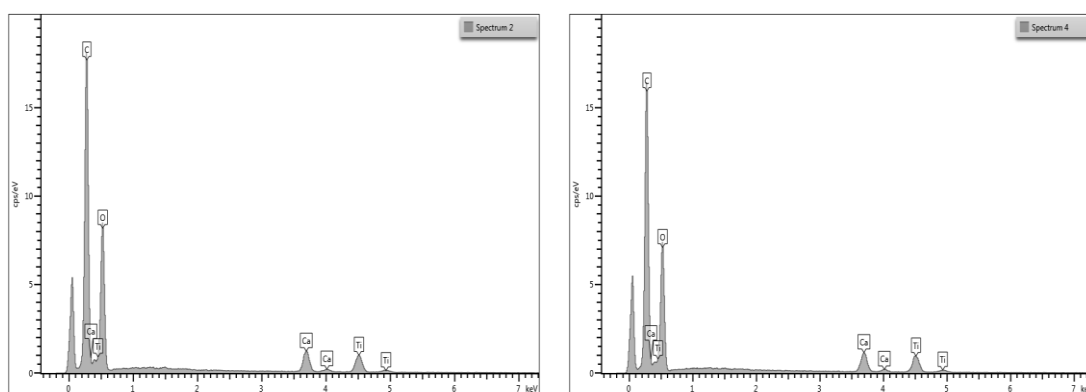


Figure 3.9: EDXA spectra for two sites of the MUV-10(Ca) sample.

Table 3.3: EDXA data for two sites of the MUV-10(Ca) sample.

| Spectrum 2: Elements | Atomic % | Spectrum 4: Elements | Atomic % |
|-------------------------|----------|-------------------------|----------|
| Ti | 4.2 | Ti | 4.5 |
| Ca | 3.2 | Ca | 3.3 |

3.4 Synthesis and Scalability of MUV-10

The initial synthesis of MUV-10 reported in the literature was carried out in a 25 mL Schott bottle with reagents added in a glove box and subsequently heated at 120 °C for 48 hours.

The initial experiments for this project involved repeating the procedure reported in the literature but modifying it so that a 23 mL autoclave was used rather than a Schott bottle, and also in the absence of a glove box to provide a much quicker and simpler set-up. MUV-10(Mn) was initially synthesised in a 23 mL autoclave and produced a yield of 71% at 120 °C in 48 hours. The synthesis time could be reduced to 24 hours, without compromising the crystallinity and yield of the material, producing 82% yield of sample at 120°C. MUV-10(Mn) was then successfully scaled up further using a 45 mL autoclave and a 200 mL autoclave, and then under reflux conditions, using a microwave reactor and using a large Reactor-Ready™ reactor (250 mL). Initial refluxes were completed in nitrogen; however, it was also confirmed to work in air without the Ti(OⁱPr)₄ precursor undergoing hydrolysis, which was advantageous since this can be a prevalent issue in the synthesis of Ti MOFs, which subsequently causes amorphous materials to be produced or for the sample to be contaminated with TiO₂. A summary of the solvothermal MUV-10(Mn) syntheses with corresponding yields is shown below in Table 3.4. Reductions in yields can be mostly attributed to product loss during filtration and subsequent losses from transferring samples. It can be observed that when working on the largest scales investigated in this project (reflux and Reactor-Ready™), the % yield is highest. This shows that when working on a larger scale with MUV-10, work up losses are minimised and therefore this would be appropriate for industry.

Table 3.4: MUV-10(Mn) synthesised for different lengths of time and on different scales, with corresponding reported yields.

| Metal precursors | Linker | Method | Solvent | Temperature (°C) | Synthesis time (hours) | Yield (%) |
|---|---------------|-----------------------------------|-------------------------------|-------------------------|-------------------------------|------------------|
| MnCl ₂ .4H ₂ O, Ti(O ⁱ Pr) ₄ | BTC | Solvothermal (23 mL autoclave) | DMF (12 mL), AcOH (3.5 mL) | 120 | 48 | 71 |
| MnCl ₂ .4H ₂ O, Ti(O ⁱ Pr) ₄ | BTC | Solvothermal | DMF (12 mL), | 120 | 24 | 82 |

| | | | | | | |
|--|-----|---------------------------------------|--------------------------------|-----|----|----|
| | | (23 mL autoclave) | AcOH (3.5 mL) | | | |
| MnCl ₂ .4H ₂ O, Ti(OiPr) ₄ | BTC | Solvothermal (45 mL autoclave) | DMF (18 mL), AcOH (5.25 mL) | 120 | 48 | 77 |
| MnCl ₂ .4H ₂ O, Ti(OiPr) ₄ | BTC | Solvothermal (200 mL autoclave) | DMF (96 mL), AcOH (28 mL) | 120 | 48 | 73 |
| MnCl ₂ .4H ₂ O, Ti(OiPr) ₄ | BTC | Reflux (500 mL round bottomed flask) | DMF (144 mL), AcOH (42 mL) | 120 | 24 | 93 |
| MnCl ₂ .4H ₂ O, Ti(OiPr) ₄ | BTC | Reactor-Ready™ Large reactor (250 mL) | DMF (216 mL), AcOH (63 mL) | 120 | 24 | 98 |

The corresponding XRD patterns from the different solvothermal synthesis methods are shown below in Figure 3.10, with only slight broadening of the peaks apparent for the Reactor-Ready™ sample.

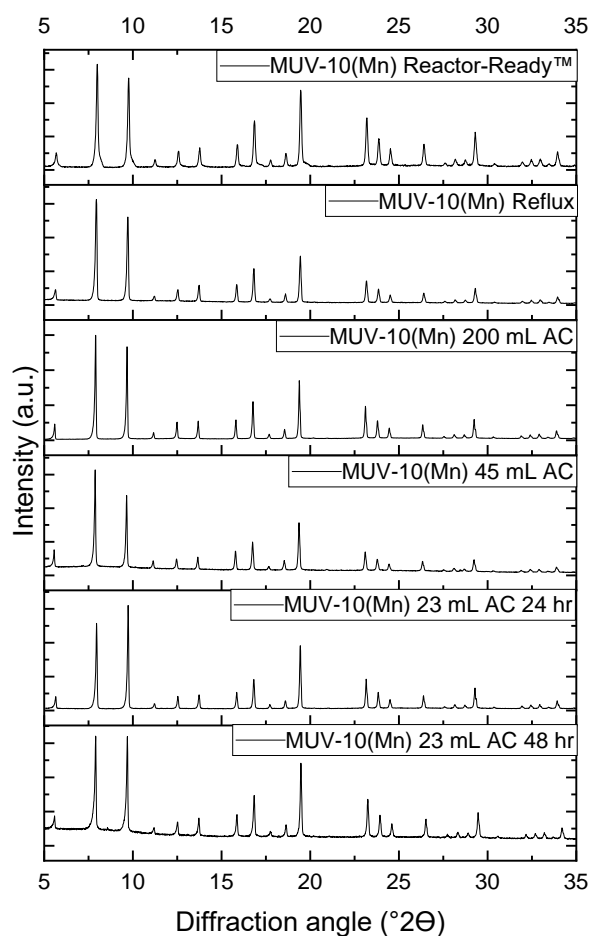


Figure 3.10: Powder XRD patterns for MUV-10(Mn) synthesised under various solvothermal conditions. AC stands for autoclave.

MUV-10(Mn) was also successfully synthesised using a microwave reactor (maximum power 850 W), significantly reducing the synthesis time compared to the methods previously listed, without compromising yield and structure. The synthesis time of 60 minutes was further able to be reduced to 45 minutes without compromise to yield or crystallinity (see Table 3.5). The slight increase in yield with decreased synthesis time was unexpected, as it would be expected that, if anything, the yield would decrease as there is less time for the linker and metals to combine. However, this can be accounted for since there is often slight product loss during the washing and centrifuging process, which may have occurred with the 60-minute sample.

Table 3.5: MUV-10(Mn) synthesis using a microwave reactor at reduced synthesis times.

| Metal precursors | Linker | Method | Solvent | Temperature (°C) | Synthesis time (minutes) | Yield (%) |
|--|--------|--------------|--------------|------------------|--------------------------|-----------|
| MnCl ₂ .4H ₂ O, Ti(OiPr) ₄ | BTC | Solvothermal | DMF, AcOH | 120 | 60 | 78 |
| MnCl ₂ .4H ₂ O, Ti(OiPr) ₄ | BTC | Solvothermal | DMF, AcOH | 120 | 45 | 88 |

The corresponding XRD patterns for the MUV-10(Mn) samples synthesised using a microwave are shown below in Figure 3.11.

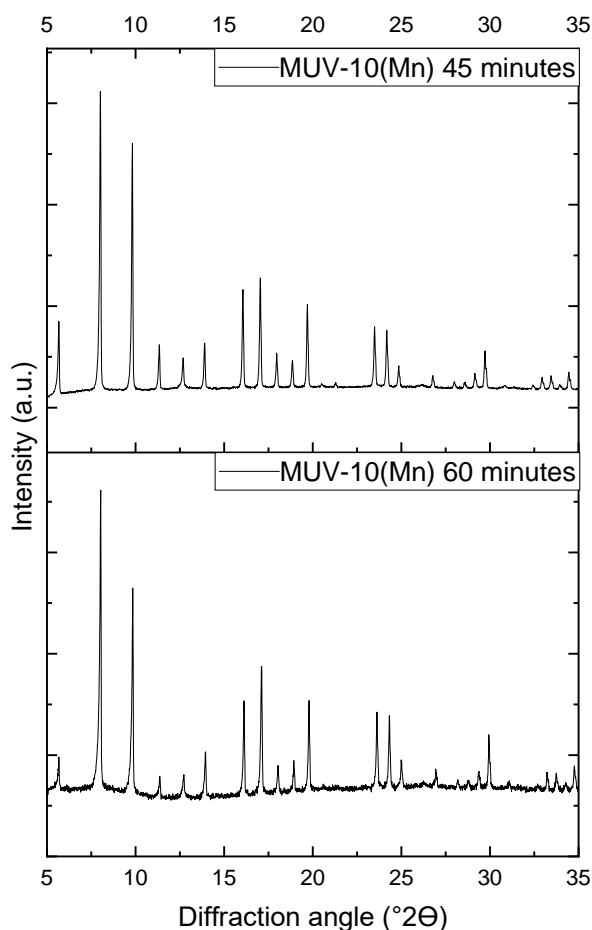


Figure 3.11: Powder XRD patterns for MUV-10(Mn) synthesised using a microwave for 45 minutes and for 60 minutes.

MUV-10(Ca) was initially synthesised in a 23 mL autoclave, producing a yield of 80% at 120°C in 48 hours. Like with MUV-10(Mn), the synthesis time was then reduced to 24 hours, without compromising the crystallinity and yield of the material, producing a yield of 88% at 120°C.

MUV-10(Ca) was then scaled up further, also using a variety of sizes of autoclaves, reflux conditions, a microwave reactor and a large Reactor-Ready™ reactor. A summary of the solvothermal MUV-10(Mn) syntheses with corresponding yields is shown below in Table 3.6.

Table 3.6: MUV-10(Ca) synthesised on different scales, with corresponding reported yields.

| Metal precursors | Linker | Method | Solvent | Temperature (°C) | Synthesis time (hours) | Yield (%) |
|--|---------------|------------------------------------|--------------------------------|-------------------------|-------------------------------|------------------|
| CaCl ₂ , Ti(OiPr) ₄ | BTC | Solvothermal (23 mL autoclave) | DMF (12 mL), AcOH (3.5 mL) | 120 | 48 | 80 |
| CaCl ₂ , Ti(OiPr) ₄ | BTC | Solvothermal (23 mL autoclave) | DMF (12 mL), AcOH (3.5 mL) | 120 | 24 | 88 |
| CaCl ₂ , Ti(OiPr) ₄ | BTC | Solvothermal (45 mL autoclave) | DMF (18 mL), AcOH (5.25 mL) | 120 | 48 | 98 |
| CaCl ₂ , Ti(OiPr) ₄ | BTC | Solvothermal (200 mL autoclave) | DMF (96 mL), AcOH (28 mL) | 120 | 48 | 80 |

| | | | | | | |
|--|-----|---------------------------------------|-------------------------------|-----|----|----|
| CaCl ₂ , Ti(OiPr) ₄ | BTC | Reflux (500 mL round bottomed flask) | DMF (144 mL), AcOH (42 mL) | 120 | 48 | 73 |
| CaCl ₂ , Ti(OiPr) ₄ | BTC | Reactor-Ready™ Large reactor (250 mL) | DMF (216 mL), AcOH (63 mL) | 120 | 24 | 90 |

The corresponding XRD patterns from the different solvothermal synthesis methods are shown below in Figure 3.12. Similarly to with MUV-10(Mn), the largest scale of synthesis (Reactor-Ready™) produced an XRD pattern with the broadest peaks compared to the other samples.

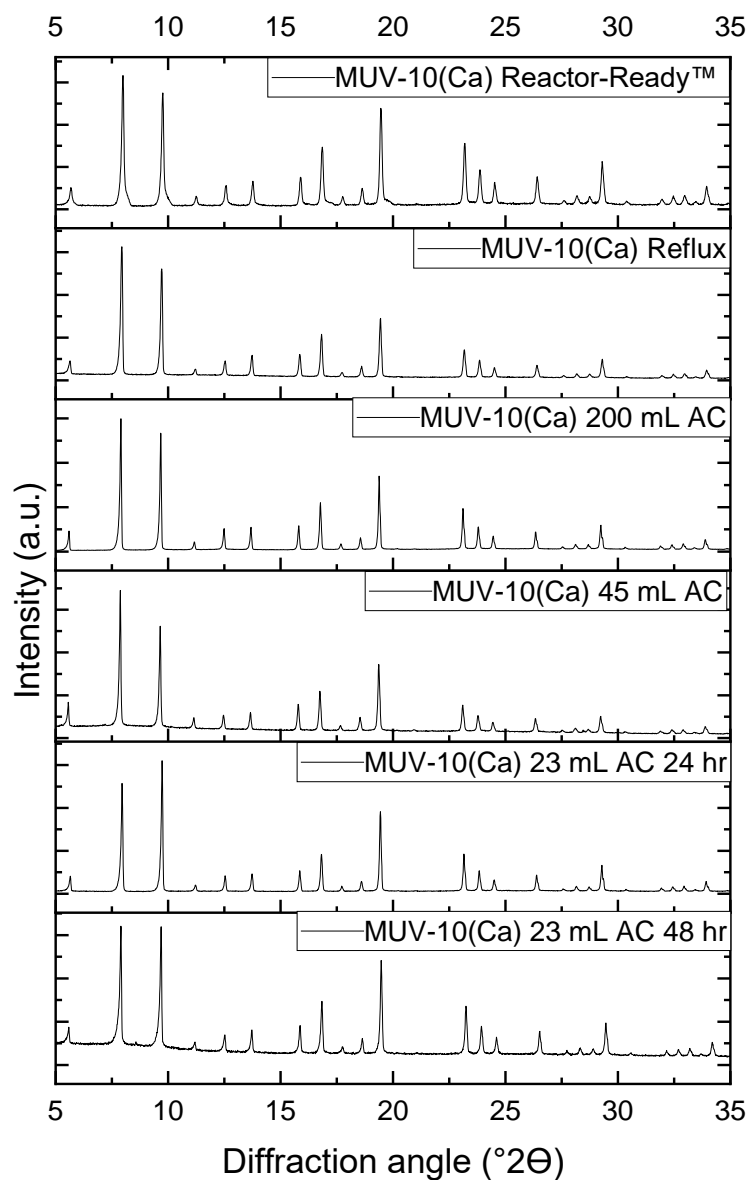


Figure 3.12: Powder XRD patterns for MUV-10(Ca) synthesised under various solvothermal conditions. AC stands for autoclave.

MUV-10(Ca) was also able to be synthesised using a microwave reactor, significantly reducing the synthesis time compared to the methods previously listed, without compromising yield and crystallinity. The synthesis time of 60 minutes was further able to be reduced to 45 minutes with no compromise (Table 3.7).

Table 3.7: MUV-10(Ca) synthesis using a microwave reactor at reduced synthesis times.

| Metal precursors | Linker | Method | Solvent | Temperature (°C) | Synthesis time (minutes) | Yield (%) |
|--|--------|--------------|--------------|------------------|--------------------------|-----------|
| CaCl ₂ , Ti(OiPr) ₄ | BTC | Solvothermal | DMF, AcOH | 120 | 60 | 94 |
| CaCl ₂ , Ti(OiPr) ₄ | BTC | Solvothermal | DMF, AcOH | 120 | 45 | 86 |

The corresponding XRD patterns for the MUV-10(Ca) samples synthesised using a microwave are shown below in Figure 3.13.

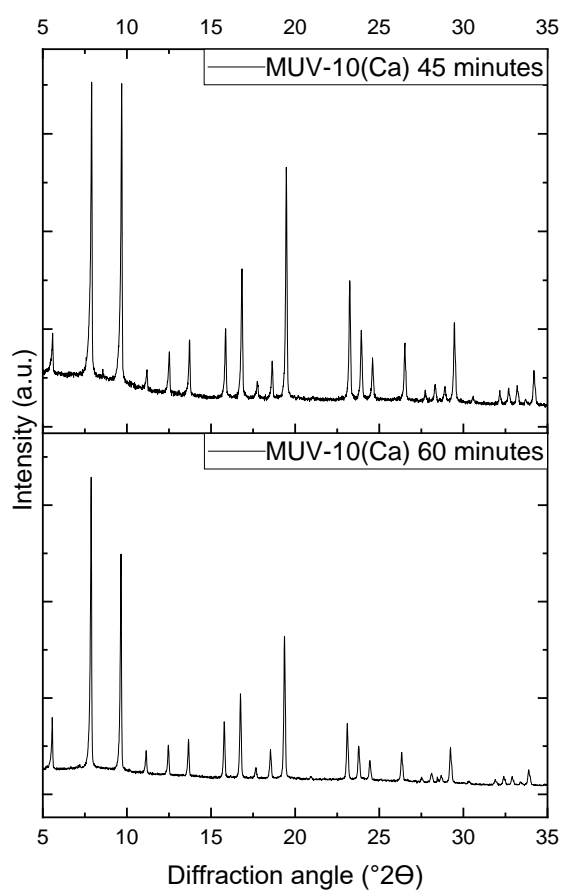
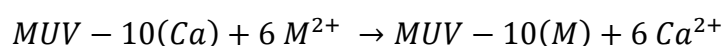


Figure 3.13: Powder XRD patterns for MUV-10(Ca) synthesised using a microwave for 45 minutes and for 60 minutes.

3.5 Attempted Metal(II) Substitution in MUV-10

Initially calculations predicting the stability of MUV-10 materials using different metal(II) ions were explored by Castells-Gil *et al.*¹ Enthalpies and free energy change for the process of exchanging the Ca²⁺ ions by M²⁺ were calculated using experimental hydration enthalpy and free energy of the cations, via the following equation:



The results from initial calculations determined that Mn(II) had a negative Gibbs free energy, meaning the reaction would likely proceed, as was also the case for V(II).¹ Mn(II) was expected to be most likely to be successfully exchanged due to the fact that it is a d⁵ metal that prefers a trigonal prism geometry. A series of other M(II) ions, however, did not give the same result from the calculations, and included Cr, Fe, Co, Ni, Cu, Zn, Pd and Cd.¹

Experimentally, it was then verified that Ni(II) and Zn(II) were unable to be used in the MUV-10 structure using identical synthesis conditions. Attempts were also made using Sn(II) and Mg(II), which also proved unsuccessful, as shown by the amorphous PXRD patterns that were yielded (Figure 3.14). Since the initial reporting of MUV-10, there has been another paper published that revealed the synthesis of MUV-101(Fe, Co, Ni, Zn) and MUV-102(Cu), produced by post-synthesis metal exchange reactions.²

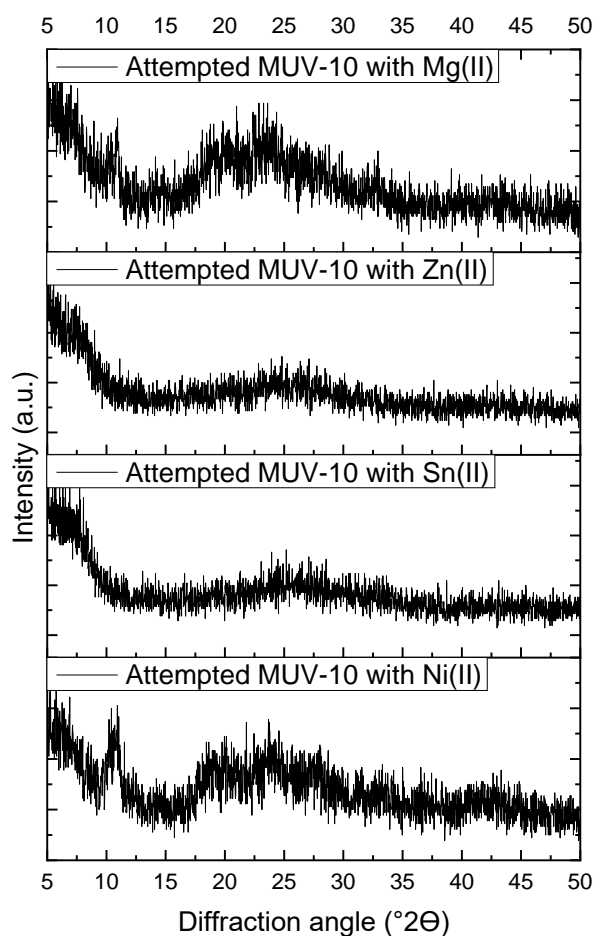


Figure 3.14: Powder XRD patterns from the attempts to exchange Ca(II) for Ni(II), Zn(II), Sn(II) and Mg(II) in the MUV-10(Ca) structure.

3.6 Substitution of Titanium(IV) in MUV-10

Attempts were made to swap the Ti(IV) for Sn(IV) in the MUV-10 structure for a variety of reasons. Firstly, it was thought to be a viable swap since both metals in the +4 oxidation state are small and highly charged cations producing electrostatic interactions with anionic linkers, which are often carboxylates. The ionic radii of Sn(IV) and Ti(IV) are 0.83 Å and 0.605 Å, respectively. A benefit of these strong metal-linker bonds is that the materials formed are likely to be highly stable in a variety of conditions, making them suitable for a range of applications. If full Sn(IV) substitution for Ti(IV) was possible, this would be the first reported Sn(IV) MOF to date.

For the substitution of Sn(IV) into MUV-10, the $\text{Sn}(\text{O}^i\text{Pr})_4$ starting material was chosen based on the fact that it was supplied in solution and could be easily injected into autoclaves or round-bottomed flasks for reflux. Previous work had used other Sn(IV) reagents, such as Sn(IV) acetate, which proved to readily hydrolyse, and so $\text{Sn}(\text{O}^i\text{Pr})_4$ was used as an alternative.⁵ When all Ti was exchanged for Sn in the synthesis, the MUV-10 structure did not form, and instead an XRD pattern was found with broad peaks corresponding to SnO_2 . Figure 3.15 shows an example with code KE018, which corresponds to a synthesis exchanging all Ti for Sn. The powder XRD pattern of SnO_2 is shown for reference and verifies that this was what was produced in KE018.

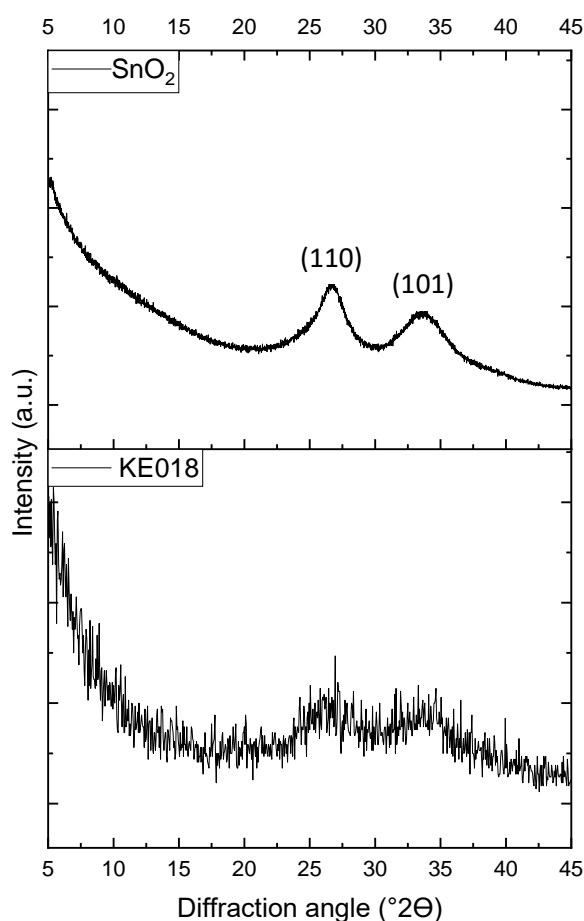


Figure 3.15: Powder XRD patterns for sample KE018, where all Ti had been exchanged for Sn in the synthesis, and SnO_2 for reference.

Work then focussed on exchanging smaller amounts of Ti for Sn in MUV-10. Work initially focused on the Mn version over the Ca version, due to the fact that it already

had a smaller band gap with the capability to absorb in the visible region, and also because it was stable over a wider pH range. Later, the focus then shifted to incorporating Sn into the MUV-10(Ca) structure since the paramagnetism of the Mn would be more problematic for additional analytical techniques that had potential to be explored, such as solid-state NMR.

The PXRD patterns show that MUV-10 containing Sn has the same pattern as those without Sn (see Figure 3.16). It might have been expected that there would be a slight peak shift to lower angles due to the size increase of Sn compared to Ti causing an increase in the unit cell volume, but negligible change is observed. However, for a bimetallic MOF, this effect may be diluted, causing the minimal change in XRD patterns. Each XRD pattern with varying % of Sn also appears to be the same (see Figure 3.16).

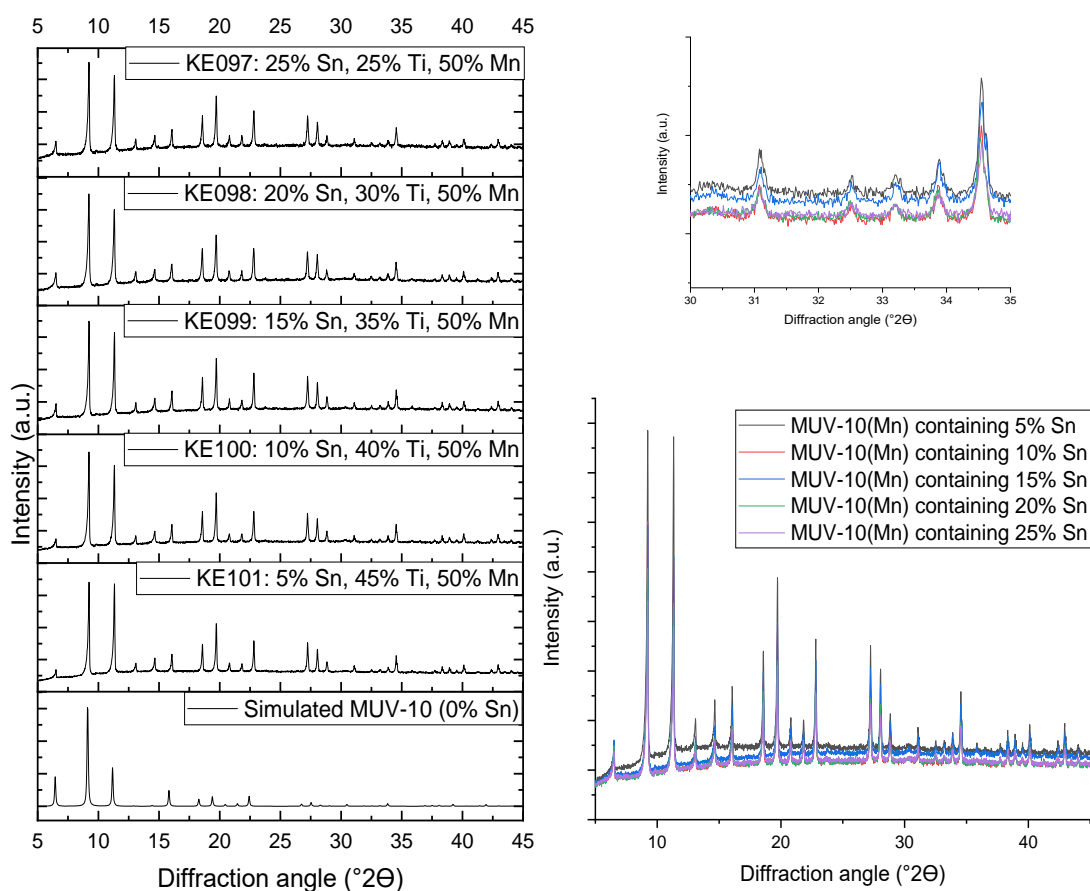


Figure 3.16: Powder XRD patterns for MUV-10(Mn) with varying amounts of Ti exchanged for Sn, with the simulated MUV-10 pattern for reference (left-hand side). Overlaid patterns are also shown, with a close-up view of a higher angle region, where no significant peak shifts can be seen (right-hand side).

To investigate the expected change in XRD patterns further, a pattern was simulated where 50% of the Ti was swapped for Sn. As was shown experimentally above, the change in pattern is very subtle. Figure 3.17 shows the simulated pattern containing Sn, as well as a zoomed in, overlaid plot. This shows a very subtle change in relative peak intensities, due to the increased number of electrons in Sn, as was anticipated. To the best of knowledge, this type of investigation into the alteration of unit cell parameters for metal substituted MOFs has not been extensively completed before.

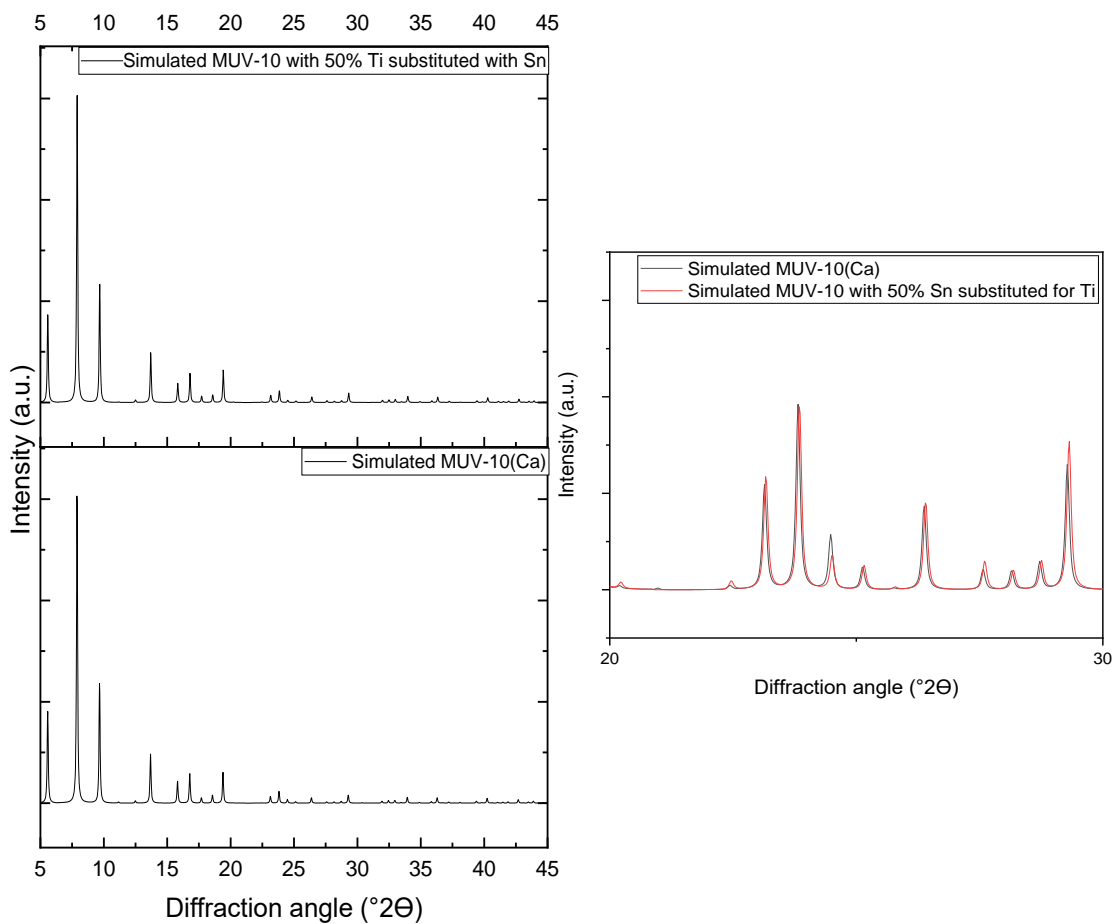


Figure 3.17: Powder XRD patterns for simulated MUV-10(Ca) and simulated MUV-10(Ca) with 50% Ti and 50% Sn. An overlaid plot at higher angle is also shown, where no significant peak shifts can be seen (right-hand side).

Additional evidence to support the incorporation of Sn into MUV-10 as opposed to a side product was that the mass yield of the reactions did not reduce upon addition of increasing amounts of Sn. If the Sn had remained in solution then the yield of the solid MOF produced would have reduced as more Sn was added.

Similarly to MUV-10(Mn) containing varying amounts of Sn, the XRD patterns for the MUV-10(Ca) samples containing varying amounts of Sn also showed no changes between XRD patterns (Figure 3.18).

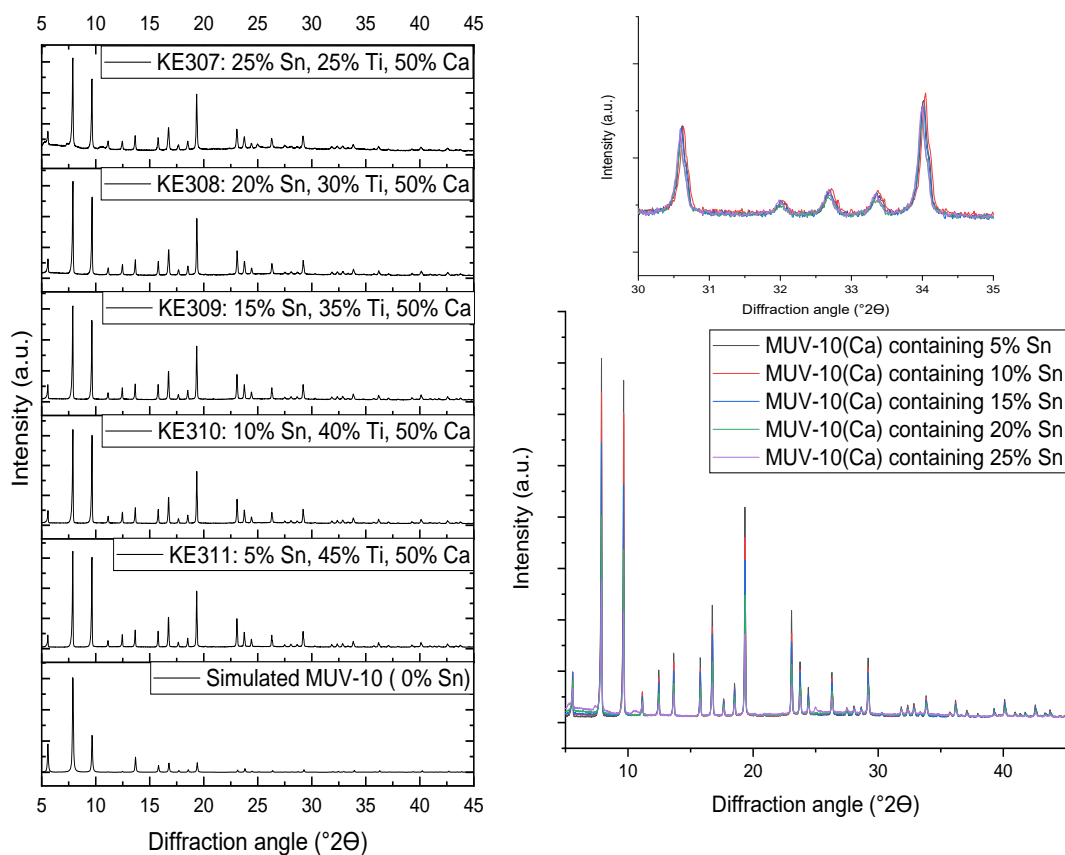


Figure 3.18: Powder XRD patterns for MUV-10(Ca) with varying amounts of Ti exchanged for Sn, with the simulated MUV-10 pattern for reference (left-hand side). Overlaid patterns are also shown, with a close-up view of a higher angle region, where no significant peak shifts can be seen (right-hand side).

GSAS-II software was used to perform a Le Bail profile to obtain the lattice parameter and to prove there was a good fit between the original MUV-10 pattern and the samples containing Sn. An example of a fitting for MUV-10(Ca) containing 20% Sn is shown in Figure 3.19. The space group from all of the fittings was confirmed to be $Pm\bar{3}$ (space group number 200), which is the same as that of MUV-10, where the Bravais lattice is primitive cubic ($a=b=c$).

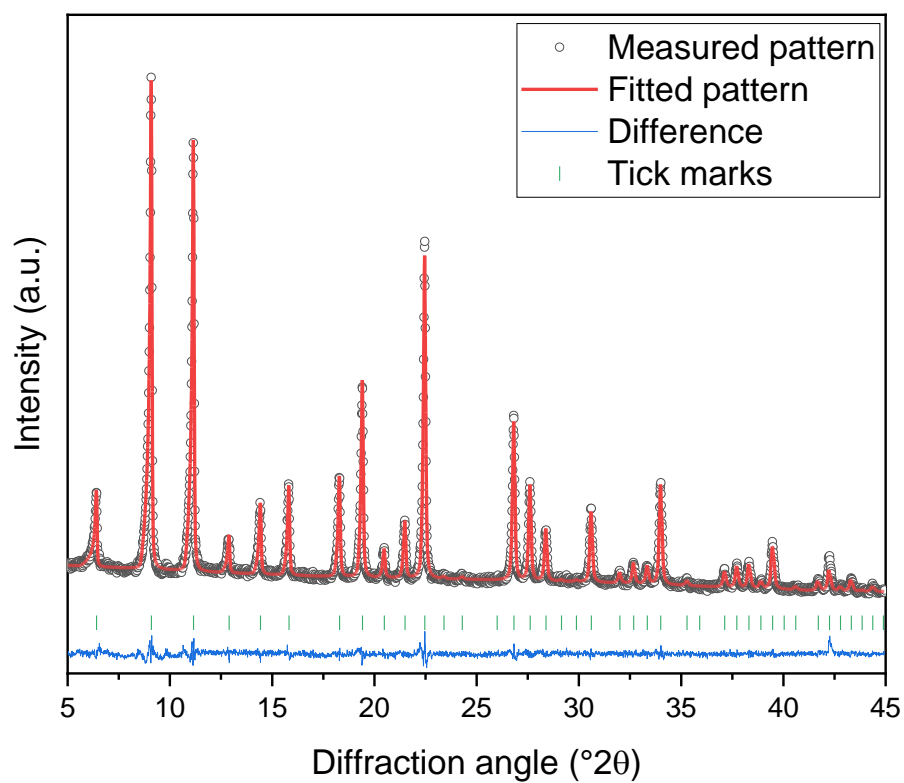


Figure 3.19: A graph showing the fitting of MUV-10 with MUV-10(Ca) containing 20% Sn using GSAS-II software.

All of the Sn-substituted samples were found to have the same space group, however, subtle differences in the lattice parameter were observed with increasing amount of Sn. As the Sn increased, the lattice parameter value decreased slightly (Figure 3.20).

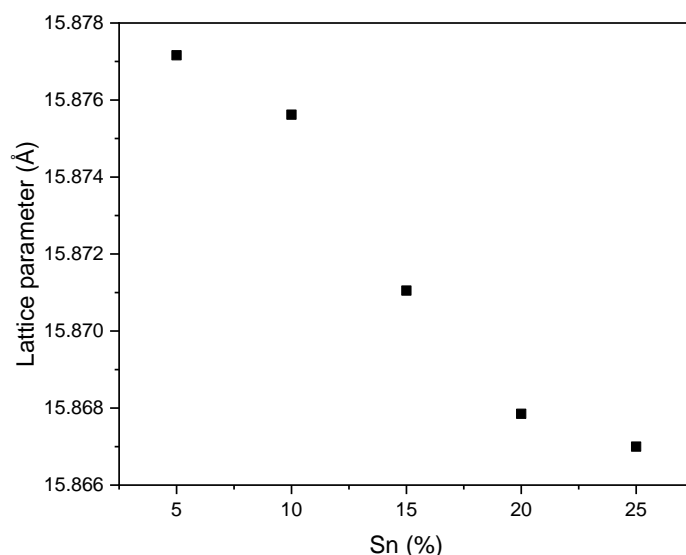


Figure 3.20: A graph showing how lattice parameters obtained from GSAS-II fittings change with increasing % of Sn.

Initially it was suspected that upon substitution of Ti(IV) for Sn(IV), the maximum amount of Sn that could be incorporated into the structure was limited to 20%. This was because at a composition consisting of 25% Sn, 25% Ti and 50% Mn, the background on the PXRD pattern started to appear slightly broader, where it was suspected to be due to a small amount of SnO₂. The detection of a small amount of SnO₂ is potentially likely due to the sensitivity of the Sn(OⁱPr)₄ starting material, which can readily hydrolyse to SnO₂. Whilst trying to inject larger amounts, it is more likely that the starting material has greater exposure to air, picking up moisture and subsequently becoming hydrolysed. It is also possible that the structure may only be able to accommodate a certain amount of Sn before it becomes unstable. As was identified above in Figure 3.15, 100% Sn substitution for Ti is not possible. However, upon closer inspection and looking at a log(intensity) scale to show the weaker peaks in the background, which could potentially correspond to SnO₂, the theory that 25% Sn was too much, was eliminated (Figure 3.21).

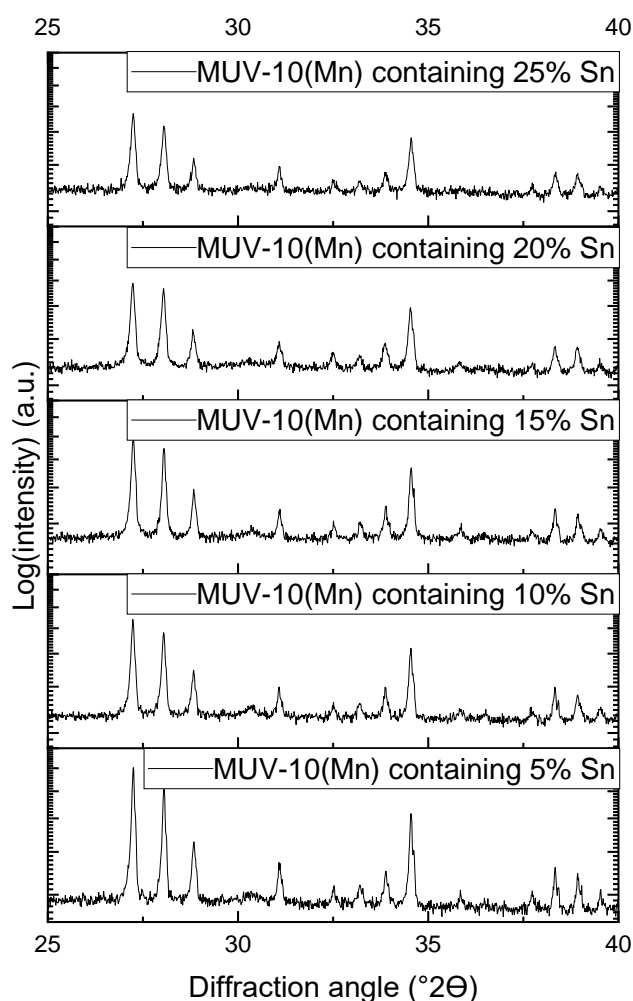


Figure 3.21: Log(intensity) powder XRD patterns for diffraction angles between 25-40 ($^{\circ}2\theta$) for MUV-10(Mn) containing varying amounts of Sn in order to check for the presence of broad SnO_2 peaks.

The theory that samples may contain SnO_2 was also confirmed to be incorrect by Sn K-edge EXAFS data, obtained from Diamond Light Source. The EXAFS signals for the MUV-10 samples doped with Sn are very different to that of SnO_2 and higher R shells are missing on Fourier transform plots (Figure 3.22). This comparison is shown below for the MUV-10(Ca) sample containing 25% Sn. Adding the next shell expected in SnO_2 gave only a slightly better fit but the Debye-Waller factor for that shell becomes very large, suggesting SnO_2 is not present. Adding further shells also gave no improvement. The corresponding table showing the fitting can be seen in Table 3.8.

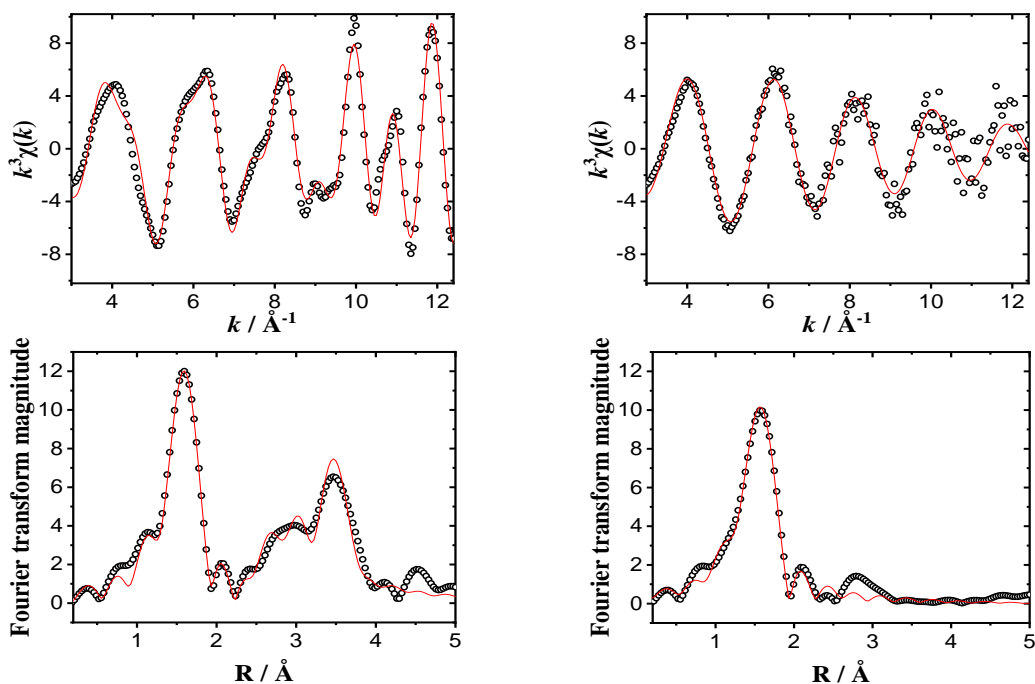


Figure 3.22: Sn K-edge EXAFS data for SnO_2 (left-hand side) and for MUV-10(Ca) containing 25% Sn (right-hand side). The bottom plots are the Fourier transforms.

Table 3.8: EXAFS fitted parameters for MUV-10(Ca) containing 25% Sn using a single oxygen shell. N = the number of neighbouring atoms, R (\AA) = fitted distance, R_{cryst} (\AA) = expected distance, σ^2 (\AA^2) = the Debye-Waller factor, S_0^2 = amplitude reduction factor, E_0 (eV) = refined threshold energy and R -factor = the extent to which the experimental data and model agree.

| Shell | N | $R / \text{\AA}$ | $\sigma^2 / \text{\AA}^2$ | S_0^2 | E_0 / eV | R -factor |
|-------|-----|------------------|---------------------------|---------|-------------------|-------------|
| O | 6 | 2.045(13) | 0.0051(16) | 1.056 | 2.688 | 0.067 |

For comparison, Table 3.9 shows the fitted parameters for SnO_2 .

Table 3.9: The EXAFS fitted parameters for SnO_2 . N = the number of neighbouring atoms, R (\AA) = fitted distance, R_{cryst} (\AA) = expected distance, σ^2 (\AA^2) = the Debye-Waller factor, S_0^2 = amplitude reduction factor, E_0 (eV) = refined threshold energy and R -factor = the extent to which the experimental data and model agree.

| Shell | N | $R / \text{\AA}$ | $R_{\text{cryst}} / \text{\AA}$ | $\sigma^2 / \text{\AA}^2$ | S_0^2 | E_0 / eV | R -factor |
|-------|-----|------------------|---------------------------------|---------------------------|---------|-------------------|-------------|
| O | 6 | 2.052(9) | 2.054 | 0.0036(12) | 0.999 | 2.368 | 0.052 |
| Sn | 2 | 3.208(15) | 3.187 | 0.0038(14) | | | |
| O | 4 | 3.583(69) | 3.591 | 0.0038(91) | | | |
| Sn | 8 | 3.727(20) | 3.710 | 0.0090(22) | | | |

The conclusion that can be drawn is that there is only isolated SnO_6 in the MUV-10 materials that are doped with Sn, since no longer Sn-Sn distances are observed. This is consistent with the MUV-10 crystal structure which shows that the closest metal to the Ti site is a pair of Ca atoms at 3.63\AA , which is not seen by EXAFS (Figure 3.23). Therefore the best model is that Sn(IV) replaces some of the Ti(IV) in MUV-10 and the amount of nano- SnO_2 is negligible, even in the 25 % sample, where if it is present its contribution is too small to be detected by EXAFS.

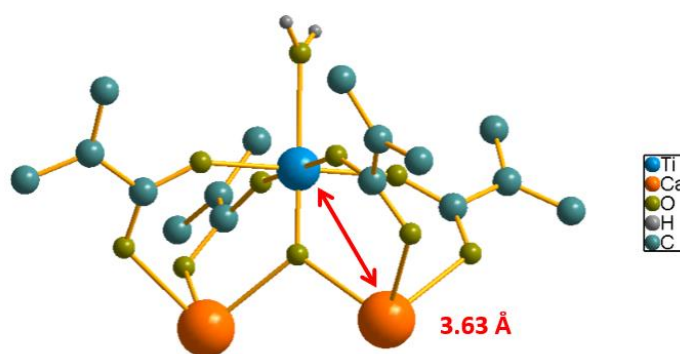


Figure 3.23: The MUV-10 crystal structure showing the distance between Ti and Ca.

The same results were found for the MUV-10(Mn) samples, where only one shell was required to fit the EXAFS spectrum; adding extra SnO_2 shells gave no improvement to the fit. This can be seen below in Figure 3.24 and Table 3.10.

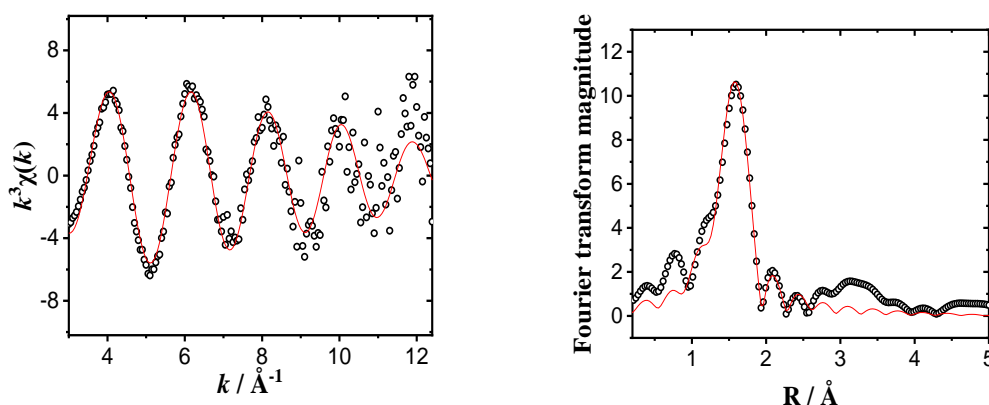


Figure 3.24: EXAFS data for MUV-10(Mn) containing 25% Sn.

Table 3.10: EXAFS fitted parameters for MUV-10(Mn) containing 25% Sn using a single oxygen shell.

| Shell | <i>N</i> | <i>R</i> / Å | <i>s</i> ² / Å ² | <i>S</i> ₀ ² | <i>E</i> ₀ / eV | <i>R</i> -factor |
|-------|----------|--------------|--|------------------------------------|----------------------------|------------------|
| O | 6 | 2.046(16) | 0.0044(19) | 1.002 | 4.362 | 0.089 |

Despite no significant difference in the PXRD patterns of the samples of varying metal composition, it can, however, be seen from TGA that samples with the greater % of Sn decompose at lower temperature (Figure 3.25), and generally samples with the greater % of Sn have greater residual masses, which is expected if substitution has occurred (Table 3.11). The residual mass is expected to be higher for samples containing more Sn since upon burning the organic components of the MOFs, TiO₂ and SnO₂ are left, where Sn is atomically heavier than Ti, meaning a greater residual mass is expected. A column has been added for the calculated theoretical residual masses after Sn substitution. The actual values are slightly lower than the calculated theoretical residual masses for the first three samples and are slightly higher for the last two values, however the results seem in good alignment when error is taken into consideration, showing good substitution efficiency.

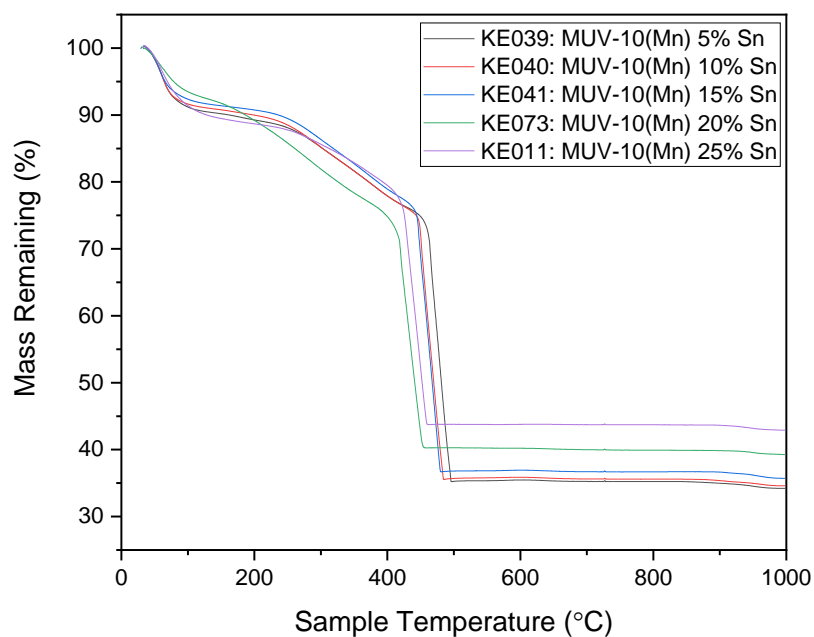


Figure 3.25: TGA for the MUV-10(Mn) structure with varying amounts of Sn present.

Table 3.11: MUV-10(Mn) samples containing varying amounts of Sn and their respective residual masses compared to theoretical residual masses from TGA.

| Sample | Residual Mass (%) | Theoretical Residual Mass (%) |
|--------------------------------------|-------------------|-------------------------------|
| KE039 – MUV-10(Mn) containing 5% Sn | 34.5 | 35.6 |
| KE040 – MUV-10(Mn) containing 10% Sn | 34.6 | 36.2 |
| KE041 – MUV-10(Mn) containing 15% Sn | 35.8 | 36.7 |
| KE073 – MUV-10(Mn) containing 20% Sn | 39.4 | 37.2 |
| KE011 – MUV-10(Mn) containing 25% Sn | 43.0 | 37.7 |

As was anticipated, the replacement of some Ti for Sn in MUV-10 has further modified the electronic properties of the material. UV-Vis measurements of the original MUV-10 materials confirmed a band gap of 3.1 eV for the Ca version of MUV-10 and 2.6 eV for the Mn version. As the amount of Sn increases in the MUV-10 structure, replacing Ti atoms, the band gap of the material is shown to decrease, as shown by UV-Vis measurements where band gaps were extrapolated by Tauc plot analysis (Figure 3.26). This method is not the most accurate, however should have provided consistent and reliable results since the same method of extrapolation was used each time.

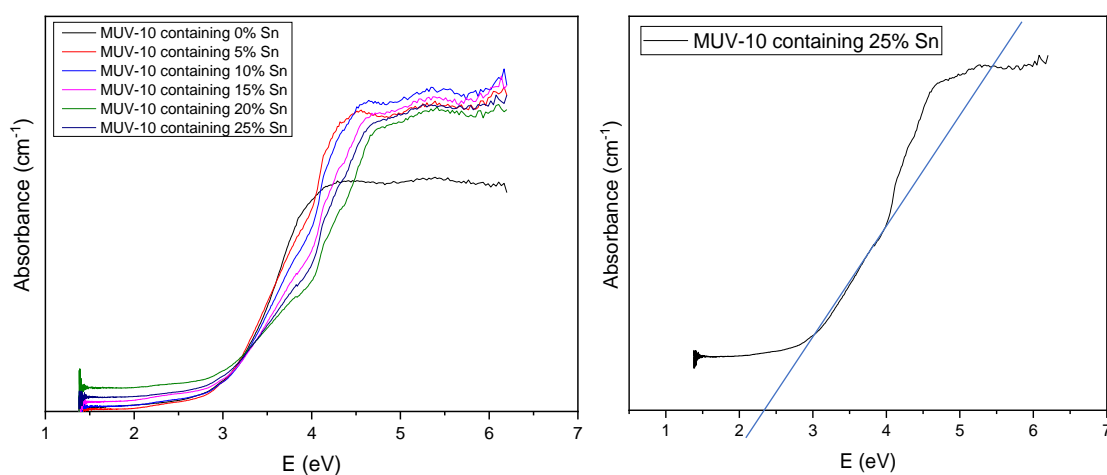


Figure 3.26: UV-Vis measurements for MUV-10(Mn) containing varying amounts of Sn (left-hand side). A Tauc plot for MUV-10(Mn) containing 25% Sn to show the extrapolation of the band gap (right-hand side).

The corresponding plot for the band gap versus the % of Sn included in each sample is shown below in Figure 3.27. This did not cause a linear decrease, which may have been expected, and there are only very subtle changes in the band gap between 0

and 15% Sn incorporation. 20% Sn substitution has the most significant effect on the band gap.

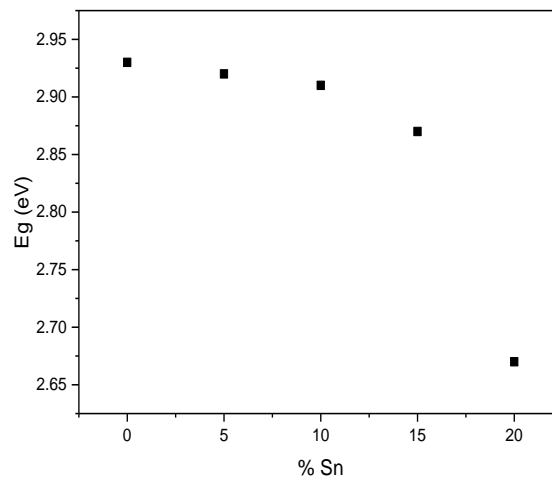


Figure 3.27: A plot of Band Gap Vs. % Sn for doped MUV-10(Mn) samples.

To further confirm the presence of Sn(IV) in the samples, XPS was measured. Firstly, XPS was completed for the ordinary MUV-10(Mn) sample, which did not contain any Sn. Figure 3.28 shows that the oxidation state of Ti is +4 and the oxidation state of Mn is fixed at +2, as was expected. These fittings were assigned using TiO_2 and MnO since they contain Ti(IV) and Mn(II).

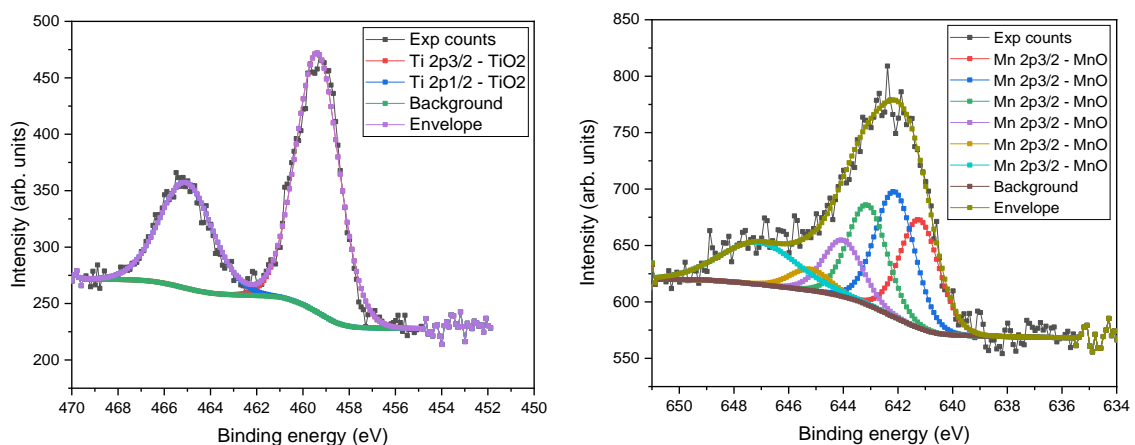


Figure 3.28: XPS spectra for MUV-10(Mn) showing the Ti region (left-hand side) and Mn region (right-hand side) to verify their oxidation states.

For completeness and for comparison against the MUV-10(Mn) sample containing Sn, the Sn region was probed for the ordinary MUV-10(Mn) sample to show the absence of Sn(IV), which can be seen in Figure 3.29.

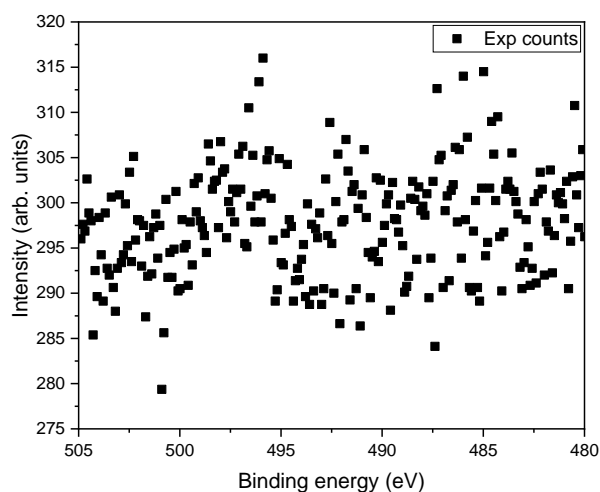


Figure 3.29: An XPS spectrum verifying the absence of Sn(IV) in ordinary MUV-10(Mn).

XPS was then completed on the sample of MUV-10(Mn) containing 30% Ti, 20% Sn and 50% Mn. From the fittings using TiO_2 and MnO, it is evident that the oxidation states of Ti and Mn are as expected, being +4 and +2 respectively (Figure 3.30).

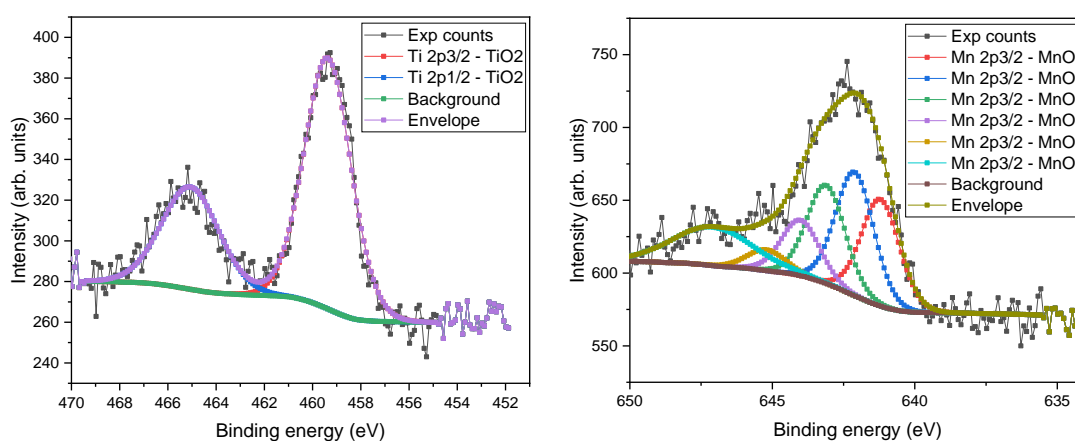


Figure 3.30: XPS spectra of the Ti and Mn regions of a MUV-10 sample containing Ti, Mn and Sn metals.

Compared to the Sn region shown for ordinary MUV-10 (Figure 3.29), the Sn containing sample clearly shows the presence of Sn(IV) ions. This is shown by the fitting that utilised SnO₂ as an Sn(IV) reference in Figure 3.31.

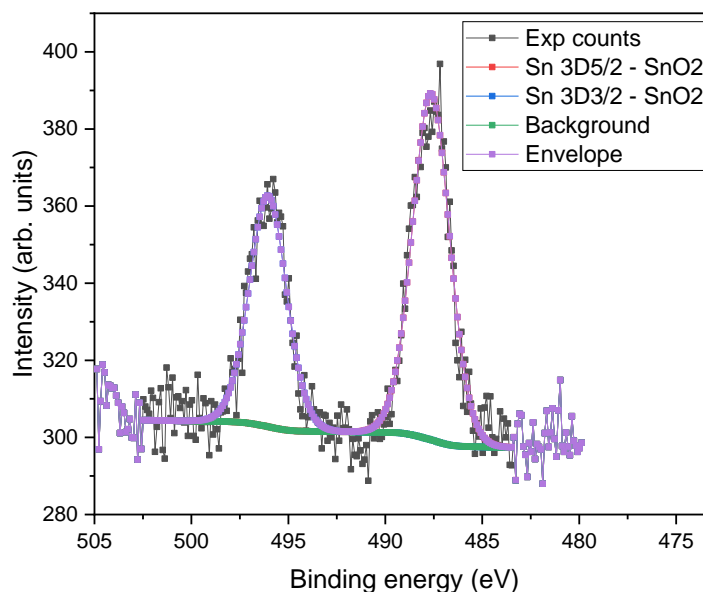


Figure 3.31: An XPS spectrum showing the Sn region for a sample of MUV-10 containing 50% Mn, 30% Ti and 20% Sn, using SnO₂ as an Sn(IV) reference.

The elemental composition from the XPS for MUV-10(Mn) shows that the proportions of Mn and Ti are roughly as expected. The sample of MUV-10(Mn) containing 20% Sn, 30% Ti and 50% Mn confirms 20.9% of Sn in the structure, which is roughly as was expected, alongside Ti and Mn in expected quantities. The composition of these two materials are shown below in Table 3.12. The nitrogen present can be attributed to residual DMF present on the surface of the MOF from the washing process of the MOFs. The washing involves one wash with DMF followed by another with MeOH, where the intention is then to remove the DMF from the pores of the material. However, not all of this is necessarily removed and replaced with MeOH. Many further MeOH washes could help to eliminate this further. Note that XPS is surface sensitive so the composition may not match perfectly the bulk expected values, but in fact the agreement to the expected values for these materials is very good.

Table 3.12: Elemental compositions from XPS for MUV-10(Mn) and MUV-10(Mn) containing 20% Sn.

| Elemental composition (at%) | | | | | | |
|-----------------------------|------|------|-----|-----|-----|-----|
| Element | O | C | Mn | Ti | Sn | N |
| MUV-10(Mn) with 0% Sn | 31.3 | 64.0 | 1.7 | 1.8 | 0.0 | 1.2 |
| MUV-10(Mn) with 20% Sn | 27.2 | 70.0 | 1.0 | 0.9 | 0.2 | 0.7 |

Sn K-edge XANES data were obtained from Diamond Light Source in order to also confirm whether or not the Sn present in the MUV-10 materials was in the +4 oxidation state or not. Sn is probed at the K edge, meaning an electron is promoted from a 1s orbital into an orbital with p-orbital symmetry.⁶ Both the MUV-10(Ca) and MUV-10(Mn) materials were investigated, with the Sn content ranging in the samples from 5-25% (in 5% increments).

The Sn K-edge XANES for MUV-10(Ca) (Figure 3.32), shows Sn(II) sulfate as a reference material to represent the +2 oxidation state of Sn, and Sn(IV) acetate as a reference material for the +4 oxidation state of Sn. The data obtained confirm that the Sn is present in the +4 oxidation state within the MUV-10(Ca) Sn-doped structure, as shown by the Sn(IV) appearing at higher energy, whilst the Sn(II) sulfate reagent appears at lower energy.

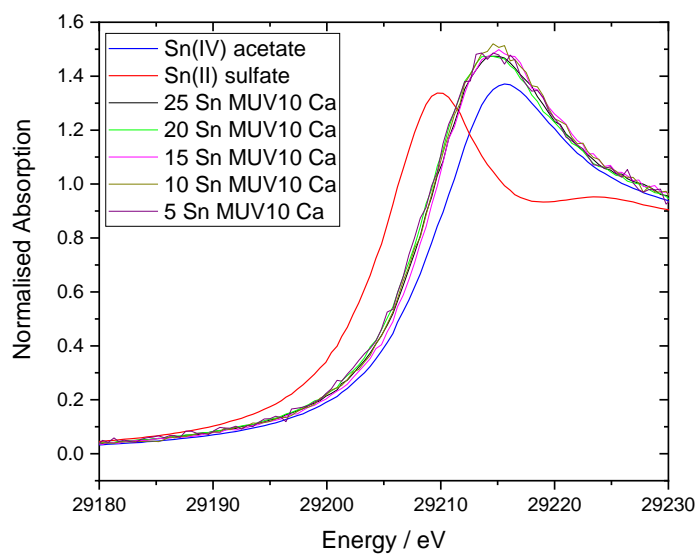


Figure 3.32: Sn K-edge XANES data of Sn-containing MUV-10(Ca) with samples ranging from 5% Sn to 25% Sn. Sn(IV) acetate and Sn(II) sulfate are shown for reference.

The Sn K-edge XANES for MUV-10(Mn) (see Figure 3.33), suggests that the Sn is present in the +4 oxidation state in the structure, in the same way as was shown for MUV-10(Ca).

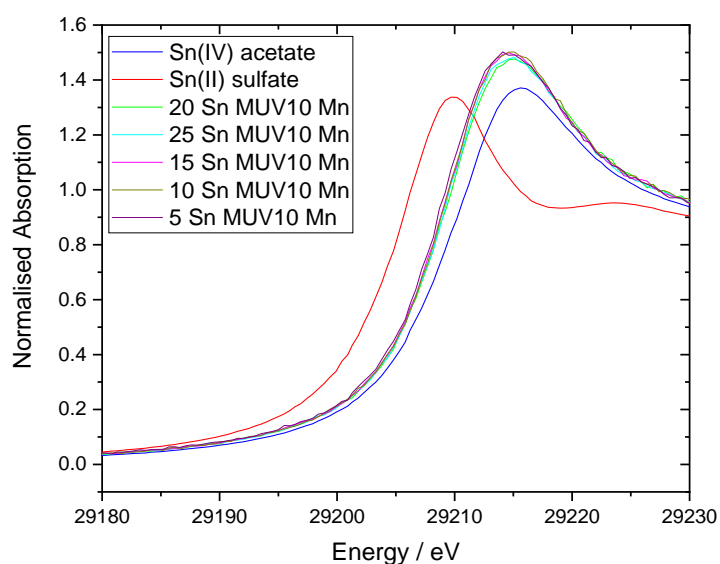


Figure 3.33: Sn K-edge XANES data of Sn-containing MUV-10(Mn) with samples ranging from 5% Sn to 25% Sn. Sn(IV) acetate and Sn(II) sulfate are shown for reference.

3.7 Exchanging the Organic Linker in MUV-10

An additional change made to the MUV-10 structure included swapping some BTC linker for 2-aminoterephthalate (ATP), where both ligand structures are shown in Figure 3.34. The ATP linker was of interest since the addition of amine groups in MOFs for the photocatalytic reduction of CO₂ has been shown to enhance catalytic activity and yield greater amounts of the desired formic acid product.^{7,8} This occurs by alteration of the electronic properties of the MOFs, where generally the -NH₂ group has been shown to cause reduction in the band gaps of the MOFs, meaning they often operate under visible light in addition to other regions. This is advantageous since a greater range of wavelengths are able to be harvested for catalysis, meaning more efficient photocatalysis. The reduction in band gap also means that often bands better align with reactant molecules for more effective catalysis.

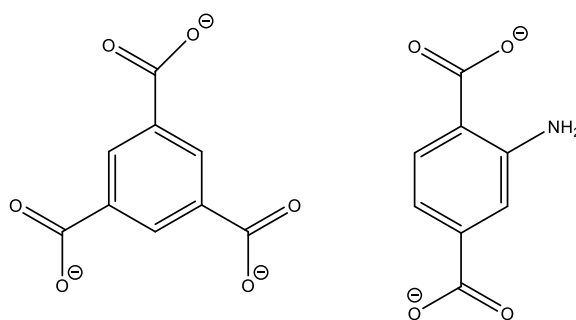


Figure 3.34: The BTC linker (left-hand side) and 2-aminoterephthalic acid (right-hand side).

The addition of the -NH₂ group is also of interest for other applications, such as gas separations. This is due to the addition of a basic nitrogen atom, which has been shown to enhance the binding and activation of the bonds in CO₂. The adsorbed CO₂ can then be used for other reactions, such as the fixation of CO₂ with epoxides to form cyclic carbonates.

Therefore, was investigated whether a new structure could be created with the ATP linker. It was not expected that the structure would be the same as MUV-10 since the ATP linker cannot bind in the same way as BTC does in MUV-10 because there is one less carboxylate group and the two that remain are not in the correct orientation.

The original MUV-10(Ca) is white in colour whilst MUV-10(Mn) is a very pale pink/white shade. The BTC linker is white in colour and ATP is bright yellow in colour. Synthesis of MUV-10(Mn) containing 50% BTC and 50% ATP yielded a pale-yellow material (Figure 3.35).

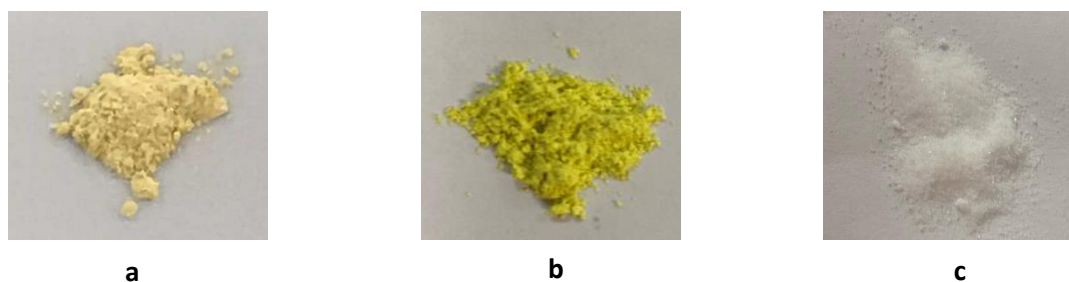


Figure 3.35: a) MUV-10(Mn) containing 50% BTC/50% ATP b) ATP linker shown for reference c) BTC linker shown for reference.

Initially, the colour change of the MOF was a good indication that the linker was present in the structure, whether surface bound, integral to holding the MOF together or trapped in the pores. Powder XRD patterns showed that there was no change between the MUV-10 structure using just BTC compared to the sample synthesised using 50% BTC/50% ATP (Figure 3.36). The XRD pattern for the 50% BTC/50% ATP sample also did not show any crystalline H₂ATP. However, if ATP were in the pores, then the relative peak intensities would change without seeing H₂ATP peaks on the XRD pattern, which does not occur with this sample. Since the MOFs were thoroughly washed after synthesis, it was further deduced that the sample was not simply composed of MUV-10 with unreacted linker present, and that there was likely not H₂ATP blocking the pores. The fact that the XRD pattern is the same as is seen for MUV-10 suggests that ATP could be bound to the surface of the MOF, rather than being integral to the structure, otherwise a completely different structure would have formed due to the different binding modes of ATP compared to BTC, providing a unique XRD pattern.

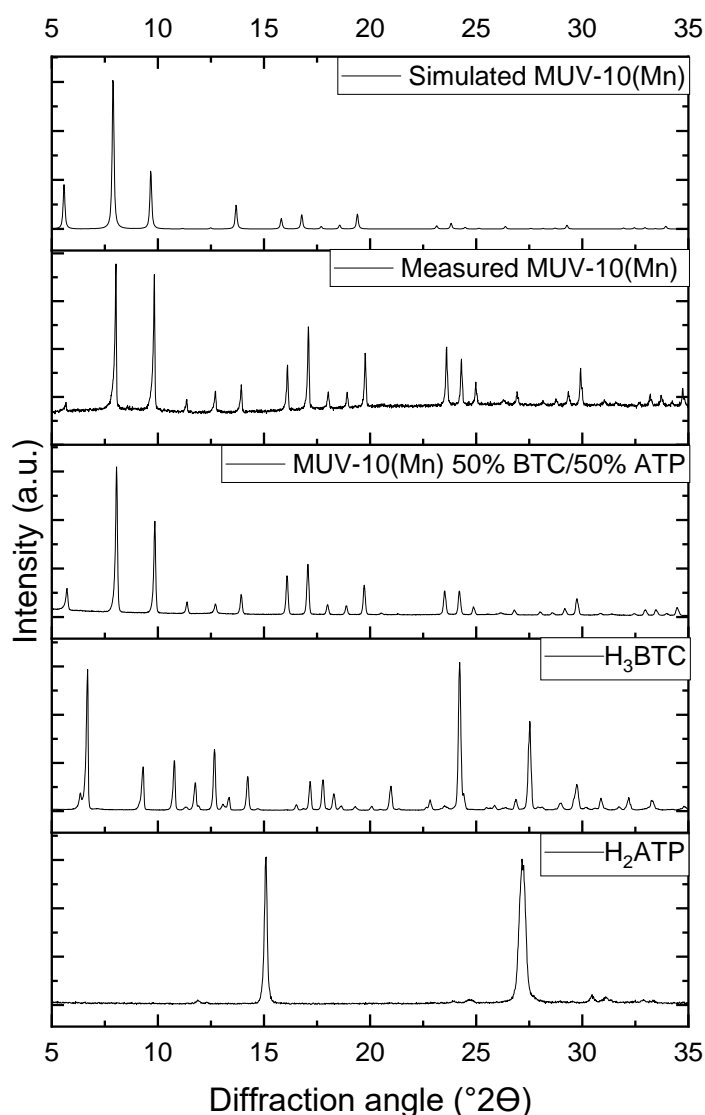


Figure 3.36: Powder XRD patterns of H_2ATP and H_3BTC organic linkers, with $MUV-10(Mn)$ containing 50% BTC/50% ATP and simulated pattern of $MUV-10(Mn)$ for comparison.

UV-Vis spectra showed a reduction in band gap of $MUV-10$ upon the addition of ATP. $MUV-10(Mn)$ showed a reduction in band gap from 2.9 eV to 2.2 eV, whilst $MUV-10(Ca)$ showed a reduction in band gap from 3.4 eV to 2.6 eV, which can be useful for efficient charge separation in photocatalytic applications (Figure 3.37). However, in addition to this, the band alignment of materials does also need to be considered for effective photocatalysts.

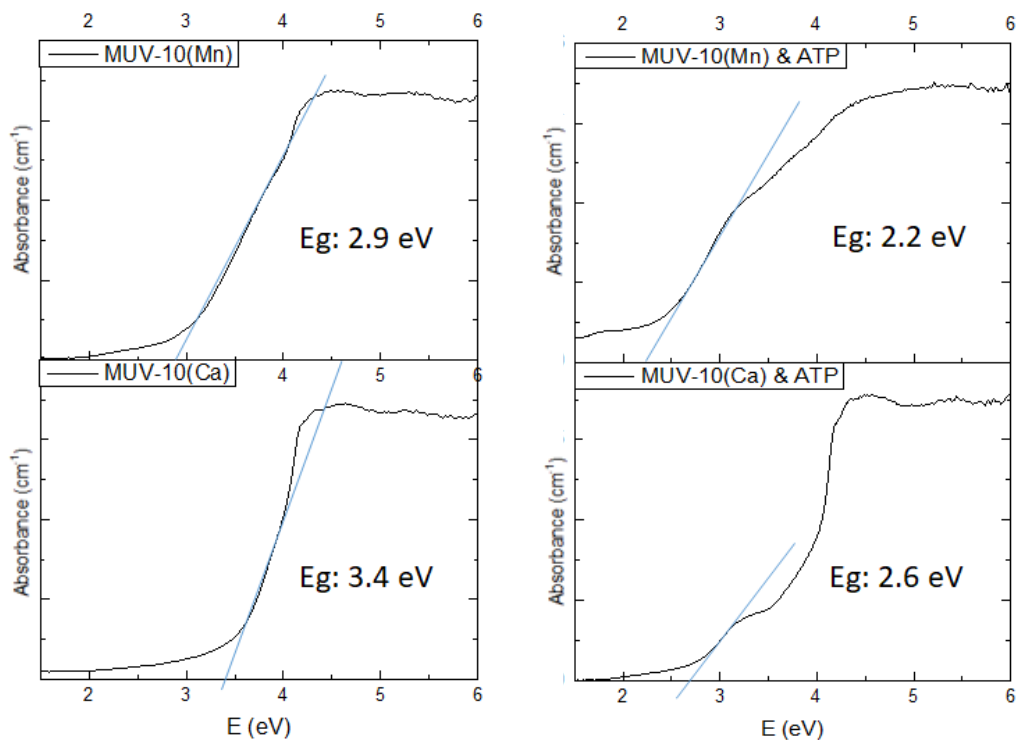


Figure 3.37: UV-Vis plots showing ordinary MUV-10 materials containing only BTC on the left-hand side, with modified versions of MUV-10 containing 50% BTC/50% ATP for both Mn and Ca versions on the right-hand side.

TGA was completed to also provide evidence for ATP being bound to the structure, as it was expected to differ to the version of MUV-10 containing only BTC (Figure 3.38). The ATP-containing version of MUV-10(Mn) proved to combust at lower temperature, meaning the addition of the ATP linker, potentially as a surface-modified linker, made the material less thermally stable.

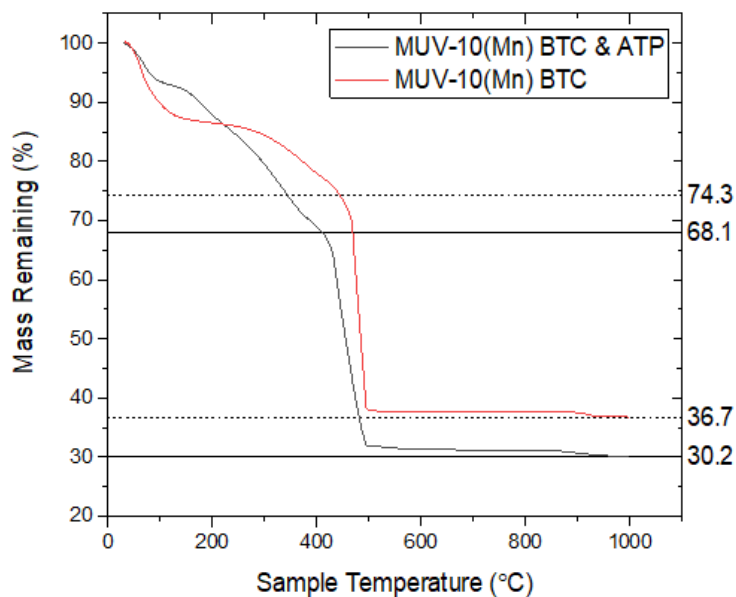


Figure 3.38: TGA of MUV-10(Mn) containing only BTC compared to MUV-10(Mn) containing 50% BTC/50% ATP.

It then needed to be determined where the ATP linker was bound in the structure. Due to the fact that BTC coordinates via three carboxylate groups to the metallic clusters, it was highly unlikely that the ATP could form an integral part of the MUV-10 structure. Therefore, it was more likely that the ATP was surface bound, present in the pores, or was a small defect within the MUV-10 structure, causing the PXRD pattern to still appear the same.

CHN analysis was also used to determine the relative amount of nitrogen present, since the ATP contains nitrogen, unlike BTC. It was found that a greater proportion of N in the ATP modified MUV-10 sample compared to the MUV-10 sample (see Table 3.13), due to the N in the ATP linker. The N found in ordinary MUV-10 can be attributed to a small quantity of residual DMF from the washing process of the MOF after its synthesis, although it is expected to be 0% after washing with methanol. If this base amount of N from DMF is subtracted from both samples, it is clear that there is additional N in the ATP modified sample.

Table 3.13: CHN analysis for MUV-10 containing only BTC linker (left-hand side) and CHN analysis for MUV-10 containing BTC and ATP linker (right-hand side).

| CHN analysis for MUV-10 containing only BTC linker | | CHN analysis for MUV-10 containing BTC and ATP linker | |
|--|-----------------|---|-----------------|
| Element | Result (%wt/wt) | Element | Result (%wt/wt) |
| Carbon | 30.8 | Carbon | 35.2 |
| Hydrogen | 3.3 | Hydrogen | 3.2 |
| Nitrogen | 1.1 | Nitrogen | 3.7 |

For completeness, a whole range of the modified BTC/ATP MOFs were synthesised, from 0% to 100% ATP incorporation where the % increments were 5%. All XRD patterns match that of the original MUV-10 pattern, except for 100% ATP, Figure 3.39. There was also no reduction in sample yield upon addition of ATP, which would be expected if for example the samples had been comprised of MUV-10 using solely BTC in preference to utilising ATP in the structure. Excess ATP would then have been removed during the washing and filtration process, leaving a smaller residual mass. The plot of ATP (%) vs. sample yield, Figure 3.40, shows no clear trend to suggest this happening. Small differences in sample yield are attributed to losses during the washing and filtering process. Therefore, these findings help reinforce the theory that the ATP could be surface bound, but still part of the structure as opposed to in a side product or as existing as unbound linker.

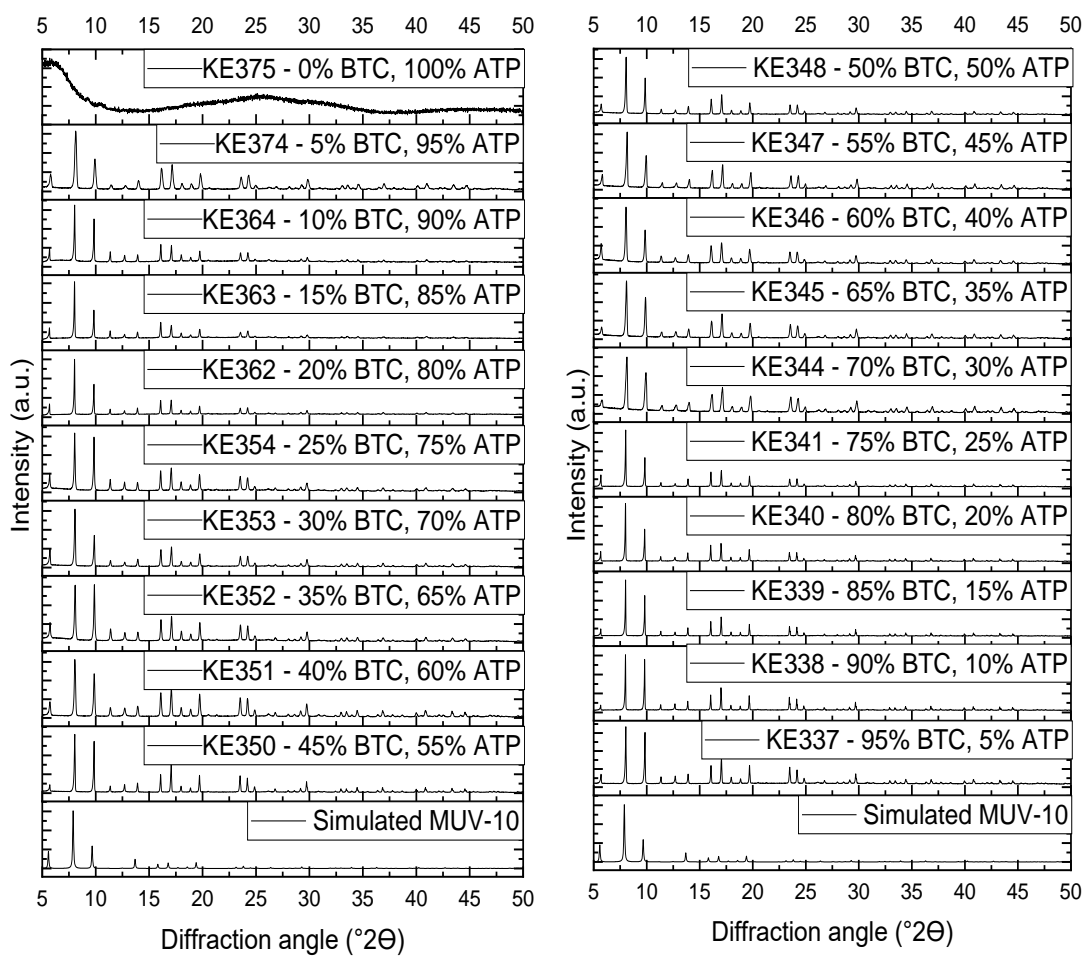


Figure 3.39: XRD patterns for simulated MUV-10 alongside samples containing varying amounts of BTC and ATP.

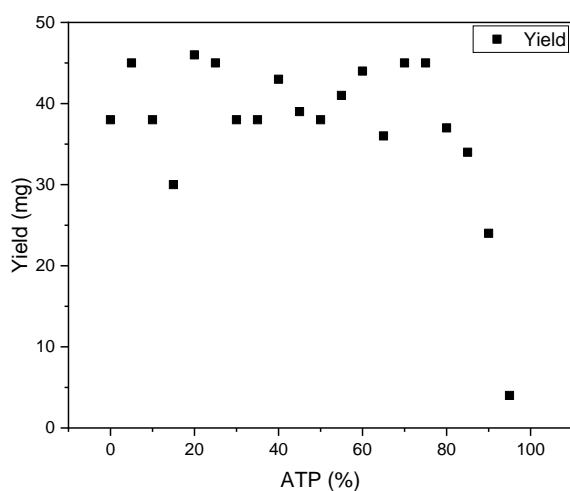


Figure 3.40: Plot of ATP (%) vs. sample yield (mg). 100% ATP sample does not have the MUV-10 XRD pattern and so is treated as a distinct sample to the rest.

In order to obtain full structural information for these ATP-modified MOFs, single crystals would be needed. However, even if single crystals were obtained, the disorder of ATP compared to BTC would be difficult to refine, and if the ATP is surface bound or in the pores, it may not give any extra diffraction. Currently, it is expected that surface modified MOFs have been created, giving rise to new coloured materials, which would be excellent candidates for CO₂ photoreduction given the varying band gaps obtained.

Another change to the MUV-10 structure was to try using 5-aminoisophthalate (AIP) as a linker. AIP exists as a pale-yellow solid. Similarly to the ATP shown previously, there are two carboxylate groups and an amino group in replacement of three carboxylate groups in BTC. The difference between AIP and ATP however, is simply the position of the amine group. AIP resembles BTC but with one carboxylate group exchanged for the amino group, which was deemed as a more reasonable replacement than ATP in the MUV-10 structure (see Figure 3.41). This is because AIP might link more similarly than ATP in replacement of BTC, by use of two carboxylate groups in the correct relative orientation.

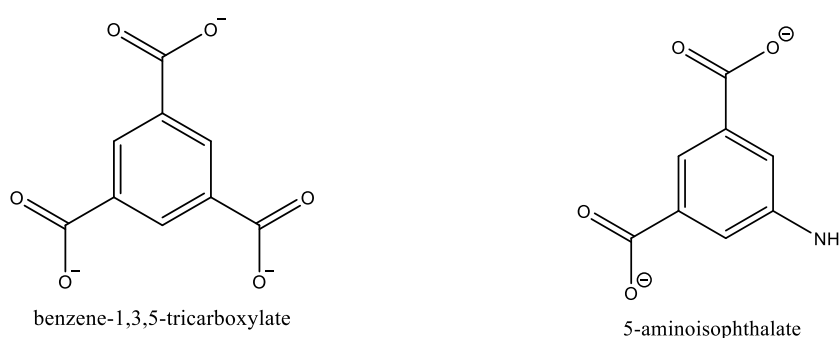


Figure 3.41: Benzene-1,3,5-tricarboxylate (BTC) shown on the left-hand side and 5-aminoisophthalate (AIP) shown on the right-hand side.

A series of MUV-10(Mn) materials were synthesised using AIP, ranging from 5% AIP to 100% AIP, increasing in 5% increments. The PXRD patterns (see Figure 3.42) show

the maintenance of the MUV-10 structure up until 95% and 100% AIP. 100% AIP with 0% BTC does not form MUV-10 at all, whilst 95% AIP with 5% BTC shows the MUV-10 pattern with a slightly amorphous background. This suggests that MUV-10 has formed with BTC, with AIP in another form in the pores or on the surface. It can be concluded that there is not pure H₂AIP linker as this would show on the PXRD, but it could be a separate amorphous phase, possibly a salt of the AIP with Ti.

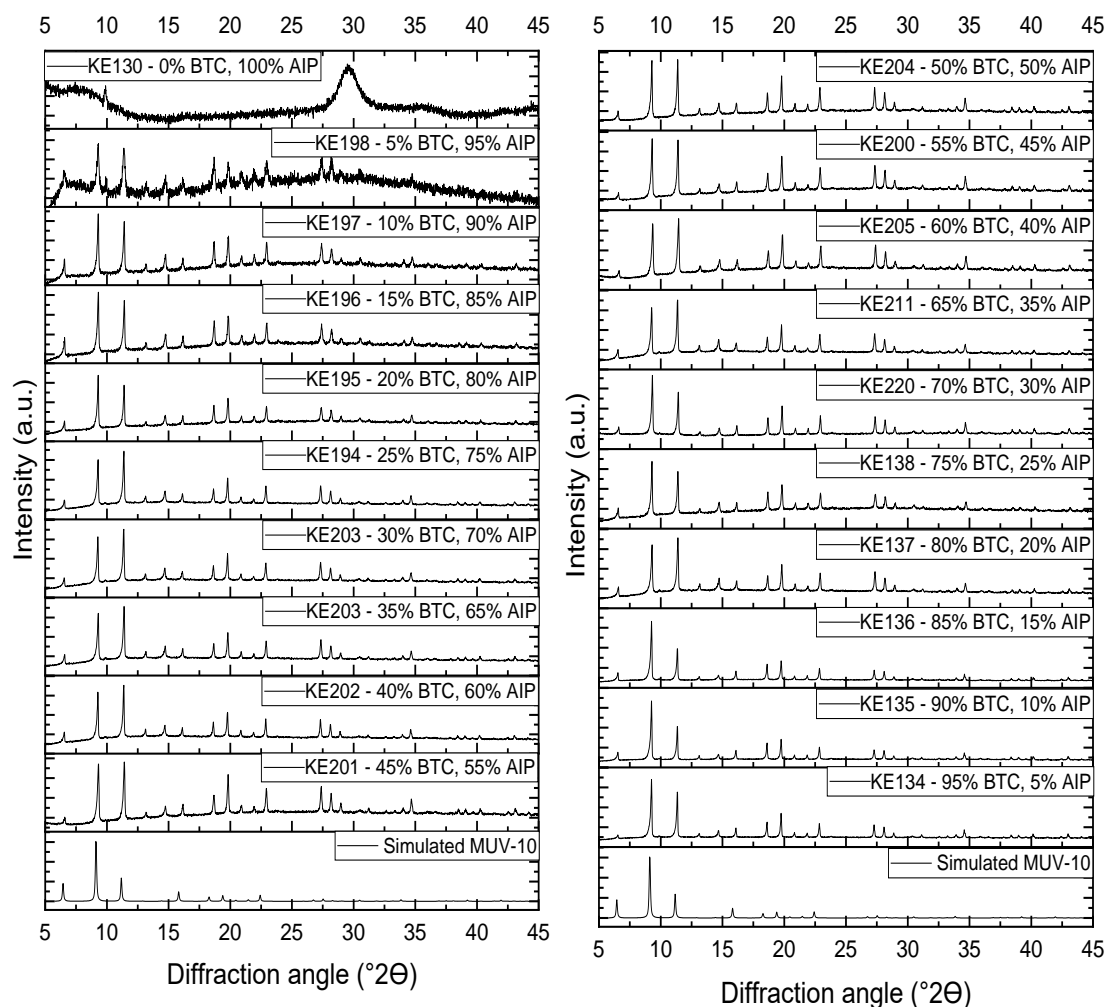


Figure 3.42: XRD patterns for simulated MUV-10 alongside samples containing varying amounts of BTC and AIP.

Yields were recorded (see Figure 3.43) in order to identify whether it was likely that the AIP was creating a surface modified MOF or whether there was simply the MUV-10 material and then a separate coloured material formed from the AIP linker being stuck in the pores of the MUV-10. However, the yields do not display a clear trend to

draw any conclusions from, and as with the ATP/BTC samples reported above, small differences in yield can be attributed to the washing and filtering process. Additionally, the last two yields should be excluded when drawing conclusions since the XRD patterns showed them to be distinct samples to the others.

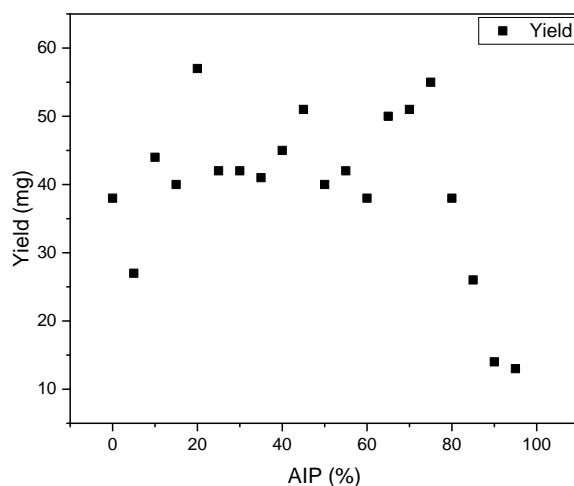


Figure 3.43: Plot of AIP (%) vs. sample yield (mg). 100% and 95% AIP samples do not have the MUV-10 XRD pattern and so are treated as distinct samples.

The colours of the materials produced varied significantly (see Figure 3.44) whilst UV-Vis data (see Figure 3.45) only showed subtle differences in the band gaps obtained. As previously discussed, band gap extrapolation holds some error and so this could contribute to the subtle changes observed. Since the 95% and 100% AIP samples did not produce the MUV-10 structure, their band gap values should be ignored when comparing to the other BTC/AIP samples.

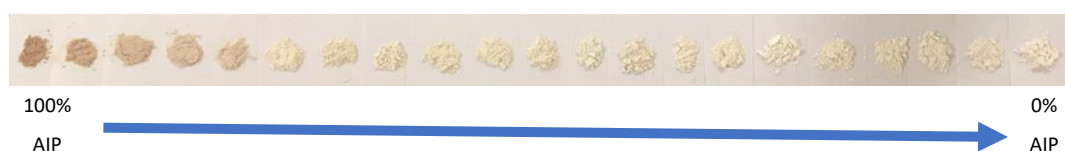


Figure 3.44: Samples in order of 100% AIP to 0% AIP incorporation into the MUV-10 structure.

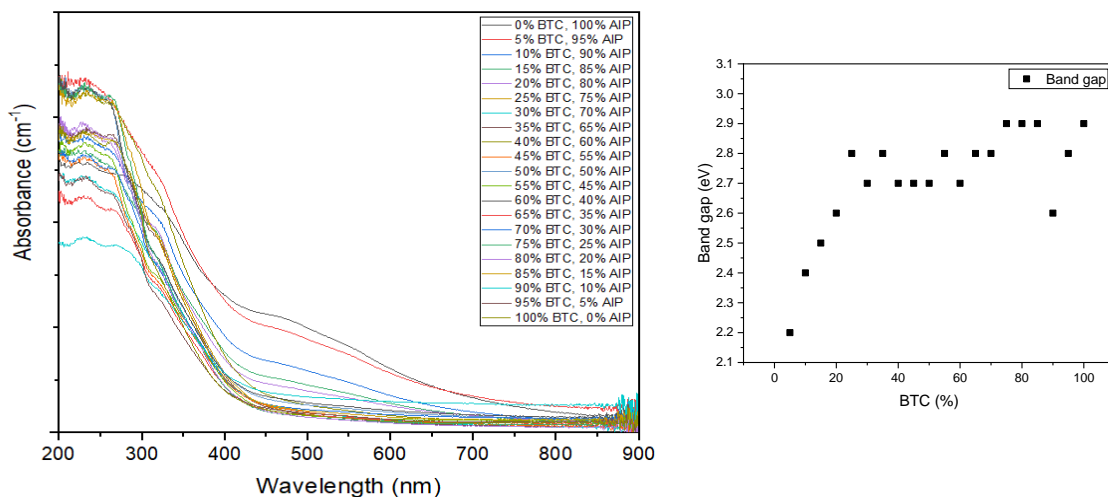


Figure 3.45: UV-Vis data (left-hand side) and corresponding plot of % BTC vs. band gap (right-hand side) for samples containing varying amounts of BTC/AIP.

TGA data (Figure 3.46) shows sample decomposition at roughly the same temperature, and the samples containing 0% BTC, 5% BTC and 10% BTC have the greatest residual masses. After these three samples, the TGA not show any other clear trends based upon % increase in amount of AIP with % decrease in amount of BTC.

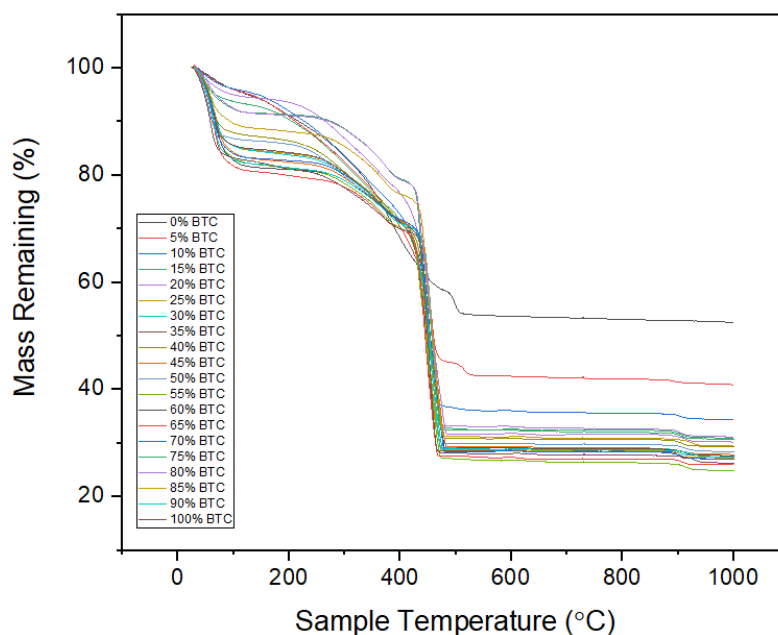


Figure 3.46: TGA data for samples containing varying amounts of BTC and AIP in the MUV-10 structure. Samples containing 0% BTC and 5% BTC can be excluded in the comparison since XRD verified they did not form the MUV-10 structure.

Like with the ATP samples, CHN analysis was completed to see the amount of nitrogen present in the sample (see Table 3.14). Compared to in the ordinary MUV-10(Mn) sample containing 100% BTC, the sample containing 50% BTC and 50% AIP, contained more nitrogen (2.84% cf. 1.12%), where the 1.12% in the 100% BTC sample occurred from the DMF used in the washing of the sample.

Table 3.14: CHN analysis on a sample containing 50% BTC, 50% AIP.

| Element | Result (%wt/wt) |
|----------|-----------------|
| Carbon | 32.53 |
| Hydrogen | 2.83 |
| Nitrogen | 2.84 |

3.8 Conclusions

The mixed-metal MOF MUV-10 was selected as a starting point for the work in this thesis due to its excellent chemical stability and robustness. It was found that various modifications to the structure were possible, which included incorporating Sn(IV) into the structure, enabling MUV-10 to be a MOF comprised of three metals with the BTC linker. Various spectroscopic techniques were used to confirm the modified structures, including XPS, EXAFS and XANES, despite the XRD powder patterns showing little change upon inclusion of Sn. Other techniques showed changes in the electronic properties of the modified MOFs, such as UV-Vis.

Other alterations to the MUV-10 structure included attempting to put small amounts of other linkers into it, such as 2-aminoterephthalic acid and 5-aminoisophthalic acid. It was hoped that the electronic structures of these modified materials could form great candidates for photocatalytic applications. Further work would need to be completed in order to try to obtain single crystals of the ATP samples so that further structural confirmation could be completed. Ongoing work has consisted of altering

reaction concentrations, synthesis durations, use of modulators and more, however none to date have yielded single crystals.

As with the ATP samples, single crystals would also need to be obtained for the AIP samples in order to gain more information on the MOF structure. Further modifications could be made to the synthesis to try to achieve this, such as altering concentrations, synthesis temperature, use of modulators and more. As it stands, it is believed that surface modified MUV-10 materials have been created using both ATP and AIP.

Overall, several successful modifications to the MUV-10 structure were made, forming MOFs able to be tested in a variety of applications that are explored further in this thesis. In particular, the successful incorporation of Sn into MUV-10 proved interesting for further study.

3.9 References

- 1 J. Castells-Gil, N. M. Padial, N. Almora-Barrios, J. Albero, A. R. Ruiz-Salvador, J. González-Platas, H. García and C. Martí-Gastaldo, *Angew. Chemie - Int. Ed.*, 2018, **57**, 8453-8457.
- 2 N. M. Padial, B. Lerma-Berlanga, N. Almora-Barrios, J. Castells-Gil, I. Da Silva, M. De La Mata, S. I. Molina, J. Hernández-Saz, A. E. Platero-Prats, S. Tatay and C. Martí-Gastaldo, *J. Am. Chem. Soc.*, 2020, **142**, 6638-6648.
- 3 K. Fabrizio, K. A. Lazarou, L. I. Payne, L. P. Twight, S. Golledge, C. H. Hendon and C. K. Brozek, *J. Am. Chem. Soc.*, 2021, **143**, 12609–12621.
- 4 Isabel Abánades Lázaro, *J. Mater. Chem. A*, 2022, **10**, 10466–10473.
- 5 K. J. Everden, MChem Thesis, University of Warwick, 2018.
- 6 D. W. Bruce, D. O'Hare and R. I. Walton, *Local Structural Characterisation*,

Wiley, Chichester, 2013.

- 7 C. C. Wang, Y. Q. Zhang, J. Li and P. Wang, *J. Mol. Struct.*, 2015, **1080**, 44-51.
- 8 W. Zhan, H. Gao, Y. Yang, X. Li and Q. Zhu, *Adv. Energy Sustain. Res.*, 2022, **3**, 1-30.

Chapter Four

An Investigation into Syntheses of Novel Ti(IV) and Sn(IV) MOFs

4.1 Introduction

An investigation into the synthesis of novel Ti(IV) and Sn(IV) MOFs was completed for a variety of reasons. Table 1.1 in Chapter 1 shows all of the Ti(IV) MOFs reported to date, including the metal source and organic linker used, where many of these reported MOFs are useful in applications such as photocatalysis. Therefore, synthesis of novel Ti(IV) MOFs was attempted, utilising organic linkers that had previously not been reported in Ti MOFs, in a hope that additional photocatalytic MOFs could be formed with superior properties to existing materials. A superior MOF for an application such as the photocatalytic conversion of CO₂ would ideally be water stable in order to survive in real-world applications, recyclable, have good CO₂ uptake with good conversion and selectivity, have better band alignment with CO₂ and an optimal band gap for sufficient electron-hole separation. Ti(IV) should form strong bonds with anionic linkers, potentially forming robust materials. The aim was to develop more stable Ti(IV) MOFs with the hope to use them in photocatalytic applications, and potentially screen them further in other sustainability-focused applications. Also, as previously mentioned in Chapter 1, Sn(IV) MOFs do not currently exist, but in theory Sn(IV) MOFs would be stable, since +4 is a possible oxidation state for Sn, forming strong bonds with organic linkers, as seen with other stable +4 metal ion MOFs, such as UiO-66, which utilises Zr(IV) ions. Sn(IV) has a similar but slightly larger ionic radius (0.83 Å) compared to Ti(IV) (0.605 Å), and so therefore some substitution experiments were planned, as well as experiments attempting to synthesise novel monometallic Sn(IV) and Ti(IV) MOFs. Since it remains

unknown as to why purely Sn(IV) MOFs do not exist, attempts were made to find optimum synthetic conditions to make their existence possible.

Many reported MOFs are unstable in water, limiting their applications. If stable Ti(IV) and Sn(IV) MOFs could withstand varying levels of acidity and basicity, the scope of possible useful applications for them drastically increases. Also, water-stable MOFs offer the advantage of being able to operate as catalysts in greener and often more inexpensive conditions, compared to using organic solvents. Both Ti and Sn ions are Lewis acidic, making them exceptionally useful in heterogeneous catalysis, which is another reason why their development is of interest. Both Ti(IV) and Sn(IV) precursors need to be handled with care, since upon exposure to air they can rapidly hydrolyse into TiO₂ and SnO₂, respectively. This chapter explores the attempts made to synthesise Ti(IV) and Sn(IV) MOFs and the reasoning for the different approaches, discussing and concluding the challenges and outcomes. Some highly promising materials were formed, where additional work could be completed to gain further insight into their structures. A crystal structure is also determined and described from the products of one of the attempted Sn syntheses.

4.2 Attempted Synthesis of Novel Ti(IV) MOFs

Currently, there have been no reported Ti MOFs using 1,2,4,5-benzenetetracarboxylic acid (H₄BTEC), 1,4-naphthalenedicarboxylic acid (H₂NDC), 2,6-pyridinedicarboxylic acid (H₂PDC), 2-nitro-benzene-1,4-dicarboxylic acid (H₂NBDC), 5-aminoisophthalic acid (H₂AIP), biphenyl-4,4'-dicarboxylic acid (H₂BPDC) or 2,3-pyrazinedicarboxylic acid. These linkers were chosen for the attempted synthesis of novel Ti(IV) MOFs since this sample of linkers offer a range of different features, of which it was hoped at least one feature would contribute to successful novel Ti(IV) MOF formation. For example, some linkers have more coordination sites (H₄BTEC), some include N atoms (H₂PDC) and some contain two aromatic rings (H₂BPDC), and more. It was believed that using a sample of linkers with a variety of features could offer the possibility to produce novel MOFs for sustainable

applications, and so the broadest selection available were trialled with multiple attempts using different experimental conditions. Attempts were made to use these linkers, using solvents and conditions used for previously reported Ti MOFs or formulated from a combination of previously reported conditions. Selecting conditions used in previously successful Ti MOF syntheses does not guarantee forming a new Ti MOF with a new organic linker but was nonetheless a starting point.

The attempted syntheses using H₄BTEC as the organic linker are in Table 4.1, which also displays the metal precursor as well as the solvent(s), temperature, and synthesis time. Any additional notes on which previously reported synthetic method was used or modified are also listed. Reagents were added in the typical method listed in Experimental 2.4. Linker was added to the selected reaction vessel, then metal powder, followed by solvent(s). If the metal was in solution, it was injected after the solvent was added.

The addition of base, such as triethylamine (TEA), in some of the following attempted syntheses is to aid deprotonation of the carboxylic acid, where it was hoped that a rapid combination of linker with the Ti precursor would take place, meaning a Ti(IV) MOF would form faster than the Ti could form unwanted amorphous TiO₂. However, a compromise needs to be made if MOF crystals are required, which is essential for full analysis on the structure to be completed. MOF synthesis is a reversible Lewis acid/base reaction. For crystals to be obtained, slow growth of MOFs is required, requiring manipulation of the reversibility of the acid/base reaction. Small amounts of acid are often deliberately added in MOF syntheses to promote the reverse reaction, which then slows MOF growth, forming crystals.¹ Therefore, additions of acid/base to the synthesis need to be carefully controlled when synthesising MOFs, and in this case a balance needs to be obtained in forming the MOF before TiO₂ can form, but still forming it slowly enough to obtain crystals for structural analysis.

The rationale for using H₄BTEC was that it has four possible coordination sites, meaning statistically it could be more likely to combine with the Ti precursor more quickly than the formation of TiO₂, if more carboxylate sites are more readily accessible. The Ti(OⁱPr)₄ precursor was selected owing to its easy injection and the fact it is one of the most commonly used Ti(IV) precursors reported in the literature for Ti(IV) MOFs.

Table 4.1: Attempted Ti(IV) MOF syntheses using H₄BTEC as the organic linker.

| Sample code | Metal precursor | Linker | Solvent(s) | Temperature (°C) | Synthesis time (hours) | Notes |
|-------------|---|------------------------------------|-----------------------------------|------------------|------------------------|--|
| KE020 | Ti(O ⁱ Pr) ₄ (1.32 mmol) | H ₄ BTEC (0.58 mmol) | Formic acid (10 mL) | 120 | 48 | Synthesised by reflux following synthesis of MIL-177-LT but 48 hours instead of 24 hours. |
| KE024 | Ti(O ⁱ Pr) ₄ (1.32 mmol) | H ₄ BTEC (0.58 mmol) | Formic acid (10 mL) | 120 | 24 | Synthesised by reflux following synthesis of MIL-177-LT. |
| KE030 | Ti(O ⁱ Pr) ₄ (1.32 mmol) | H ₄ BTEC (0.58 mmol) | Formic acid (10 mL), TEA (1.5 mL) | 120 | 24 | Synthesised by reflux following synthesis of MIL-177-LT but with use of TEA to aid linker deprotonation. |
| KE081 | Ti(O ⁱ Pr) ₄ (2 mmol) | H ₄ BTEC (8 mmol) | DEF (2.2 mL), MeOH (2.2 mL) | 180 | 24 | MIL-167 synthesis conditions but with H ₄ BTEC instead of H ₄ DOBDC. |

As shown by the powder XRD data obtained from the above experiments, no crystalline materials were obtained (Figure 4.1). The initial three samples show amorphous XRD patterns, attributed to either disorder or small particles. In this case, it is suspected that the amorphous material is most likely TiO₂, given how readily the

Ti(OⁱPr)₄ precursor hydrolyses. The broad background lies at the diffraction angle where generally TiO₂ can be observed, suggesting that this is what the products are, although this is most clear in sample KE030, but still cannot be confirmed for certain. Sample KE081 yielded no solid product, also providing conditions unfavourable for MOF formation with this linker.

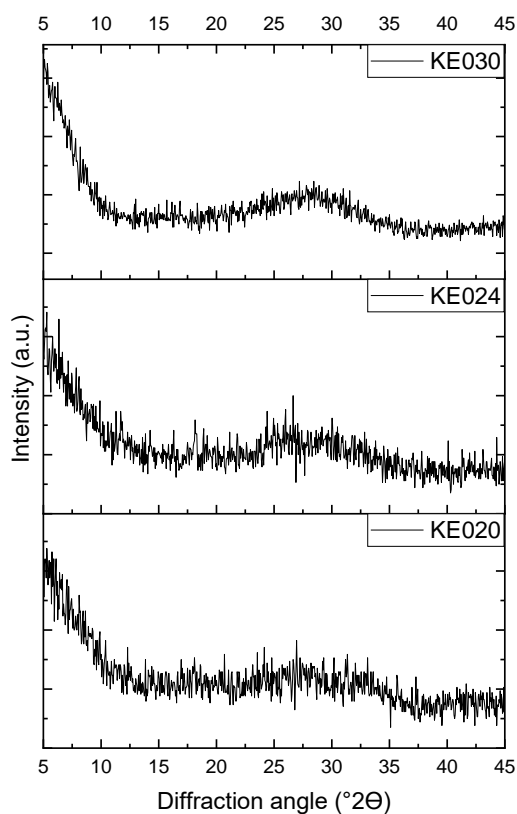


Figure 4.1: Powder XRD patterns for attempted novel Ti(IV) syntheses using H₄BTEC as the organic linker.

Subsequently, some attempts were made using H₂NDC as the organic linker. The metal precursor, solvent(s), temperature, and synthesis times are included in Table 4.2. Again, additional notes on which previously reported synthetic method was used or modified are also listed. H₂NDC was selected as the organic linker due to the presence of the second aromatic group being present, in the hope that it may provide extra structural rigidity for MOF if the synthesis were successful. Titanium butoxide was also investigated as an alternative to the usual Ti(OⁱPr)₄ that has been used in

this investigation, to see if the precursor had any effect on the successful formation of a novel MOF.

Table 4.2: Attempted Ti(IV) MOF syntheses using H₂NDC as the organic linker.

| Sample code | Metal precursor | Linker | Solvent(s) | Temperature (°C) | Synthesis time (hours) | Notes |
|-------------|---|-------------------------------|----------------------------|------------------|------------------------|---|
| KE093 | Titanium butoxide (0.75 mmol) | H ₂ NDC (3 mmol) | DMF (9 mL), MeOH (1 mL) | 150 | 72 | NH ₂ -MIL-125 synthesis but using H ₂ NDC rather than H ₂ ATP. |
| KE094 | Titanium butoxide (0.75 mmol) | H ₂ NDC (3 mmol) | DMF (9 mL), MeOH (1 mL) | 150 | 20 | MIL-125 synthesis but using H ₂ NDC rather than H ₂ BDC (20 hr version). |
| KE129 | Ti(O ⁱ Pr) ₄ (120 μmol) | H ₂ NDC (595 μmol) | DMF (12 mL), AcOH (3.5 mL) | 120 | 48 | MUV-10 synthesis but using H ₂ NDC rather than H ₃ BTC. |

As shown by the powder XRD data from the above experiments, no crystalline materials were obtained (Figure 4.2). The broad peaks seen in the attempted syntheses using H₂NDC might be attributed to TiO₂. Sample KE094 yielded no solid product, again providing details of unfavourable conditions and/or reagents for the synthesis of a Ti(IV) MOF with H₂NDC.

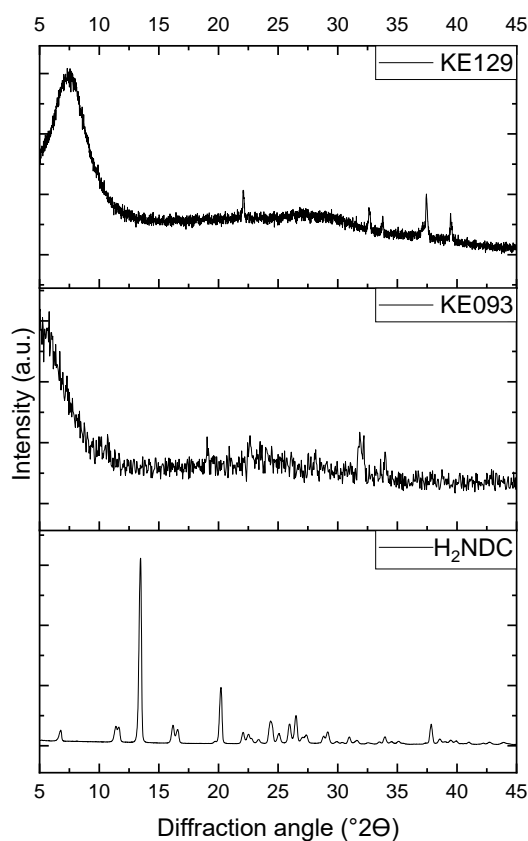


Figure 4.2: Powder XRD patterns for attempted novel Ti(IV) syntheses using H₂NDC as the organic linker.

2,3-pyrazinedicarboxylic acid is another linker that has not been previously reported in a Ti(IV) MOF. With this ligand, a set of syntheses focused on modifying the solvents used in order to obtain a MOF structure and to obtain single crystals (Table 4.3). DMF was the starting point as it solubilises the starting materials. The investigation then looked at swapping this for a less hygroscopic solvent, dimethylacetamide (DMA), to see the effects. 2,3-pyrazinedicarboxylic acid was selected owing to the presence of N atoms in the aromatic ring, which is less common in reported MOFs. It was therefore of interest as to whether this would influence the formation of a novel Ti(IV) MOF, and if successful, may have some interesting properties owing to the basicity of the N atoms.

Table 4.3: Attempted novel Ti(IV) MOF syntheses using 2,3-pyrazinedicarboxylic acid as the organic linker.

| Sample code | Metal precursor | Linker | Solvent(s) | Temperature (°C) | Synthesis time (hours) | Notes |
|-------------|-------------------------|--|-------------------------|------------------|------------------------|--|
| KE320 | Ti butoxide (0.75 mmol) | 2,3-pyrazinedicarboxylic acid (1.5 mmol) | DMA (10 mL) | 120 | 24 | Synthesis using DMA, which is less hygroscopic than DMF. |
| KE321 | Ti butoxide (0.75 mmol) | 2,3-pyrazinedicarboxylic acid (1.5 mmol) | DMF (8 mL), MeOH (2 mL) | 120 | 24 | DMF used to solubilise the organic linker and metal precursor. |

The corresponding XRD patterns show some high intensity, low-angle peaks, which is consistent with what is usually observed for crystalline MOFs (Figure 4.3), however with some broadness present.

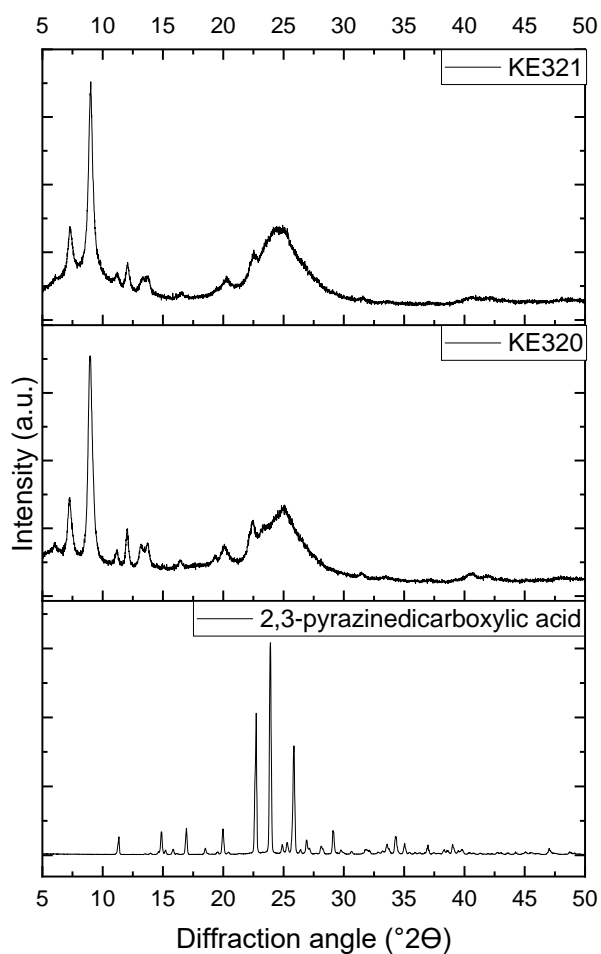


Figure 4.3: Powder XRD patterns for attempted novel Ti(IV) syntheses using 2,3-pyrazinedicarboxylic acid as the organic linker.

Several other attempts using other organic linkers for the synthesis of novel Ti MOFs are shown below in Table 4.4. These are grouped together since there was generally only one attempt for these linkers. All of these linkers had not been previously used in a Ti(IV) MOF and so would meet the criteria of being novel. H₂NBDC was of interest due to the presence of the nitro group potentially enhancing photocatalysis. H₂AIP was of interest due to the amino group having excellent light-harvesting properties, so may have also formed an enhanced Ti MOF for photocatalysis. H₂BPDC was of interest owing to the two aromatic rings, with longer linker having potential to create larger pores for adsorption. The reasoning for trying the various conditions is explained in the notes section.

Table 4.4: Remaining attempts at synthesising novel Ti(IV) MOFs using different organic linkers.

| Sample code | Metal precursor | Linker | Solvent(s) | Temperature (°C) | Synthesis time (hours) | Notes |
|-------------|---|------------------------------------|---------------------------------|------------------|------------------------|---|
| KE055 | Ti(O ⁱ Pr) ₄ (120 μmol) | H ₂ NBDC (595 μmol) | DEF (5 mL), MeOH (5 mL) | 180 | 24 | MIL-167 synthesis but reduced synthesis time and using H ₂ NBDC acid rather than H ₂ DOBDC. |
| KE132 | Ti(O ⁱ Pr) ₄ (120 μmol) | H ₂ AIP (595 μmol) | DMF (12 mL), AcOH (3.5 mL) | 120 | 48 | MUV-10 synthesis but with H ₂ AIP rather than H ₃ BTC. |
| KE234 | Ti(O ⁱ Pr) ₄ (993 μmol) | H ₂ BPDC (3500 μmol) | DMF (10.8 mL), AcOH (1.2 mL) | 150 | 24 | MIL-125 synthesis but with H ₂ BPDC rather than H ₂ BDC (24hr version). |
| KE469 | Ti(O ⁱ Pr) ₄ (1000 μmol) | H ₂ AIP (1500 μmol) | IPA (10 mL), TEA (5 drops) | 180 | 24 | Use of IPA as a solvent with TEA to assist with deprotonation of organic linker. |
| KE476 | Ti(O ⁱ Pr) ₄ (1000 μmol) | H ₂ NBDC (1500 μmol) | IPA (10 mL), TEA (3 drops) | 180 | 24 | Use of IPA as a solvent with TEA to assist with deprotonation of organic linker. |

| | | | | | | |
|-------|--|---------------------------------------|----------------------------------|-----|----|--|
| KE477 | Ti(O ⁱ Pr) ₄ (1000 μmol) | H ₂ BPDC (1500 μmol) | IPA (10 mL), TEA (3 drops) | 180 | 24 | Use of IPA as a solvent with TEA to assist with deprotonation of organic linker. |
|-------|--|---------------------------------------|----------------------------------|-----|----|--|

Syntheses with codes KE055, KE132 and KE469 yielded no solid product. As shown by the XRD data from experiments KE234, KE476 and KE477, none of the samples appear to be MOFs (Figure 4.4). Samples KE234 and KE476 have broad features, whilst KE477 appears to have some crystallinity but still exhibits some broad peaks, suggesting it is a mixed-phase sample.

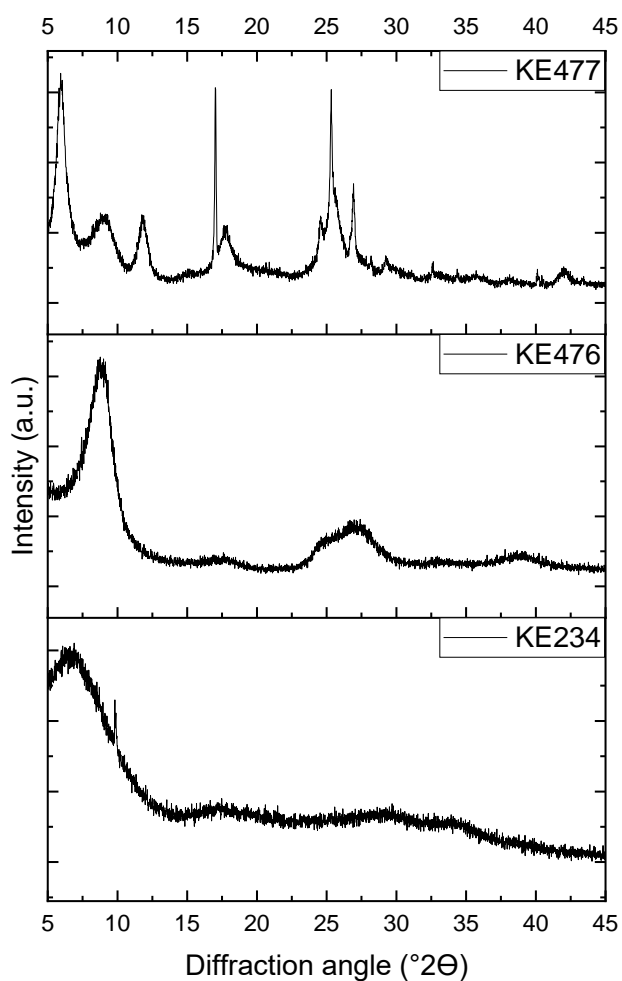
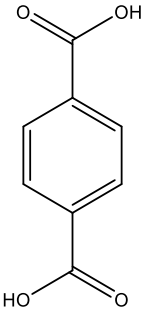


Figure 4.4: Powder XRD patterns for the attempted synthesis of a novel Ti MOF using various other organic linkers.

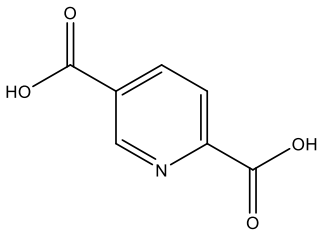
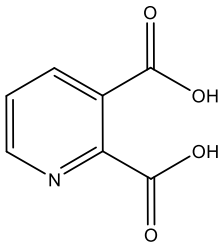
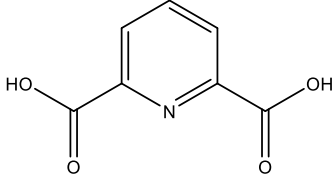
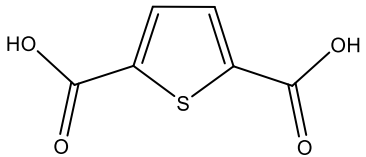
The next attempts at synthesising novel Ti(IV) MOFs involved focussing solely on the synthesis of MIL-125 and modifying it, rather than looking at multiple other synthetic methods and possibilities. The thought was to use identical synthesis conditions to MIL-125 and screen a range of linkers with this method. One reason for modifying MIL-125 is that it is well-reported in the literature, however, is unstable in water. It would be useful to have a modified version that is stable in water, as this would be the best solvent for making applications greener and more sustainable. NH₂-MIL-125 is also one of the best Ti MOFs reported for photocatalytic CO₂ reduction, and so another modified version of MIL-125 with a different linker could also produce an excellent photocatalyst to help with reducing CO₂ levels. The MIL-125 synthesis that was modified is shown in Table 4.5.

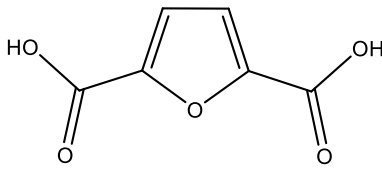
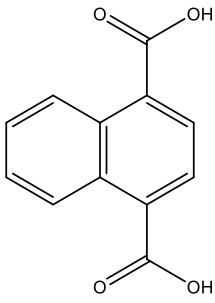
Table 4.5: The metal source, linker, solvents, temperature, and synthesis time used to synthesise MIL-125 which was then modified for subsequent experiments.

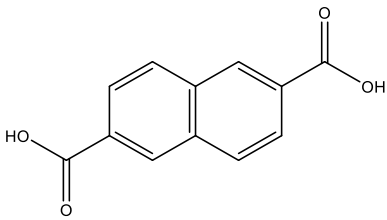
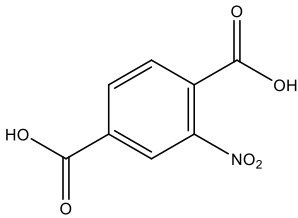
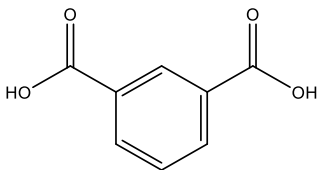
| Metal source | Linker | Solvents | Temperature (°C) | Synthesis time (hours) |
|-------------------------------|---|----------------------------|------------------|------------------------|
| Titanium butoxide (0.75 mmol) | Terephthalic acid (3 mmol)  | DMF (9 mL), MeOH (1 mL) | 150 | 24 |

The linkers that were then attempted to be utilised instead of terephthalic acid (H₂BDC), and the outcome are reported below in Table 4.6.

Table 4.6: The different attempts to synthesise novel Ti MOFs using the same synthesis conditions as with MIL-125, however with different linkers.

| Sample code | Metal source | Linker | Reasons for trying linker | Outcome |
|-------------|-----------------------|---|---|---|
| KE235 | Titanium(IV) butoxide | 2,5-pyridinedicarboxylic acid  | The carboxylate groups are in same orientation as in the terephthalic acid linker in MIL-125, but with the addition of a nitrogen atom into the ring. | Minimal yield produced. Amorphous XRD pattern. |
| KE236 | Titanium(IV) butoxide | 2,3-pyridinedicarboxylic acid  | Variation of the attempt with 2,5-pyridinedicarboxylic acid. However, the carboxylate groups are in different, less favourable positions for binding to Ti centres than those in MIL-125. | No product formed. |
| KE237 | Titanium(IV) butoxide | 2,6-pyridinedicarboxylic acid  | Variation of the attempt using 2,5-pyridinedicarboxylic acid. However, the carboxylate groups are in different positions for binding to Ti centres compared to in MIL-125. | XRD pattern looked promising. |
| KE247 | Titanium(IV) butoxide | 2,5-thiophenedicarboxylic acid  | This linker contains two carboxylate groups like with the terephthalic acid linker used in MIL-125, but not at 180° | Amorphous XRD pattern. |

| | | | | |
|-------|-----------------------|---|---|---|
| | | | to each other. The linker now contains a 5 membered ring with a sulphur atom, which could provide an interesting framework. | |
| KE248 | Titanium(IV) butoxide | 2,5-furandicarboxylic acid  | This linker contains two carboxylate groups like with the terephthalic acid linker used in MIL-125, but now is a 5 membered ring with an oxygen atom could provide an interesting framework. | No product formed. |
| KE249 | Titanium(IV) butoxide | 1,4-naphthalenedicarboxylic acid  | This linker contains two carboxylate groups in the same orientation as in the terephthalic acid linker used in MIL-125, but contains an additional aromatic ring. If the MOF can be successfully synthesised, the additional conjugation in the linker means enhanced light harvesting, meaning potential uses in photocatalysis and CO ₂ reduction. | XRD pattern looked promising, but not MOF-like. |

| | | | | |
|-------|-----------------------|---|--|-------------------------|
| KE250 | Titanium(IV) butoxide | 2,6-naphthalenedicarboxylic acid  | This linker is like the terephthalic acid used in MIL-125, but with an additional aromatic ring. This could potentially create an expanded framework with greater conjugation for enhanced light harvesting. | Amorphous PXRD pattern. |
| KE238 | Titanium(IV) butoxide | 2-nitroterephthalic acid  | This linker contains carboxylate groups in the same orientation as with terephthalic acid in MIL-125, but with the addition of an -NO ₂ group. | Amorphous PXRD pattern. |
| KE246 | Titanium(IV) butoxide | Isophthalic acid  | This linker is the same as in MIL-125, just with different orientations of carboxylate groups. | Amorphous PXRD pattern. |

Using the same metallic precursor, solvent, and synthesis conditions as in the synthesis of MIL-125, but changing the linker, was unsuccessful for most linkers, yielding amorphous XRD patterns (Figure 4.5). However, the samples using 1,4-naphthalenedicarboxylic acid (KE249) and 2,6-pyridinedicarboxylic acid (KE237) looked interesting and so were further investigated to try to identify them.

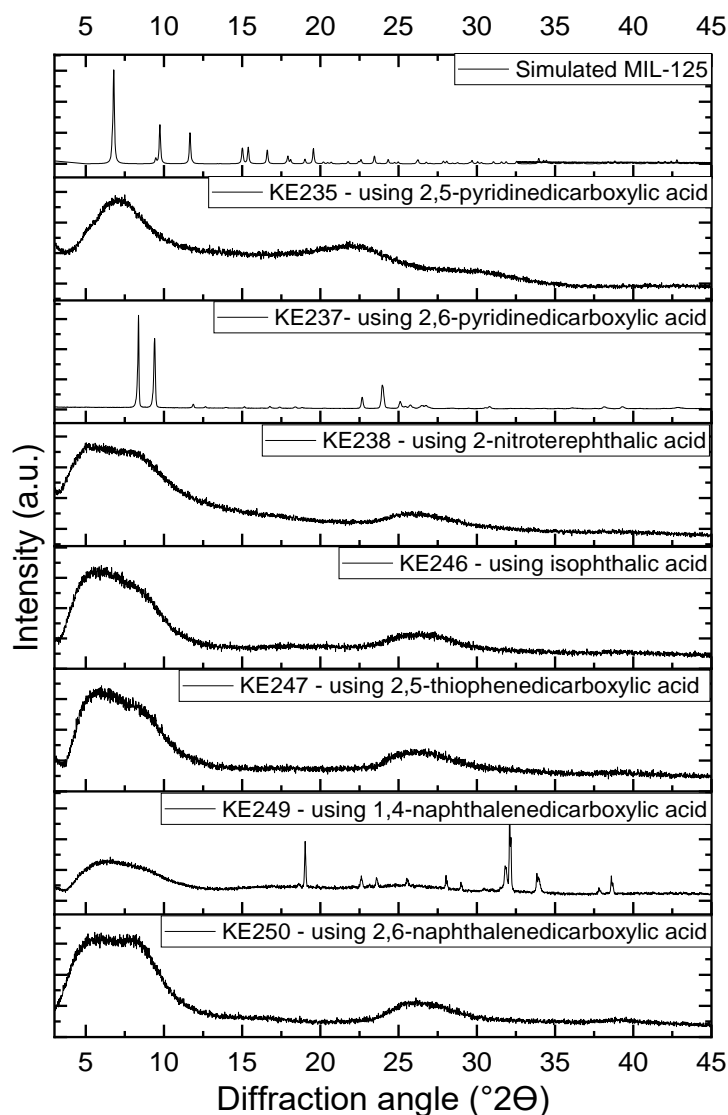


Figure 4.5: Powder XRD patterns for MIL-125 and the materials formed using the MIL-125 synthesis method but with different organic linkers.

The samples containing 1,4-naphthalenedicarboxylic acid (H_2NDC) and 2,6-pyridinedicarboxylic acid (H_2PDC) were checked against the XRD pattern of their organic linker to see whether the sample consisted of unreacted or recrystallised linker, rather than a MOF. Both samples appear distinct to their linker, meaning single crystals were required to obtain full identification of the material.

The XRD pattern for KE249 appears less MOF-like upon first inspection, compared to KE237, due to the absence of low angle, high intensity peaks. Instead, this pattern has an initial broad peak. However, TGA data looks typical for what is usually

observed with MOFs, with the initial step attributed to solvent loss, followed by decomposition of the organic linker just after 400 °C and then a residual mass attributed to remaining metal oxides (Figure 4.6).

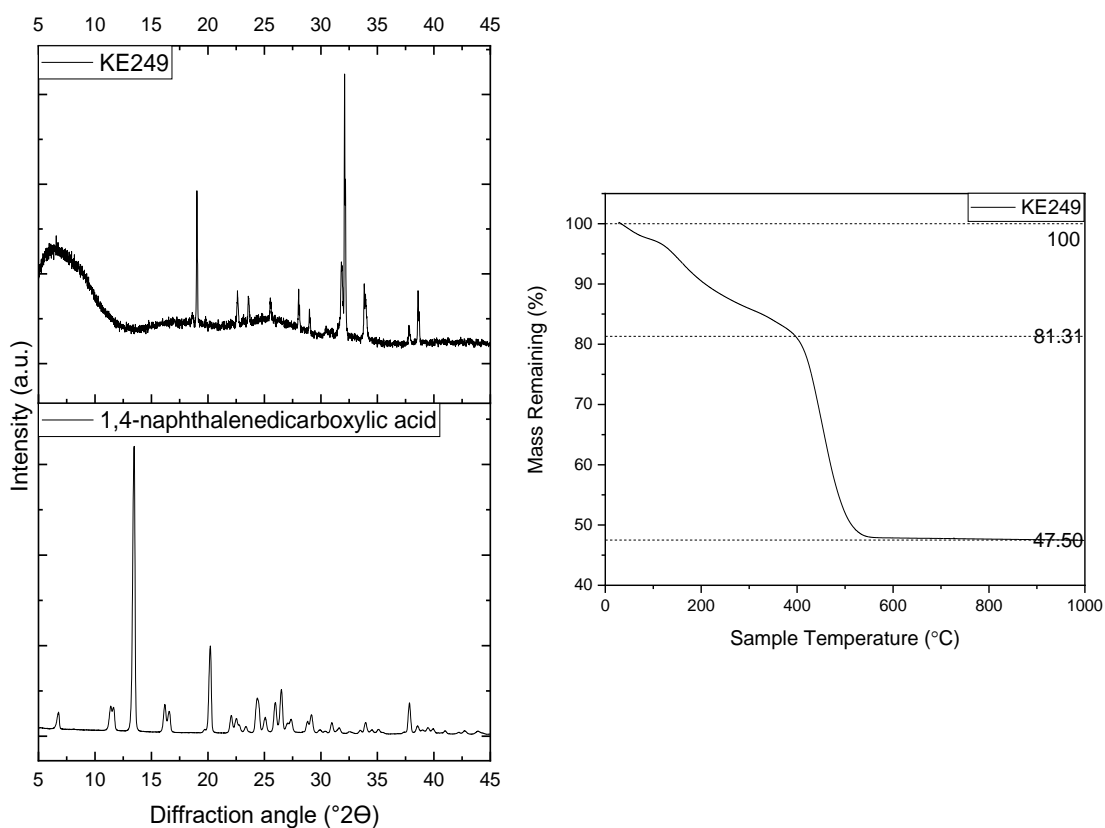


Figure 4.6: The powder XRD pattern (left-hand side) and TGA (right-hand side) for sample KE249, which utilises 1,4-naphthalenedicarboxylic acid as the organic linker.

Sample KE237 has a more typical MOF-like XRD pattern compared to sample KE249, since it exhibits the usual low-angle peaks that MOFs tend to have, and clearly shows crystallinity (Figure 4.7). However, the TGA looks slightly unconventional for a MOF since there are no distinct separate steps for solvent loss and linker loss. There is only a small first loss, however this could be due to minimal solvent having been present in the pores of the MOF. The remaining mass at the end is again attributed to metal oxide(s).

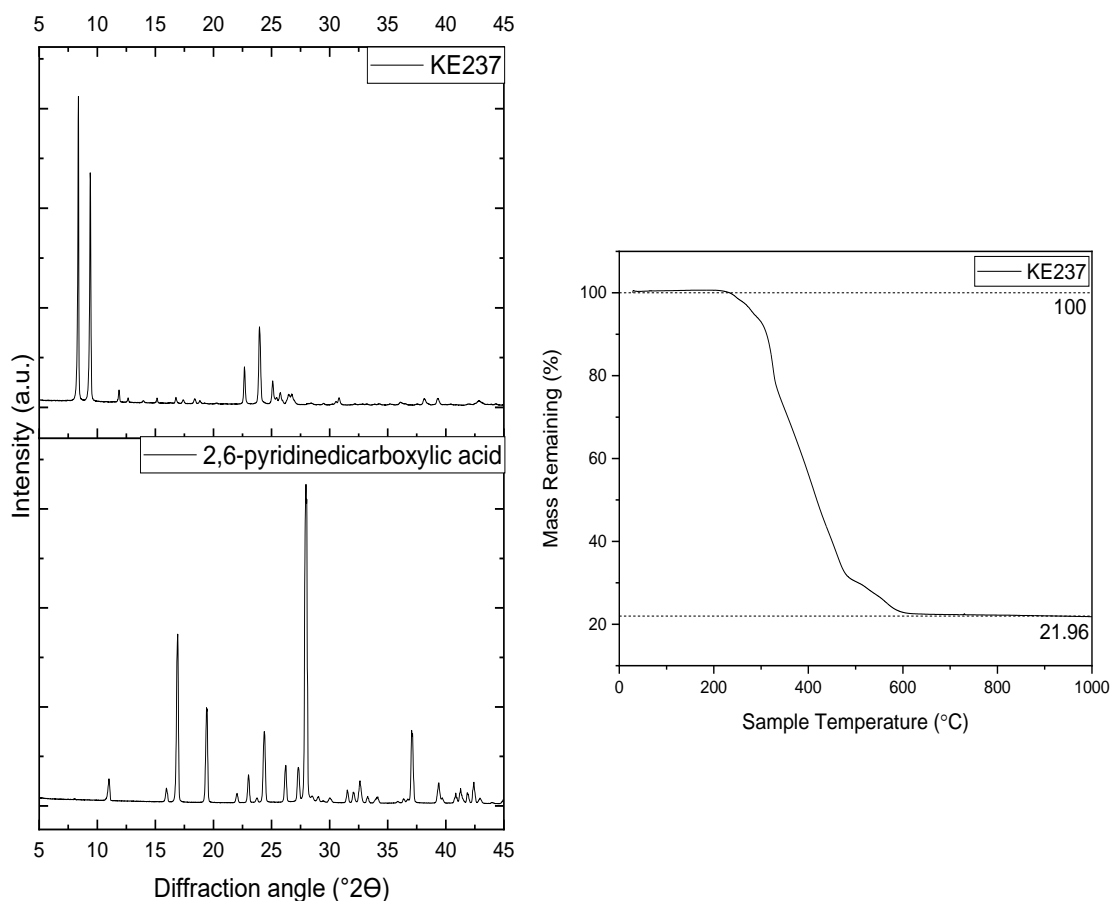


Figure 4.7: The powder XRD pattern (left-hand side) and TGA (right-hand side) for sample KE237, which utilises 2,6-pyridinedicarboxylic acid as the organic linker.

Attempts were then made to grow single crystals of these two materials, by further altering the original syntheses. Typical strategies included the addition of a few drops of TEA to encourage nucleation, and use of acetic acid as a modulator. Other alterations have included changing the synthesis temperature and time, since subtle changes in synthesis temperature and time have previously been reported to have drastic effects on materials produced.²

Despite the fact that sample KE249 did not appear to be as crystalline and MOF-like as sample KE237, this structure could still have been useful in other applications and so it was still analysed further. Modifications to the synthesis of sample KE249 are shown below in Table 4.7.

Table 4.7: Modifications made to the synthesis of sample KE249 in attempt to form single crystals for full structural analysis.

| Sample Code | Metal source | Linker | Solvents | Temperature (°C) | Synthesis time (hours) | Outcome |
|-------------|--|-------------------------------|---|------------------|------------------------|----------------------------------|
| KE249 | Titanium butoxide (0.75 mmol) | H ₂ NDC (3 mmol) | DMF (9 mL) MeOH (1 mL) | 150 | 24 | Original promising sample. |
| KE269 | Titanium butoxide (0.75 mmol) | H ₂ NDC (3 mmol) | DMF (9 mL) MeOH (1 mL), 3 drops TEA | 150 | 48 | Thick gel-like product produced. |
| KE271 | Titanium butoxide (0.75 mmol) | H ₂ NDC (3 mmol) | DMF (8 mL) MeOH (1 mL), AcOH (1 mL) | 150 | 48 | XRD displays broadness. |
| KE468 | Ti(O ⁱ Pr) ₄ (0.75 mmol) | H ₂ NDC (1.5 mmol) | IPA (10 mL), TEA (5 drops) | 180 | 24 | Thick gel-like product produced. |
| KE488 | Ti(O ⁱ Pr) ₄ (0.75 mmol) | H ₂ NDC (1.5 mmol) | DMF (10 mL), TEA (3 drops) | 180 | 24 | Thick gel-like product produced. |
| KE489 | Ti(O ⁱ Pr) ₄ (0.75 mmol) | H ₂ NDC (1.5 mmol) | DMF (10 mL), TEA (3 drops) | 150 | 48 | XRD displays broadness. |
| KE490 | Ti(O ⁱ Pr) ₄ (0.75 mmol) | H ₂ NDC (1.5 mmol) | DMF (10 mL), TEA (3 drops) | 120 | 72 | No product formed. |

Corresponding XRD data for the modifications to KE249 can be seen in Figure 4.8. The modifications did not yield crystalline materials and so full structural analysis was not possible.

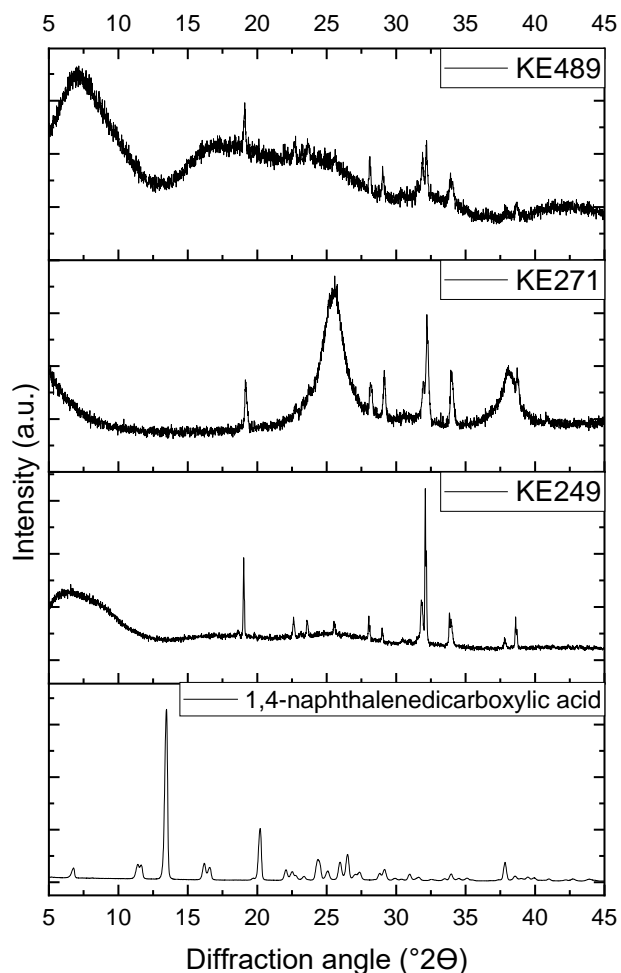


Figure 4.8: Powder XRD patterns for samples from modifications to KE249 synthesis.

Greater work was then completed on optimising the sample KE237 since the XRD pattern was more promising compared to that of KE249. Modifications to the synthesis of sample KE237 are shown below in Table 4.8.

Table 4.8: Modifications made to the synthesis of sample KE237 in attempt to form single crystals for full structural analysis.

| Sample Code | Metal source | Linker | Solvents | Temperature (°C) | Synthesis time | Outcome |
|-------------|-------------------------------|-------------------------------|--|------------------|---------------------------------|--|
| KE237 | Titanium butoxide (0.75 mmol) | H ₂ PDC (3 mmol) | DMF (9 mL) MeOH (1 mL) | 150 | 24 hours | Original promising sample |
| KE259 | Titanium butoxide (0.75 mmol) | H ₂ PDC (3 mmol) | DMF (9 mL) MeOH (1 mL) | 150 | 48 hours | Low-angle, crystalline peaks observed. |
| KE268 | Titanium butoxide (0.75 mmol) | H ₂ PDC (3 mmol) | DMF (9 mL) MeOH (1 mL), 3 drops TEA | 150 | 48 hours | Low-angle, crystalline peaks observed. |
| KE270 | Titanium butoxide (0.75 mmol) | H ₂ PDC (3 mmol) | DMF (8 mL), MeOH (1 mL), AcOH (1 mL). | 150 | 48 hours | Low-angle, crystalline peaks observed. |
| KE290 | Titanium butoxide (0.75 mmol) | H ₂ PDC (3 mmol) | DMF (9 mL), MeOH (1 mL) | 150 | 9 days | Broad, amorphous XRD pattern observed. |
| KE291 | Titanium butoxide (0.75 mmol) | H ₂ PDC (3 mmol) | DMF (9 mL), MeOH (1 mL) | 120 | 9 days | Low-angle, crystalline peaks observed. |
| KE292 | Titanium butoxide (0.75 mmol) | H ₂ PDC (3 mmol) | DMF (9 mL), MeOH (1 mL) | 180 °C | 9 days | Broad peaks observed. |
| KE302 | Titanium butoxide (0.38 mmol) | H ₂ PDC (1.5 mmol) | DMF (9 mL), MeOH (1 mL) | 120 °C | 45 minutes -microwave synthesis | No product formed. |

| | | | | | | |
|-------|--|-------------------------------|----------------------------|--------|----------|---|
| KE303 | Titanium butoxide (0.38 mmol) | H ₂ PDC (1.5 mmol) | DMF (9 mL), MeOH (1 mL) | 120 °C | 72 hours | Broad peaks observed. |
| KE313 | Titanium butoxide (0.38 mmol) | H ₂ PDC (1.5 mmol) | DMA (9 mL), MeOH (1 mL) | 120 °C | 24 hours | Broad peaks observed. |
| KE314 | Titanium butoxide (0.38 mmol) | H ₂ PDC (1.5 mmol) | DEET (9 mL), MeOH (1 mL) | 120 °C | 24 hours | No product formed. |
| KE315 | Titanium butoxide (0.75 mmol) | H ₂ PDC (3 mmol) | DEET (9 mL), MeOH (1 mL) | 120 °C | 24 hours | Broad peaks observed. |
| KE316 | Titanium butoxide (0.75 mmol) | H ₂ PDC (3 mmol) | DEET (9 mL), MeOH (1 mL) | 120 °C | 24 hours | No product formed. |
| KE481 | Ti(O ⁱ Pr) ₄ (0.75 mmol) | H ₂ PDC (1.5 mmol) | DMF (10 mL), TEA (3 drops) | 120 °C | 24 hours | Broad peaks observed. |
| KE482 | Ti(O ⁱ Pr) ₄ (0.75 mmol) | H ₂ PDC (1.5 mmol) | DMF (10 mL), TEA (3 drops) | 150 °C | 24 hours | Sharp, low-angle peaks but some broadness observed. |
| KE483 | Ti(O ⁱ Pr) ₄ (0.75 mmol) | H ₂ PDC (1.5 mmol) | DMF (10 mL), TEA (3 drops) | 180 °C | 24 hours | Sharp, low-angle peaks but some broadness observed. |
| KE373 | Titanium butoxide | H ₂ PDC (3 mmol) | DMF (9 mL), MeOH (1 mL) | 100 °C | 10 days | Sharp, low-angle peaks observed. |

| | | | | | | |
|-------|-------------------------------|-----------------------------|-------------------------|--------|-----------------------------------|--|
| | (0.75 mmol) | | | | | |
| KE493 | Titanium butoxide (0.75 mmol) | H ₂ PDC (3 mmol) | DMF (9 mL), MeOH (1 mL) | 180 °C | 24 hours | Broad peaks observed. |
| KE494 | Titanium butoxide (0.75 mmol) | H ₂ PDC (3 mmol) | DMF (9 mL), MeOH (1 mL) | 180 °C | 12 hours | Sharp, low-angle peaks observed. |
| KE497 | Sample of KE237 | / | DMF (9 mL), MeOH (1 mL) | RT | Ongoing monitoring over 6 months. | Seed experiment. No crystals observed. |

Corresponding XRD data for the modifications made to sample KE237 can be seen in Figure 4.9. None of the samples yielded single crystals for full structural analysis. All samples are distinct to the 2,6-pyridinedicarboxylic acid, eliminating the possibility of patterns being attributed to unreacted or recrystallised linker. Some patterns showed amorphous structures, whilst others resembled the KE237 pattern, without improving crystal growth.

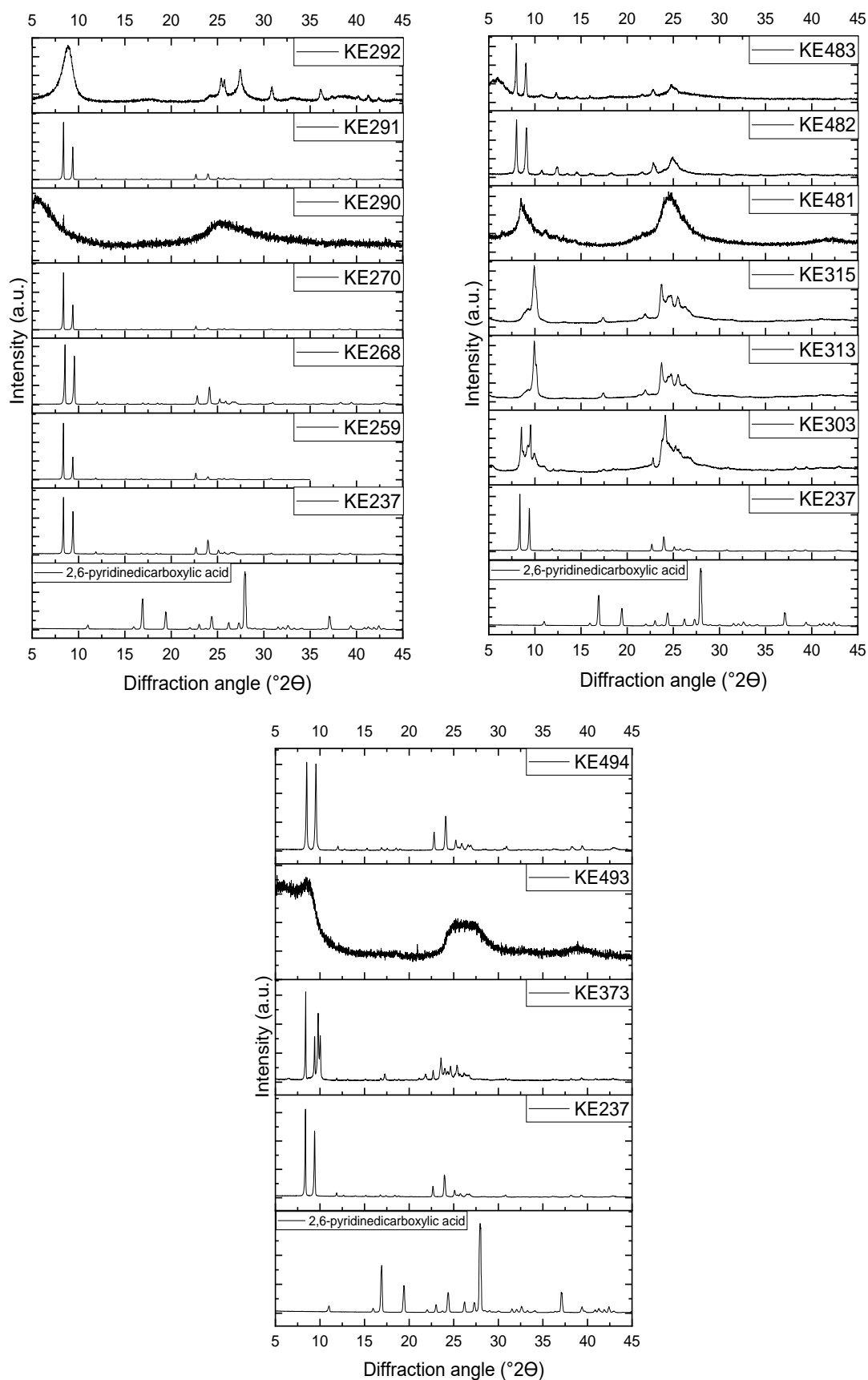


Figure 4.9: Powder XRD patterns for samples from modifications to KE237 synthesis.

In conclusion, the work presented above illustrates the often difficult nature of synthesising novel MOFs, even when a range of linkers possessing different features are trialled. MOF synthesis is often unpredictable, and this study highlights this further

4.3 Attempted Synthesis of Mixed-Metal Ti MOFs

Owing to the fact that MUV-10 is known to have interesting properties, it was decided to investigate other mixed-metal Ti MOFs. A synthesis was attempted using two metals, Mn and Ti, and two organic linkers, 2-aminoterephthalic acid and 2,5-dihydroxyterephthalic acid, in equal volumes of DEF and MeOH at 120°C for 48 hours. This combination was chosen for several reasons. Firstly, the investigation of MUV-10 showed that Ti(IV) and Mn(II) successfully combined with BTC to form a highly stable MOF, with the possibility to absorb light in the visible region, which is why these metals were then paired together again. Secondly, 2-aminoterephthalic acid and 2,5-dihydroxyterephthalic acid had been successfully incorporated individually in monometallic Ti MOFs previously,^{3,4,5} and so it was thought that attempting to combine them in the same structure could lead to an interesting material, with enhanced photocatalytic properties due to the amine functionality on the 2-aminoterephthalic acid.

The XRD pattern (KE047) that was obtained from a sample where Ti, Mn, 2-aminoterephthalic acid and 2,5-dihydroxyterephthalic acid had been combined, initially appeared to be that of a new MOF (Figure 4.10). The XRD pattern displayed low angle peaks which is common in MOFs, and also showed peaks distinct to the patterns for the two organic linkers used, showing that the sample was not comprised of recrystallised linker.

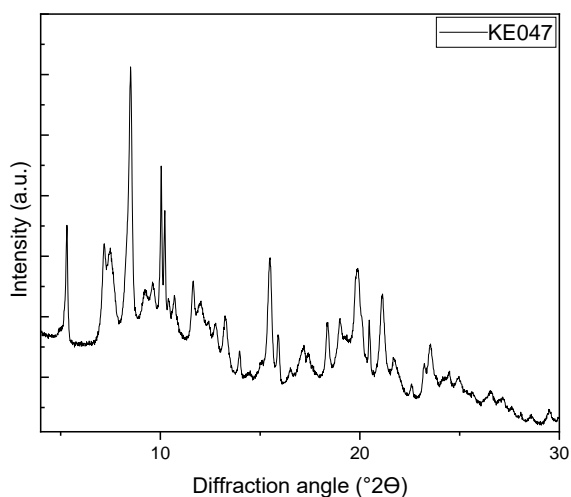


Figure 4.10: The XRD pattern for sample KE047, where the synthesis included Ti, Mn, 2-aminoterephthalic acid and 2,5-dihydroxyterephthalic acid.

One possibility that did however need to be checked was if one metal and one linker had combined preferentially to form the new structure. NTU-9 and MIL-167 are formed from Ti with 2,5-dihydroxyterephthalic acid, whereas the pattern for KE047 was distinct to these. MOF-75 is made from Mn and 2,5-dihydroxyterephthalic acid, whilst $[Mn_3(atpa)_3(dmf)_2]$ is made from Mn and 2-aminoterephthalic acid, where the pattern for KE047 appeared distinct to these (Figure 4.11).

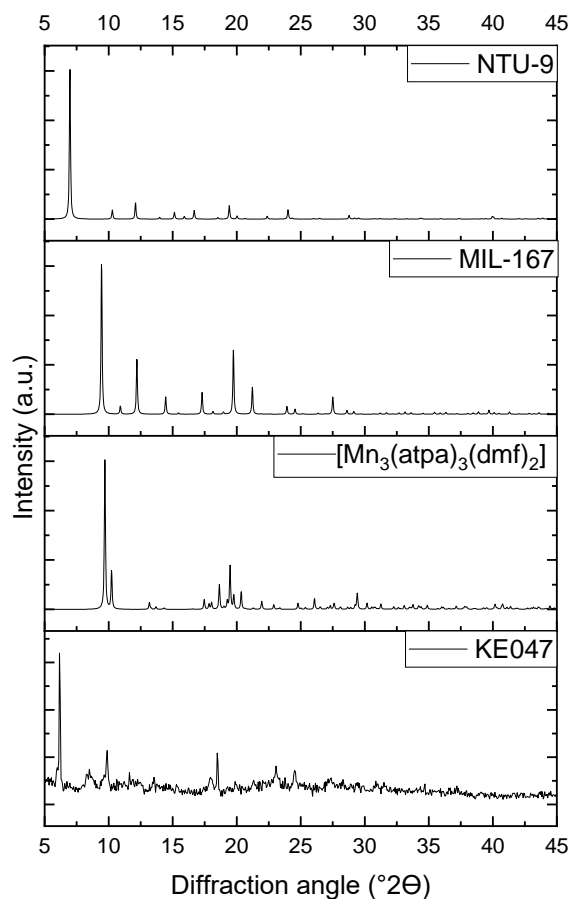


Figure 4.11: Powder XRD patterns comparing KE047 to $[\text{Mn}_3(\text{atpa})_3(\text{dmf})_2]$, MIL-167 and NTU-9.

However, it was when a single crystal was obtained and single crystal XRD was completed that greater insight into the structure of KE047 was gained. The structure was only partially solved since it emerged that the unit cell matched a structure that had already been previously reported, which was $[\text{Mn}_3(\text{atpa})_3(\text{dmf})_2]$. The peaks observed around $10^\circ 2\theta$ on the pattern for KE047 appear to match this same phase of $[\text{Mn}_3(\text{atpa})_3(\text{dmf})_2]$. The PXRD pattern for the single crystal differed to that of the bulk pattern initially obtained, verifying that a MOF had formed with one metal and one linker preferentially to using both metals and both linkers. Figure 4.12 shows the comparison of the bulk KE047 sample after an overnight scan was completed, compared to the single crystal pattern. The TGA is also included where there seems to be a very small loss attributed to solvents present in the pore, with a large loss for the organic components and a mass remaining just under 20% which is attributed to metal oxide(s).

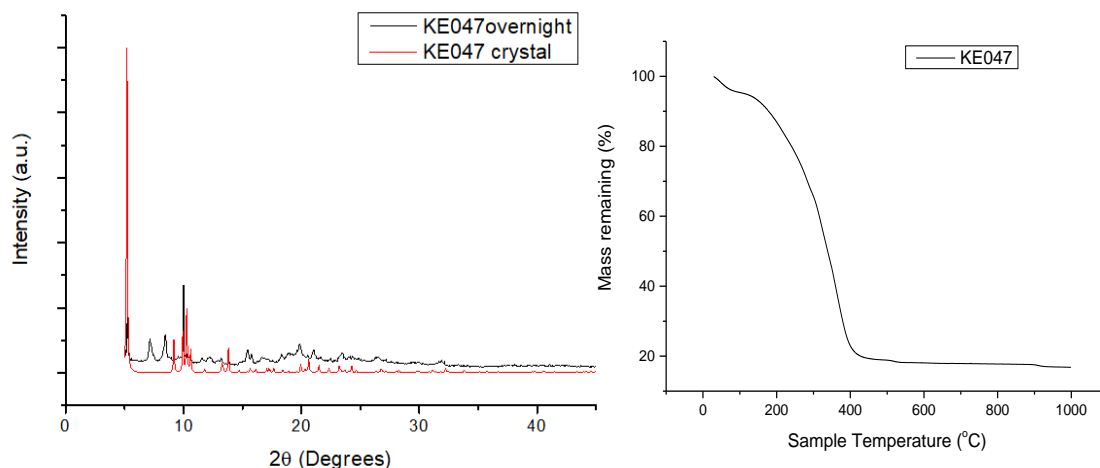


Figure 4.12: XRD patterns overlaid for a single crystal of KE047 and the bulk pattern of KE047 (left-hand side) and TGA of the bulk sample of KE047 (right-hand side).

Reference reactions were then completed, using possible combinations of metal(s) and linker, to try to determine the remainder of sample KE047 (see Table 4.9). All reference reactions were also completed in DEF (5 mL) and MeOH (5 mL) at 120°C for 48 hours, as per the conditions used in the synthesis of KE047.

Table 4.9: Different reference experiments to determine what the pattern of the single crystal of KE047 resembled.

| Sample code | Metal source | Linker |
|-------------|---|--------------------------------|
| KE060 | MnCl ₂ ·4H ₂ O | 2-aminoterephthalic acid |
| KE061 | Ti(O ⁱ Pr) ₄ | 2-aminoterephthalic acid |
| KE062 | MnCl ₂ ·4H ₂ O | 2,5-dihydroxyterephthalic acid |
| KE063 | Ti(O ⁱ Pr) ₄ | 2,5-dihydroxyterephthalic acid |
| KE064 | MnCl ₂ ·4H ₂ O and Ti(O ⁱ Pr) ₄ | 2-aminoterephthalic acid |
| KE065 | MnCl ₂ ·4H ₂ O and Ti(O ⁱ Pr) ₄ | 2,5-dihydroxyterephthalic acid |

KE047 produced a red powder, as shown in Figure 4.13. Compared to the reference materials, visually the sample KE047 most resembles the colour of KE063, which consists of Ti(OⁱPr)₄ and 2,5-dihydroxyterephthalic acid.



Figure 4.13: Samples KE060, KE061, KE062, KE063, KE064, KE065, KE047 (left to right).

Each reference reaction pattern was then compared to the single crystal of KE047 (see Figure 4.14) and it was found that one component of KE047 was KE060, which consists of Mn with 2-aminoterephthalic acid, as had been confirmed with the partial solving of the structure with single crystal data, and was found to be previously reported in the literature.⁶ The other component of the bulk sample of KE047 could be from one of the other separate combinations of metal and linker, where it is unclear as to which it is.

This investigation highlights MOF formation occurring preferentially with one metal and one linker, as opposed to incorporating multiple metals and linkers into the same structure, which has been shown to occur previously, however is less easily achieved.

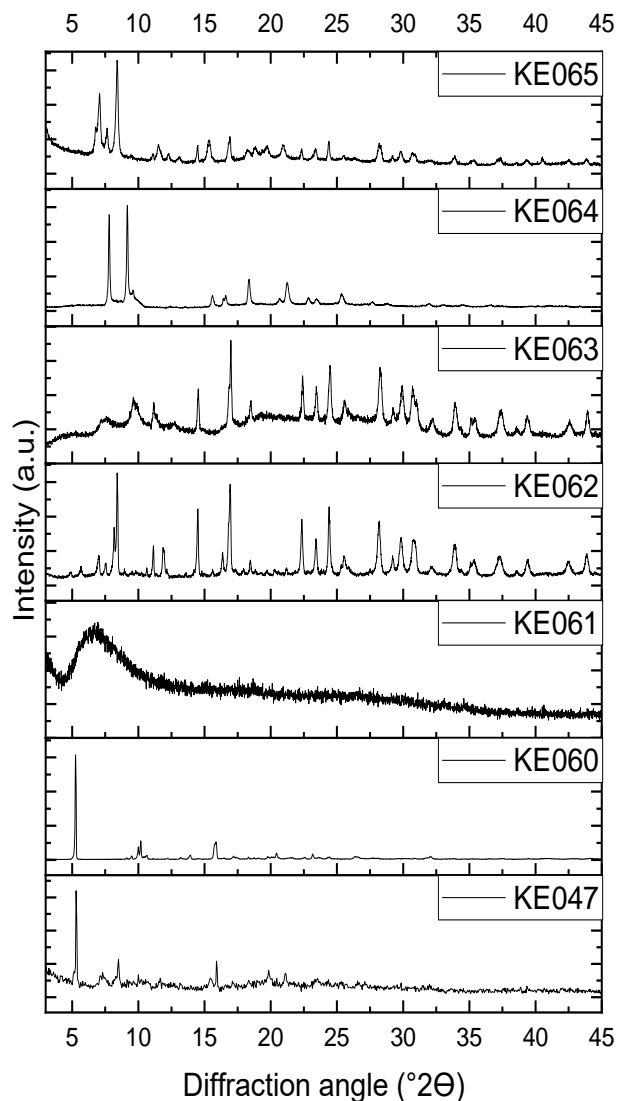


Figure 4.14: Powder XRD patterns for KE047 and the products from the subsequent reference syntheses.

4.4 Attempted synthesis of Sn(IV) MOFs

Owing to the fact that no Sn(IV) MOFs exist in the literature, and that they have great potential, an extensive range of organic linkers were tried with Sn(IV) reagents in varying conditions, utilising a range of solvents, temperatures and synthesis durations. As with the attempts to synthesise novel Ti(IV) MOFs, a sample of linkers with a range of different features were tried, in order to hopefully find a successful combination. Since no Sn(IV) MOFs have been reported, unlike with the novel Ti(IV) MOF study in this research, there were no Sn(IV) syntheses that could be used as a

starting point to modify for novel Sn(IV) MOFs. In addition, owing to Sn(IV) MOFs never having been reported, many more linkers were therefore available to try to use with Sn(IV), and therefore only a small selection were able to be investigated for the time constraints of this project. Therefore, a range of commonly used linkers in other existing MOFs were initially trialled with Sn(IV), such as H₃BTC. Then, other linkers with additional functional groups and interesting properties were examined. This has therefore left scope for many more linkers to be investigated and screened with Sn(IV) in the future. Sn(OⁱPr)₄ was generally used as the Sn(IV) precursor since it was injectable into autoclaves or round-bottomed flasks, where its exposure to air could be better minimised compared to some Sn(IV) solid precursors.

Attempts were initially made with Sn(IV) and H₃BTC, since it was thought the linker having three coordination points could encourage MOF formation compared to using linkers with fewer coordination points. Samples placed in the fridge were kept there for 2 months and checked periodically for crystals, which did not form. Samples where the temperature is recorded as 50°C were kept on a hot plate for 12 hours and checked periodically for crystals, which also did not form. All other samples were produced under normal solvothermal conditions using an autoclave, under conditions stated. Table 4.10 explores the attempts made to synthesise Sn(IV) MOFs with H₃BTC, where no crystals were obtained. Figure 4.15 shows the XRD patterns from each synthesis, where solid products formed. Overall, the most promising sample appeared to be KE155, due to the XRD pattern appearing crystalline and distinct to the organic linker, and due to the low-angle peaks which are often attributed to MOF formation. Therefore, further work based around this specific synthesis was later completed and is discussed below.

Table 4.10: Attempts at forming a novel Sn(IV) MOF with H₃BTC linker, including sample codes, metal source, linker, solvent(s), temperature, synthesis time and the outcome. RT = room temperature.

| Sample Code | Metal source | Linker | Solvent(s) | Temperature | Synthesis time | Outcome |
|-------------|------------------------------------|--------------------|----------------------------|-------------|----------------|--|
| KE018 | Sn(O ⁱ Pr) ₄ | H ₃ BTC | DMF (12 mL), AcOH (3.5 mL) | 120°C | 48 hours | XRD displays broadness. |
| KE019 | Sn(O ⁱ Pr) ₄ | H ₃ BTC | DMF (10 mL) | 180°C | 48 hours | XRD displays broadness. |
| KE077 | Sn(O ⁱ Pr) ₄ | H ₃ BTC | DMF (5 mL) | Fridge | - | No crystal growth observed. |
| KE079 | Sn(O ⁱ Pr) ₄ | H ₃ BTC | DMF (5 mL) | 50°C | 12 hours | No crystal growth observed. |
| KE0081 | Sn(O ⁱ Pr) ₄ | H ₃ BTC | DMF (5 mL), 5 drops TEA | Fridge | - | No crystal growth observed. |
| KE0083 | Sn(O ⁱ Pr) ₄ | H ₃ BTC | DMF (5 mL), 5 drops TEA | 50°C | 12 hours | XRD displays broadness. |
| KE155 | Sn(O ⁱ Pr) ₄ | H ₃ BTC | TEA (5 mL) | 150°C | 24 hours | Promising sample. Some broadness, but low-angle peaks indicative of MOF formation. |
| KE170 | Sn(IV) tert-butoxide | H ₃ BTC | DMF (10 mL) | 150°C | 24 hours | No product formed. |
| KE284 | Sn(O ⁱ Pr) ₄ | H ₃ BTC | TEA (5 mL) | 120°C | 9 days | Peaks corresponding to SnO ₂ observed. |
| KE285 | Sn(O ⁱ Pr) ₄ | H ₃ BTC | TEA (5 mL) | 150°C | 9 days | Peaks corresponding to SnO ₂ observed. |
| KE286 | Sn(O ⁱ Pr) ₄ | H ₃ BTC | TEA (5 mL) | 180°C | 9 days | Peaks corresponding to SnO ₂ observed. |
| KE287 | Sn(O ⁱ Pr) ₄ | H ₃ BTC | TEA (5 mL) | Fridge | 9 days | XRD displays broadness. |
| KE293 | Sn(O ⁱ Pr) ₄ | H ₃ BTC | | 120°C | 24 hours | XRD displays broadness. |

| | | | | | | |
|-------|------------------------------------|--------------------|-------------|-------|-----------------------------|--|
| KE294 | Sn(O ⁱ Pr) ₄ | H ₃ BTC | Isopropanol | 120°C | 24 hours | XRD displays broadness. |
| KE297 | Sn(O ⁱ Pr) ₄ | H ₃ BTC | / | RT | 24 hours | No product formed. |
| KE301 | Sn(O ⁱ Pr) ₄ | H ₃ BTC | Isopropanol | 100°C | 45 mins - microwave | XRD displays broadness. |
| KE393 | Sn(O ⁱ Pr) ₄ | H ₃ BTC | / | 80°C | 1 hour – microwave sample | XRD displays broadness. |
| KE395 | Sn(O ⁱ Pr) ₄ | H ₃ BTC | / | 100°C | 1 hour – microwave sample | XRD displays broadness with one sharp, intense peak. |
| KE396 | Sn(O ⁱ Pr) ₄ | H ₃ BTC | / | 100°C | 3.5 hour – microwave sample | XRD pattern matches that of BTC. |

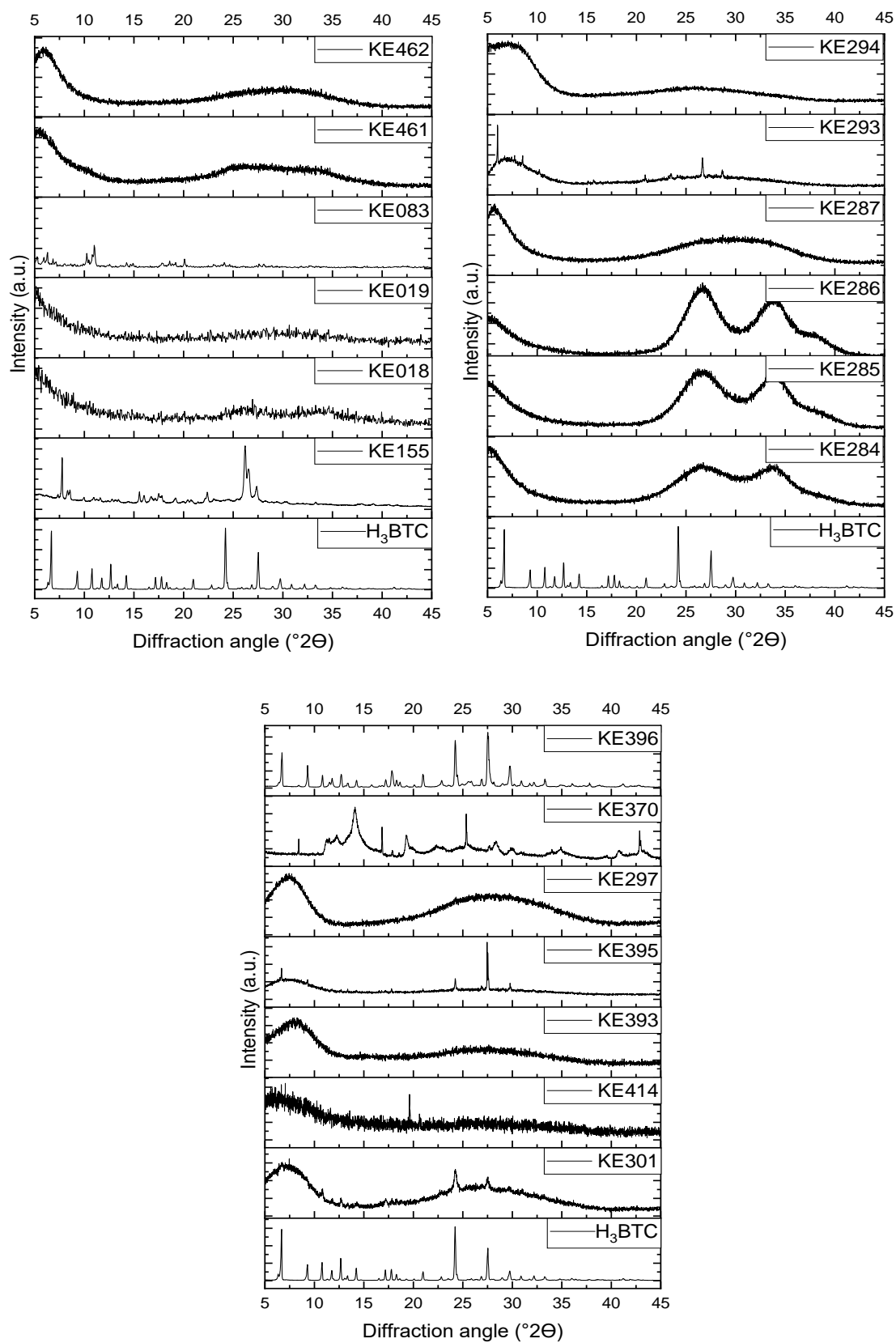


Figure 4.15: The powder XRD patterns obtained after experiments combining an Sn(IV) precursor with H_3BTC .

Some attempts were then made to form single crystals of sample KE155 to obtain the full structure from single crystal X-ray diffraction (Table 4.11). The focus of these experiments was to try lowering the temperature compared to the synthesis of investigated in the hope that crystals could form faster than Sn was hydrolysed into SnO₂, however the sample just yielded H₃BTC. This is shown in Figure 4.16, alongside the other XRD patterns for the other attempts. No single crystals could be generated by these methods explored and so further scope for this work exists.

Table 4.11: Attempts made to form single crystals of sample KE155 for further structural analysis.

| Sample Code | Metal source | Linker | Solvent(s) | Temperature | Synthesis time | Outcome |
|-------------|------------------------------------|--------------------|------------|-------------|---------------------|---|
| KE368 | Sn(O ⁱ Pr) ₄ | H ₃ BTC | / | 100°C | 45 mins - microwave | XRD pattern matches that of BTC. |
| KE369 | Sn(O ⁱ Pr) ₄ | H ₃ BTC | IPA | 100°C | 48 hours | XRD pattern contains some sharp peaks on a broad background. Single crystals of sample KE155 unable to be obtained. |
| KE370 | Sn(O ⁱ Pr) ₄ | H ₃ BTC | IPA | 100°C | 14 days | XRD pattern contains some sharp peaks on a broad background. Single crystals of sample KE155 unable to be obtained. |
| KE371 | Sn(O ⁱ Pr) ₄ | H ₃ BTC | IPA | 100°C | 10 days | XRD pattern contains some sharp peaks on a broad background. Single crystals of sample KE155 unable to be obtained. |

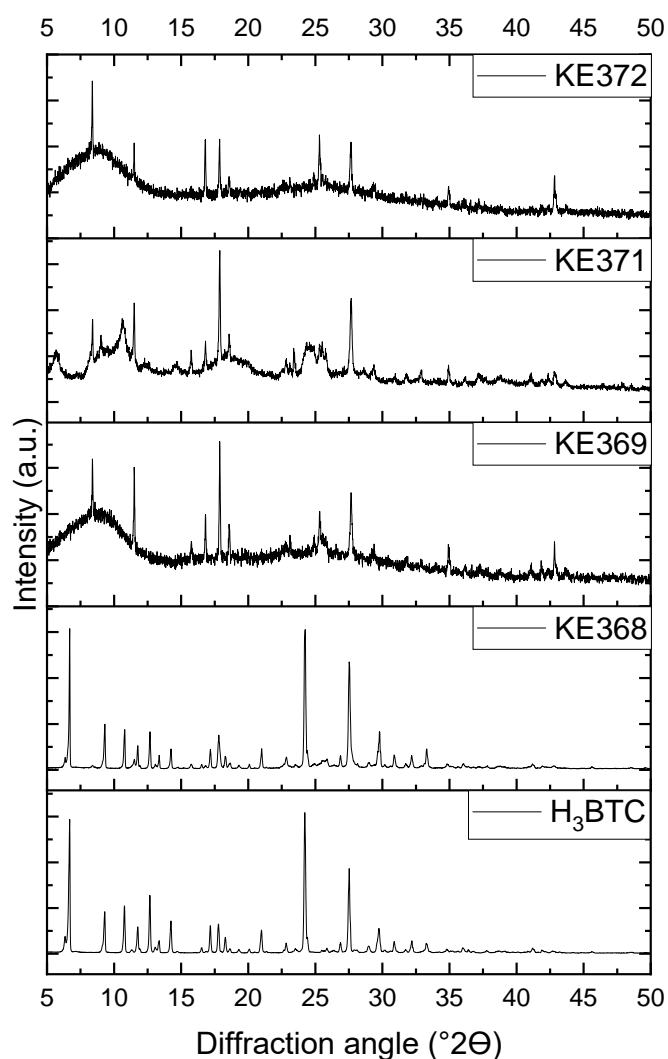


Figure 4.16 Powder XRD patterns obtained after attempts were made to form single crystals of sample KE155.

Upon further investigation into the structure of KE155, TGA was completed (Figure 4.17). This shows step losses as is usually observed with MOFs, which can be attributed to solvent loss then linker loss. The final mass is attributed to the formation of metal oxide(s), where in the sample of KE155, the residual mass is very low (7.07%), indicating that a Sn MOF may have formed but only in a small amount. However, it is possible that only a small amount of Sn was used since the Sn(OⁱPr)₄ precursor arrives as a solution in 10% w/v in isopropanol, and so only a small amount of Sn is available to combine with the linker.

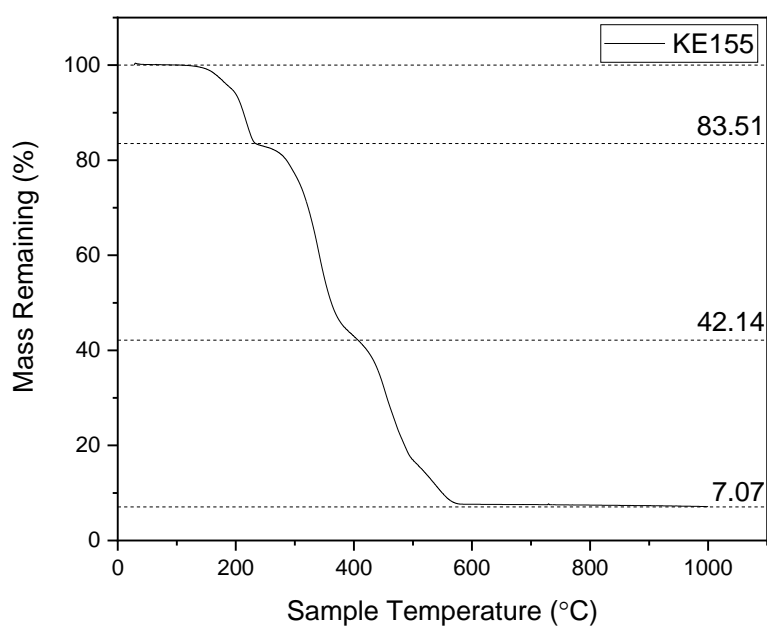


Figure 4.17: TGA for sample KE155.

Since terephthalic acid has been widely used for the formation of a variety of MOFs, it seemed an obvious starting point to try a series of experiments with Sn(IV). A wide variety of conditions were used, as detailed in Table 4.12. This included the use of DMF, DMA and TEA as solvents, with a range of temperatures. Some samples were stored in the fridge and monitored for crystal formation, as well as elevated temperatures being used. The microwave was also used in the hope that it would accelerate MOF formation before potential hydrolysis of the Sn precursor, into SnO₂. All samples using Sn(IV) and H₂BDC yielded amorphous XRD patterns, with the pattern for KE434 resembling that of H₂BDC after the microwave was used for the synthesis (Figure 4.18). Two samples were prepared using sodium terephthalate with Sn(IV) instead of H₂BDC as it was hoped the sodium form of the linker may react more favourably with the Sn(IV) precursor than the protonated form of the linker. However, these two samples displayed peaks corresponding to the precursor used rather than forming an Sn(IV) MOF.

Table 4.12: Attempts to synthesise a novel Sn(IV) MOF with H₂BDC and Na₂BDC linkers.

| Sample Code | Metal source | Linker | Solvent(s) | Temperature | Synthesis time | Outcome |
|-------------|------------------------------------|---------------------|-------------------------|-------------|----------------------------|--|
| KE078 | Sn(O ⁱ Pr) ₄ | H ₂ BDC | DMF (5 mL) | Fridge | - | No crystal growth observed. |
| KE080 | Sn(O ⁱ Pr) ₄ | H ₂ BDC | DMF (5 mL) | 50°C | 12 hours | No crystal growth observed. |
| KE0082 | Sn(O ⁱ Pr) ₄ | H ₂ BDC | DMF (5 mL), 5 drops TEA | Fridge | - | No crystal growth observed. |
| KE084 | Sn(O ⁱ Pr) ₄ | H ₂ BDC | DMF (5 mL), 5 drops TEA | 50°C | 12 hours | No crystal growth observed. |
| KE154 | Sn(O ⁱ Pr) ₄ | H ₂ BDC | TEA (5 mL) | 150°C | 24 hours | XRD displays broadness. |
| KE171 | Sn(IV) tert-butoxide | H ₂ BDC | DMF (10 mL) | 150°C | 24 hours | XRD displays broadness. |
| KE181 | Sn(IV) tert-butoxide | H ₂ BDC | DMA (10 mL) | 150°C | 24 hours | XRD displays broadness. |
| KE434 | Sn(O ⁱ Pr) ₄ | H ₂ BDC | / | 100°C | 45 mins – microwave sample | Pattern resembles H ₂ BDC. |
| KE434 | Sn(O ⁱ Pr) ₄ | H ₂ BDC | / | 100°C | 45 mins – microwave sample | Pattern resembles Na ₂ BDC. |
| KE152 | Sn(O ⁱ Pr) ₄ | Na ₂ BDC | DMF (10 mL, dried) | 150°C | 24 hours | Pattern resembles Na ₂ BDC. |
| KE433 | Sn(O ⁱ Pr) ₄ | Na ₂ BDC | / | 100°C | 45 mins – microwave sample | Pattern resembles Na ₂ BDC. |

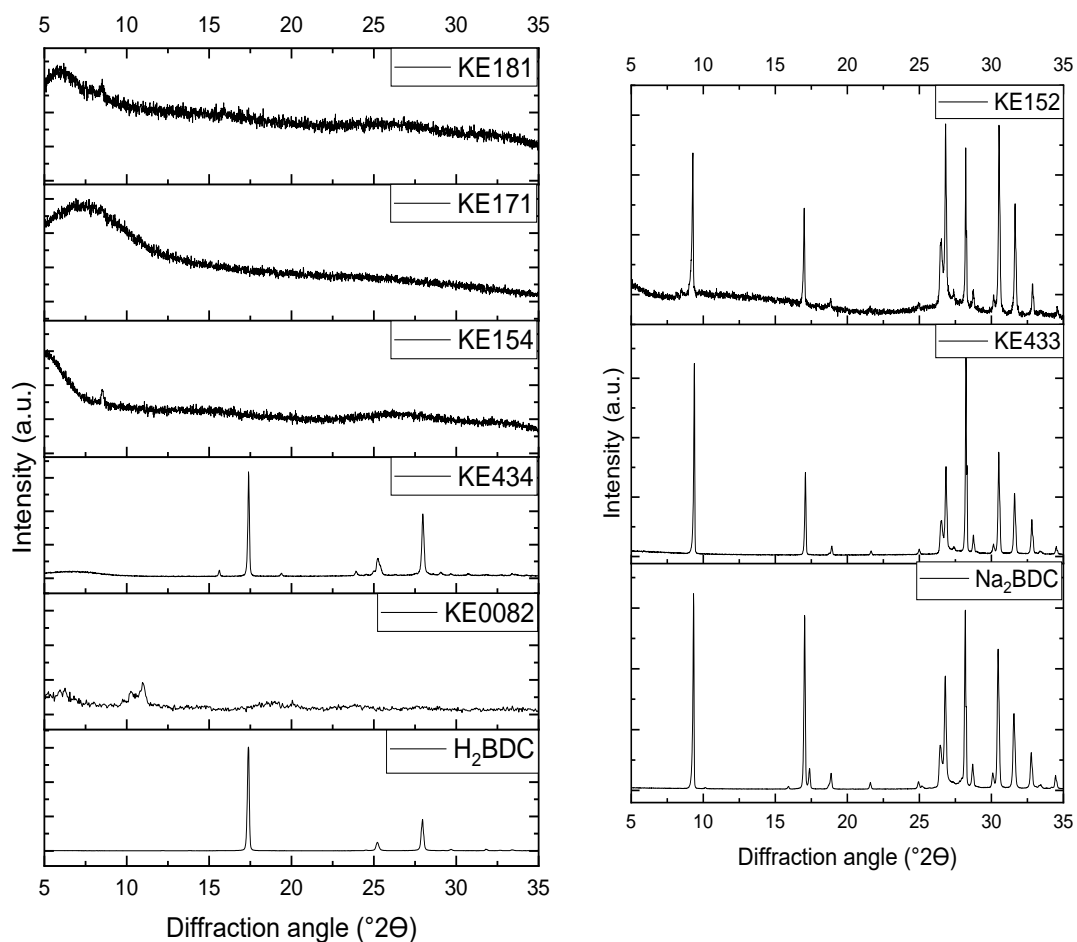


Figure 4.18: Powder XRD patterns for attempts to synthesise novel Sn(IV) MOFs with BDC, starting with either H_2BDC or Na_2BDC .

Samples combining Sn(IV) with H_4BTEC using DMF straight from the bottle, DMF that had been dried (to prevent hydrolysis of the Sn precursor) and DMA (less hygroscopic than DMF) at several different temperatures for 24 hours also yielded broad XRD patterns (Table 4.13, Figure 4.19). The initial use of DMF was because it is known to solubilise the reagents effectively, whilst the reason for drying the DMF and using DMA were to see how much of an effect a trace amount of water and how hygroscopic a solvent is can have on the final product. The use of H_4BTEC was due to the four coordination points offering more binding sites that could be utilised with the Sn(IV) faster than SnO_2 could form.

Table 4.13: Attempts to synthesise a novel Sn(IV) MOF using H₄BTEC linker.

| Sample Code | Metal source | Linker | Solvent(s) | Temperature | Synthesis time | Outcome |
|-------------|------------------------------------|---------------------|--------------------|-------------|----------------|-------------------------|
| KE157 | Sn(O ⁱ Pr) ₄ | H ₄ BTEC | DMF (10 mL, dried) | 180°C | 24 hours | XRD displays broadness. |
| KE158 | Sn(O ⁱ Pr) ₄ | H ₄ BTEC | DMF (10 mL, dried) | 120°C | 24 hours | XRD displays broadness. |
| KE172 | Sn(IV) tert-butoxide | H ₄ BTEC | DMF (10 mL) | 150°C | 24 hours | XRD displays broadness. |
| KE182 | Sn(IV) tert-butoxide | H ₄ BTEC | DMA (10 mL) | 150°C | 24 hours | XRD displays broadness. |

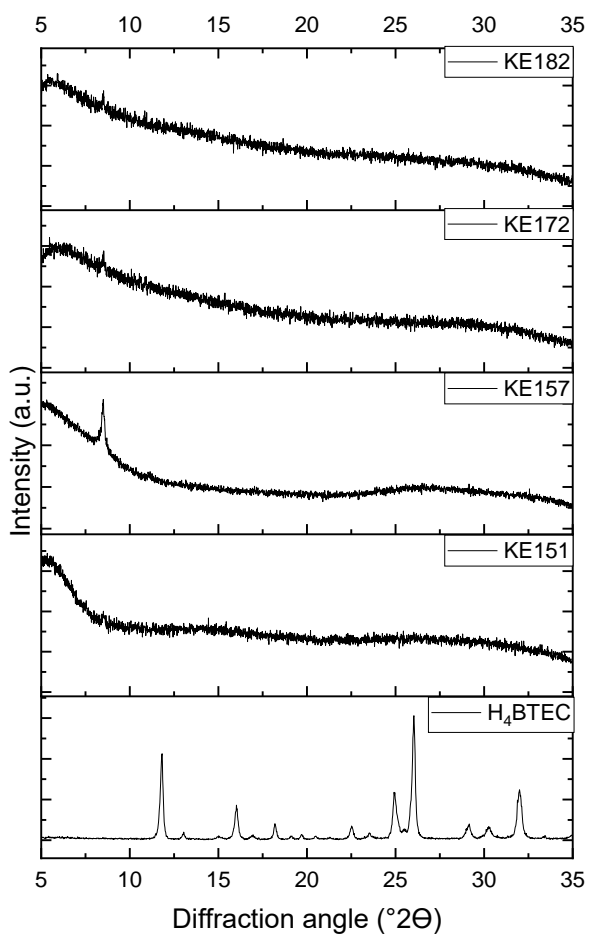


Figure 4.19: Powder XRD patterns showing the resulting products from attempting to synthesise novel Sn(IV) MOFs with H₄BTEC linker.

Some experiments were completed using Sn(IV) and 5-aminoisophthalic acid (H₂AIP), where a focus on making changes to the temperature was explored, but did not help with product crystallinity or MOF formation (Table 4.14, Figure 4.20). An experiment that was completed at a further reduced temperature in the microwave did not yield a product at all. H₂AIP was selected owing to the amine functional group having potential uses in photocatalysis if the MOF formation were successful.

Table 4.14: Attempts at synthesising a novel Sn(IV) MOF with H₂AIP linker.

| Sample Code | Metal source | Linker | Solvent(s) | Temperature | Synthesis time | Outcome |
|-------------|------------------------------------|--------------------|--------------------|-------------|----------------------------|-------------------------|
| KE159 | Sn(O ⁱ Pr) ₄ | H ₂ AIP | DMF (10 mL, dried) | 120°C | 24 hours | XRD displays broadness. |
| KE187 | Sn(O ⁱ Pr) ₄ | H ₂ AIP | DMF (10 mL, dried) | 150°C | 24 hours | XRD displays broadness. |
| KE436 | Sn(O ⁱ Pr) ₄ | H ₂ AIP | / | 100°C | 45 mins – microwave sample | No product formed. |

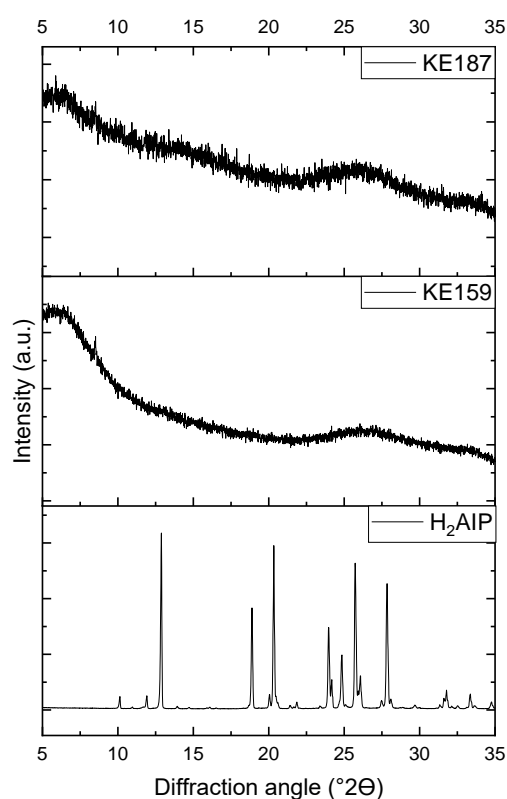


Figure 4.20: Powder XRD patterns from the attempts to synthesise a novel Sn(IV) MOF using H₂AIP.

The use of H₂ATP with Sn(IV) proved unsuccessful in both an autoclave experiment and a microwave experiment (Table 4.15), where both yielded broad XRD patterns (Figure 4.21).

Table 4.15: Attempts to synthesise a novel Sn(IV) MOF using H₂ATP as the linker.

| Sample Code | Metal source | Linker | Solvent(s) | Temperature | Synthesis time | Outcome |
|-------------|------------------------------------|--------------------|-------------|-------------|----------------------------|---|
| KE179 | Sn(O ⁱ Pr) ₄ | H ₂ ATP | DMF (10 mL) | 150°C | 24 hours | XRD displays broadness. |
| KE432 | Sn(O ⁱ Pr) ₄ | H ₂ ATP | / | 100°C | 45 mins – microwave sample | XRD displays broadness with some peaks present. |

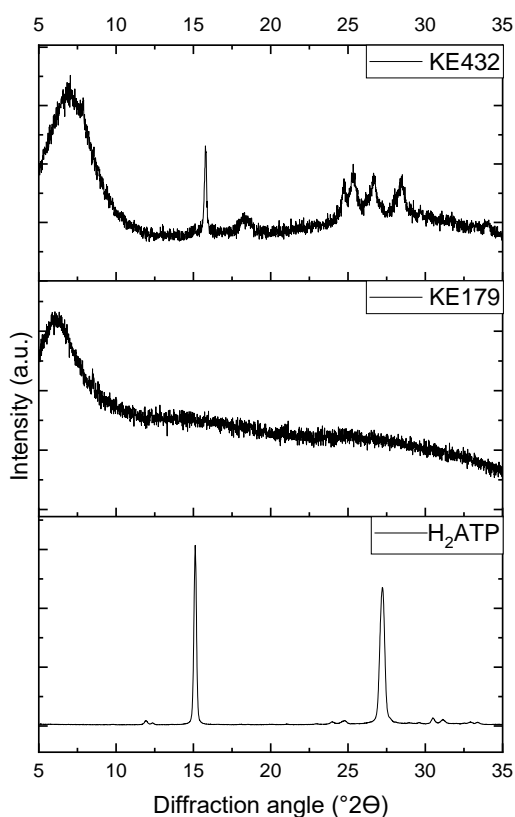


Figure 4.21: Powder XRD patterns for the attempted syntheses of a novel Sn(IV) MOF with ATP linker.

The next experiments investigated the combination of Sn(IV) with 1,4-naphthalenedicarboxylic acid (H₂NDC). This linker was of interest to see if having an additional aromatic ring encouraged MOF formation, and if successful, would likely create a more robust material. For experiments completed in autoclaves, 150°C and 24 hours were selected since this combination yielded the most successful looking results with the attempted synthesis of novel Ti(IV) MOFs, as reported above, whilst an investigation into changing the solvent took place (Table 4.16). Using DMF, no product formed. Using DMA and DMF/MeOH, broad XRD patterns were obtained (Figure 4.22), showing that in this case altering the solvent did not achieve the formation of a crystalline MOF. Another synthesis, using a reduced temperature of 100°C and no solvent (just the use of the Sn(OⁱPr)₄ solution), was also unable to yield a crystalline sample.

Table 4.16: Attempted syntheses of an Sn(IV) MOF with NDC linker.

| Sample Code | Metal source | Linker | Solvent(s) | Temperature | Synthesis time | Outcome |
|-------------|------------------------------------|--------------------|-------------------------|-------------|----------------------------|-------------------------|
| KE177 | Sn(O ⁱ Pr) ₄ | H ₂ NDC | DMF (10 mL) | 150°C | 24 hours | No product formed. |
| KE183 | Sn(IV) tert-butoxide | H ₂ NDC | DMA (10 mL) | 150°C | 24 hours | XRD displays broadness. |
| KE252 | Sn(O ⁱ Pr) ₄ | H ₂ NDC | DMF (9 mL), MeOH (1 mL) | 150°C | 24 hours | XRD displays broadness. |
| KE435 | Sn(O ⁱ Pr) ₄ | H ₂ NDC | / | 100°C | 45 mins – microwave sample | XRD displays broadness. |

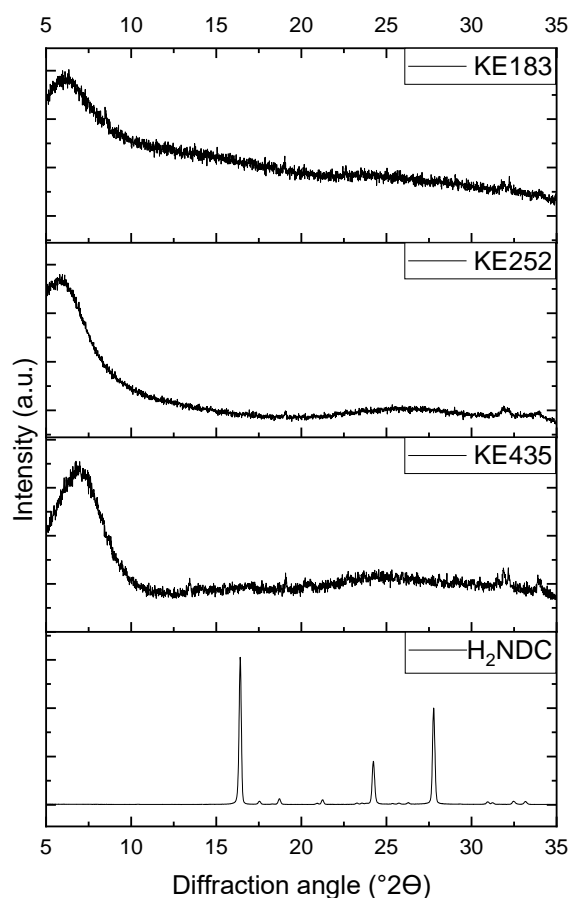


Figure 4.22: Powder XRD patterns for attempted syntheses of novel Sn(IV) MOFs with H₂NDC linker.

The combination of 2,5-dihydroxyterephthalic acid (H₂DOBDC) with Sn(IV) also proved unsuccessful under the conditions used and reported below in Table 4.17. It was of interest to use H₂DOBDC in the attempted synthesis since if successful, the incorporation of two hydroxy groups into an Sn(IV) MOF could have extended the applications of the material. Under solvothermal synthesis in an autoclave, broad peaks can be observed on the XRD pattern, whilst under microwave synthesis, an XRD pattern resembling that of the organic linker is observed (Figure 4.23).

Table 4.17: Attempted MOF syntheses using Sn(IV) and H₂DOBDC as a linker.

| Sample Code | Metal source | Linker | Solvent(s) | Temperature | Synthesis time | Outcome |
|-------------|------------------------------------|----------------------|-------------|-------------|----------------------------|----------------------------------|
| KE178 | Sn(O ⁱ Pr) ₄ | H ₂ DOBDC | DMF (10 mL) | 150°C | 24 hours | XRD displays broadness. |
| KE439 | Sn(O ⁱ Pr) ₄ | H ₂ DOBDC | / | 100°C | 45 mins – microwave sample | Peaks match those of the linker. |

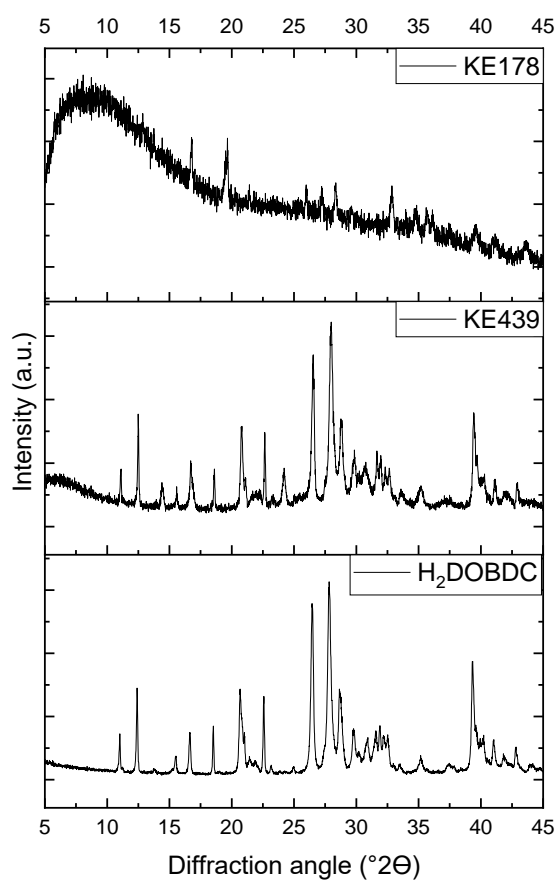


Figure 4.23: Powder XRD patterns from attempted syntheses using Sn(IV) and H₂DOBDC.

Two additional attempts at synthesising Sn(IV) MOFs included using 2,6-pyridinedicarboxylic acid, with the use of DMF and MeOH at 150 °C. 2,6-pyridinedicarboxylic acid was of interest to be used since it formed the promising structure reported above using Ti(IV). 2,5-pyridinedicarboxylic acid was also available

and so it was of interest to see if changing the position of one of the carboxylate groups had any effect on the material produced. The synthesis conditions are shown in Table 4.18 and the XRD patterns shown in Figure 4.24. No crystalline material was observed, proving the combination of these linkers with Sn(IV) to be unsuccessful under these conditions reported.

Table 4.18: Attempts to synthesise a novel Sn(IV) MOF with 2,6-pyridinedicarboxylic acid and 2,5-pyridinedicarboxylic acid.

| Sample Code | Metal source | Linker | Solvent(s) | Temperature | Synthesis time | Outcome |
|-------------|------------------------------------|-------------------------------|-------------------------|-------------|----------------|-------------------------|
| KE253 | Sn(O ⁱ Pr) ₄ | 2,6-pyridinedicarboxylic acid | DMF (9 mL), MeOH (1 mL) | 150°C | 24 hours | XRD displays broadness. |
| KE254 | Sn(O ⁱ Pr) ₄ | 2,5-pyridinedicarboxylic acid | DMF (9 mL), MeOH (1 mL) | 150°C | 24 hours | XRD displays broadness. |

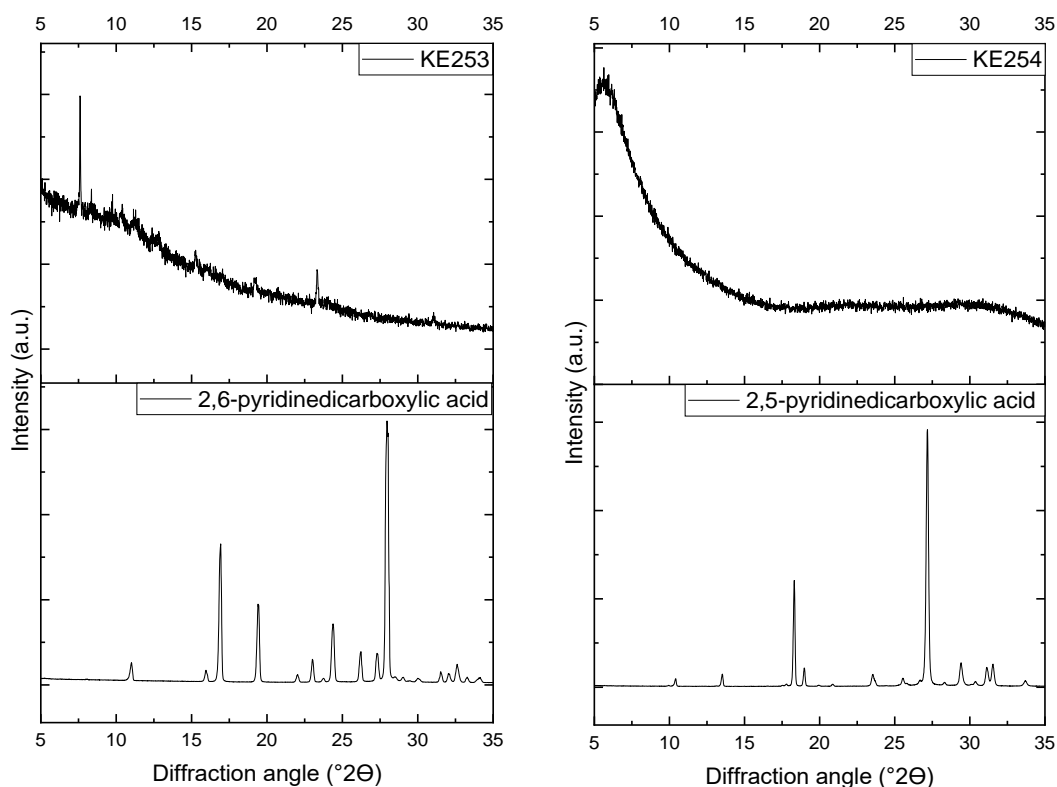


Figure 4.24: XRD patterns for the attempted synthesis of an Sn(IV) MOF with 2,6-pyridinedicarboxylic acid and 2,5-pyridinedicarboxylic acid.

The remaining experiments completed to try to synthesise an Sn(IV) MOF involved using chelidamic acid. Chelidamic acid appeared to be an ideal candidate for the development of an Sn(IV) MOF since it has two carboxyl groups which act as binding sites for metal ions (Figure 4.25). The lone pair of electrons on the N atom makes it basic, with the potential to enhance adsorption of acidic CO₂ for the application of CO₂ photoreduction. The nitrogen could also bind to the metal making it a very effective ligand as seen in other chelidamate structures.

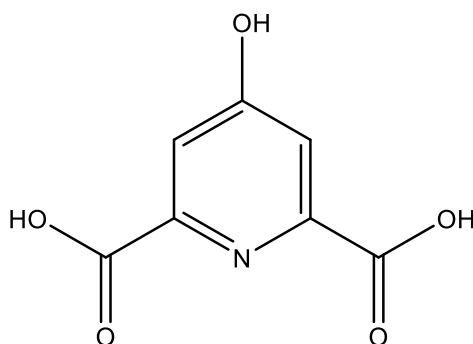


Figure 4.25: The structure of chelidamic acid, which contains two carboxylate groups as metal binding sites, as well as an -NH₂ and an =O group.

Attempts were made to synthesise a Sn-chelidamate structure, as shown in Table 4.19. Synthesis conditions were initially set to 150°C as this was in the middle of the range typically used in previous MOF syntheses explored in this project (120°C - 180°C). Like with previous MOF syntheses, the linker was added in an excess to the metal source, and a synthesis of 24 hours was selected as an initial starting point. Dried DMF was selected as a possible solvent to try, in order to avoid the hydrolysis of the sensitive Sn(OⁱPr)₄ starting material. DMA was also tried as it is less hydroscopic than DMF, and so the aim was to avoid the solvent attracting water molecules and subsequently hydrolysing the Sn(OⁱPr)₄ precursor. Ordinary DMF was also tried as a reference to the dried DMF and DMA, in order to see if this made any difference to the results. The other solvents that were selected to try were those that have been previously used in Ti MOF syntheses. The XRD patterns (Figure 4.26) showed that use of isopropanol (KE176) and use of DMA (KE180) did not produce any crystalline Sn-chelidamate structure, and instead produced amorphous PXRD patterns. The synthesis product using toluene (KE175) appears to be residual or recrystallised

linker. Syntheses in dried DMF (KE156) and ordinary DMF (KE169) produced PXRD patterns that appeared MOF-like, and so subsequent work was completed on these materials.

Table 4.19: The attempts to synthesise an Sn(IV) MOF with chelidamic acid.

| Sample Code | Metal source | Linker | Solvent | Temperature | Synthesis time |
|-------------|------------------------------------|-----------------|---------------------|-------------|----------------|
| KE156 | Sn(O ⁱ Pr) ₄ | Chelidamic acid | DMF (10 mL, dried) | 150°C | 24 hours |
| KE169 | Sn(IV) tert-butoxide | Chelidamic acid | DMF (10 mL) | 150°C | 24 hours |
| KE175 | Sn(O ⁱ Pr) ₄ | Chelidamic acid | Toluene (10 mL) | 150°C | 24 hours |
| KE176 | Sn(O ⁱ Pr) ₄ | Chelidamic acid | Isopropanol (10 mL) | 150°C | 24 hours |
| KE180 | Sn(IV) tert-butoxide | Chelidamic acid | DMA (10 mL) | 150°C | 24 hours |

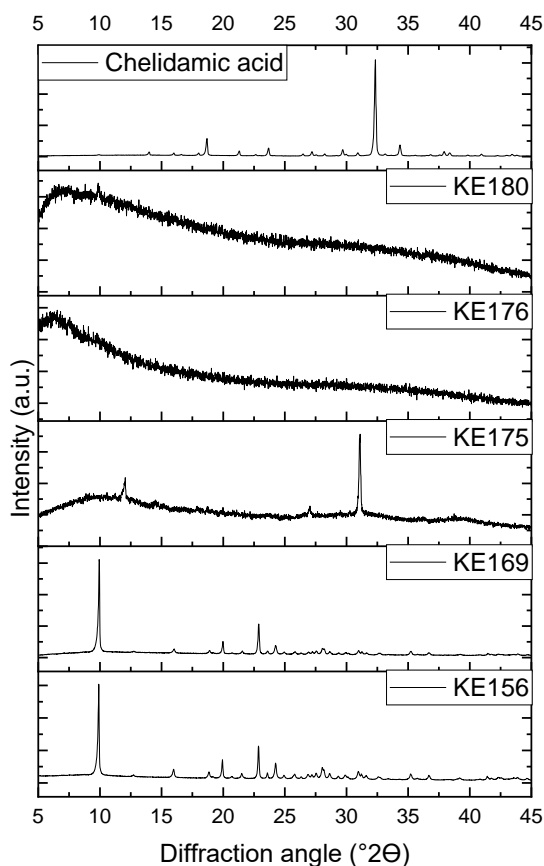


Figure 4.26: Powder XRD patterns for the attempted synthesis of an Sn(IV) MOF with chelidamic acid.

TGA was completed on sample KE156 (Figure 4.27), where a large decrease can be seen between 99.32% and 43.50% due to linker combustion, where the remaining mass is attributed to the formation of SnO₂. The calculations from this sample suggest that there are two tin atoms present per one linker, which is unlikely for a MOF structure, therefore suggesting there was some SnO₂ present in the sample.

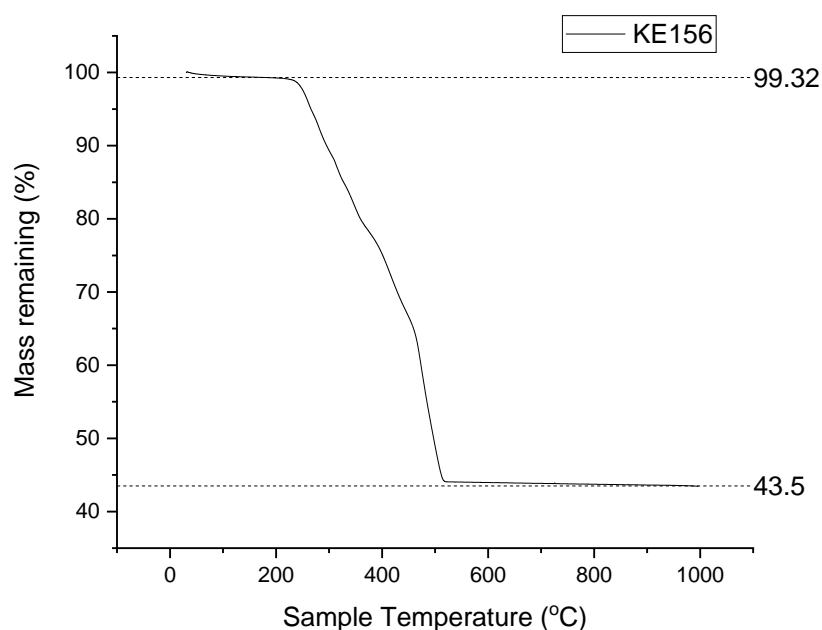


Figure 4.27: TGA for sample KE156 showing a large mass loss from 99.32% to 43.5%.

Repeat reactions of sample KE156 were then completed (KE153 and KE160), where the XRD patterns are shown below in Figure 4.28. These patterns match that of KE156, demonstrating the reproducibility of the synthesis. The PXRD pattern of chelidamic acid is also shown to demonstrate that sample KE156 is not simply comprised of unreacted linker or recrystallised linker. A reference reaction was also completed, which was identical to KE156 but without any Sn(OⁱPr)₄ added, which did not produce any product. This proved that chelidamic acid in dried DMF did not just produce a recrystallised version of the linker.

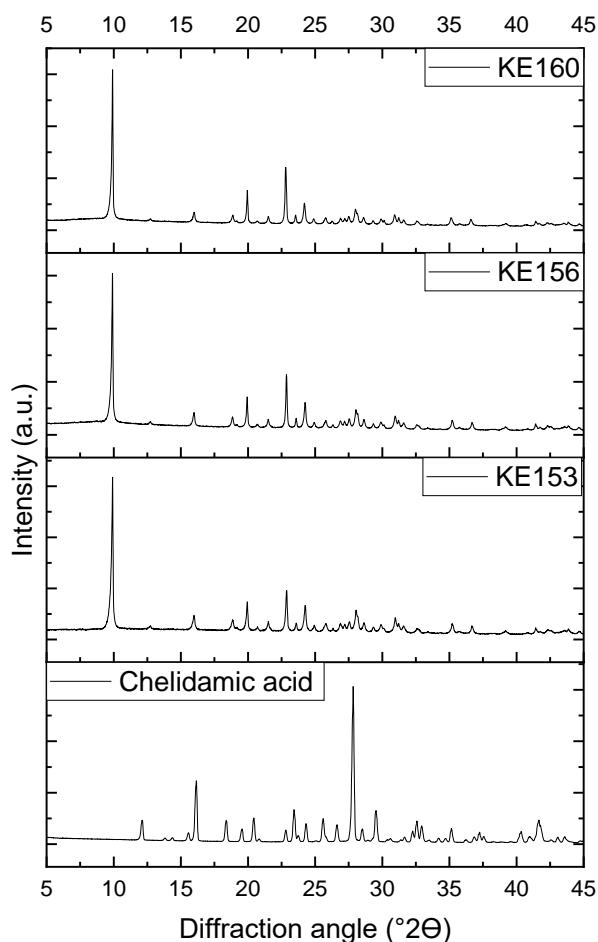


Figure 4.28: Powder XRD patterns comparing sample KE153 with two repeat syntheses to see the reproducibility of the synthesis. Chelidamic acid is also shown for reference.

Single crystal data from sample KE156 revealed that the structure formed was a Sn(II) material, rather than Sn(IV) (see Figure 4.29). The asymmetric unit contained chelidamic acid coordinated to tin with a dimethylammonium cation. An infinite one-dimensional chain was formed by chelation of the tin by both carboxyl groups of one chelidamic acid and also the phenoxy of a symmetry related chelidamic acid. Both the carboxyls and the phenol are ionised and there is a dimethylammonium counterion, likely to be from the hydrolysis of DMF. The two hydrogen atoms were located on the dimethylammonium counter ion but were placed at a calculated position for the refinement. The chains of the tin chelate are then linked by H bonding, bridged via the dimethylammonium counter ion.

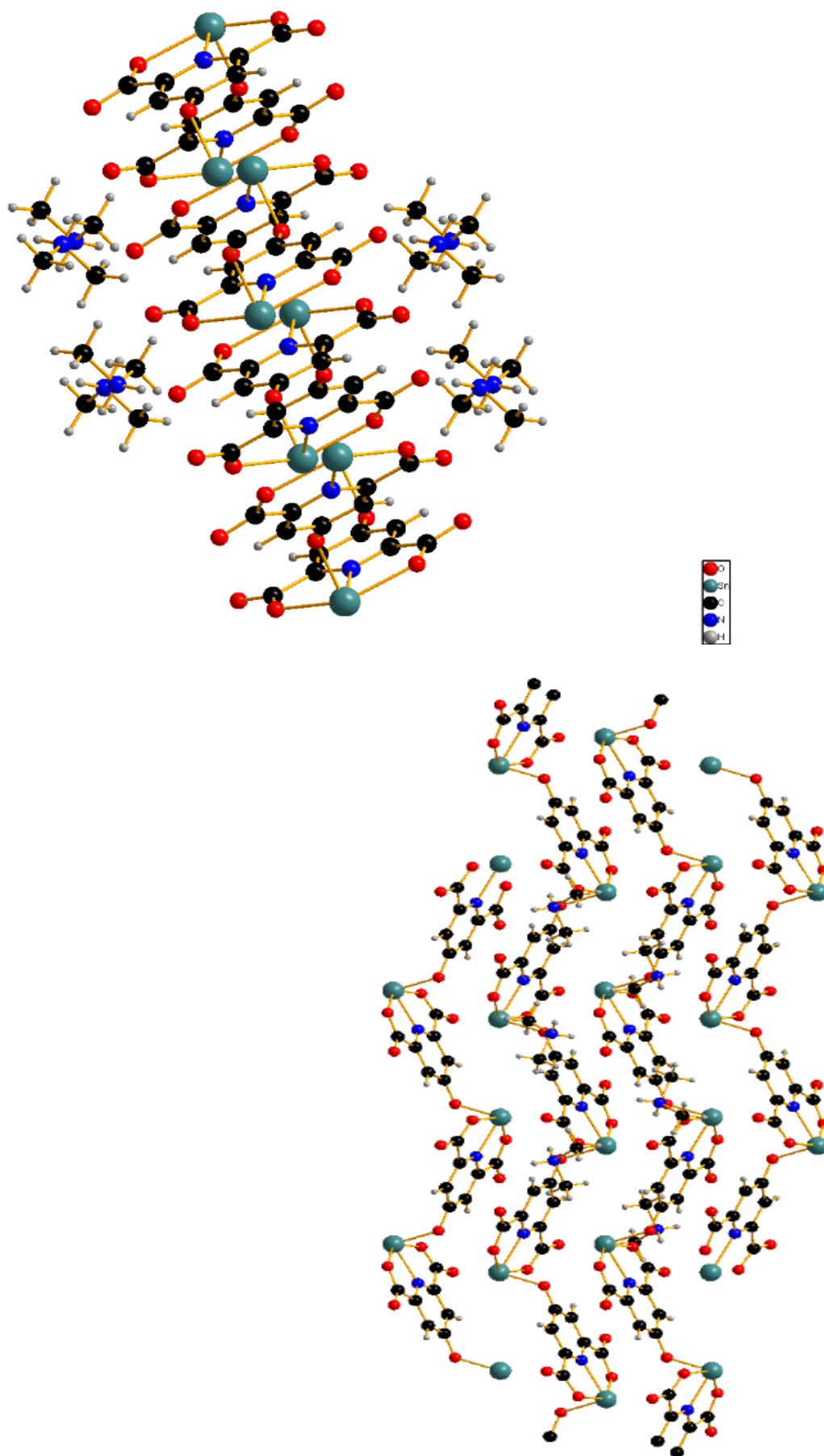


Figure 4.29: The structure of KE156 shown in two different orientations. O atoms are shown in red, Sn atoms are shown in green, C atoms are shown in black, N atoms are shown in dark blue and H atoms are shown in grey.

The crystallographic data and refinement for KE156, Sn(chel)(DMA), is shown below in Table 4.20. The structure contains Sn(II) rather than Sn(IV) as it balances the charge and the unsymmetrical local geometry around Sn(II) is also observed. Sn(II) MOFs appear to be unusually stable with carboxylate ligands, and this material is another example of such. An Sn(II)-chelidamate structure has been previously reported, however differs to the below sample which also contains a DMA cation and was synthesised using a different solvent.⁷

Table 4.20: Crystallographic data obtained from a single crystal of sample KE156.

| | |
|---|--|
| Identification code | KE156 |
| Empirical formula | C ₉ H ₁₀ N ₂ O ₅ Sn |
| Formula weight | 344.88 |
| Temperature/K | 150(2) |
| Crystal system | Monoclinic |
| Space group | <i>P</i> 2 ₁ / <i>c</i> |
| a/Å | 10.68490(10) |
| b/Å | 12.83580(10) |
| c/Å | 8.97700(10) |
| α/° | 90 |
| β/° | 105.5870(10) |
| γ/° | 90 |
| Volume/Å³ | 1185.91(2) |
| Z | 4 |
| P_{calc}/cm³ | 1.932 |
| μ/mm⁻¹ | 17.297 |
| F(000) | 672.0 |
| Crystal size/mm³ | 0.6 x 0.15 x 0.08 colourless block |
| Radiation | CuKα (λ = 1.54184) |
| 2θ range for data collection (°) | 8.592 to 155.352 |
| Index ranges | -13 ≤ h ≤ 13, -16 ≤ k ≤ 15, -11 ≤ l ≤ 10 |
| Reflections collected | 22742 |
| Independent reflections | 2508 [<i>R</i> _{int} = 0.0504, <i>R</i> _{sigma} = 0.0196] |

| | |
|---|----------------------------------|
| Data/restraints/parameters | 2508/0/156 |
| Goodness-of-fit on F^2 | 1.091 |
| Final R indexes [$I > 2\sigma(I)$] | $R_1 = 0.0274$, $wR_2 = 0.0759$ |
| Final R indexes [all data] | $R_1 = 0.0274$, $wR_2 = 0.0759$ |

A comparison between the measured powder XRD pattern and the simulated pattern from the single crystal structure of sample KE156 can be seen in Figure 4.30 below. The measured pattern matches the simulated well, with a difference in relative peak intensities being observed.

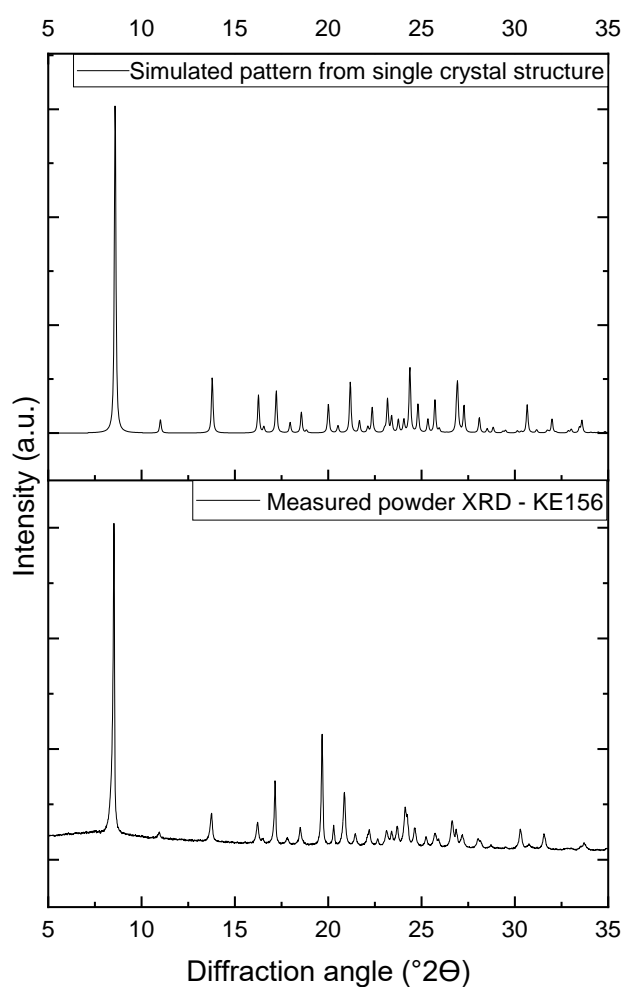


Figure 4.30: A comparison of the measured powder XRD pattern from sample KE156 and the simulated pattern from the single crystal structure of sample KE156.

A stability test was then completed on the Sn-chelidamate structure (Figure 4.31). A sample of KE156 was heated at 180°C for 24 hours in water. After drying, the XRD pattern obtained showed that SnO₂ had been produced. Interestingly, during the reaction of Sn(OⁱPr)₄ and chelidamic acid, the Sn(IV) reduces to Sn(II), however during the water stability test, this Sn(II) is then oxidised back to Sn(IV).

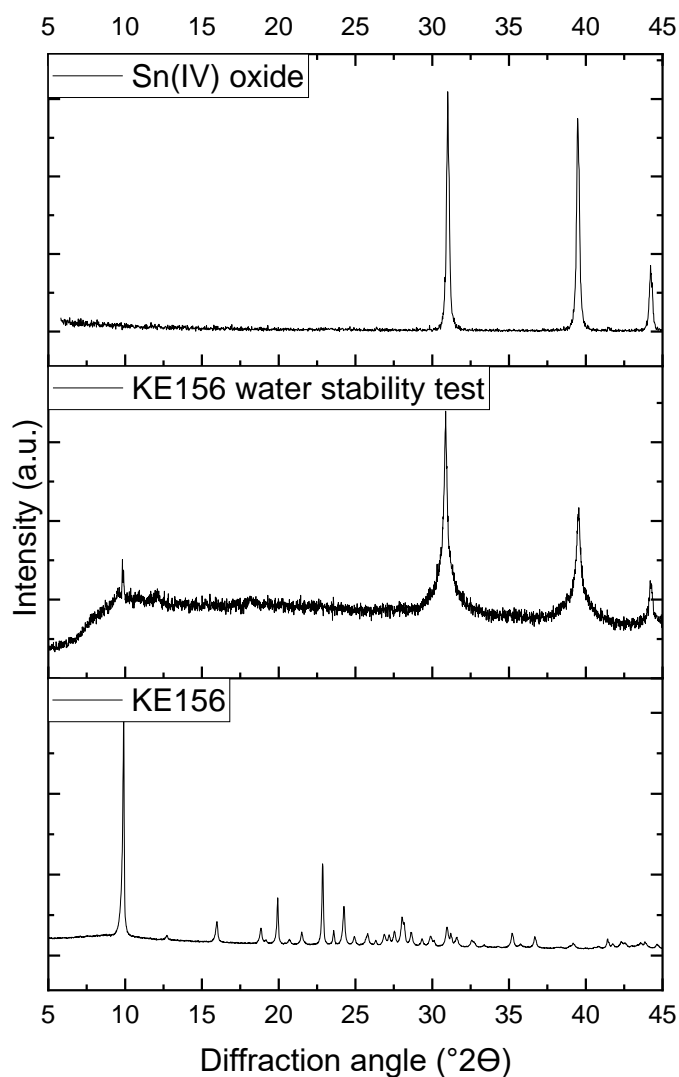


Figure 4.31: Powder XRD patterns for sample KE156, sample KE156 after a water stability test, and Sn(IV) oxide for reference.

It would be of interest to further investigate some potential uses for the Sn-chelidamate structure that has been synthesised. In order to find some applicable

uses, a greater number of stability tests at different temperatures and in different solvents should be completed as further work.

In a similar approach to attempting to produce an Sn(IV) MOF with chelidamic acid, mandelic acid was also used. This was primarily tried since mandelic acid has been shown to react with Zr(IV) ions, and so was suspected to have potential to react with Sn(IV).⁸ Mandelic acid should be capable of forming an isolated complex with Sn(IV) due to the two -OH groups present (one hydroxyl, one carboxyl), which offer binding sites to metallic ions once the -OH groups have been deprotonated. Mandelic acid could also be useful for photocatalysis, as the aromatic ring is useful for light-harvesting, whilst also providing rigidity to the structure. Even if mandelic acid was not able to form a MOF structure, it would also be interesting to still obtain an Sn(IV) structure to analyse further for applications. The structure of mandelic acid is shown below in Figure 4.32.

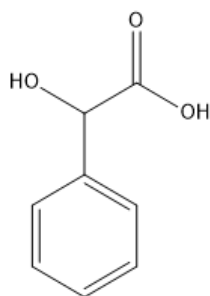


Figure 4.32: The structure of mandelic acid, which was used with Sn(IV) to try to form an Sn(IV) MOF.

The attempted syntheses of a Sn-mandelate structure are reported in Table 4.21 below. Zr-mandalate has been synthesised using HCl and H₂O, and so this was completed with Sn for reference, despite the sensitivity of Sn to H₂O.⁸ Like with the syntheses using chelidamic acid, a temperature of 150°C was used as it is the average of the temperatures usually used (120°C-180°C). The linker was in excess compared to the metal source and 24 hours was selected as an initial starting point. Figure 4.33 shows the XRD patterns for two of the syntheses, with mandelic acid shown for reference.

Table 4.21: Attempted syntheses of a Sn-mandellate structure.

| Sample Code | Metal source | Linker | Solvent(s) | Temperature (°C) | Synthesis time | Outcome |
|-------------|------------------------------------|---------------|-------------------------------------|------------------|----------------|---|
| KE184 | Sn(O ⁱ Pr) ₄ | Mandelic acid | DMF (10 mL, dried) | 150 | 24 hours | No product formed. |
| KE185 | Sn(O ⁱ Pr) ₄ | Mandelic acid | Toluene (10 mL) | 150 | 24 hours | No product formed. |
| KE186 | Sn(O ⁱ Pr) ₄ | Mandelic acid | Isopropanol (10 mL) | 150 | 24 hours | No product formed. |
| KE188 | Sn(O ⁱ Pr) ₄ | Mandelic acid | HCl (1 mL), H ₂ O (9 mL) | 150 | 24 hours | XRD shows some peaks present on an amorphous background that are distinct to mandelic acid. |
| KE191 | Sn(O ⁱ Pr) ₄ | Mandelic acid | DMA (10 mL) | 150 | 24 hours | XRD shows peaks present on an amorphous background. |

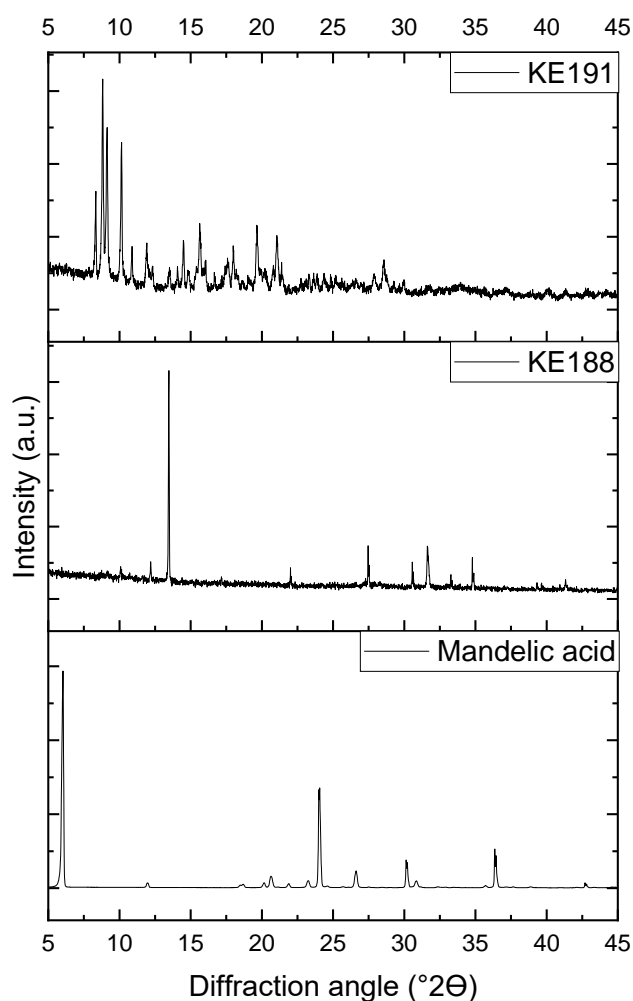


Figure 4.33: Powder XRD patterns from the attempted syntheses using Sn(IV) and mandelic acid. Samples shown are KE191 and KE188, with the XRD pattern for mandelic acid shown for reference.

Interestingly, the use of identical conditions but with a change of solvent yielded two different XRD patterns. Neither sample yielded single crystals, so full structural analysis was not possible. Further work would need to be completed to yield single crystals in order to deduce whether a structure similar to that of the Sn-chelidamate structure reported above was possible or not. Then, additional investigations into potential uses and applications could take place.

This investigation further highlights the difficult nature of forming an Sn(IV) MOF, even when a range of linkers with different features are tried. This work also shows

the preference to form Sn(II) materials, when theoretically Sn(IV) materials should be stable.

4.5 Conclusions

Attempts to synthesise novel Ti(IV) and Sn(IV) MOFs proved challenging, with hydrolysis of the metal precursors being a prevalent issue, leading to amorphous or poorly crystalline solids. Two materials, prepared using Ti(IV) and 1,4-naphthalenedicarboxylic acid and Ti(IV) and 2,6-pyridinedicarboxylic acid appeared promising, however in the absence of single crystal data, full characterisation has not been possible. Similarly, the XRD pattern obtained from the synthesis using Ti(IV) and 2,3-pyrazinedicarboxylic acid looked interesting and distinct to the linker. Further work could explore obtaining crystals of this material, by varying synthesis conditions further, in the hope that a novel and robust Ti(IV) MOF could form for catalysis applications.

Another attempt was made in this work to incorporate two linkers and two metals into a structure. The sample initially obtained looked hopeful, however upon further investigation it was proved that one linker and metal had combined preferentially, highlighting the preference and selectivity that certain metals and linkers often have to form MOFs in certain orientations, over other possibilities. Mixed-metal and mixed-linker MOFs have been reported in the literature, however this particular attempted combination proved unfavourable at forming a mixed structure.

Similarly to with the novel Ti(IV) MOF attempts, the formation of novel Sn(IV) MOFs proved challenging. One synthesis that combined Sn(IV) and H₃BTC appeared promising, however after many attempts, single crystals were still unattainable. The combination of Sn(IV) with chelidamic acid was also explored, and did yield an Sn(II)-chelidamate structure, which was solved from single crystal diffraction. This example illustrates how easily the reduction of Sn(IV) occurs, which complicates the synthesis

of potential Sn(IV) MOFs. Greater investigations into the stability of this structure in a range of solvents at different temperatures would be useful for future work. In addition, potential applications for this material could be explored.

Growing MOFs as single crystals still remains a challenge.⁹ However, in the future, structure determination from polycrystalline samples may become more routine with the development of 3d-electron diffraction methods.¹⁰ Therefore, the determination of many of the samples explored in this chapter may be possible. This investigation into novel Ti(IV) and Sn(IV) MOFs confirms the serendipitous nature of many MOF syntheses, and that logical combinations of metal and linker do not necessarily result in MOF formation. This investigation has helped emphasise how difficult MOF formation can be, despite trying different experimental set-ups, including use of autoclaves and microwave synthesis, and despite trying different precursors, temperatures, synthesis durations and solvent combinations. This work therefore offers a good starting point for further investigations in attempts to synthesise novel Ti(IV) and Sn(IV)-based MOFs, especially with the samples where single crystals could be generated from promising XRD patterns.

4.6 References

- 1 A. Schaate, P. Roy, A. Godt, J. Lippke, F. Waltz, M. Wiebcke and P. Behrens, *Chem. - A Eur. J.*, 2011, **17**, 6643-6651.
- 2 R. Seetharaj, P. V. Vandana, P. Arya and S. Mathew, *Arab. J. Chem.*, 2019, **12**, 295-315.
- 3 T. N. Nguyen, S. Kampouri, B. Valizadeh, W. Luo, D. Ongari, O. M. Planes, A. Züttel, B. Smit and K. C. Stylianou, *ACS Appl. Mater. Interfaces.*, 2018, **10**, 30035-30039.
- 4 J. Gao, J. Miao, P. Z. Li, W. Y. Teng, L. Yang, Y. Zhao, B. Liu and Q. Zhang, *Chem. Commun.*, 2014, **50**, 3786-3788.

- 5 H. Assi, L. C. Pardo Pérez, G. Mouchaham, F. Ragon, M. Nasalevich, N. Guillou, C. Martineau, H. Chevreau, F. Kapteijn, J. Gascon, P. Fertey, E. Elkaim, C. Serre and T. Devic, *Inorg. Chem.*, 2016, **55**, 7192-7199.
- 6 T. Ladrak, S. Smulders, O. Roubeau, S. J. Teat, P. Gamez and J. Reedijk, *Eur. J. Inorg. Chem.*, 2010, **2010**, 3804-3812.
- 7 G. M. De Lima, R. I. Walton, G. J. Clarkson, R. S. Bitzer and J. D. Ardisson, *Dalt. Trans.*, 2018, **47**, 8013-8022.
- 8 J. M. Crosland, E. K. Corlett, D. Scapens, N. Guillou, S. P. Brown and R. I. Walton, *Chem. Commun.*, 2020, **56**, 10159-10162.
- 9 N. Stock and S. Biswas, *Chem. Rev.*, 2012, **112**, 933-969.
- 10 Z. Huang, E. S. Grape, J. Li, A. K. Inge and X. Zou, *Coord. Chem. Rev.*, 2021, **427**, 1-14.

Chapter Five

Sustainable Catalysis using MOFs

5.1 Introduction

This chapter explores three different applications for the original and modified MUV-10 materials already reported in this thesis (Chapter 3). All three applications focus on sustainable catalysis, namely the photocatalytic reduction of CO₂, the conversion of glucose to 5-HMF, and the conversion of CO₂ to cyclic carbonates using epoxides. The focus of two of these applications has been to find relatively inexpensive and effective routes for CO₂ reduction or utilisation, where this could offer positive environmental impacts. In these applications, CO₂ is captured, and either chemically useful or value-added products are produced, as well as being intended to contribute to helping with environmental issues. Relevant reference materials are also included, and comparisons have been made between these and the MUV-10 materials. The other application explored, glucose conversion, offers a greener approach to chemicals production, avoiding the use of fossil products, and offers potential positive environmental impacts.

5.2 MOFs for the Photocatalytic Reduction of CO₂

The experimental set up for the photocatalytic reduction of CO₂ is explained in Experimental Section 2.5.1. The final set-up did not deviate much from the original design (Figure 5.1). The CO₂ cylinder was connected to a mass flow control meter to ensure the rate of CO₂ delivery was constant for each experiment. A removable shield, painted black, was placed around each experiment to avoid external light influences from the lab. For each experiment, stirring was controlled, and the lamp was fixed to a reference intensity of 1 sun per experiment.

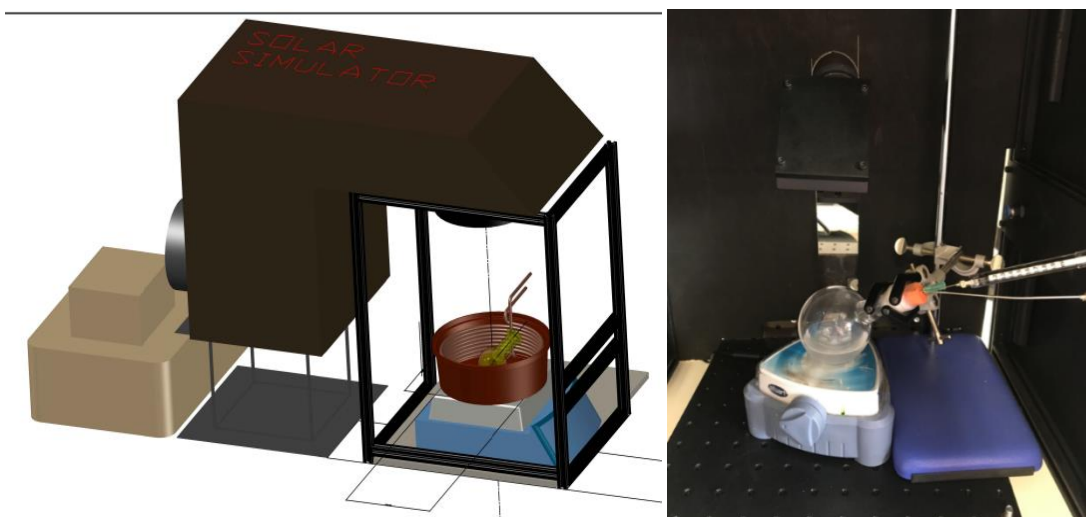


Figure 5.1: The initial design of the solar simulator set-up (left-hand side) and an image of the final set-up (right-hand side), which utilises a 100 mL quartz round-bottomed flask.

MUV-10 was deemed a good candidate for the application of the photoreduction of CO_2 to less-harmful products such as formic acid, due to the redox activity of the Ti, which is contained in the nodes of MUV-10. MUV-10(Mn) was also shown to have a band gap large enough such that it could operate in the visible region and the UV-region. Therefore, it was expected that effective charge separation could occur, with the aim to avoid electron-hole recombination. Something to consider when using MOFs for this application is that they need a small enough band gap for electron-hole separation without charge recombination, but also the bands need to effectively align with CO_2 for the electron transfer and subsequent reduction of CO_2 to occur. Knowing where the conduction and valence bands lie is useful for this application to see how effective the band alignment is with the reactants.

Ultraviolet photoelectron spectroscopy (UPS) is a technique that can identify the HOMO/LUMO levels of a material, however when attempted with the MUV-10 samples, they charged under the X-ray beam used for alignment purposes. Since the UV source is much more intense than the X-ray beam, the technique would not have worked.

The Mott-Schottky method was then investigated to try to get further detail on the band positions of the MUV-10 materials. 4 mg of MOF were sonicated for 5 minutes in a 20 μ L liquid Nafion and 1 mL methanol solution. A glassy carbon (GC) electrode was used, where a picture of the GC with the MOF loaded can be seen in Figure 5.2. The potential window was -0.6 to 0.6 V vs. Standard calomel electrode (SCE). The increments used were 0.005 or 0.05 V, the amplitude was 0.005 V and the frequency was 1-10 kHz. During Mott-Schottky measurements, several different frequencies are used to check that the flat-band potential is consistent, however this was not possible using MUV-10. A Mott Schottky plot was generated, but due to it not being frequency independent, little confidence could be found in the results. Some things that could be done in the future would be to repeat the measurements using a different instrument with better impedance capacities, ensuring the GC-MOF electrode is completely in the dark when the measurement is being taken, and altering the ratio of Nafion and methanol used.



Figure 5.2: An image of the GC electrode with MOF loaded for Mott-Schottky experiments. The MOF coverage was not very homogeneous.

Some attempts at the photocatalytic reduction of CO_2 were made with MUV-10 and some of the modified samples, despite not being able to identify their HOMO/LUMO levels, and only their band gaps approximately known from Tauc plot extrapolation as shown in Chapter 3.

The use of triethanolamine (TEOA) as a sacrificial electron donor for the photocatalytic reduction of CO_2 is generally reported in the literature (Figure 5.3). Acetonitrile and water has also often been reported as the solvent system, however, was replaced with just water for the experiments reported in this thesis since MUV-10 is water-stable. This therefore makes this process greener and advantageous compared to the use of other non-water stable MOFs used previously, such as MIL-125. Additionally, the product analysis for this application was completed using NMR, and the peaks attributed to acetonitrile overlapped with the internal standard used, which was 1,4-dioxane, making quantification of products impossible. This overlap of peaks was avoided when just water was used, making quantification with NMR possible.

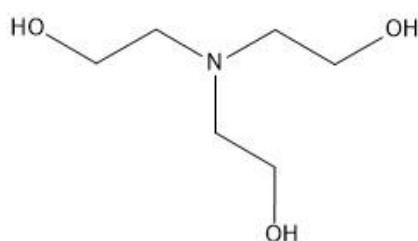


Figure 5.3: The structure of triethanolamine (TEOA), commonly used as a sacrificial electron donor in the photocatalytic reduction of CO_2 .

Initial experiments using MUV-10 for the photocatalytic reduction of CO_2 appeared promising (Table 5.1). Both MUV-10(Ca) and MUV-10(Mn) were tried as a catalyst for the photocatalytic reduction of CO_2 (5 mL/min flow rate), with TEOA (5 mL) as a sacrificial electron donor, where the MOF was stirred in water (25 mL) for 24 hours. In addition, 4 hour experiments were completed for MUV-10(Ca) to see the yield of formic acid that could be obtained in a reduced time frame. This experiment showed that approximately a third of the formic acid generated occurs in the first 4 hours of a 24 hour experiment. Reference experiments were completed in the dark to prove whether light was essential for the process. The zirconium MOF UiO-66 was also synthesised as a reference material for the conversion and was found to produce less formic acid than the MUV-10 materials. Data for TiO_2 were also recorded, since this has been widely used for photocatalytic applications reported previously.¹ In the

literature it had also been previously reported that NH₂-UiO-66 generated 13.2 μmol of formate in 10 hours, whilst NH₂-MIL-125 yielded 8.14 μmol. These values came from similar experimental conditions used in the experiments reported in this thesis, however used 50 mg photocatalyst, acetonitrile/TEOA (5:1) and a solution volume of 60 mL.²

Table 5.1: Results from solar simulator experiments using MUV-10(Ca) and MUV-10(Mn) for CO₂ reduction. Reference experiments completed without light irradiation are also reported, alongside UiO-66 and TiO₂ as reference materials. Catalysts had not been activated prior to use.

| Sample | Average formic acid yield μmol/hr/g |
|--|--|
| MUV-10(Ca) with light irradiation – 24 hours | 29.65 |
| MUV-10(Ca) without light irradiation – 24 hours | 0 |
| MUV-10(Ca) with light irradiation – 4 hours | 10.87 |
| MUV-10(Mn) with light irradiation – 24 hours | 31.42 |
| MUV-10(Mn) without light irradiation – 24 hours | 0 |
| UiO-66 with light irradiation – 24 hours | 25.97 |
| UiO-66 without light irradiation – 24 hours | 20.33 |
| TiO ₂ with light irradiation – 24 hours | 9.34 |

Interestingly, UiO-66 also produced formic acid whilst operating in the dark, as well as under the lamp, showing that light is not necessary to activate the process with this MOF, whilst the other MOFs all required the lamp for activity to be observed. To the best of knowledge, this has not been reported in the previously, and so could be investigated further in the future. Interestingly, when TiO₂ was used, the yield of formic acid recorded when light irradiation was present was less than half of the yields reported with MUV-10 and UiO-66, showing that MOFs could exhibit superiority in terms of CO₂ conversion to formic acid, most likely due to the higher surface area of the MOFs.

An example of a labelled NMR spectrum is shown in Figure 5.4, which was taken from the solution after a sample of MUV-10(Ca) had been stirred in H₂O/TEOA for 24 hours. Of key importance is the identification of the formic acid (~8.4 ppm), and 1,4-dioxane internal standard (~3.8 ppm), so that quantification via NMR integration is possible. Other possible reduction products also include methanol.

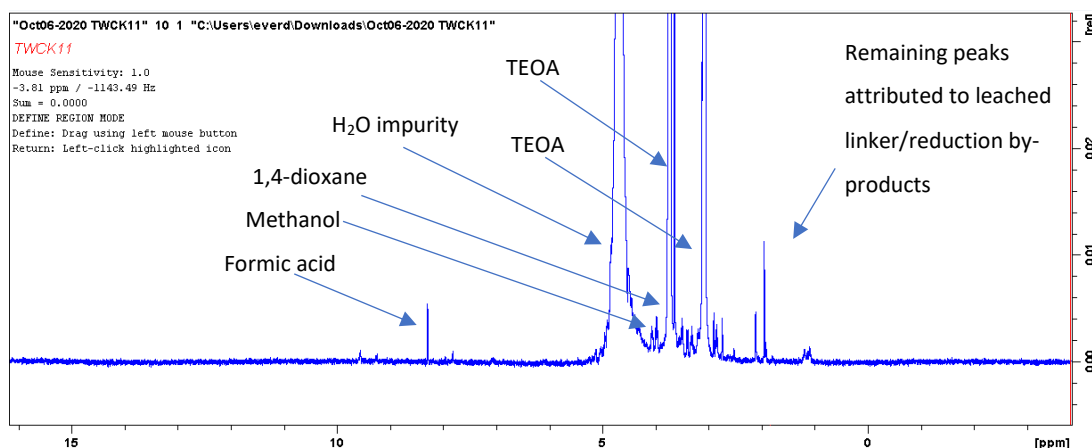


Figure 5.4: An example of an NMR spectrum from a solar simulator experiment, with key peaks labelled.

When XRD was completed on the samples recovered from the solar simulator experiments it was apparent that MUV-10 had collapsed during the CO₂ photoreduction (Figure 5.5), where the product in the XRD was then identified as MnCO₃. It was also found that for the equivalent MUV-10(Ca) experiments, CaCO₃ was produced.

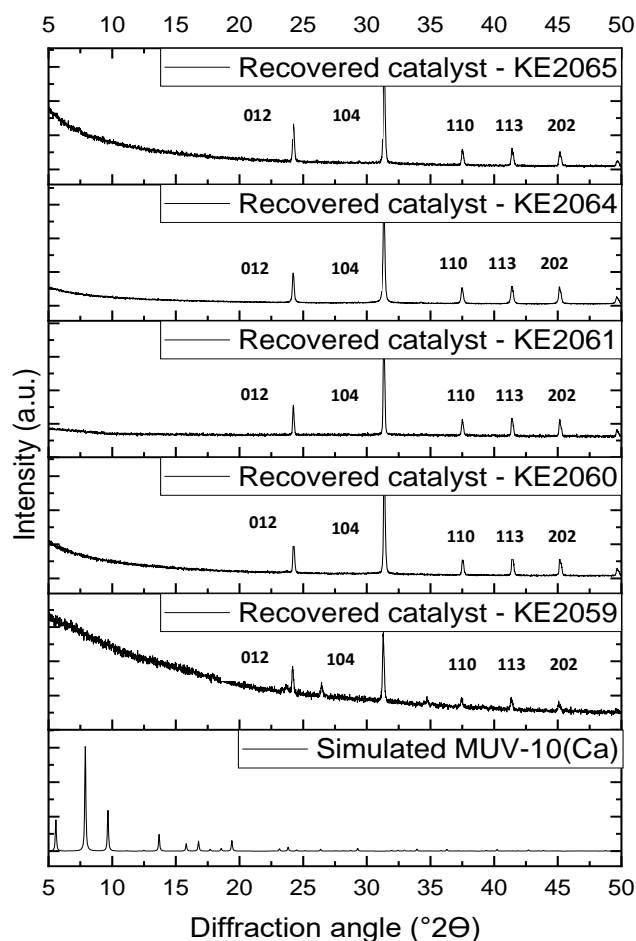


Figure 5.5: Powder XRD patterns showing the simulated MUV-10 pattern with the patterns of the recovered catalysts from various solar simulator experiments. Catalysts had not been activated prior to use. Sample KE2065 was a standard sample of MUV-10(Mn) stirring in 25 mL H₂O with 5 mL TEOA under light irradiation with a CO₂ flow rate of 5 mL/min for 24 hours. KE2064 is an identical experiment, with the time reduced to 4 hours. Sample KE2060 is a reference experiment, under the conditions employed for KE2064, but with no light as a reference. Sample KE2061 is MUV-10(Mn) modified with 50%AIP/50% BTC, whilst KE2059 is MUV-10(Mn) containing 20% Sn, both under identical conditions to KE2065.

On the powder XRD patterns shown in Figure 5.5, sample KE2065 was the standard sample of MUV-10(Mn) stirring in 25 mL H₂O with 5 mL TEOA under light irradiation with a CO₂ flow rate of 5 mL/min for 24 hours. KE2064 is an identical experiment, only with the time reduced to 4 hours, however this demonstrates that MUV-10 is unstable under these conditions even in a reduced time. Sample KE2060 is a reference experiment, where the conditions employed for KE2064 were used, but with no light as a reference. Again, this shows the material to be unstable, eliminating the light source as being the cause of the MOF collapse. Sample KE2061 is MUV-10(Mn) modified with 50%AIP/50% BTC, whilst KE2059 is MUV-10(Mn) containing 20% Sn. Both of these experiments were completed under identical conditions to

KE2065, however the samples still collapse, showing the substitution of AIP and Sn to not offer any additional stability to prevent the collapse of MUV-10 under the conditions of the photocatalytic reduction of CO₂ experiments.

ICP was completed on a sample of solution of MUV-10(Mn) after a 24 hour photocatalysis experiment (KE25), which confirmed the leaching of metals into solution, and therefore is consistent with the collapse of the MUV-10 materials (Table 5.2). Therefore, the formic acid that was produced using MUV-10, was likely due to catalysis by metal ions in solution, although this is difficult to confirm. Additionally, ICP on a sample after a 4 hour photocatalysis experiment (KE26) also showed metal ions leaching, suggesting it was not the length of time that the MOF was irradiated under the conditions stated that was the issue. Despite the fact that less of each element is leached at reduced time, it still verifies that MOF collapse had started.

Table 5.2: ICP results for a sample of MUV-10(Mn) after a 24 hour photocatalysis experiment (KE25) and a 4 hour photocatalysis experiment (KE26).

| Sample | Element | Amount (ppm) |
|-----------------|----------------|---------------------|
| KE25 – 24 hours | Mn | 149 |
| | Ti | 220 |
| | | |
| KE26 – 4 hours | Mn | 2 |
| | Ti | 161 |

Due to the initial reported stabilities of MUV-10(Ca) and MUV-10(Mn), it was expected that they would have been stable for the photocatalytic reduction experiments. The lamp used was unlikely to have caused degradation, unless it was due to the UV fraction, and so the most likely cause was the use of TEOA, despite it being widely used with MOFs previously in the literature.

The first step in identifying the cause of MOF collapse involved checking the reported stabilities of MUV-10 in acid, base and water (Figure 5.6). It was already reported in the literature that the structural integrity of MUV materials was maintained between 1-12 and 2-12 for MUV-10 Mn and Ca respectively, and so it was of interest to check the accuracy in order to determine whether the key issue was the basicity of the TEOA used.

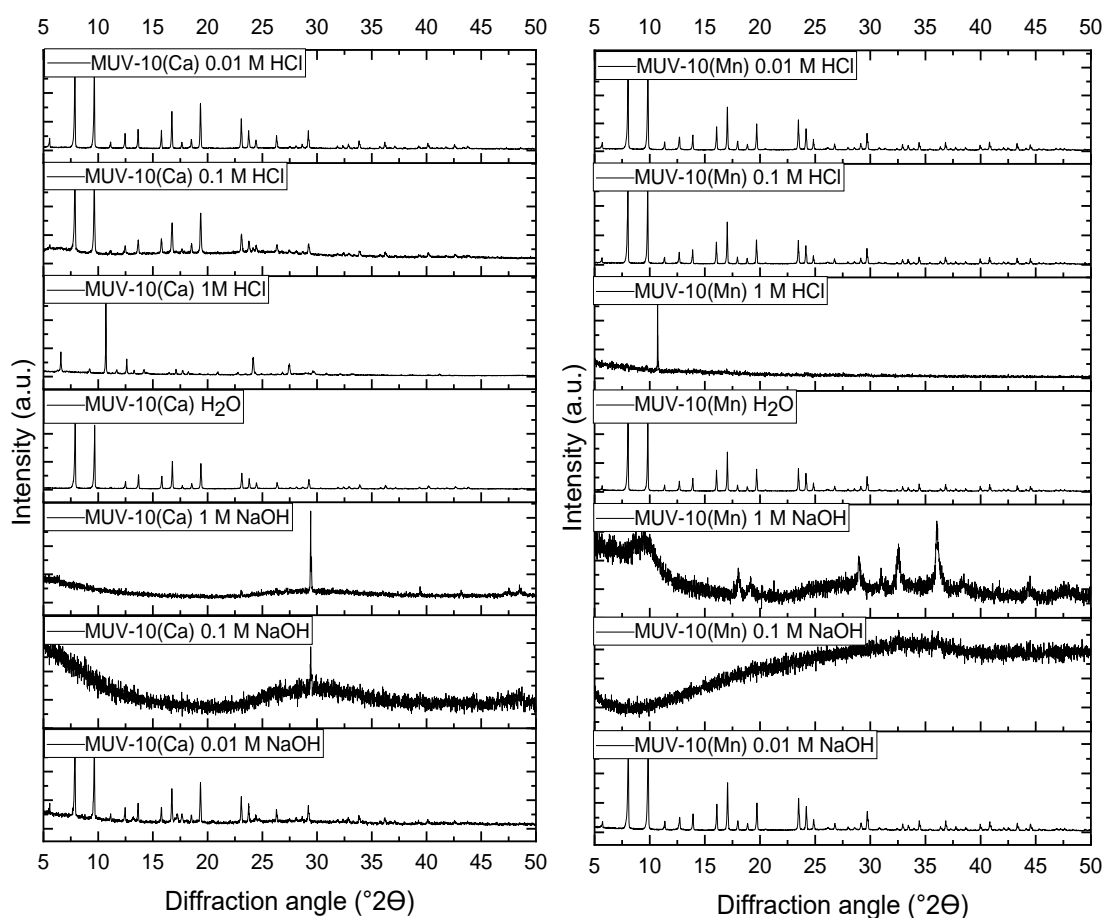


Figure 5.6: Powder XRD patterns obtained after 24 hour acid, base and water stability tests for MUV-10(Ca) (left-hand side) and MUV-10(Mn) (right-hand side).

From the stability tests, it can be observed that MUV-10 is unstable in more basic solutions. MnCO_3 and CaCO_3 are not produced after these tests, showing that the CO_2 flowing through in the photocatalysis experiments aids the formation of the carbonate products. The XRD patterns from the acid and water stability tests

resemble that of the original MUV-10 patterns, however 1 M and 0.1 M NaOH proved too basic and so broad XRD patterns were observed.

It was therefore suspected that it was the basicity of the TEOA that was causing the degradation. Stability tests in TEOA were then completed to check this theory. The original solar simulator experiments were completed in a solution of 25 mL H₂O with 5 mL TEOA. After completing a reference experiment (KE37) of MUV-10(Mn) stirring in H₂O with the same CO₂ flow rate without any TEOA, the catalyst was recoverable (Figure 5.7), and so it was deduced that neither the water, CO₂ or lamp were responsible for the degradation of MUV-10, and that it was due to the TEOA as suspected.

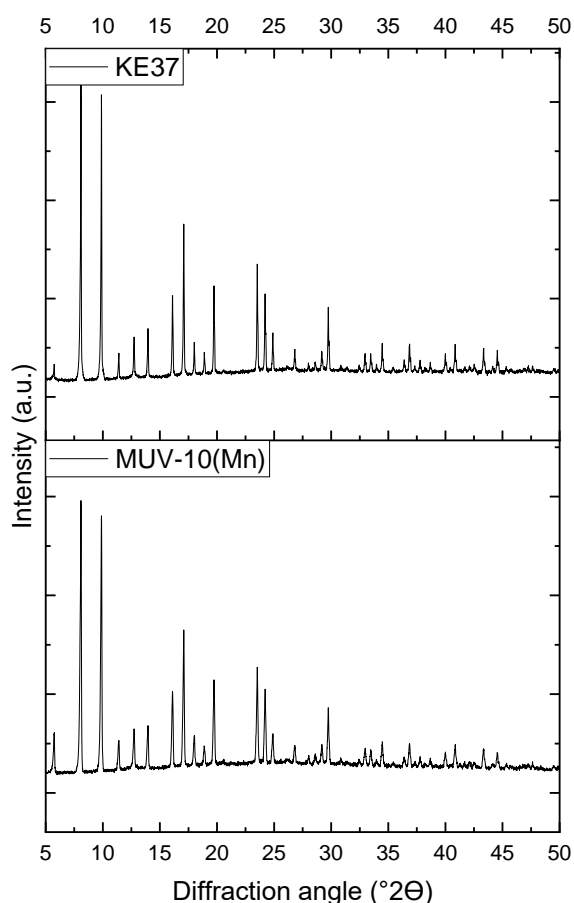


Figure 5.7: The powder XRD pattern after a reference experiment was completed using MUV-10(Mn) in H₂O, with CO₂ and with light irradiation for 24 hours (KE37), without any TEOA. The powder XRD pattern for MUV-10(Mn) is also shown for reference.

However, without the presence of TEOA, no formic acid was produced, where the peak attributed to formic acid around 8.4 ppm was not present, and only one large peak was observed on the NMR spectrum (Figure 5.8). This verified TEOA to be necessary for CO₂ reduction to take place.

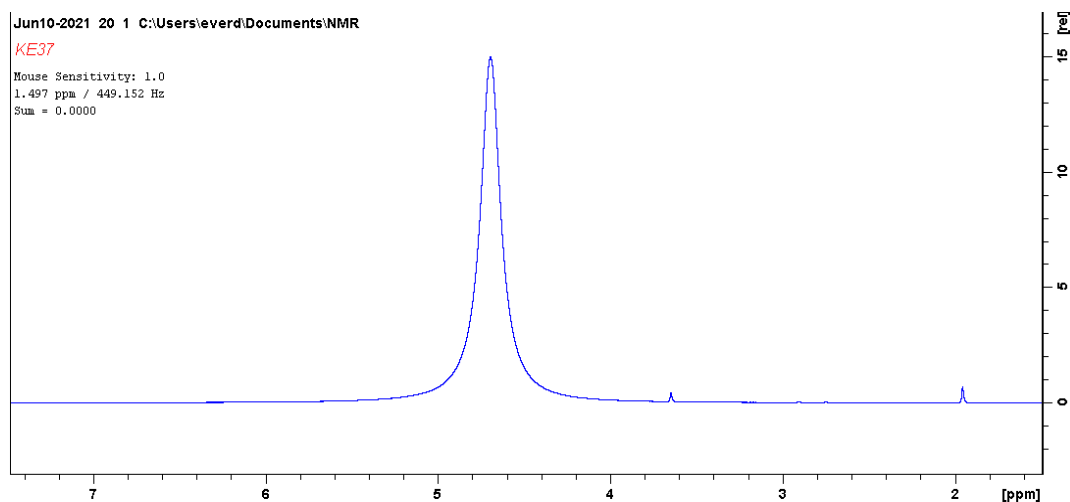


Figure 5.8: The NMR spectrum from sample KE37, a reference experiment without the use of TEOA, where subsequently no formic acid was generated.

It was then calculated that a 1% solution of TEOA/H₂O had pH ~10 which was within the range that MUV-10 was stable. It was calculated that using 25 mL H₂O with 5 mL TEOA was roughly a ~17% solution. Therefore, the ratio was then altered to see if making it less basic maintained the MUV-10 structure during the photocatalytic experiments.

MUV-10(Mn) was then stirred in three different concentrations of TEOA for 24 hours (Figure 5.9). In solutions containing 1 mL TEOA/25 mL H₂O (4% solution), 1 mL TEOA/50 mL H₂O (2% solution), and 1 mL TEOA and 100 mL H₂O (1% solution), MUV-10(Mn) had collapsed. It was expected due to its tested stability that it should have survived in the 1% solution, however, still did not.

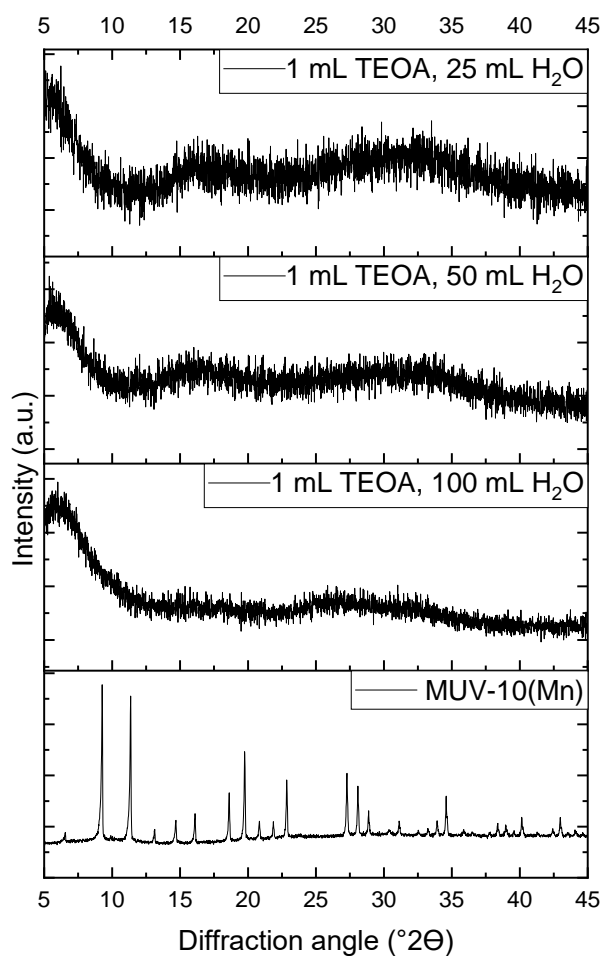


Figure 5.9: Powder XRD patterns after stability tests were completed on MUV-10(Mn) in different mixtures of TEOA and H₂O.

In addition, had MUV-10 survived in the 1% solution of TEOA as it was expected to based on its stability range, the amount of TEOA proved too little to act as an effective sacrificial electron donor and generate any conversion. Table 5.3 is shown below summarising the key findings relating the amount of TEOA to the formation of formic acid and the MOF stability.

Table 5.3: A table summarising the key findings relating the amount of TEOA, the formation of formic acid and MOF stability.

| Sample | Formic acid formation (as determined from NMR) | Stability of MOF (as verified by XRD) |
|--|---|--|
| MUV-10(Mn) in 25 mL H ₂ O, 5 mL TEOA (20%) | Formic acid produced | MOF collapses |
| MUV-10(Mn) in 25 mL H ₂ O, 1 mL TEOA (4%) | Formic acid produced | MOF collapses |
| MUV-10(Mn) in 30 mL H ₂ O, 1 mL TEOA (3.33%) | Formic acid produced | MOF collapses |
| MUV-10(Mn) in 50 mL H ₂ O, 1 mL TEOA (2%) | Formic acid produced | MOF collapses |
| MUV-10(Mn) in 50 mL H ₂ O, 0.5 mL TEOA (1%) | No formic acid produced | MOF recoverable |

Overall, it is concluded that TEOA is unfavourable when used with MUV-10(Mn) and MUV-10(Ca), resulting in collapse to MnCO₃ and CaCO₃, respectively. Some further attempts were made to utilise MUV-10 and its modified versions, by investigating the use of alternative sacrificial electron donors to eliminate MOF collapse from use of TEOA. One paper previously reported some alternatives, and so one option, ascorbic acid, was selected and tested.³

MUV-10(Mn) was again tested in identical conditions as before, only using ascorbic acid and water instead of TEOA and water (sample labelled KE51). However, no formic acid was observed from the NMR, where the one large peak is attributed to H₂O and 1,4-dioxane (Figure 5.10).

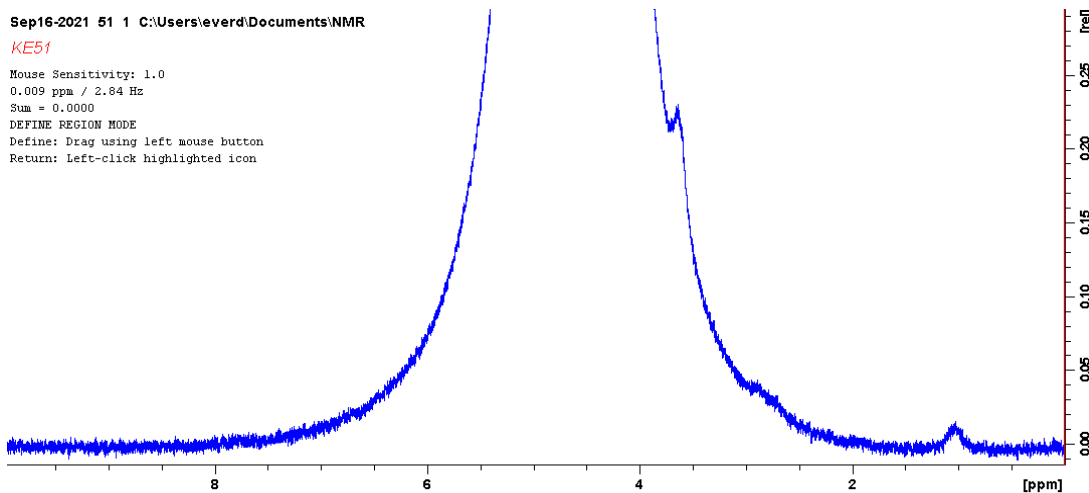


Figure 5.10: The NMR spectrum from sample KE51, which used ascorbic acid as an alternative to TEOA.

Future work could involve the investigation of other sacrificial electron donors and/or different solvent systems than those investigated in this project. One option could be to use 4-(2,3-dihydro-1,3-dimethyl-1H-benzimidazol-2-yl)-*N,N*-dimethylbenzenamine (BIH). Alternatively, different amounts of ascorbic acid could also be tried in this work, as only a few experiments were tried. Had these initial experiments worked, NH₂-UiO-66 and NH₂-MIL-125 would have been used as reference materials, and so could therefore be used in the future to compare to MUV-10 once a different sacrificial electron donor has been selected. One consideration that needs to be accounted for is the cost of the sacrificial electron donor, and therefore whether this is an economically advantageous route for CO₂ conversion, or whether efforts are better placed in other technologies.

5.3 MOFs for the Conversion of Glucose to 5-HMF

Another conversion explored with the MUV-10 materials was of glucose to 5-hydroxymethylfurfural (5-HMF). In Chapter 2, Section 2.5.3 discussed the experimental set-up for the glucose conversion experiments, where HPLC was used to analyse the reaction products.

The scheme below shows a general two step conversion from glucose to 5-HMF via fructose (Figure 5.11).

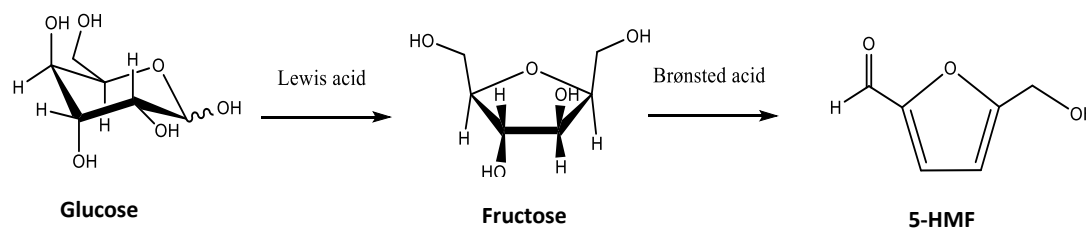


Figure 5.11: A scheme showing the conversion of glucose to 5-HMF via fructose, where the first step requires a Lewis acid and the second step requires a Brønsted acid.

In addition to fructose, mannose is another possible isomer of glucose, whilst 5-HMF can also convert to levulinic acid if water is added, or can convert to furfural via the loss of formaldehyde (Figure 5.12).⁴ Often with the conversion of glucose to 5-HMF, some other unwanted by-products are also produced, such as oligomers, which are known as humins.

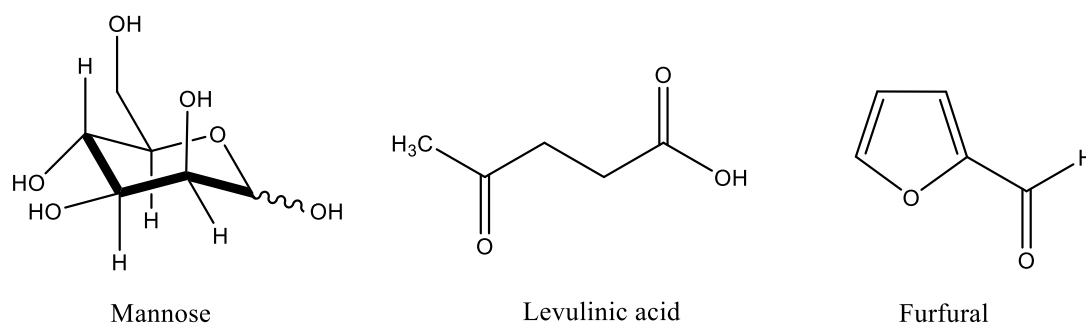


Figure 5.12: The structure of mannose, levulinic acid and furfural, which are all other possible products from the conversion of glucose to 5-HMF.

Firstly, the MUV-10(Ca) materials containing varying amounts of Sn were examined, initially without adding any additional acid. Figure 5.13 shows the results, where in the absence of HCl, the glucose conversions and 5-HMF yield are higher than the control experiment (*i.e.* in the absence of any catalyst), but increasing the % of Sn in MUV-10(Ca) does not have much impact on glucose conversion and 5-HMF yield.

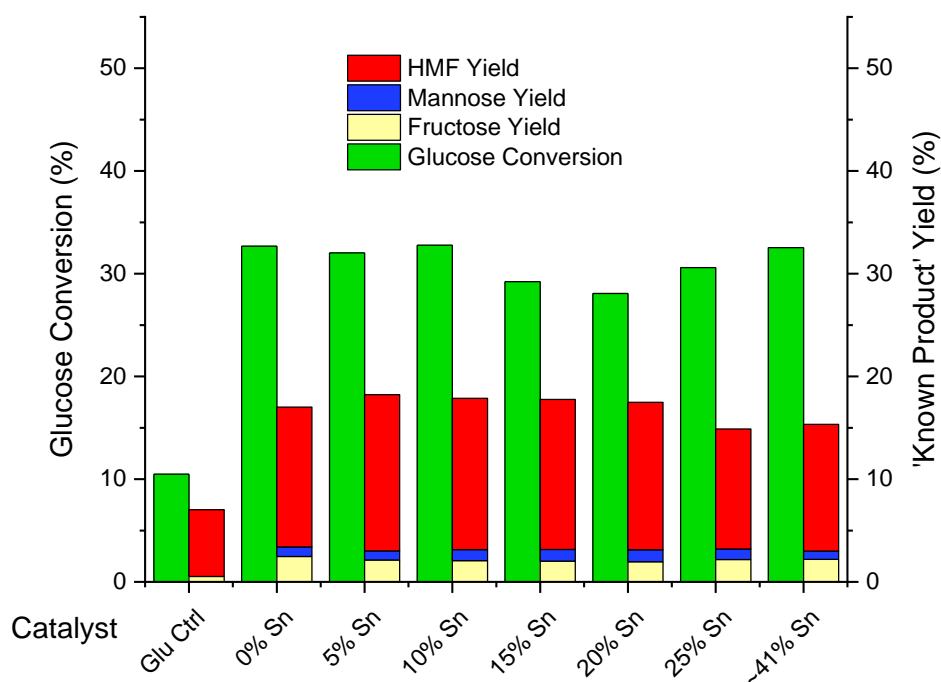


Figure 5.13: A graph showing the comparison of a glucose control experiment and MUV-10(Ca) containing varying amounts of Sn(IV) substituted for Ti(IV). Glucose selectivity and product yields are shown. Catalysts were not activated prior to use.

The same was also observed for the MUV-10(Mn) samples when there was an absence of HCl, in that increasing the % of Sn present did not increase glucose conversions and 5-HMF yield (Figure 5.14).

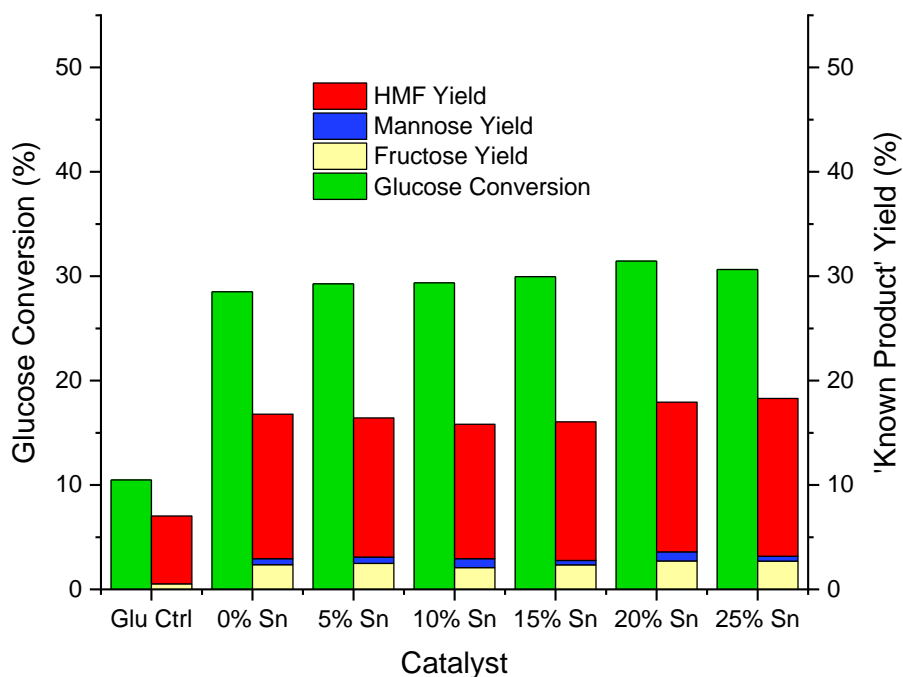


Figure 5.14: A graph showing the comparison of a glucose control experiment and MUV-10(Mn) containing varying amounts of Sn(IV) substituted for Ti(IV). Glucose selectivity and product yields are shown. Catalysts were not activated prior to use.

0.1 M HCl was then used in the experiments, however this was too concentrated and yielded high glucose conversions, with very little 5-HMF, mannose, or fructose obtained. This suggests that the main products were unwanted side products such as humins. Figure 5.15 shows results from some of the MUV-10 samples alongside UiO-66 for comparison. This pH also proved too low when used with UiO-66, which is the benchmark reference MOF for this conversion.⁵

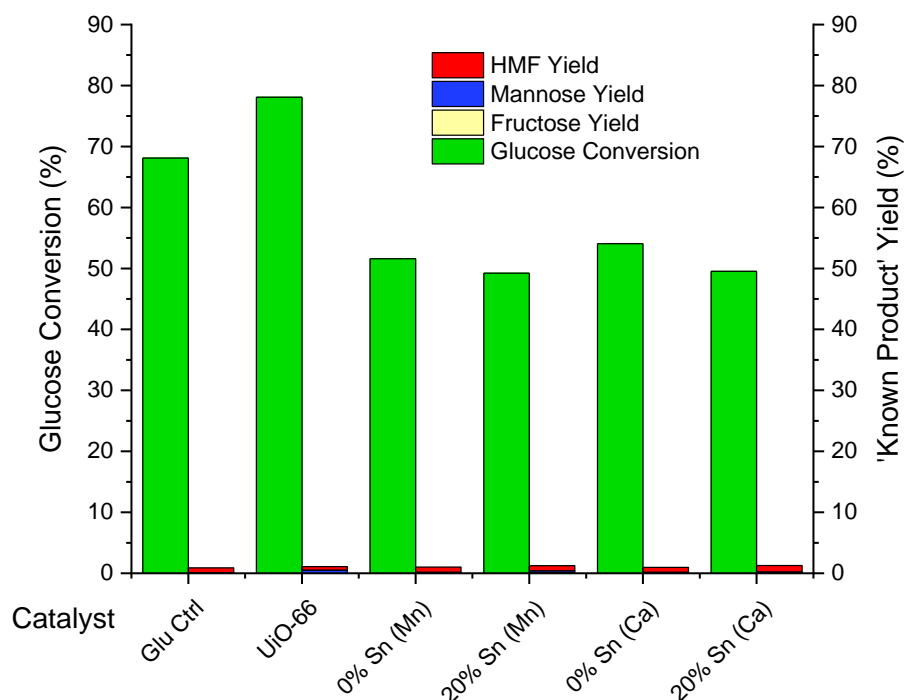


Figure 5.15: A graph comparing a glucose control, UiO-66 reference, and both MUV-10(Mn) and MUV-10(Ca) with and without Sn, when 0.1 M HCl were used for the glucose conversion experiment. Catalysts were not activated prior to use.

Increased pH of acid was then explored. When 0.01 M HCl were used, the MUV-10 materials produced more 5-HMF than UiO-66 and were also more selective for the formation of 5-HMF as opposed to mannose (Figure 5.16). These results obtained also suggest that UiO-66 could have produced more humins than the MUV-10 materials. The MUV-10 materials containing 20% Sn also show a slight increase in glucose conversion and 5-HMF yield compared to the MUV-10 materials without containing any Sn. However, the results from using no acid (shown in Figure 5.13 and Figure 5.14), showed greater glucose conversion and HMF yield for the MUV-10 materials compared to when 0.01 M acid was added. This concludes that adding acid does not improve the performance of MUV-10.

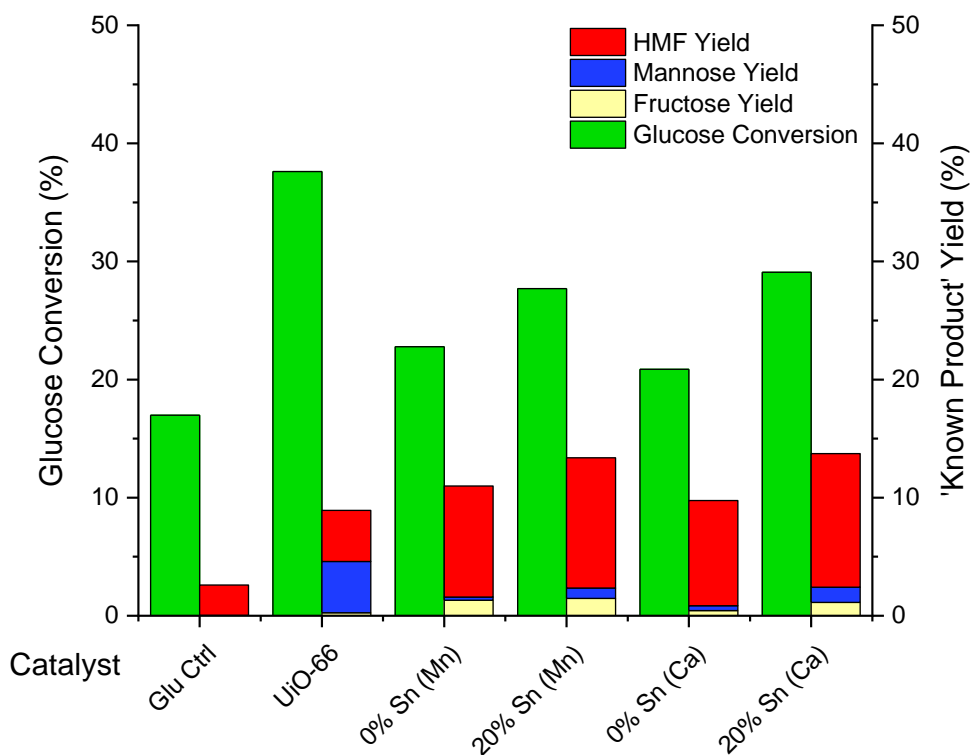


Figure 5.16: A graph comparing a glucose control, UiO-66 reference, and both MUV-10(Mn) and MUV-10(Ca) with and without Sn, when 0.01 M HCl were used for the glucose conversion experiment. Catalysts were not activated prior to use.

When 0.001 M HCl were used, the glucose conversion was greater for the MUV-10 materials than the UiO-66 benchmark (Figure 5.17). The 5-HMF yields are also comparable, if slightly increased for some samples, besides the MUV-10(Mn) with 0% Sn.

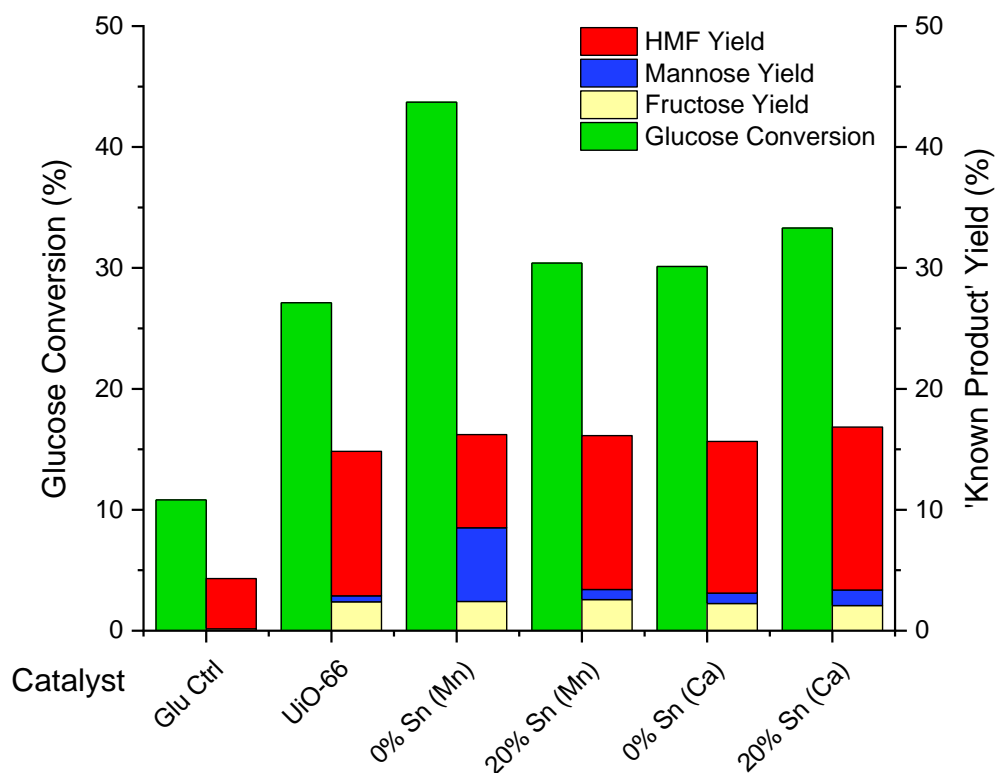


Figure 5.17: A graph comparing a glucose control, UiO-66 reference, and both MUV-10(Mn) and MUV-10(Ca) with and without Sn, when 0.001 M HCl were used for the glucose conversion experiment. Catalysts were not activated prior to use.

When the pH was increased further, and 0.0001 M HCl were used, the glucose conversion for the MUV-10 materials and the modified versions containing Sn were lower than that of UiO-66, however had comparable 5-HMF yields and produced less mannose and fructose as alternative products (Figure 5.18). The addition of Sn into the MUV-10 samples did not have significant impact on the yield of 5-HMF, compared to MUV-10 without Sn. Overall, it is also observed that the addition of acid to the experiments did not offer much benefit.

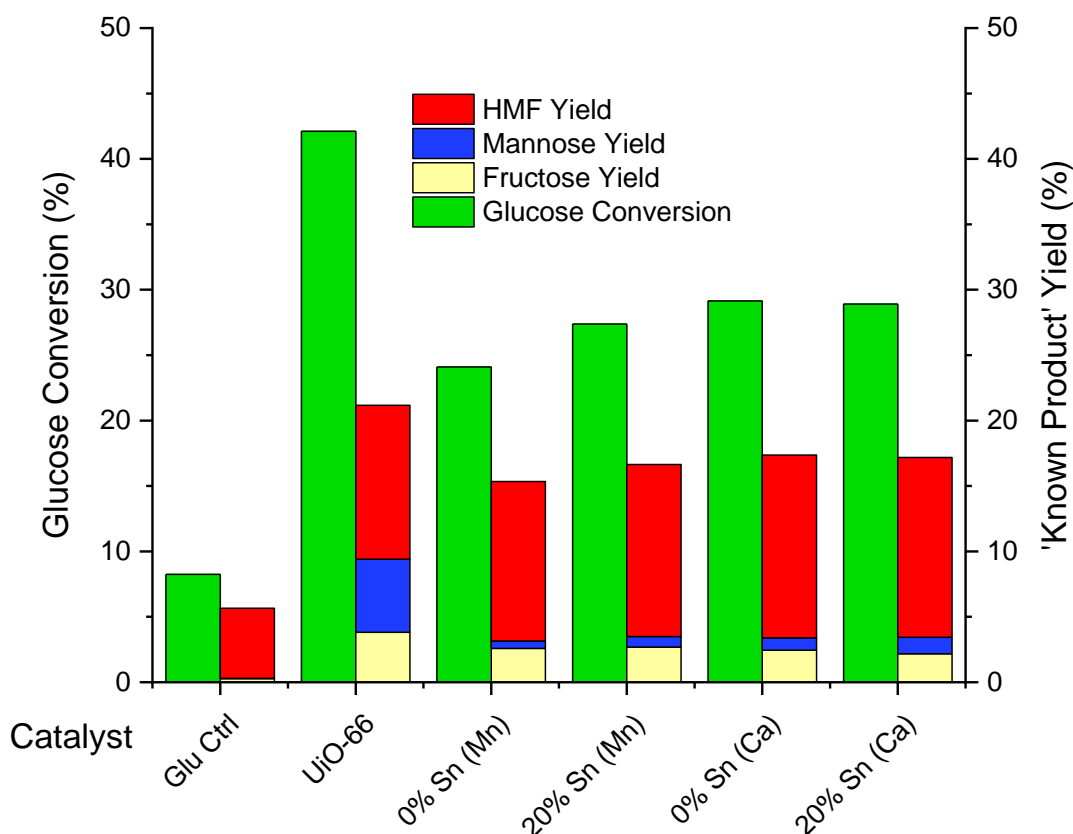


Figure 5.18: A graph comparing a glucose control, UiO-66 reference, and both MUV-10(Mn) and MUV-10(Ca) with and without Sn, when 0.0001 M HCl were used for the glucose conversion experiment. Catalysts were not activated prior to use.

Overall, these results show that the MUV-10 materials are superior catalysts compared to UiO-66 for glucose conversion in 0.01 M HCl, where they are more selective to the desired formation of 5-HMF. However, increasing the pH of HCl further did not improve the conversion and selectivity compared to UiO-66. Overall, the addition of acid did not improve conversion and selectivity for the MUV-10 materials.

Final tests involved examining the extraction of 5-HMF into a non-aqueous solvent where methyl isobutyl ketone (MIBK) was used to try to improve the yields of 5-HMF obtained. The results for MUV-10(Mn) show that generally having the Sn in the structure improves the glucose conversion and yields of 5-HMF extracted into each layer, with the exception of the 20% Sn sample (Figure 5.19).

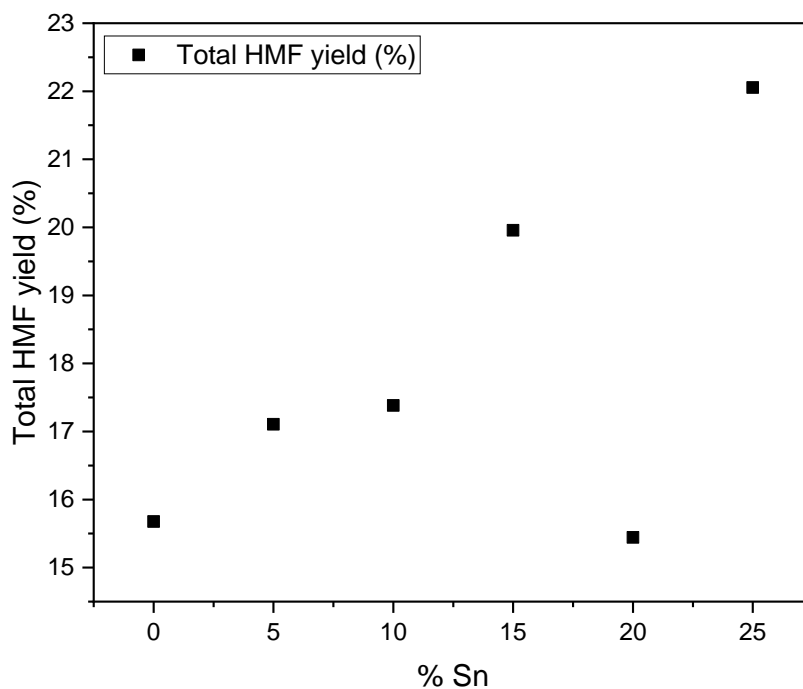
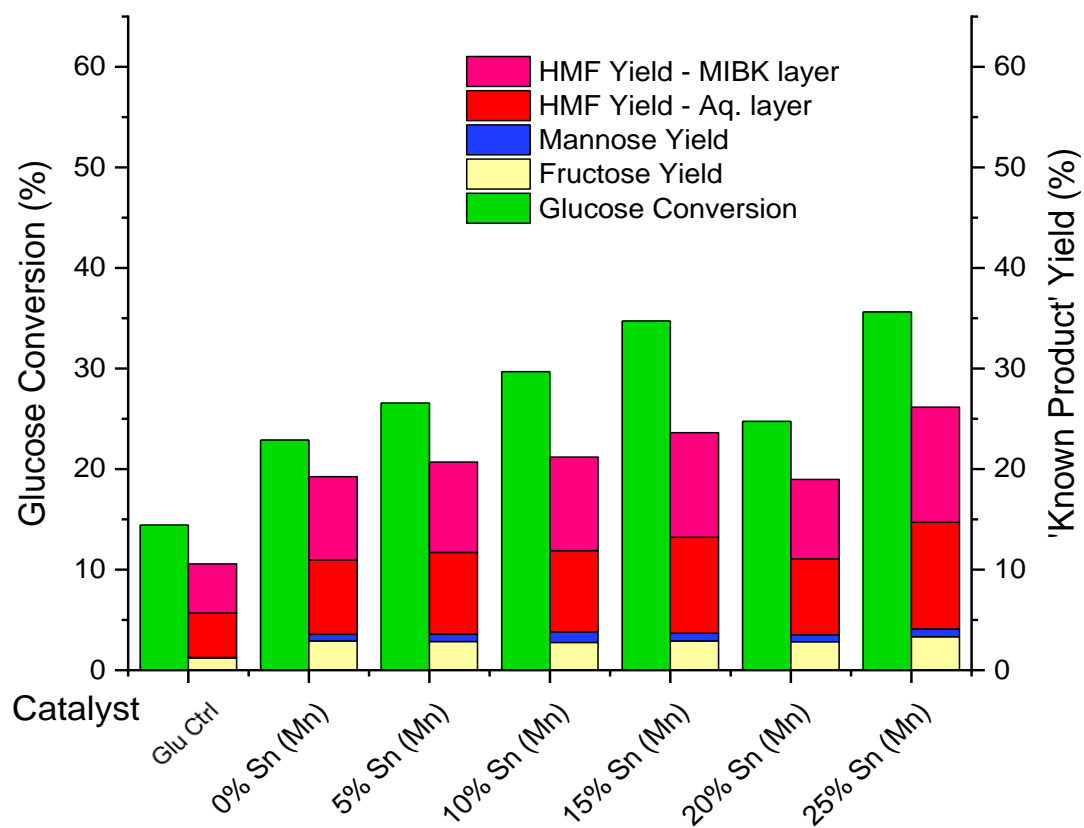


Figure 5.19: Top - A graph comparing conversion and products of a glucose control and varying Sn-containing samples of MUV-10(Mn). Catalysts were not activated prior to use. Bottom: A plot showing % Sn used in MUV-10 with total yield of HMF (%) obtained.

This same extraction method was tried with MUV-10(Ca), with slight improvements generally observed in terms of the glucose conversion and yields of 5-HMF, showing the MUV-10(Ca) and its Sn-incorporated versions to be superior to the Mn equivalents (Figure 5.20).

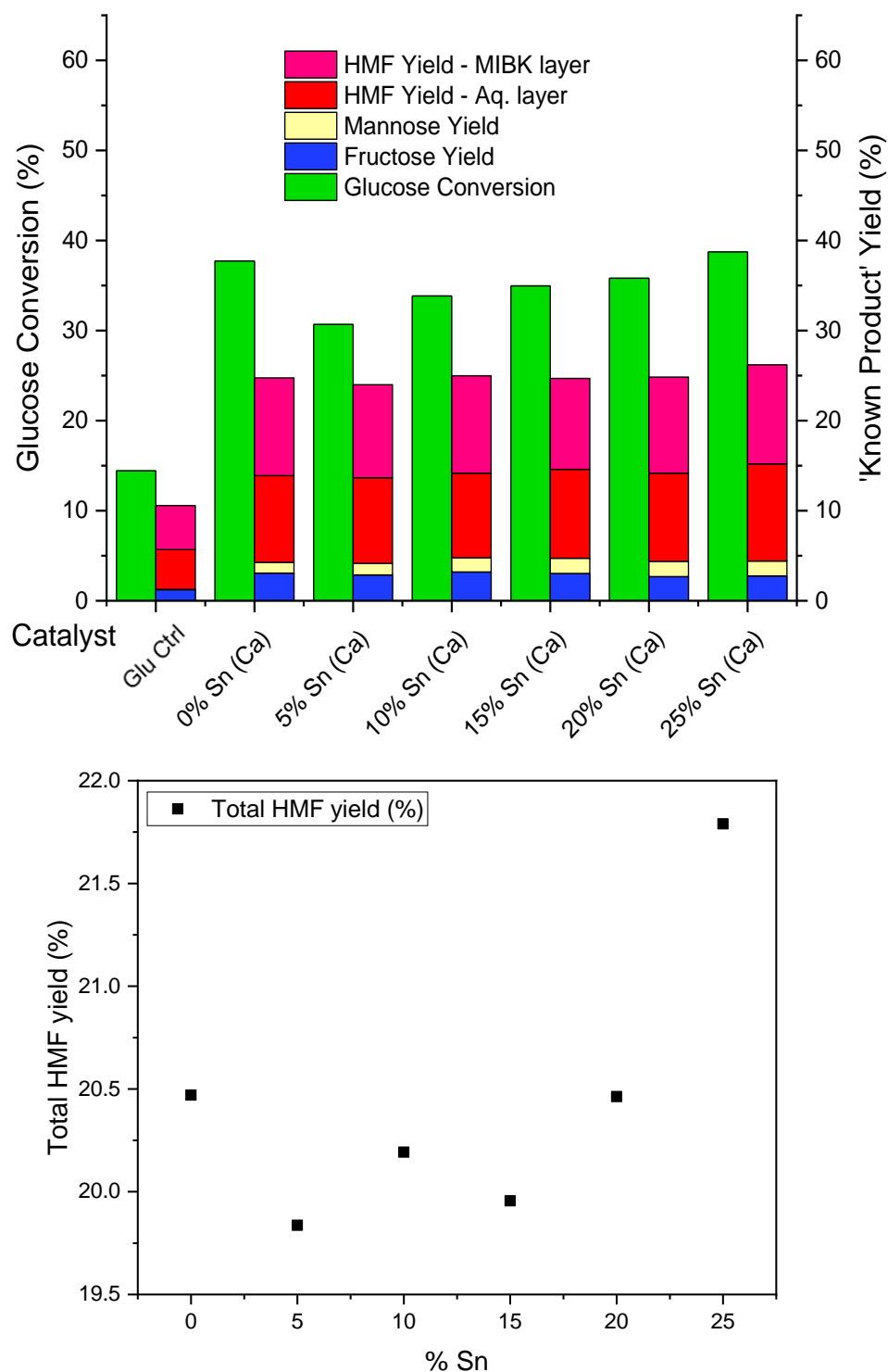


Figure 5.20: Top - A graph comparing conversion and products of a glucose control and varying Sn-containing samples of MUV-10(Ca). Catalysts were not activated prior to use. Bottom: A plot showing % Sn used in MUV-10 with total yield of HMF (%) obtained.

Catalyst stability was also checked, and MUV-10(Mn), MUV-10(Ca) and MUV-10 with Sn substituted, were all shown to withstand 24 hours at 140°C during the catalysis, as shown by the powder XRD patterns which show the maintenance of the structure (Figure 5.21). There is a slight change in the relative peak intensity, which indicates that some products may remain trapped in the pores of the MOF after catalysis.

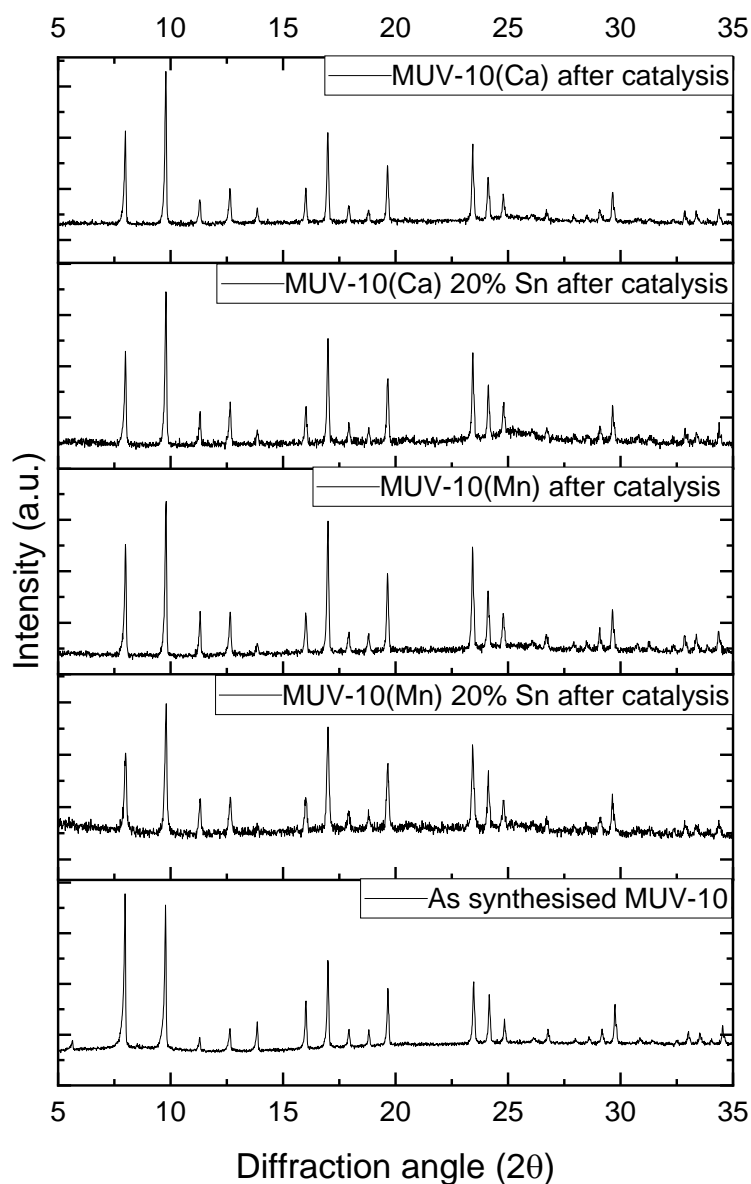


Figure 5.21: Powder XRD patterns from samples after 24 hour glucose conversion experiments completed at 140°C.

Overall, the MUV-10 samples showed comparable activity to the current benchmark MOF, UiO-66. However, MUV-10 showed greater production of 5-HMF than the UiO-66 benchmark material, where performance was enhanced with samples with increased substitution of Sn, compared to MUV-10 without Sn, for samples in 0.01 M HCl. However, MUV-10 with Sn did also produce more by-products compared to MUV-10 without Sn, although all MUV-10 materials yielded fewer by-products compared to UiO-66. An advantage of using these MUV-10 materials is that the structure is highly tuneable, and further attempts to modify the MOF to enhance activity even further could be made. In comparison to other reference materials, such as Sn-beta zeolite, the MUV-10 materials exhibit higher glucose conversions and are often easier and safer to synthesise.⁴ In addition, the MUV-10 materials proved superior for the conversion of glucose to 5-HMF compared to many other MOFs besides UiO-66 that was used as a control in these experiments. Table 1.3 in the Introduction listed other MOFs and their conditions for converting glucose. In comparison the MUV-10 materials also exhibit greater yields of HMF compared to MOFs such as MIL-88B and MIL-101, including modified versions.

5.4 MOFs for the Conversion of CO₂ to Cyclic Carbonates using Epoxides

A final application that was investigated was the use of MUV-10 and its modified versions for the conversion of epoxides and CO₂ to cyclic carbonates. In Chapter 2, Section 2.5.2, the experimental procedure was shown and discussed. The set-up was relatively simple and involved adding dry ice pellets to a flask containing the epoxide starting material, MOF, and co-catalyst, with balloon attached to the top. The flask was then sealed and either stirred at room temperature, or at elevated temperatures using an oil bath. The dry ice pellets were periodically added to ensure that the flask was saturated with CO₂. This procedure was based on one previously reported in the literature.⁶ An example of an experiment carried out at room temperature is shown in Figure 5.22. At elevated temperatures the procedure was the same, however, was with an oil bath underneath.

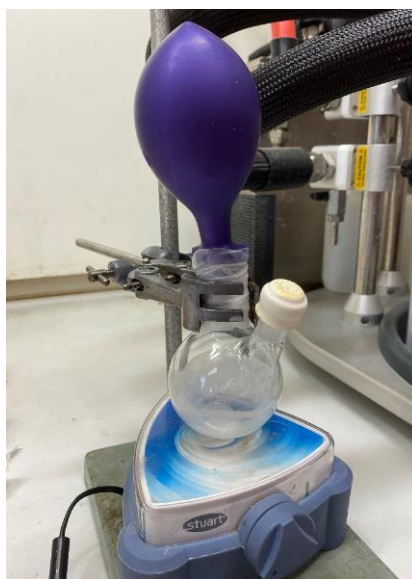


Figure 5.22: An example of the set-up of an epoxide conversion experiment carried out at room temperature.

Initial experiments were completed using propylene oxide as a starting material, however, this proved to readily evaporate due to its relatively low boiling point (34°C), leaving little product, which was subsequently unable to be quantified.

Epichlorohydrin was then examined as it had been widely used in the literature and has a much higher boiling point than propylene oxide.⁶ In addition, the presence of the activating chlorine group also proved beneficial for the conversion, so the remaining experiments were completed with this starting material. The two schemes using propylene oxide and epichlorohydrin are shown in Figure 5.23.

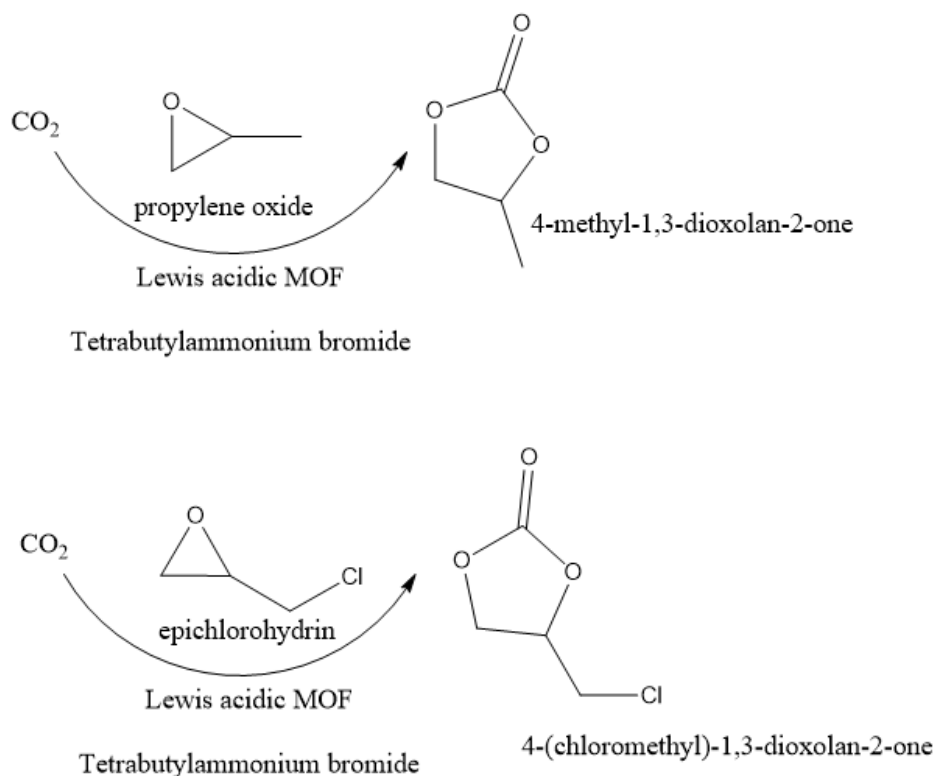


Figure 5.23: Schemes showing the conversion of propylene oxide (top) and epichlorohydrin (bottom) using CO₂, a Lewis acidic MOF and tetrabutylammonium bromide co-catalyst.

The first experiments proved that the co-catalyst, tetrabutylammonium bromide (TBAB), was necessary for the catalysis to take place (initially discussed in Chapter 1), since in the absence of TBAB, no product was formed.

Initial experiments looked at using varying quantities of MUV-10(Mn) at different temperatures (Figure 5.24). Conversion of epichlorohydrin to the cyclic carbonate product is seen to generally increase with temperature, although does not differ much between 60°C and 80°C. Selectivity also increases slightly going from the lower to the higher of the three different temperatures. Overall, it is observed that increasing the amount of MOF catalyst does not have a significant impact on the conversion and selectivity observed, but increasing the temperature generally gives an improvement on each.

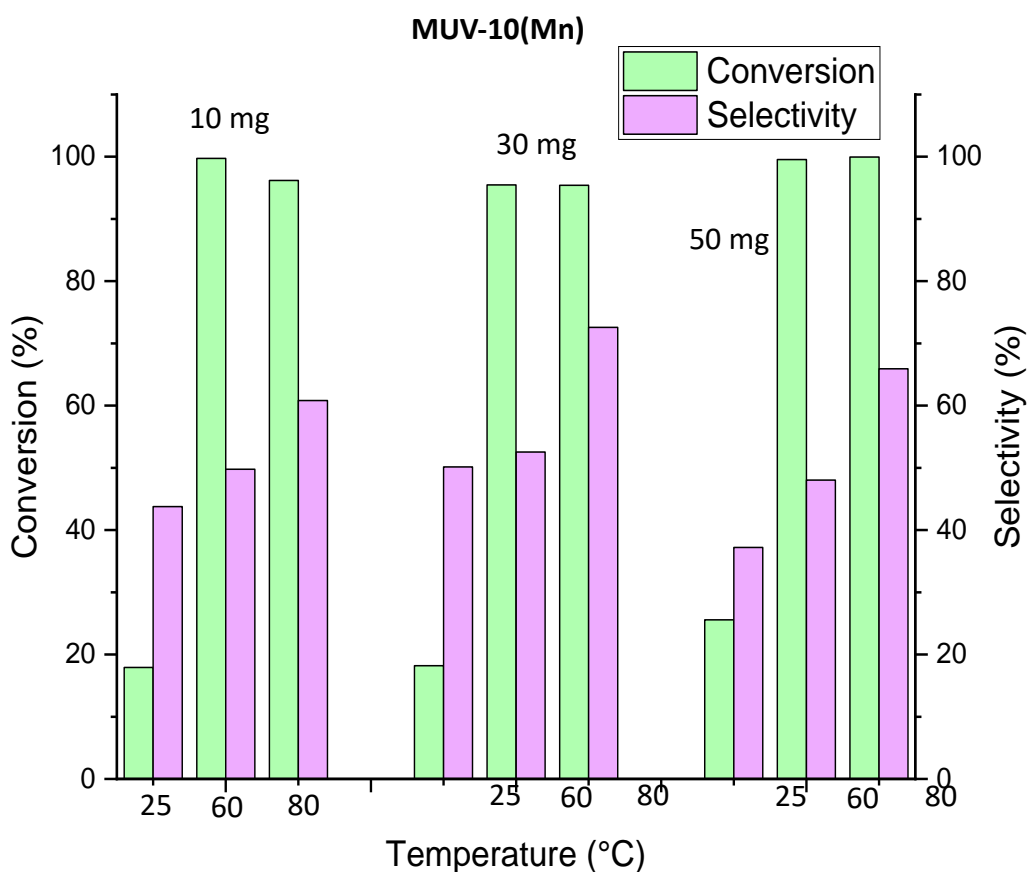


Figure 5.24: A graph comparing the conversion and selectivity of epichlorohydrin to the cyclic carbonate product using MUV-10(Mn) in varying quantities, at varying temperatures. MOF loading is stated above/next to bars. TBAB = 30 mg each time. Catalysts were not activated prior to use.

Next, MUV-10 was tested at 40°C at varying times (Figure 5.25), to try to identify a clearer difference between conversion and selectivity trends. This temperature was chosen to study an intermediate conversion in order to make a better comparison between different times of reaction. The results showed that conversion increased slightly with time, however the selectivity decreased, suggesting that the conversion at longer times is for other products besides the cyclic carbonate product. The data also suggest that the desired product is formed early in the reaction.

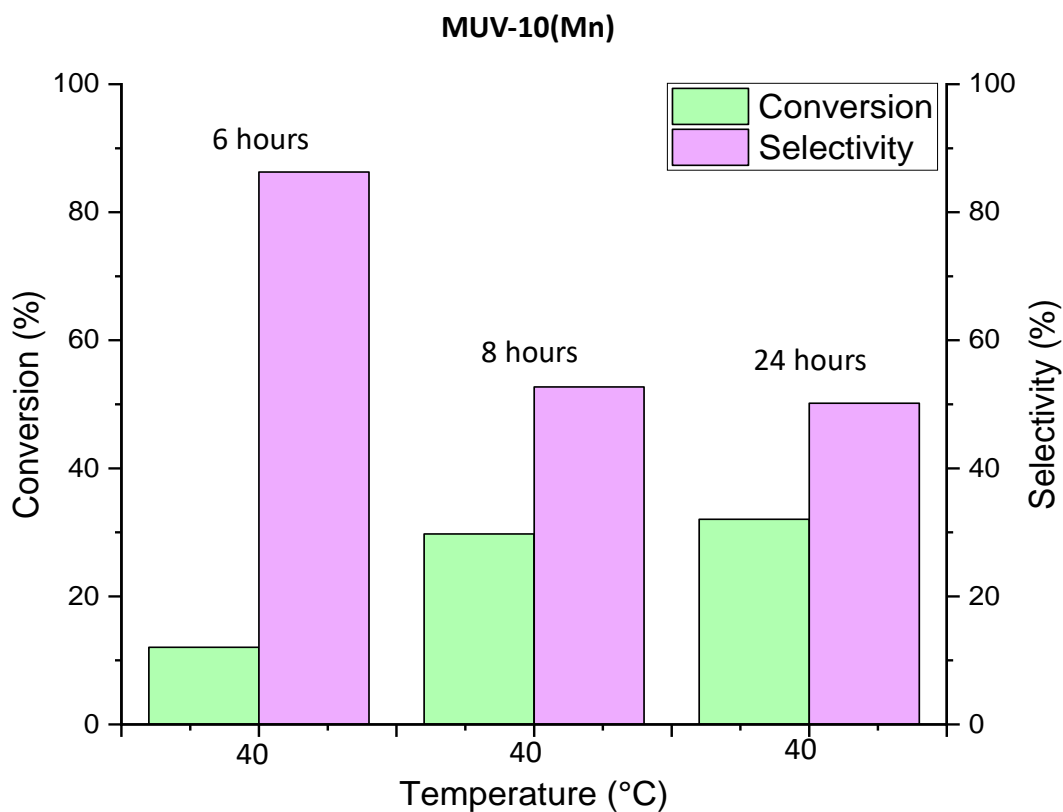


Figure 5.25: Results from the conversion of epichlorohydrin to the cyclic carbonate product using MUV-10(Mn), at 40°C at varying experimental times. Catalysts were not activated prior to use.

These same experiments were completed with MUV-10(Mn) containing 20% Sn in replacement to Ti, and again show the same trend that at 40°C, conversion increases with time, however, selectivity decreases (Figure 5.26). The difference from the addition of the Sn is that at 24 hours, the conversion is greater than the selectivity, which was not the case for the previous experiments.

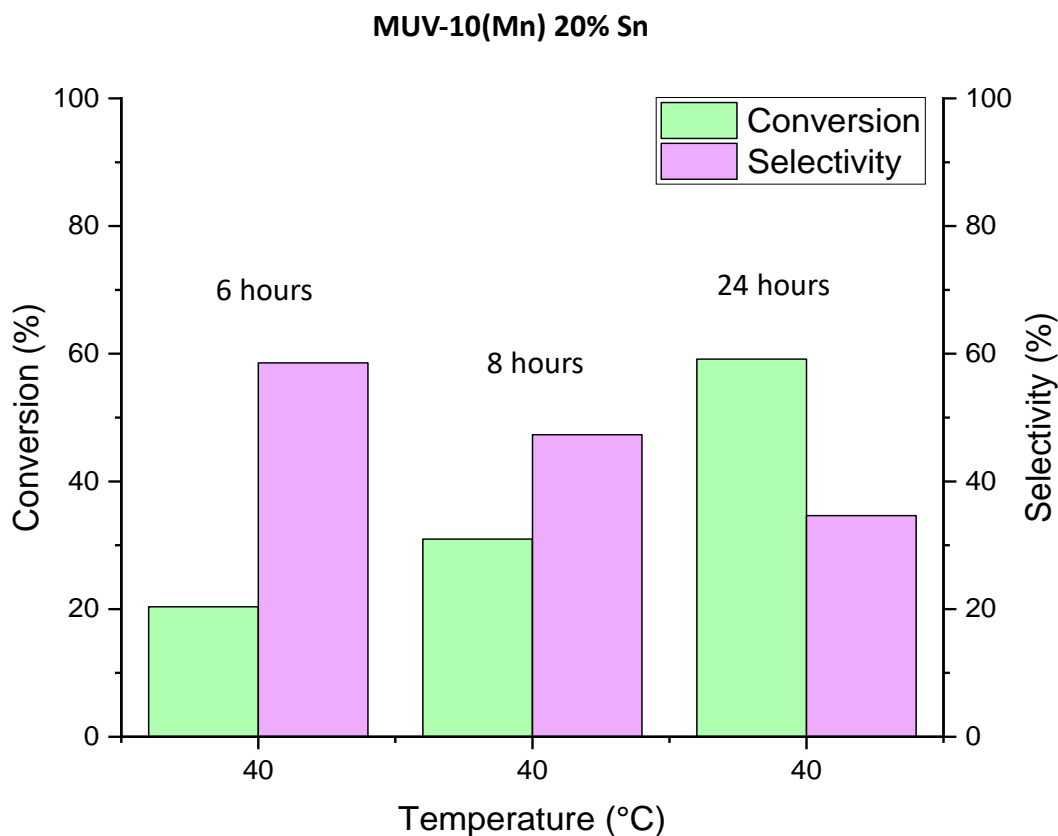


Figure 5.26: Results from the conversion of epichlorohydrin to the cyclic carbonate product using MUV-10(Mn) containing 20% Sn, at 40°C at varying experimental times. Catalysts were not activated prior to use.

MUV-10(Mn) with 20% Sn substituted was also investigated in terms of conversion and selectivity after different temperatures and different amounts of MOF catalyst were used (Figure 5.27). Conversion is shown to generally increase with temperature, although for the 10 mg and 50 mg experiments there is a slight decrease for the samples at 80°C, although this could be within the error of the experiment and analysis. Selectivity also generally increases with temperature, with the only exception being a slight decrease for the 10 mg and 30 mg samples when the experiments were held at 60°C.

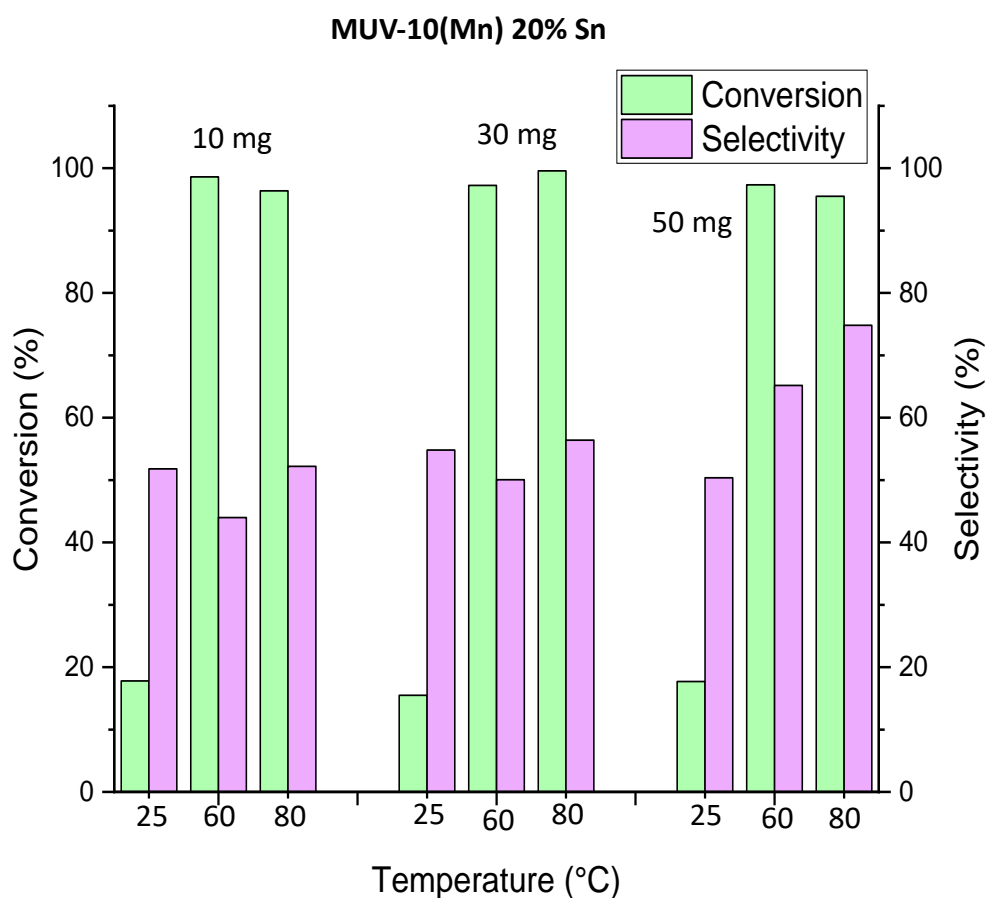


Figure 5.27: A graph comparing the conversion and selectivity of epichlorohydrin to the cyclic carbonate product using MUV-10(Mn) containing 20% Sn in varying quantities, at varying temperatures. Catalysts were not activated prior to use.

It can also be observed that when 50 mg of catalyst is used, selectivity is significantly improved for MUV-10(Mn) with 20% Sn, compared to MUV-10(Mn) without any Sn. Figure 5.28 directly compares MUV-10(Mn) without Sn to MUV-10(Mn) with 20% of Ti substituted for Sn. Excluding at 25°C, MUV-10(Mn) and MUV-10(Mn) with 20% Sn show similar high conversions of nearly 100%. However, of key importance is that the addition of the Sn into the structure appears to significantly improve the selectivity for the cyclic carbonate product, from around 65% to around 75% at 80°C, over other by-products.

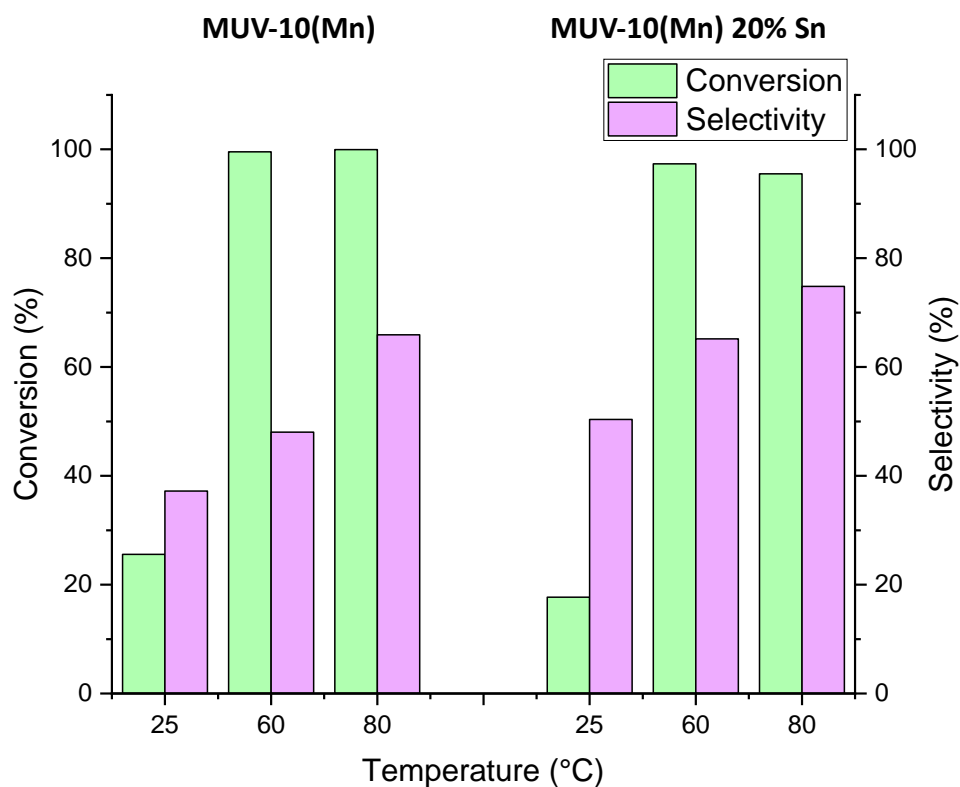


Figure 5.28: A graph showing the conversion and selectivity for conversion of epichlorohydrin to a cyclic carbonate product using MUV-10(Mn) compared to MUV-10(Mn) containing 20% Sn at different temperatures. Catalysts were not activated prior to use.

As an extra comparison, a Ce reference MOF material, Ce-BDC-NH₂, was synthesised following the paper from which the experimental set-up for this work was based (Figure 5.29).⁶ Although direct comparisons cannot be made to the MUV-10 materials since the number of active sites is not accurately known, some similar trends are still observed. Conversion, again, generally increased with temperature, and selectivity generally increased with temperature, with the only exception being for the 30 mg sample at 60°C, where there is a slight decrease.

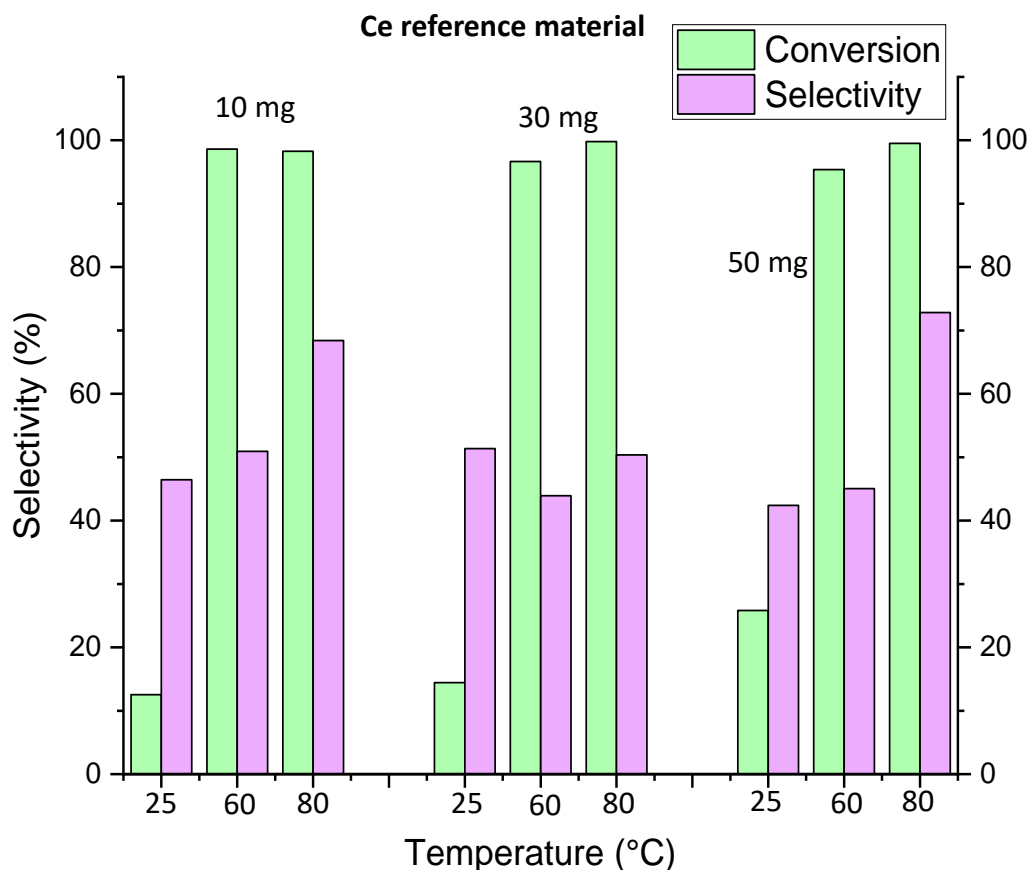


Figure 5.29: A graph comparing the conversion and selectivity of epichlorohydrin to the cyclic carbonate product using a Ce reference material in varying quantities, at varying temperatures. Catalysts were not activated prior to use.

Also of interest was whether or not activating the MOF catalysts by heat treatment had an effect on the catalysis results. Figure 5.30 shows the conversion and selectivity for MUV-10(Mn) and MUV-10(Mn) with 20% Sn, both with and without activation. Where activation was completed, a temperature of 150°C was used for 5 hours, in order to remove any water or methanol from the MOF pores. Subsequent catalysis was then using 50 mg catalyst at 60°C for 24 hours. MUV-10(Ca) and MUV-10(Ca) containing 20% Sn, were also investigated to see if there was any effect from using Ca instead of Mn in MUV-10. For most samples, activation had little effect on the conversion, generally only increasing it a very small amount. Additionally, the selectivity was not overly affected, where the only sample that activation seemed to significantly improve selectivity for was MUV-10(Ca) with 20% Sn. Compared to values reported in the literature (see Introduction Table 1.2), the MUV-10 materials

generally exhibit much higher conversions. For example, ZIF-8 not only required harsher experimental conditions (7 bar, 70-100°C), but also only yielded conversions ranging from 65.5-98.2%, with yields ranging from 33.4-63.4% and selectivity ranging from 32.8-43.7%.⁷

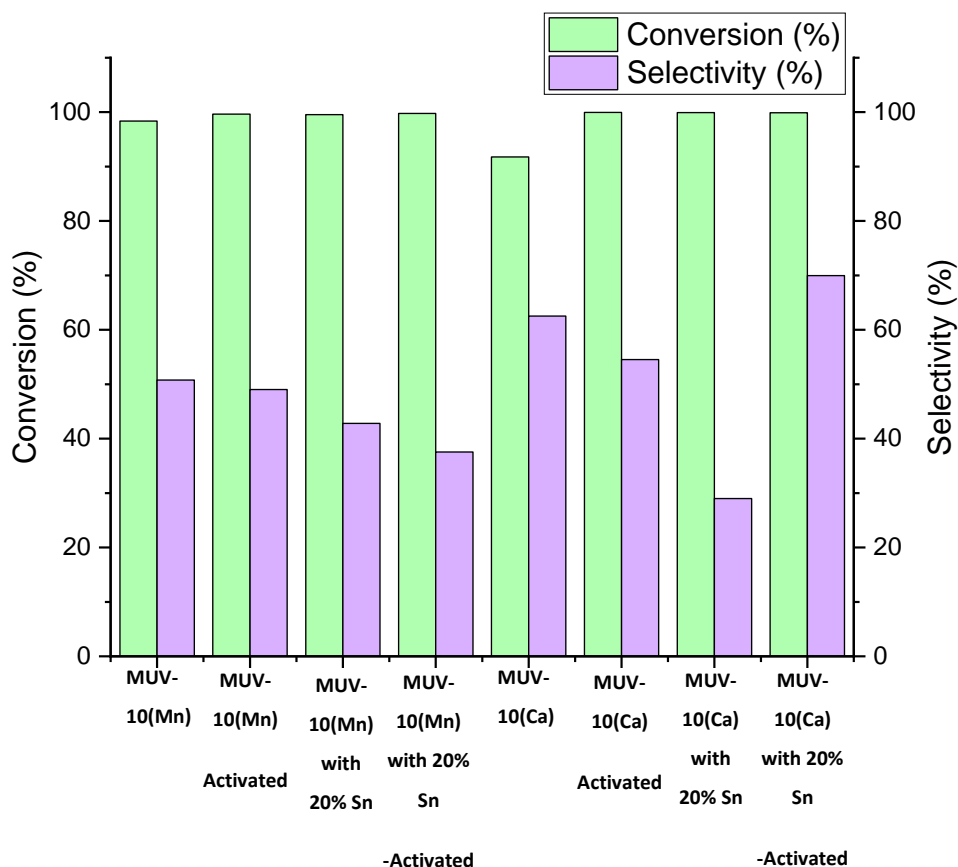


Figure 5.30: A graph showing the conversion and selectivity of epoxide to cyclic carbonate product for MUV-10(Mn), MUV-10(Mn) containing 20% Sn, MUV-10(Ca) and MUV-10(Ca) containing 20% Sn, all with and without activation prior to catalysis.

Powder XRD patterns were also obtained after catalysis, to check the MOFs were stable during the conversion. Figure 5.31 shows MUV-10(Mn) before and after catalysis, where the post-catalysis sample is labelled as KE561. The pattern matches that from before catalysis, however of key significance is the absence of the lowest angle peak after catalysis, which is indicative of blocking of the pores of the MOF.

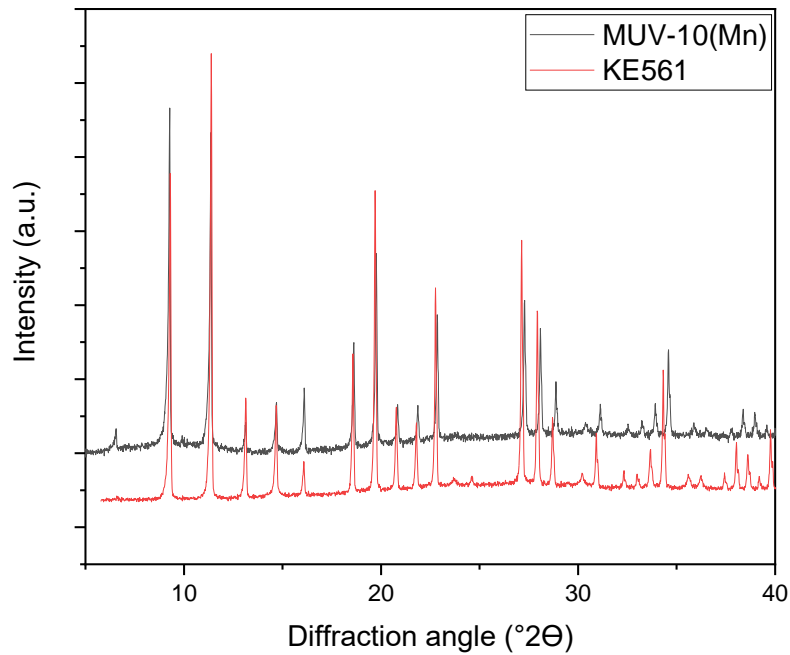


Figure 5.31: Overlaid powder XRD patterns of MUV-10(Mn) before and after (KE561) catalysis.

MUV-10(Mn) containing 20% Sn was also examined after catalysis (sample labelled KE110), and the same absence of the lowest angle peak was observed (Figure 5.32). If the pores of the MOFs contained products or unreacted starting material, this could also explain why the selectivity of the reaction was not 100%.

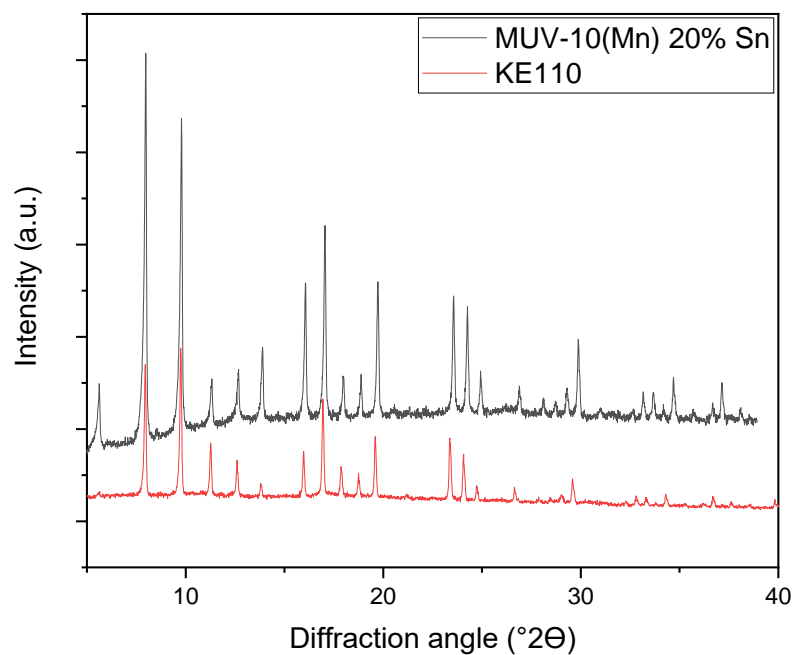


Figure 5.32: Overlaid powder XRD patterns of MUV-10(Mn) containing 20% Sn before and after (KE110) catalysis.

Therefore, washing the sample in chloroform after catalysis and seeing if the NMR showed a larger quantity of product being released was tested. This did not occur, and so IR was completed on the MOF before catalysis and after catalysis, in order to see if something strongly bound was present in the pores.

The overlaid IR are shown below in Figure 5.33, where additional peaks are present in the MUV-10(Mn) sample after catalysis (KE117). There are additional peaks between 3500-2750 cm^{-1} , which can be attributed to O-H stretching, and an additional peak at around 1750 cm^{-1} , which can be attributed to C=O stretching.⁸ Therefore, it is possible to attribute the loss of the low angle peak on the XRD patterns after catalysis to the blocking of the pores. The cyclic carbonate product is the thermodynamic product of the reaction between CO_2 and epoxides, however other products also form from this reaction, including metal alkoxides, which is therefore another reason why complete selectivity is not achieved.⁹

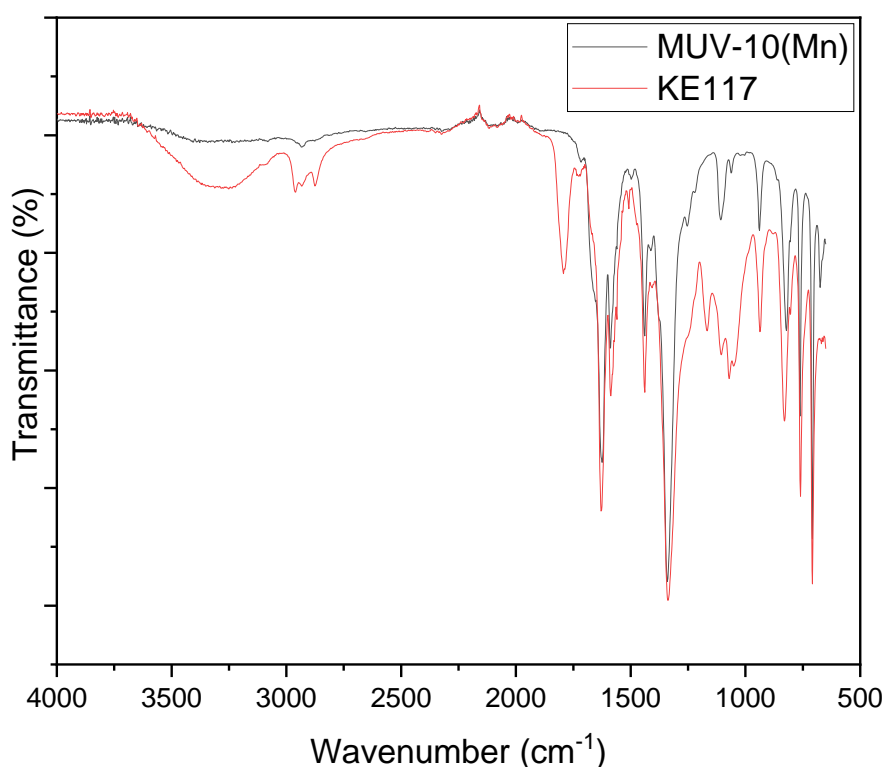


Figure 5.33: Overlaid IR spectra for MUV-10(Mn) before catalysis and after catalysis (KE117).

A final assessment on the use of the MUV-10 materials for the conversion of epoxides using CO₂ to cyclic carbonates involved looking at the recyclability of the catalyst. When 50 mg MUV-10(Mn) were used at 60°C for 3 cycles at 24 hours each, conversion and selectivity were not compromised (Figure 5.34).

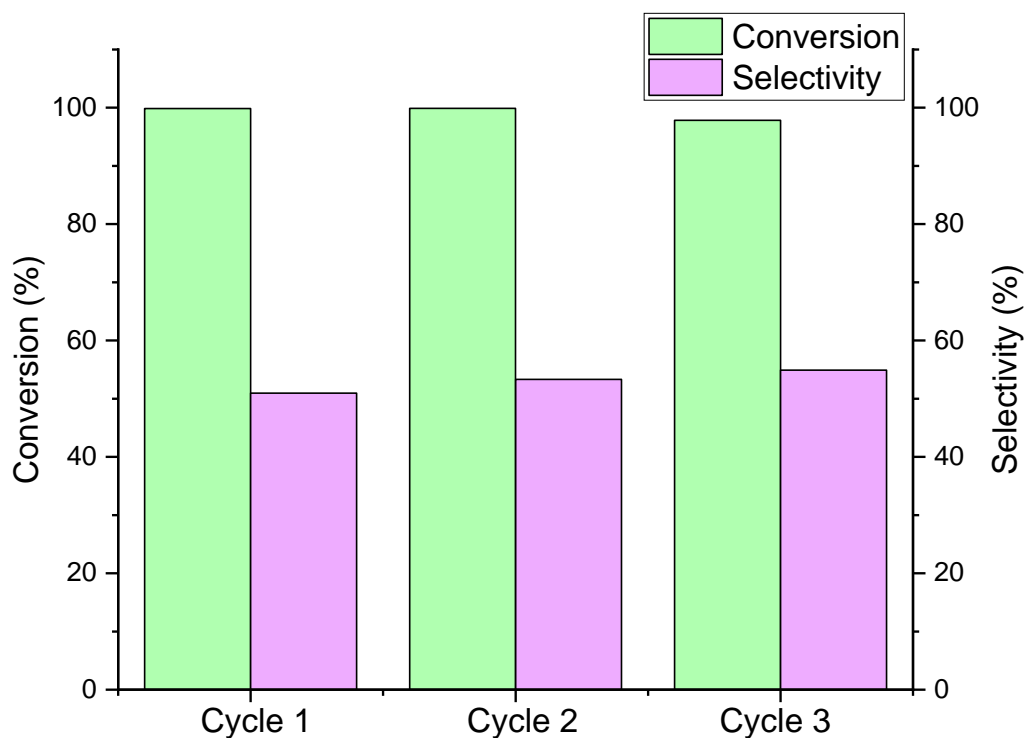


Figure 5.34: A graph to show the recyclability of MUV-10(Mn) after 3 cycles as a catalyst in the conversion of epichlorohydrin to a cyclic carbonate product.

In addition, the powder XRD pattern of the MOF after catalysis showed that the structure remained stable for three cycles, therefore making it an appropriate candidate for further investigation on an industrial level (Figure 5.35).

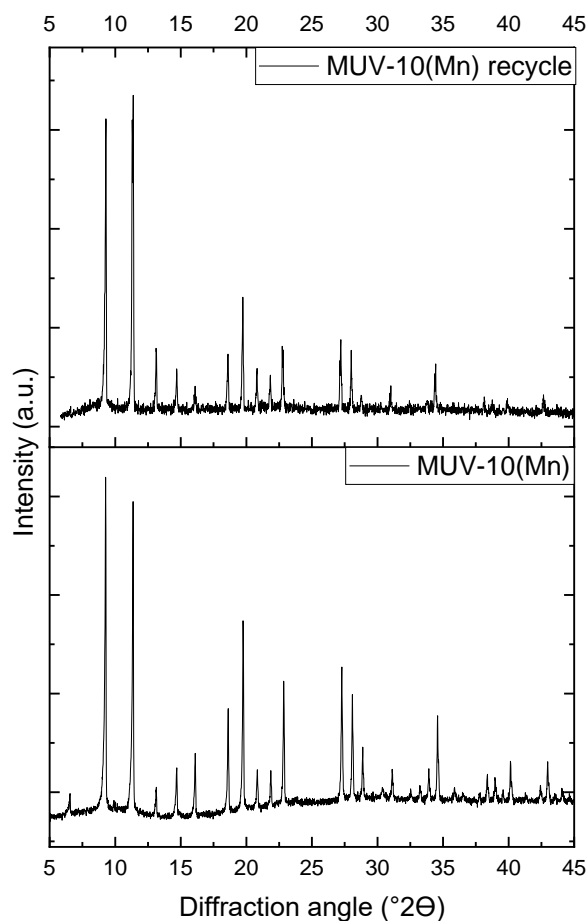


Figure 5.35: Powder XRD patterns for as-synthesised MUV-10(Mn) and MUV-10(Mn) after three cycles of converting epoxide to cyclic carbonate at 60°C.

5.5 Conclusions

The first application investigated was using MUV-10 for the photocatalytic reduction of CO₂, which proved that the use of TEOA as a sacrificial electron donor can be detrimental when used with certain MOFs. TEOA has been reported previously with some materials, such as MIL-125-NH₂, however with MUV-10, it caused the MOFs to collapse. The catalysis and subsequent generation of formic acid that was observed, was confirmed by ICP-OES to likely be due to metal ions in solution. Compared to experimental values, the leaching of these ions catalysed the production of formate more efficiently than some reported MOFs (29.65 μmol/hr/g for MUV-10(Ca) and 31.42 μmol/hr/g for MUV-10(Mn) compared to 13.2 μmol in 10 hours for NH₂-UiO-66 and 8.14 μmol for NH₂-MIL-125). Future work could involve looking at alternative sacrificial electron donors since the MUV-10 materials otherwise should be highly

stable in acid and base, exhibit redox activity, and could offer good band alignment for the reduction of CO₂.

The next application that was investigated was the conversion of glucose to 5-HMF, where MUV-10 using 0.01 M of HCl proved to yield a greater amount of 5-HMF than the UiO-66 reference material. For experiments investigating the extraction of 5-HMF into a non-aqueous solvent and MIBK, MUV-10(Mn) showed that generally having Sn in the structure improved the glucose conversion and yields of 5-HMF that were extracted into each layer. Performance was also enhanced with increased substitution of Sn into MUV-10, and all materials were stable during catalysis and were able to be regenerated. The tuneability of MUV-10 means that the structure could be modified further to potentially offer even greater conversion and selectivity.

A final application that was investigated was the conversion of epoxides to cyclic carbonates using CO₂, where in the literature this approach has been shown to have industrial applications such as reducing the pollution associated with flue gas, and so is of importance to recent environmental concerns.¹⁰ MUV-10 offered excellent conversions, recyclability and stability during these epoxide conversion experiments. When 30 mg or 50 mg of MUV-10(Mn) containing 20% Sn was used, selectivity was better than a reported Ce reference material for the same reaction. Generally, the conversions with MUV-10(Mn) containing 20% Sn were also higher than the Ce reference. MUV-10 without any Sn also performed better generally in terms of selectivity and conversion than the Ce reference material. Compared to other MOF materials, MUV-10 has the advantages that it is water-stable and can operate in humid conditions, increasing its potential on an industrial level. In addition, MUV-10 can operate using lower loadings of co-catalyst, and using lower CO₂ pressures, providing further advantages compared to other materials.¹⁰ For example, various reported MOFs using epichlorohydrin as the starting material have required pressures ranging from 10-15 atm, such as MOF-5-MIX requiring 12 atm.¹⁰ This material also exhibits a much smaller surface area compared to the MUV-10

materials. Future work could involve further testing other temperatures, epoxides, co-catalysts and synthesis times to find even better conversions and selectivity.

5.6 References

- 1 H. Abdullah, M. M. R. Khan, H. R. Ong and Z. Yaakob, *J., CO2 Util.*, 2017, **22**, 15-32.
- 2 D. Sun, Y. Fu, W. Liu, L. Ye, D. Wang, L. Yang, X. Fu and Z. Li, *Chem. - A Eur. J.*, 2013, **19**, 14279-14285.
- 3 Y. Pellegrin and F. Odobel, *Comptes Rendus Chim.*, 2017, **20**, 283-295.
- 4 W. Guo, H. J. Heeres and J. Yue, *Chem. Eng. J.*, 2020, **381**, 1-13.
- 5 R. Oozeerally, D. L. Burnett, T. W. Chamberlain, R. J. Kashtiban, S. Huband, R. I. Walton and V. Degirmenci, *ChemCatChem.*, 2021, **13**, 2517-2529.
- 6 S. Payra and S. Roy, *J. Phys. Chem. C.*, 2021, **125**, 8497-8507.
- 7 C. M. Miralda, E. E. Maclas, M. Zhu, P. Ratnasamy and M. A. Carreon, *ACS Catal.*, 2012, **2**, 180-183.
- 8 Merck, IR Spectrum Table & Chart, <https://www.sigmaaldrich.com/GB/en/technical-documents/technical-article/analytical-chemistry/photometry-and-reflectometry/ir-spectrum-table>, (accessed August 2022).
- 9 L. Liang, C. Liu, F. Jiang, Q. Chen, L. Zhang, H. Xue, H. L. Jiang, J. Qian, D. Yuan and M. Hong, *Nat. Commun.*, 2017, **8**, 1-10.
- 10 S. G. Musa, Z. M. A. Merican and O. Akbarzadeh, *Polymers.*, 2021, **13**, 1-32.

Chapter Six

Conclusions and Future Work

6.1 Introduction

In this chapter, the previous results chapters are discussed in terms of their key findings as well as future work suggested to give greater understanding of the structures and properties of the MOFs that have been studied. Many promising results have been obtained throughout this project, with scope for further work to be completed that ultimately can contribute to a more sustainable future.

6.2 Modifications to MUV-10: Conclusions and Future Possibilities

In Chapter 3, modifications to an existing MOF, MUV-10, were completed. It was shown for the first time that Sn(IV) could successfully replace certain amounts (5-25%) of Ti(IV), although 100% replacement was not possible as shown by an amorphous XRD pattern. The series of successful substitutions were verified by many techniques including XRD, XPS, EXAFS and XANES.

Some attempts were also made to exchange some of the Mn(II) or Ca(II) for other metal +2 ions, which were unsuccessful. Another alteration was the exchange of some of the trimesate linker for either 2-aminoterephthalate or 5-aminoisophthalate. These substitutions yielded a series of coloured materials with slightly modified band gaps, where it was hoped these could later be used in photocatalytic reduction experiments. XRD data and other analysis implied that it was likely a series of surface-modified versions of the MUV-10 material had been synthesised.

Therefore, several possible directions have emerged from this work. In terms of Sn substitution, more samples with higher percentages of Sn could be investigated. It would be interesting to find the limit of Sn substitution, since it was discovered that 100% substitution was not possible. These could then be used in some of the sustainable catalysis applications that are later mentioned in Chapter 5 of this thesis.

Other characterisation of these modified MUV-10 materials could also be completed. The characterisation of MUV-10 has been extensive in this project, however other techniques could have been used, such as solid-state NMR, looking at Sn nuclei. However, it is worth noting that this technique would have worked for MUV-10(Ca), but may be more challenging for MUV-10(Mn) due to the paramagnetism of Mn.

Overall, some promising materials have been developed, where further applications, particularly for the Sn-substituted MUV-10 materials, could be explored. The Lewis acidity of these materials makes them promising candidates for an array of sustainable catalysis applications. Some applications were examined in Chapter 5, and the possibility for future work here is discussed in section 7.4.

6.3 Attempted Syntheses of Novel Ti(IV) and Sn(IV) MOFs:

Conclusions and Future Possibilities

Many attempts were made to synthesise novel Ti(IV) and Sn(IV) MOFs, where Sn(IV) MOFs have not yet been reported in the literature to date. A range of different linkers with different features were selected, alongside different experimental conditions, in the hope that at least one combination could develop a novel material. Some promising samples were developed using Ti(IV) and 2,3-pyrazinedicarboxylic acid. The powder XRD pattern looks promising for this combination, however single crystal data is required for fuller structural analysis. This could be completed by further studying the reaction conditions, including altering the quantities of acid/base, the synthesis temperature, synthesis time and ratios of metal precursor to organic linker.

Other promising samples containing Ti(IV) and 1,4-naphthalenedicarboxylic acid and Ti(IV) and 2,6-pyridinedicarboxylic acid also required single crystals in order to get further structural information. The same methods as explored above could be used, and also consideration of the use of modulators or different types of experiments such as seed experiments could be further investigated.

A sample prepared from Sn(IV) and H₃BTC also appeared promising, however various attempts could not yield single crystals for full analysis and characterisation. Therefore, some additional attempts could be investigated, as mentioned previously with the Ti(IV) materials. Another promising sample was that using Sn(IV) and chelidamic acid, which ended up yielding an Sn(II) material which was deduced from single crystal XRD. Despite not being an Sn(IV) MOF, it would still be interesting to examine the stability of this material further, and to investigate some potential uses for it.

Other attempts to synthesise a novel Sn(IV) MOF could include investigating much larger linkers with more coordination points, in the hope that with more binding sites, the Sn(IV) would react faster with the linker than it hydrolyses to SnO₂.

Overall, many opportunities exist to develop further the synthesis of novel Ti(IV) and Sn(IV) MOFs for applications in catalysis, however it remains a challenge to avoid the hydrolysis of the metal precursors. So far, several options have been screened, but based on this work there is scope for some other combinations of solvents, reactant ratios, temperatures and more.

6.4 Sustainable Catalysis Applications: Conclusions and Future Possibilities

Chapter 5 examined some potential sustainable catalysis applications for the MOFs developed earlier in this thesis. The first application explored was the photocatalytic reduction of CO₂, where results initially seemed hopeful, however it was later revealed that the TEOA was causing the MOF to collapse, forming MnCO₃ or CaCO₃. It was discovered that leached metal ions were catalysing the formation of formate, where generated values were higher than many values reported from the use of MOFs in the literature. It was then hoped that a replacement to TEOA could be explored, however due to time constraints, this was not possible. Further work would focus greatly on finding an alternative sacrificial donor to TEOA that the MOFs would be stable in and could be recycled. One option could be to use 4-(2,3-dihydro-1,3-dimethyl-1H-benzimidazol-2-yl)-*N,N*-dimethylbenzenamine (BIH). Alternatively, different amounts of ascorbic acid could also be tried in this work, as only a few experiments were tried. One consideration that needs to be accounted for is the cost of the sacrificial electron donor, and therefore whether this is an economically advantageous route for CO₂ conversion, or whether efforts are better placed in other technologies. Additionally, other considerations could be taken in the different possible routes of activating CO₂ prior to use.

The experiments investigating using MUV-10 for the conversion of glucose into 5-HMF generated some interesting results. Of key significance was Sn-incorporated MUV-10 proving superior to the UiO-66 benchmark in terms of yield of 5-HMF, and proving superior to MUV-10 without Sn, for experiments completed in 0.01 M HCl. When MIBK experiments were completed, it became evident that generally having Sn in the MUV-10 structure improved glucose conversion and yields of 5-HMF extracted into each layer. Further modifications to the experimental procedure, such as investigating the reaction temperature, could improve the conversion and

selectivity further. In addition, further work should involve testing the recyclability of the MOFs in this application.

For the experiments converting epoxides to cyclic carbonates, MUV-10(Mn), MUV-10(Mn) containing 20% Sn, MUV-10(Ca), MUV-10(Ca) containing 20% Sn and a Ce-BDC-NH₂ reference material were examined. These materials, in particular the Sn-substituted MUV-10, showed great promise for this application. With refinement of the optimal synthesis duration and catalyst quantities, it is hoped that this material could produce extremely high conversion and selectivity when compared to existing MOFs for this process. So far, a direct comparison of the materials could not be drawn since the number of active sites in each catalyst differs and is not accurately known, however the Sn materials showed excellent conversion, selectivity and stability in experiments completed in this thesis. MUV-10 also offers the advantage of operating in less harsh conditions compared to some that have been reported in the literature. The recyclability of MUV-10(Mn) was also investigated, proving the MOF to operate for three cycles without compromise to conversion or yield. The experimental set-up has also shown a very simple yet effective system for converting CO₂ into useful products, whilst not requiring high reaction temperatures or large quantities of catalyst. Further work could include investigating altering the ratios of catalyst to co-catalyst required, and also investigating more temperatures to get the optimum conditions for high selectivity and conversion, as well as investigating effects on increased or reduced stirring. Further work into investigating the alternative by-products should also be completed, so that conversion is better understood, as well as identifying what appears to block the pores of the MOF during catalysis. Additionally, some more recycle tests could be included on the other MOFs for comparison. MUV-10(Mn) was selected as the focus for these experiments since it proved to have a wider range of pH that it was stable in, however, it would also be interesting to see how MUV-10(Ca) performs in more experiments. One final study that could be completed, could be to simulate flue gas, as has been done previously in the literature, to see how the catalyst would perform in a real-life setting. Scaling

up the existing set-up would also be interesting to observe any changes in conversion and selectivity.